UNIVERSITY OF HULL

Improving Thermal Performance of Buildings using Smart Inspections and Peltier-driven Heat Recovery

being a thesis submitted for the degree of Doctor of Philosophy at the University of Hull

by

Muhammad Hasan Shariq

MSc in Mechatronics, Newcastle University

BEng Hons. in Mechanical Engineering, Heriot-Watt University

July 2024

Publications

The following research outputs were produced during this PhD programme:

Papers Published / Accepted:

1. M. H. Shariq and B. R. Hughes, 'Revolutionising building inspection techniques to meet large-scale energy demands: A review of the state-of-the-art', Renewable and Sustainable Energy Reviews, vol. 130, p. 109979, Sep. 2020, doi: 10.1016/J.RSER.2020.109979

2. M. H. Shariq and B. R. Hughes, 'Real-time pixel-level fusion of colour and thermal (RGB-T) imagery via extrinsic optical alignment: Scope for automating building inspections', Proceedings of the International Conference on Evolving Cities, Feb. 2021, doi: 10.55066/PROC-ICEC.2021.30

3. M. H. Shariq and B. R. Hughes, 'Toward Zero-Carbon HVAC for Temperate Regions: Cooling using Thermoelectric Heat Exchanger - An Experimental Study', Proceedings of the 20th International Conference on Sustainable Energy Technologies, vol 1, p.138, Aug 2023 (Accepted: 05/08/2023)

Newsletter Contribution:

- M. H. Shariq and B. R. Hughes, "Automating passive wind tower to improve heat recovery efficiency through natural ventilation: Research and Development", World Society of Sustainable Energy Technologies (WSSET), Newsletter, Dec. 2021, p5-6

Acknowledgement

Firstly, I would like to thank the University of Hull for providing the opportunity and facilities to carry out this research. I extend special thanks to the funding body InnovateUK for the financial support that made this research possible.

I am deeply grateful to my supervisor, Professor Ben Hughes, for his guidance, support, inspiration, and valuable feedback throughout my PhD journey. His experience and insightful remarks have significantly impacted my professional development; his unwavering and optimistic confidence towards me greatly encouraged me to explore and implement innovative ideas, many of which are reflected in this Thesis.

Very special thanks to my wife, Amna, for her selfless and persistent motivation, understanding, and patience throughout. Thank you to all my colleagues, especially Harry, Sheen and Diana, for their valuable support and inspiration through this journey.

Finally, I dedicate this PhD to my parents, Mr. and Mrs. Shariq Rasheed, for their immeasurable encouragement, endless support, heartfelt prayers, and above all, their immense devotion to my upbringing that has led to this moment.

Abstract

Buildings account for 40% of overall carbon emissions in the UK which have significant impacts on the environment. The overconsumption of energy for heating and cooling is primarily caused by thermal leakages due to building defects. Existing techniques of building façade inspections are often manual, time-consuming and/or labour-intensive, while retrofit techniques like evaporative cooling windcatchers, PCMs, and Earth-to-air Heat Exchangers (EAHE) present massive installation and maintenance challenges.

This study first qualitatively investigates a smart building inspection framework using a novel instantaneous thermal-visible image fusion technique. The data capture results showed pixel-level accuracy invariant to parallax errors. The fused thermal-visible imagery was further evaluated using a self-supervised machine-learning model with pre-trained pseudo labels for defects. The results showed promising fault identification capabilities thanks to the collective visible-thermal information in each dataset.

The primary focus of this research is a detailed quantitative examination of the proposed Peltier-driven cooling mechanism designed for integration with a passive wind tower. This thermoelectric cooling (TEC) system uses heat pipes to rapidly absorb ambient heat through conduction, cooling the air as it passes through multiple layers of actively cooled pipes via convection. The cooling performance was examined and validated through CFD modelling and a full-scale prototype of the cooling unit.

Preliminary results showed a 3.66°C air temperature drop at a 50L/s airflow rate. Three augmentation techniques were proposed: a regulated damper before the cooler, an additional layer of cooling pipes, and an axial fan system to ensure necessary ventilation. In an adiabatic room model of 3m x 2.5m x 2.5m with the proposed TEC cooling through a wind tower, results showed up to 6°C of indoor cooling using the damper before the cooler and up to 8°C of cooling using all three optimisations in combination. This was achieved while maintaining a minimum ventilation rate of 47.9 L/s regardless of external wind speeds. This solar-compatible system promises a large-scale potential to reduce building HVAC loads.

Acronyms

ACST   Active Solar Cooling Technology

ANN   Artificial Neural Network

BEM   Building Energy Modelling

CFD   Computational Fluid Dynamics

CNN   Convolutional Neural Networks

CO2   Carbon Dioxide

COP   Coefficient of Performance

EAHE   Earth-to-Air Heat Exchanger

FDD   Fault Detection and Diagnosis

GHG   Greenhouse Gases

GPU   Graphical Processing Unit

HVAC   Heating, Ventilation, and Air Conditioning

IEA   International Energy Agency

LiDAR   Light Detection and Ranging

ML   Machine Learning

PCM   Phase Change Material

SfM   Structure from Motion

SSL   Self-Supervised Learning

TEC   Thermoelectric Cooler/Thermoelectric Cooling

TEG   Thermoelectric Generator

TEM   Thermoelectric Modules

UAV   Unmanned Aerial Vehicle

Nomenclature

c_p	Specific heat capacity (J/kgK)
h	Convection heat transfer coefficient (W/m^{2}K)
ΔT_r	Room Temperature difference (°C)
ΔT_p	Pipe surface temperature difference (°C)
T_r	Average room (indoor) temperature (°C)
T_p	Pipe surface temperature (°C)
T_{bp}	Temperature below the pipes (°C)
T_{SUP}	Supply temperature (°C)
T_{FA}	Fresh Air temperature (°C)
T_{EXT}	Extract temperature (°C)
T_{EXH}	Exhaust temperature (°C)
T_{ss}	Steady state temperature (°C)
T_{amb}	Ambient Temperature (°C)
ΔT_{avg}	Average pipe surface temperature (°C)
t_{ss}	Steady state time (s)
$\dot{m}$	Mass flow rate (kg/s)
$\dot{V}$	Volume flow rate (m3/s)
Q	Heat flux (W/m)
$\dot{Q}$	Rate of heat transfer (W)
P_i	Electrical power input (W)
V_i	Supply voltage (V)
I	Current consumption (A)
v	Air/wind velocity (m/s)
θ	Damper louvre angle (°)

Table of Contents

List of Figures

List of Tables

Chapter 1 - Introduction

Greenhouse Gases (GHG) are known to trap heat from the sun within the Earth's atmosphere. High emissions of GHG pose an extremely consequential and potentially irreversible risk to the Earth's climate and ecosystems [1]. Carbon Dioxide (CO_2), being the prime constituent of Greenhouse gases, is largely responsible for the global warming. This unwanted global temperature rise causes a range of negative impacts and dangers, such as the melting of polar ice caps, more severe weather events, excessive rise in sea levels, and ocean acidification [2], all of which have profound harmful effects on human health and safety.

The Industrial Revolution significantly escalated human-induced CO_2 emissions through burning fossil fuels for energy generation. During the last century, global CO_2 concentrations rose from the previously highest 300ppm to now over 400ppm [3] resulting in 82% of overall greenhouse emissions that are now comprised of fossil fuel related CO_2 emissions alone [4].

Figure 1 shows the impact of this rise in CO_2 emissions on the average global temperature since 1850 as a global average land-see temperature anomaly relative to the 1961-1990 average temperatures. Hence, decarbonising is now vital to prevent catastrophic environmental conditions in the near future. To accomplish that, it is important to understand what contributes most towards CO_2 emissions.
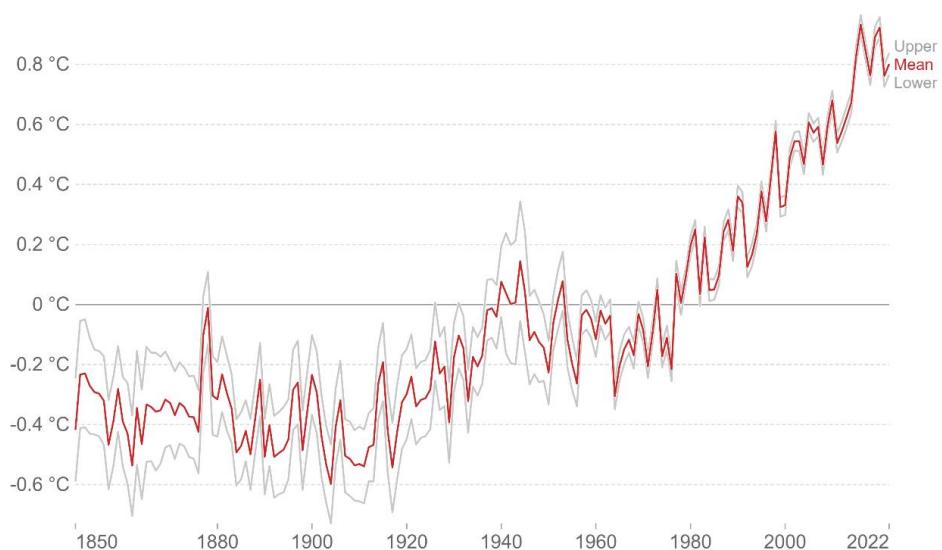
Figure 1 - Global average temperature anomaly due to global warming [5]

The buildings sector has a very large carbon footprint with both direct and indirect CO_2 emissions [6]. According to the 'International Energy Agency' (IEA) 2022, the built environment produces 40% of annual global CO_2 emissions [7]. Figure 2 shows the distribution of each building sector responsible towards this overall annual global CO_2 emissions. Industrial processes and space heating account for above 70% of energy consumption in industries [8]. According to IEA, around 75% of the existing building stock in Europe alone (i.e. 220 million buildings) is energy inefficient [9]. This shows that the major proportion of overall CO_2 emissions is directly associated with excessive amounts of unwanted heating and cooling in buildings. Moreover, over 75% of the overall building sector is expected to remain in use beyond 2050 [10], [11]. Hence, improving the energy performance of existing buildings not only helps lower the energy demands but is also one of the fundamental ways to reduce direct and indirect carbon emissions [12].
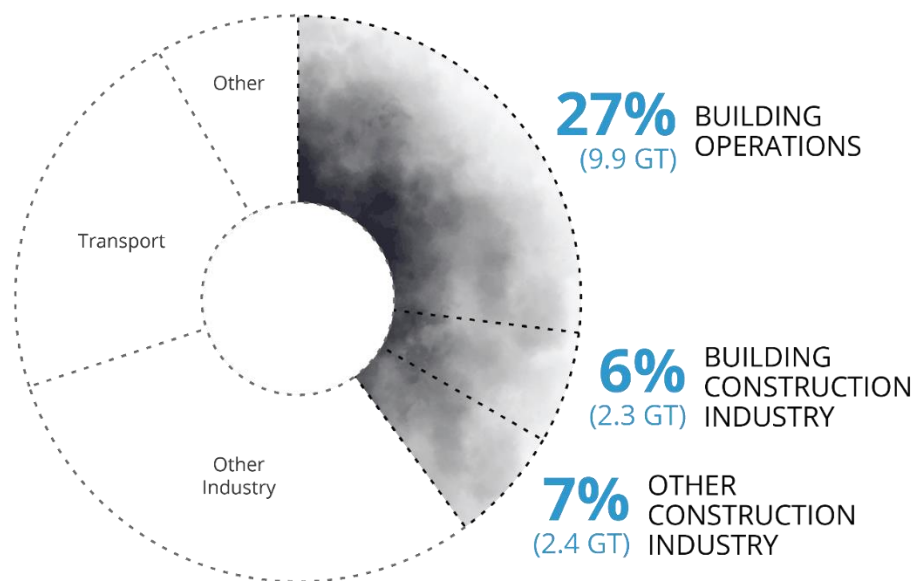
Figure 2 - Global contributions of various sectors towards CO_2 emissions [7]

Among building operations, space cooling is the fastest growing end use worldwide. The energy consumption due to space cooling has not only tripled since 1990 but is also expected to increase ten-fold in major countries by 2050 [13], whereas other sources of energy usage are projected to decline as depicted in Figure 3. Considering the potential threats to the world's climate due to rapidly rising energy demands and carbon emissions, a range of 'net zero' targets are legislated around the globe. Net

2

zero emissions refer to removing at least the same amount of emissions from the environment as they are emitted. China, the USA and Europe being the top 3 emitters of GHG with 26.1%, 12.7% and 7.5% of overall GHG emissions respectively, have established the carbon emissions target to reach net zero by 2050 [14][15]. However, to accomplish this, drastic measures need to be taken with a much larger-scale impact.
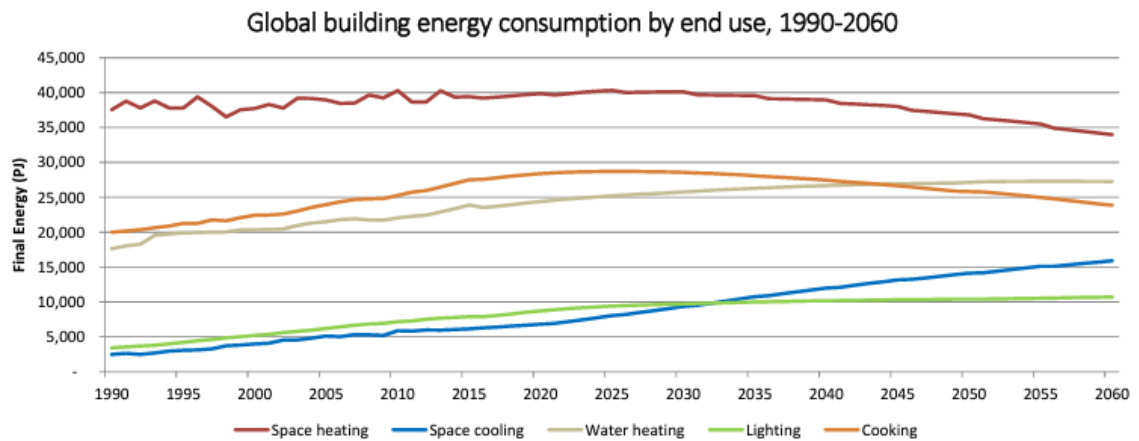
Figure 3 – Global building energy consumption by end-use 1990-2060 [13]

Decarbonising or reducing the energy consumption of existing buildings is a challenging and resource-intensive task due to its wide-scale nature. Hence, two different but complementary approaches are imperative to tackle carbon emissions in buildings, i.e. 1) Energy inspections to identify heat losses and implementing energy efficiency measures [12], and 2) Retrofitting renewable energy sources [16]. Prioritising building energy measures is crucial for maximising results with a significant impact. Likewise, for large buildings of the industrial and commercial sector that may require constant ventilation and/or where appropriate building insulation is unviable, the adoption of renewable energy sources for space cooling/heating and/or passive ventilation must be considered.

Building performance quantifies the sustainability of a building to be energy efficient [17]. Defects in the envelopes of buildings, such as air leakages, heat losses, moisture, damaged thermal insulation, etc. are the foremost reason that affects building performance [18]. These faults consequently increase energy consumption and the associated CO_2 emissions. There has been an increase in studies addressing heating and cooling in buildings and industries to substantially boost energy performances and

reduce carbon footprint. However, building thermal inspections, energy modelling and the corresponding adoption of energy-efficiency interventions at scale remain limited by the cost and time taken to survey relevant buildings and generate accurate models from high-granularity data on the building structure and façade. Existing manually intensive approaches to internal building surveys are invasive, inefficient and/or access-limited. This presents time and cost barriers to building energy inspections and modelling. Section 1.1 further details the drawbacks of existing inspection techniques while providing a brief overview of how this work aims to provide a qualitative solution to these limitations.

The retrofit approach to reducing building energy consumption, which is the primary theme of this thesis, is through the adoption of passive ventilation with a potential heat recovery mechanism. Most early architectural structures were designed with wind catchers (now more commonly known as wind towers), which provided ventilation as well as passive cooling to the interior of the building. The need for such passive cooling systems is again vital due to the rise in global warming with increasing cooling and heating demands and the associated CO_2 emissions. However, in more extreme climates, the addition of an energy-friendly active cooling system could provide a more sustainable, long-term, and large-scale solution to reducing building energy consumption. Section 1.2 discusses existing passive cooling systems with recent efforts to combine cooling/heating mechanisms for harsh environments.

1.1 Building Inspections

In the building sector, energy inspections play a vital role in the detection of building defects with the promise to reduce overall energy consumption and associated carbon emissions. These defects commonly include heat losses, moisture, moulds, cracks, spalls, etc. An infrared thermal camera is typically used to observe temperature differences on the façade/surface to detect potential areas of heat loss or moisture on building façades. Existing inspection techniques largely rely on a manual approach to identifying defects through thermal cameras that are time-consuming and labour-intensive [19][20][21].

Over recent years, there have been many studies in structural thermography primarily focused on detecting water/heat leakages and other faults in building envelopes that affect energy efficiency in buildings [22]. This includes a non-destructive means of inspection of the interior as well as the exterior of a building. Figure 4 shows a thermal image of a building façade with heat leakages using infrared thermography (IRT). The size and complexity of a building play an important role during an inspection. Hence, the efficiency of thermal analysis of buildings is not only limited to the resolution of thermography results or its accuracy, but also the speed of inspection and the cost.
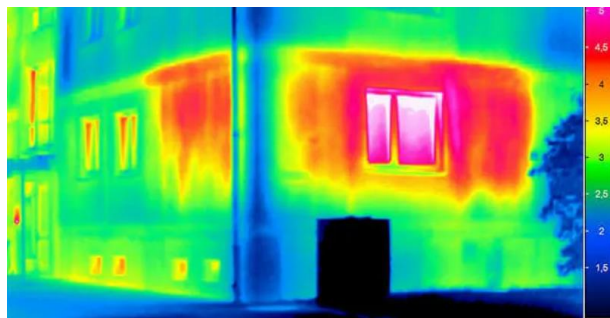
Figure 4 - Heat leakages on building façade using IRT [23]

During the last decade, UAVs (or drones) have increasingly been adopted for building inspections as they provide a low-cost, safer, and time-efficient solution to manually intensive inspections with more reachability to normally inaccessible areas. These drones are battery-operated and typically carry an optical and thermal camera for data collection. Recent developments in drone technologies allow a reliable pre-programmed autonomous building survey using a pre-defined path by the user that the drone follows without human interaction. This increases efficiency during a high-rise building survey as well as eliminates the risk of fatal accidents [24]. However, although the data is captured and collected automatically by the drone, the image interpretation remains manual and often requires enormous post-processing of raw data, which makes the process complex and time-consuming for the inspection experts after (or during) the data collection survey. This labour-intensive approach to qualitatively identifying building defects by comparing visible and thermal imagery is one of the key limitations in terms of the scalability of such inspections.

Machine learning (ML) provides an automated solution to identifying defects on various structural surfaces including building façades. ML techniques, similar to UAVs,

5

have also been progressively implemented for building inspections, especially for detecting and/or classifying cracks and other visible anomalies [25]. However, research related to ML for defect detection has focused exclusively on visible defects (through a regular camera) rather than hidden defects such as heat losses (through an infrared thermal camera). This inadequate research and development seen on Deep Learning (DL) for infrared thermal data is primarily due to the ambiguity in the thermal data in detecting (lack of) distinctive features observed in a potential heat loss or moisture. Besides, infrared thermal images are captured at a much lower resolution and reduced texture [26]. A visible-thermal image fusion would help with more accurate feature detection, however, it would also require an enormously larger training and testing data set and its associated manual labelling, while inevitably being highly computationally intensive.

To summarise, over the past few years, building energy inspection has seen notable advancements in its methodologies towards improving the efficiency of fault detection and diagnosis (FDD). A variety of approaches have been investigated for infrared thermography-based building assessment, focusing on the integration of image processing methods to enhance the visualisation of surface defects [26]. Meanwhile, Artificial Intelligence (AI) is becoming increasingly popular in FDD, although the area remains underexplored, despite its potential [27]. Several methodological and existing challenges originate from IRT in building energy audits to make inspections more time-efficient [29]. Unmanned Aerial Systems (UAS) have been a viable alternative to streamline the energy audit process, reducing the amount of manual labour required. However, the field of drone-based thermal inspections needs further research and standardisation [30], especially in terms of integrating automatic FDD systems [27]. Currently, a significant gap exists in developing an automated, adaptable, and cost-effective mechanism to address the energy crisis due to the building sector.

1.2 Heat Recovery and Passive Cooling

Heating, Ventilation and Air-Conditioning (HVAC) systems are commonly used in buildings to provide the necessary indoor thermal comfort. However, these mechanical systems are the largest energy consumers globally [28] with 32% in residential and 47% in commercial sectors [29]. These HVAC systems, which are typically powered by non-renewable energy sources, are prime contributors towards the rising CO_2 levels and resulting global warming. Consequently, this induced policymakers and researchers to explore environmentally friendly solutions against the rising demands and use of heating and cooling in buildings to mitigate CO_2 emissions.

One of the common and favourable alternate solutions is the implementation of passive ventilation, which utilises outdoor natural air to freshen indoor air quality and regulate temperatures [30]. This further aligns with the government policies and guidelines (such as ASHRAE [31], BSRIA [32], CIBSE [33], etc.) towards the importance of maintaining appropriate ventilation and air quality. Table 1 presents the causes and health impact of the most common contaminants in an indoor environment that are prone to develop due to a lack of ventilation. In recent years, there has been a rise in interest and the adaption of passive ventilation systems in buildings, such as the use of wind towers, especially after the health crisis caused by the COVID-19 pandemic [34].

Table 1 – Sources and health impact of common indoor-based contaminants [32]

Contaminant	Sources	Effects on health
Carbon dioxide (CO_2)	Combustion, breathing	Drowsiness, headaches, and dizziness at high concentrations.
Mould spores	Mould growth on damp surfaces	Sneezing, red eyes, skin rashes, asthma attacks
Viruses / Bacteria	Infected people	Short to long-term adverse effects from irritation through to death due to complications or susceptibility
Body odours	Building occupants	Discomfort, Psychological Stress

Wind towers (also known as wind catchers) offer a passive ventilation solution that works by utilising pressure differences created by wind forces [35]. Wind catchers have been used for centuries particularly in Iran and later in other Middle Eastern countries

to facilitate natural ventilation and passive cooling [36]. Various studies have emerged in recent years to utilise wind towers for space cooling and heating applications through the use of heat pipes to reduce or eliminate energy demands [37]–[39]. However, existing methods rely on capturing the heat from the exhaust stream of air and transferring it to the incoming stream. Figure 5 illustrates the pre-heating process using horizontal heat pipes incorporated passive wind tower. With no active elements to promote heating/cooling, the capacity of preheating (or precooling) fresh air is inevitably limited by the range of exhaust temperatures from within the room.
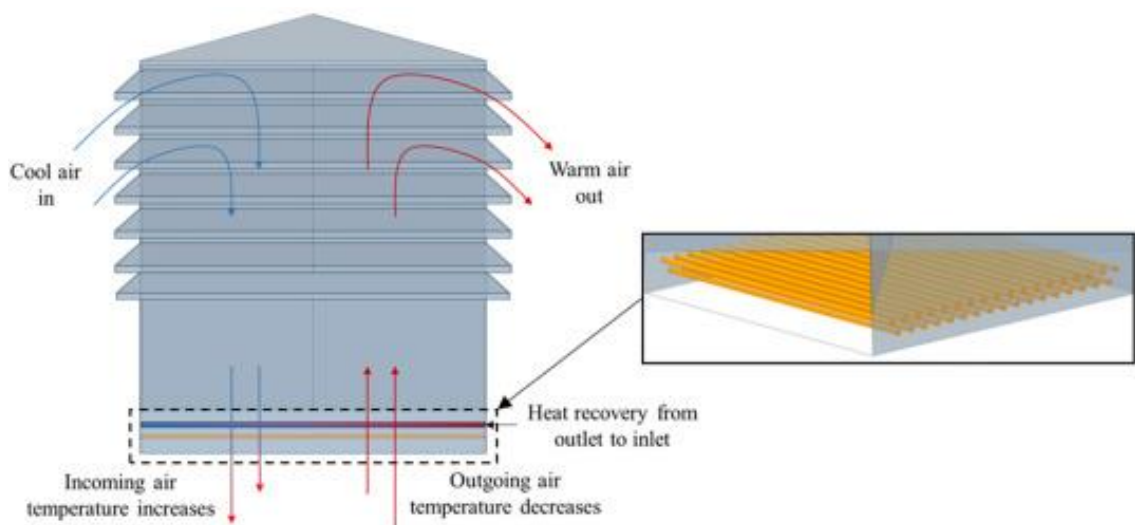
Figure 5 – Pre-heating of air through heat pipes inside a wind tower [37]

As a result, passive cooling alone will not effectively reduce CO_2 emissions in significantly hotter climates, and active approaches must be combined with passive cooling [40]. While HVAC systems could be powered by solar panels or other renewable sources, the initial investment and installation costs would be considerably large due to the number of units. Thermoelectric modules (TEMs), also known as thermoelectric coolers (TECs) in low-power applications, convert electrical power to produce a harvestable temperature difference across their sides. This environmentally-friendly technology has been frequently applied in recent years, particularly in hybrid heat recovery systems such as thermoelectric generators (TEGs) [41]. However, the research focus lacks the use of TECs towards building HVAC due to their low efficiencies [42]. Nevertheless, the integration of TECs with passive ventilation through conductive cooling of heat pipes shows promising potential to bridge this research gap.

In summary, wind towers provide a natural and energy-friendly potential to reduce the use of mechanical HVAC systems, however, the passive ventilation also limits the capacity of potential cooling in extreme ambient temperatures. There is a noticeable lack of research and development towards combining solar-powered active cooling techniques with the use of wind towers to replace existing HVAC systems. While thermoelectric modules are less energy efficient when used standalone, they do present the potential to leverage the thermal distribution using heat pipes to enhance their performance. This presents an opportunity for further research and development to facilitate a solar-powered thermoelectric-based active cooling (and heating) mechanism through wind towers.

1.3 Research Aim and Objectives

The overall aim of this research is to reduce energy consumption in buildings by first developing smart inspection methods to identify heat losses, and then providing an energy-efficient mechanism to integrate active cooling with passive ventilation to regulate thermal comfort.

The objectives to help achieve the research aim are:

1. Conduct a comprehensive review of existing works on building inspection techniques as well as active and passive cooling methods to identify gaps in the literature;

2. Develop an instantaneous, extrinsic method to superimpose thermal and visible images, aimed at reducing computational and hardware demands, and qualitatively evaluate its effectiveness in building inspection applications;

3. Integrate and examine conductive cooling of heat pipes with TECs and assess their cooling potential through physical experiments;

4. Assemble a full-scale prototype of a TEC cooling unit to validate CFD analyses for Peltier-driven convective cooling under varying external wind speeds.

5. Investigate optimisation strategies through the proposed TEC-based cooling in passive wind towers to enhance cooling capabilities in hot climates, aiming to achieve an indoor temperature reduction of at least 5°C below the ambient temperature.

1.4 Research Methodology

This research project explores two innovative approaches that aim to reduce energy consumption in buildings. The first approach targets buildings with no natural ventilation and proposes a smart building inspection technique. The second approach focuses on buildings that are passively ventilated (or ventilatable), aiming to enhance cooling with integration of an active Peltier-driven cooling mechanism.
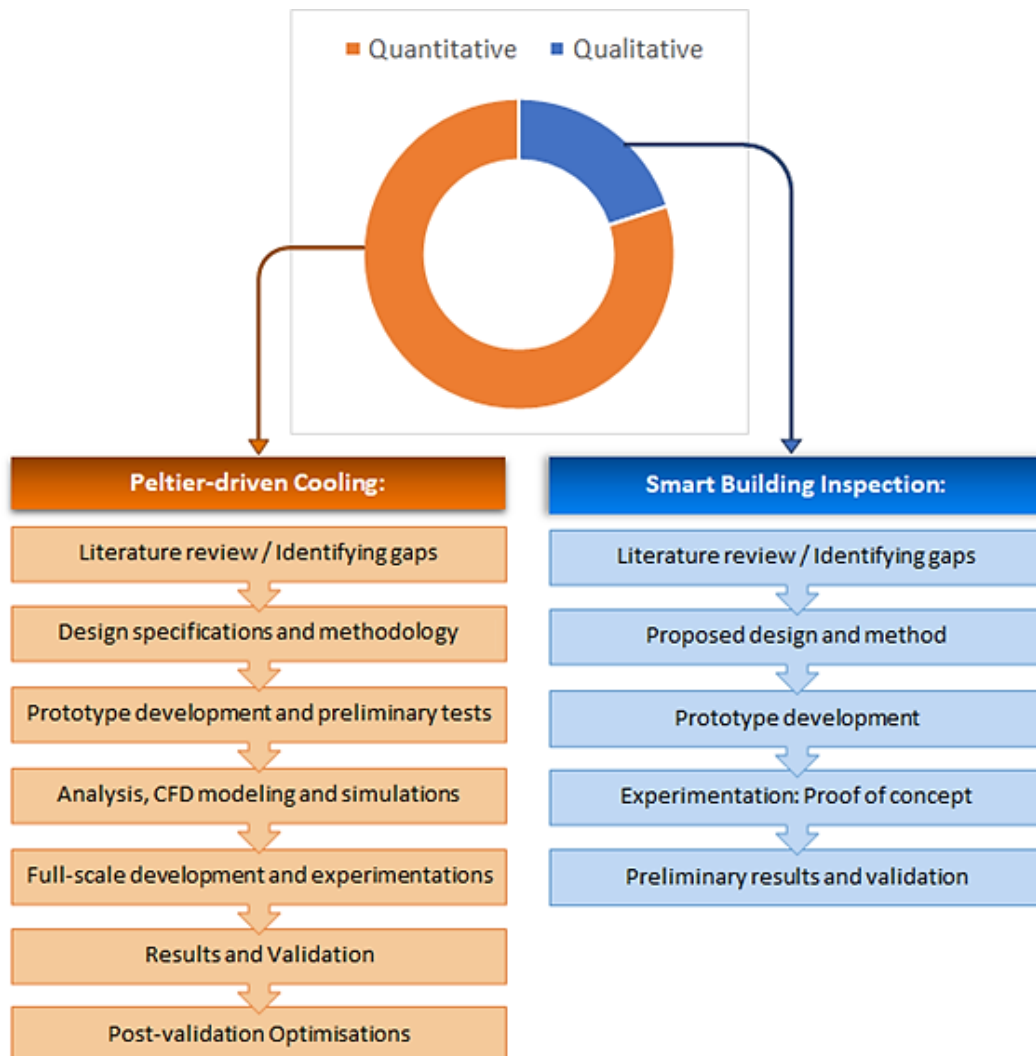
Figure 6 - Research focus and methodology

The research is divided into qualitative and quantitative methodologies. The smart building inspection method is investigated using a qualitative research, while the thermoelectric cooling system is studied through quantitative analysis. The primary focus of this work is on the quantitative aspect, which includes design, development, computational and experimental analysis of the proposed TEC cooling system.

Both research methodologies—qualitative for smart inspections and quantitative for thermoelectric cooling—are outlined in Figure 6.

1.5 Thesis Structure

The chapter-wise structure of this thesis is detailed below:

Chapter 1 provides an overview of the context and purpose of this thesis.

Chapter 2 presents a detailed literature review of relevant previous studies and developments, which highlight the research gaps that this thesis aims to accomplish.

Chapter 3 describe the methods for (1) smart building inspection, which discusses a thermal-visible image fusion technique followed by its qualitative proof-of-concept, and (2) Peltier-cooling, which uses thermoelectric cooling of heat pipes to develop a ventilation-assisted active cooling system for wind towers.

Chapter 4 defines the experimental and simulation methodology to study the Peltier-cooling approach. This includes setup and procedure for each experiment and the corresponding CFD simulation model.

Chapter 5 presents the experimental and CFD simulation results. The CFD results are validated through their corresponding experimental results as per the methodology defined in chapter 4.

Chapter 6 concludes the thesis while summarising the results and the outcomes from the overall aim and objectives of the research. Further opportunities derived from the findings of this research and development are also presented as future scope.

Finally, a complete list of references is compiled that is followed by the Appendices that are referred to in this thesis.

Chapter 2 - Literature Review

2.1 Introduction

This chapter aims to provide a detailed critical review of previous work related to reducing building energy consumption through various inspection techniques and passive/active cooling methods. A total of 132 papers have been reviewed, which are categorised into the following areas: (a) Building inspections, (b) 3D model reconstruction, (c) Heat recovery and cooling methods, and (d) Thermoelectric methods. These categories are reviewed in sections 2.2 to 2.5 in this chapter.

Finally, a summary of this review is then presented in section 2.6 which presents the key findings from the literature review and section 2.7 highlights the research gaps that were identified in the literature.

2.2 Building Inspections

2.2.1 Visible-Thermal Fusion

Thermal cameras detect infrared (IR) radiation that is emitted from an object's surface and convert it into a thermal image consisting of temperature gradients that can be interpreted [43]. A variety of studies explore thermal cameras to identify building defects. For example, Lagüela et al. [44] developed a technique to accurately map thermographic imagery onto digital imagery semi-automatically. Two thermographic images capturing the same region were first combined to register a thermographic mosaic and create a dense thermal image, which was then fused with the corresponding high-resolution digital (photographic) imagery using a dense surface modelling algorithm. This helped produce a high thermal- and geometric resolution of an 'orthothermogram' (a thermal 3D model) as shown in Figure 7. This method helps minimise time to qualitatively identify and assess a defect.
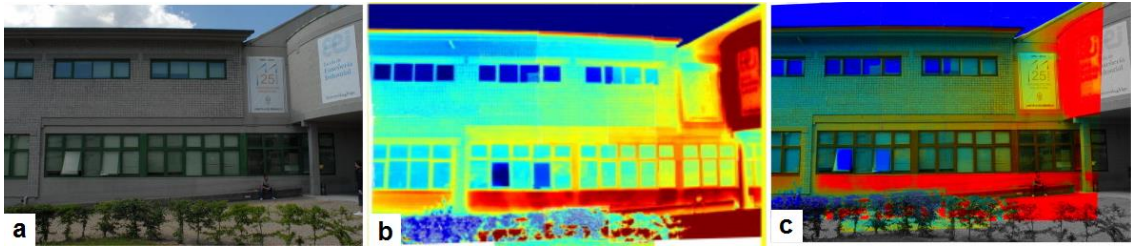
Figure 7 - (a) Visible camera image of a building fused with (b) its thermographic image to produce an (c) Orthothermogram [44]

The authors concluded that infrared thermography is a self-sufficient technique for building inspection if the thermographic imagery is presented on a digital 3D model. However, although it is applicable for both, indoors and outdoors, this approach is time-consuming considering an inspection of a large building due to terrestrial scanning methods.

Fox et al. [45] explored building defect detection using external and internal thermography. Their main focus was on building damages related to missing insulation, cracks, heat losses, thermal bridging, and moisture defects. The authors investigated and compared the traditional (i) walk-through thermography, in which the thermographer walks around the building while recording all external buildings, against the emerging (ii) 'walk-past' methodology, which requires the thermographer to capture the images of only the designated dwelling one at a time. Later, all images are compared together qualitatively. The authors concluded the walk-past method to be much quicker and cheaper to perform. However, this approach could be more efficient if the images were captured and compared digitally and automatically. The authors also acknowledged that despite a much greater number of defects detected using a walk-past approach, there were still many defects unfound since the thermography was performed from single external elevations.

Barreira et al. [46] and more recently, Cai et al. [47] investigated IRT passive techniques to detect and assess the effect of leakages in buildings. The latter authors outlined an energy-saving detection method for buildings' energy efficiency through thermal imager and infrared image processing. A digital image processing method was presented to effectively eliminate noise interference (of thermal imagery) through a

Butterworth low pass filter, which notably speeds up image processing and noise cancellation. This opens up a variety of opportunities and applications if this approach is built on, for example, employing an unmanned aerial vehicle for building thermography.

2.2.2 Machine Learning Techniques

This section will review recent investigations and developments towards building interior/exterior and/or civil infrastructure inspection (for defect detection) through image-processing techniques, essentially with the help of machine learning algorithms. A large number of studies have been carried out in recent years for the classification of defects from digital image data using computer vision and ANN (Artificial Neural Networks). Although computer vision techniques for remote building inspection have been investigated for more than two decades [48], due to more recent advances in computing power and handling of big data, Convolutional Neural Networks (CNNs) have been the backbone of most computer-vision decision making. Current developments and research that apply CNNs with computer vision for defect detection primarily aim to automate the process in order to reduce the time and cost of inspections [49].

Xu et al. [50] investigated a framework to detect cracks in metal surfaces through infrared thermal image processing. Previously, the detection of cracks on metal was performed manually by observing a complete thermal video, which was extremely time-consuming. The studied method used a superpixel algorithm to filter and process raw IR thermal imagery and identify cracks on metal surfaces automatically and at high speed. The authors proposed that this framework has a scope to be applied to other materials and applications to allow automatic, accurate and time-efficient inspections.

Galantucci and Fatiguso [51] proposed a non-destructive survey technique for historical buildings using digital photogrammetry, image processing and 3D surface model reconstruction. The authors used digital image processing techniques with an edge-extraction filter to identify cracks, lacks and erosions on scanned surfaces. The authors concluded that it was impossible to automate the fault identification process

without human intervention for validation. This is due to environmental factors, physical variables, inconsistencies in defect images, etc. Hence, it is evident that machine learning techniques (such as ANNs) need to be implemented in order to automate the fault identification process (to detect moisture and heat losses) with high accuracy.

In recent years, a large number of studies [52]–[58] used a CNN to fuse IR and Visible images. Liu et al. [59] developed a CNN-based Siamese network for infrared and visible image fusion. Their method used segmented image patches and their respective weight maps to construct fused images, however, the authors required additional image processing procedures to obtain the final fused images. Mustafa et al. [60], along with Li and Wu [61] proposed unsupervised learning based on an encoder-decoder framework to extract features and then automatically reconstruct the dataset into a fused image.

However, all of the above image fusion techniques are either time-consuming (needing post-processing steps) or require considerable computational resources (needing complex computations) to execute or both. For a general-purpose image fusion application, these limitations could be resolved using an FPGA or CUDA-based hardware [62] or other high-end general-purpose GPUs, nevertheless, for an ideal real-time low-powered automatic and aerial building inspection, these hefty methods cannot be implemented and there exist a lack of solutions that reduces both time and computational demands together.

Similarly, Wang et al. [63] investigated and developed a cost-effective mobile-enabled deep- learning-based automatic damage detection of historic buildings. CNNs were first trained for 30,000 iterations and 2.5 hours with 500 images of a variety of experimental cases that included spalling and efflorescence. High accuracy of CNN output with reliable and consistent identification was achieved to detect and locate spalling and fluorescence damages instantly. The damages on the surface/façade seen through a mobile (smartphone) camera were detected and identified by the CNN algorithm in real time. These damage types were highlighted and displayed on the mobile screen as shown in Figure 8. This instantaneous, cost-effective automatic fault

detection system is highly applicable for a potential real-time and roving fault detection for time- and cost-efficient qualitative building inspection at a large scale.

Figure 8 - Damages identified by CNN and shown in real-time via a smartphone [63]

Hoskere et al. [64] examined a vision-based post-earthquake structural inspection of civil infrastructure through CNN. The automated defect classification technique through computer- vision could identify spalling, corrosion, and various types of cracks in a structure with an accuracy of 86.7%. The authors suggested that this approach can be deployed on a UAV for an automatic and real-time structural inspection to reduce both time and cost during a large-scale inspection.

Similarly, Chow et al. [65] developed a deep learning-based framework for defect detection and inspection in concrete structures automatically. The authors used deep learning methods to detect façade defects such as cracks and spalling before combining this data into LIDAR-based model reconstruction for a complete BIM representation. Likewise, Chen et al. [66] combined a convolutional neural network (CNN) with the U-Net segmentation technique to detect cracks in building envelopes with high reliability and precision. However, both studies were limited to visible defects and did not apply to identifying thermal faults.

In relation to saving building energy, a novel deep learning-based fault detection approach to detect faults in a refrigerant flow air-conditioning system was investigated by Guo et al. [67] which performed an unsupervised fault identification framework with high accuracy. Hence, trained CNNs can certainly be used for the detection of a

larger variety of damages (using a larger training data set) in existing building envelopes, plus, the real-time wireless mobile-based damage detection feature notably allows the feasibility of a drone-based remotely controlled aerial inspection as well.

2.2.3. UAV (Drones) for Inspections

Aerial surveys that used fixed-wing aircraft or helicopters have been around since the 1980s [43]. However, in recent years, there has been an increase in the use of multi-rotor drones (or UAVs) for surveillance and monitoring applications [52]–[58] due to their long-ranged inspection, applications for aerial photogrammetry, efficient data logging, dynamic control, and mobility. One of the many challenges of such inspection is the ability of the drone to reliably perform in extreme and/or unknown environments. A variety of studies are reviewed that relate to drone operation in various building or structural inspections.

Lucchi [70] reviewed IRT-based inspections of buildings among almost 150 literature sources from the last fifty-five years. Different passive thermographic approaches; aerial, automated fly-past (i.e. via drone), street pass-by, perimeter walk-around, walk-through, etc. were compared. The author (in reference to Fox et al. [43], who referred to an older study [71] of 2012) reiterates that drones for energy audit pose a variety of drawbacks including vibrations, reduced spatial resolution and accuracy, the cost of equipment, and licensing restrictions.

Zorbas et al. [56] discussed a range of solutions to minimise costs in the operation of drone surveys, which primarily includes energy consumption. As the drone's altitude increases to observe a larger area, the energy consumption rises with it. The authors hence developed mathematical models to compute the optimal placement coverage area for a drone to hover to extract information about a target area. Several areas to further improve and optimise energy- consumption were also highlighted by the authors, including the possible addition of static sensors to enhance localisation. This presents an opportunity for an unmanned drone to perform thermographic 3D model reconstruction of buildings' interiors and façades efficiently by ensuring the longest

possible flight time.

Seo et al. [72] investigated a drone-based bridge inspection methodology for damage detection. In their study, a bridge and an abutment in South Dakota were inspected as a subject through a DJI Phantom 4 drone through which various damages were effectively detected through a real-time inspection. The authors observed an improved image resolution and damage detection capability as well as the considerably lower cost of the drone-based inspection compared to other conventional inspection methods. Similar aerial inspections can provide an effective solution to inspecting high-rise buildings and/or unreachable areas of a building envelope.

Yang et al [73], performed real-time mapping through a micro aerial vehicle. Their approach overcomes a variety of limitations including inaccessibility of scanning hidden areas, and real-time point-cloud mapping. The only gap, in the context of building inspection, is the lack of thermographic 3D modelling on the 3D reconstruction, which is an achievable integration as will be discussed in section 2.3.3.

Gao et. al [74] introduced a novel and low-cost approach to attain high-resolution imagery to produce ortho-images and topographic data of a terrain. Multi-view photogrammetry was used to compute three-dimensional vertices of homologous image points from two adjacent photographs of the target area. The authors managed to achieve a resolution of 0.065 of the digital elevation model (DEM) while capturing the images through a UAV. This helps in detecting faults/defects more effectively and accurately. However, despite this system being specifically designed to map and reconstruct terrains, this method has the potential to be applied to building exteriors for model reconstruction.

Similarly, Entrop and Vasenev [75] featured a real-time thermography approach by combining thermal sensors with a UAV in order to monitor, assess and detect flaws in building structures (through thermal imagery) remotely in real time. This innovative technique by the authors does indeed solve the time and cost problem in detecting flaws in building structures, however, the two major shortcomings of this process are that (1) the pilot cannot practically ensure sensing every portion of a large or complex

building, and second (2) due to lack of 3D mapping, once a flaw has been identified, there is no way to save, record or relocate the same location again except by remembering it. Hence, for a large, complex, or unknown target building, the heat/water leakages may not be relocatable.

Table 2 summarises the UAV-based inspection methods studied and/or employed by twenty recent studies (since 2016) specifically for building and/or structural inspections. This summary helps highlight and compare the features and focus of these studies.

Table 2 - Features of recent UAV/Drone-based building/structural inspections

Authors / References	Year	Visible Defects Detection	BIM / Model Reconstruction (Photogrammetry / LiDAR)	Deep Learning / CNNs	Thermal Defects Detection	Visible-Thermal Image Fusion	Real-time and/or Automatic Aerial Inspection
Ciampa et al. [76]	2019	✓	-	-	-	-	-
Chen et al. [77]	2021	✓	-	-	-	-	-
Serrat et al. [78]	2019	✓	-	-	-	-	-
Seo et al. [79]	2018	✓	✓	-	-	-	-
Khaloo et al. [80]	2017	✓	✓	-	-	-	-
Jung et al. [81]	2019	✓	✓	-	-	-	-
Bolourian and Hammad [82]	2020	✓	✓	-	-	-	-
Morgenthal et al. [83]	2019	✓	✓	-	-	-	-
Ribeiro et al. [84]	2020	✓	✓	-	-	-	-
Ellenberg et al. [85]	2016	✓	-	-	✓	-	-
Tan et al. [24]	2021	✓	✓	-	-	-	-
Tan et al. [86]	2022	✓	✓	✓	-	-	-
Entrop and Vasenev [87]	2017	✓	-	-	✓	-	-
Gopalakrishnan et al. [88]	2018	✓	-	✓	-	-	-
Chaiyasarn et al. [89]	2020	✓	✓	✓	-	-	-
Liu et al. [90]	2019	✓	✓	-	-	-	✓

Luo et al. [91]	2021	✓	-	✓	-	-	✓
Chow et al. [65]	2021	✓	✓	✓	-	-	✓
Jalil et al. [92]	2019	-	-	✓	✓	✓	-
Su et al. [93]	2022	✓	-	-	✓	✓	-

However, despite the promising scope of drone-based inspections for buildings, the research focus currently lacks the investigations to standardise an automated fly-past passive thermal inspection of building interiors and exteriors for fault detection [70]. In a detailed review of automated building inspection through drones, Rakha and Gorodetsky [94] argued that the innovation of drones with thermal cameras for surveying has presented a massive opportunity towards automated building inspection with minimal manual workflow and post-processing. This can allow speedy energy audits on large buildings at a considerably reduced cost.

2.3 3D Model Reconstruction

2.3.1 LiDAR

A three-dimensional (3D) model of the target building is typically required for identifying and relocating defects in buildings. This helps to map the exact location of all defective areas onto a three-dimensional model of the interior or exterior of the buildings to help visualise and inspect the defects quantitatively. Recently, a large amount of work has been done to optimise LiDAR sensing and mapping processes. The applications and purposes of LiDAR usually range from generating point clouds for three-dimensional (3D) modelling of indoors, and the exterior of buildings or structures, as well as for producing accurate elevation or topographic maps of farmlands, forests, waterways, etc. In this review, studies with laser scanning applicable for only building indoor and/or façades are examined.

For example, Garwood et al. [95] investigated the potential application of model reconstruction for Building Energy Modelling (BEM) by producing detailed 3D models of a large industrial building using the LiDAR-based terrestrial laser scanning (TLS) method. The authors had to capture 86 distinct positions manually around the building, which took five working days. Point cloud data of a single scan and the

combined fusion of 86 scans are shown in Figure 9. In addition to the time taken by the laser scanning, it also took an extensive amount of manual post-processing due to a large amount of data from the point cloud. The authors acknowledged that "an opportunity exists for increasing the speed of 3D geometry creation of existing industrial buildings for application in BEM and subsequent thermal simulation".
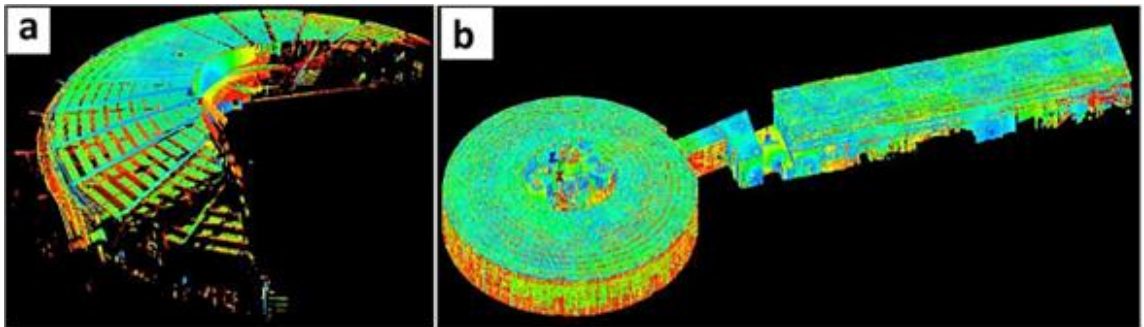
Figure 9 - (a) Point cloud data of a single LiDAR scan, (b) Fusion of 86 scans of the entire building [95]

A similar study was performed by Son et al. [96] with an emphasis on reducing the number of laser scans to achieve the same result. The authors managed to reduce the amount of laser scanning, and yet achieve the desired result, by mapping each nearby thermal imagery with a common point cloud data with the help of camera-based digital mapping techniques. Figure 10 shows the mapping of texture onto 3D point clouds and then the mapping of thermal imagery onto the 3D model. The idea works well for an average-sized building, however, this method of 'image matching' would take exponentially more time as the size or complexity of the building increases. This is because the graphics need to be mapped manually each time in order to generate a 3D model. Hence, despite the thermographic data mapping time is reduced, the overall time barrier has not been resolved.
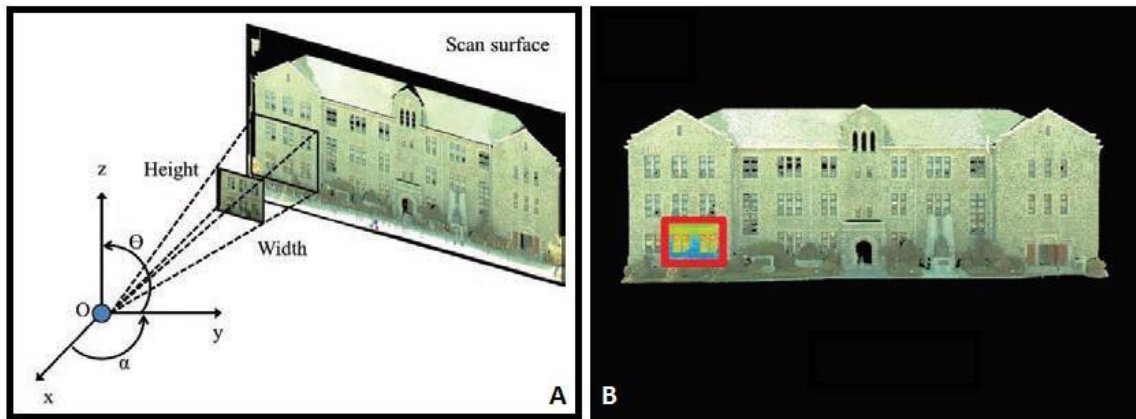
Figure 10 - (a) Mapping texture on point clouds, (b) mapping thermal imagery onto final 3D model [96]

To improve the time taken to produce 3D models, Ochmann et al. [97], in 2016, presented a parametric-based automatic approach for 3D model reconstruction from indoor point clouds. A 3D reconstructed model was produced that combined different scans from different rooms together to automatically detect the wall openings such as doors and windows. Although these methodologies reduced the time for post-processing, the approach however required laser scans from fixed positions in every room and a manual room segmentation to start the process. In their next research, the authors [98] presented a revised and novel approach to automatically reconstruct a completely volumetric 3D model of buildings from oriented point clouds. The new technique eliminated the need for manual room segmentation, as the authors integrated probabilistic assumptions to auto-detect room spaces, walls, doors, etc. This approach, however, is not applicable to reconstructing exterior of buildings.

In a very recent investigation by Zhan et al. [99], a 'diffraction optical element' (DOE)-based structured-light method has been proposed to capture 3D objects as point clouds with extremely high resolution. This method relies on structured laser patterns to capture perfectly aligned grid points of the object and then applies a pre-trained 'convolution neural network' (CNN) to identify pattern-element. This helps construct a highly accurate 3D model of the scanned object. Although the results show great potential in 3D scanning for a variety of applications, this technique also requires scans from fixed locations and will be too time-consuming for scanning a building for inspection purposes.

22

To enable a mobile LiDAR system, Park et al. [100] investigated and proposed a unique solution to the motion distortion in LiDAR scanning, which can help in efficient loop closures during mapping. The authors used LiDAR fusion for a Continuous-Time Simultaneous Localisation and Mapping (i.e. CT-SLAM) system using local mapping for continuous-time trajectory, and global mapping for loop closure and global map building. The experiments proved that with the help of simultaneous map fusion and continuous-time trajectory, the measurements storage to obtain an optimised 3D model is no longer required, and motion distortion can be effectively compensated in real-time, which makes this framework time- and cost-effective. However, the amount of computing resources required to process the data presents many challenges for rapid inspection of buildings at a larger scale.

While LiDAR surveying and mapping provide the best accuracy and high-density results [101], a range of real-world applications where LiDAR is being deployed pose a variety of challenges. For example, the continuous real-time optimisations (such as loop closures, motion distortion and sparse data correction) [100] as well as post-processing (such as data refinement, noise and misalignment correction and 3D mapping) [95] demand high computing power and processing time. Hence, laser scanning for building energy audit applications shows lesser scope for large-scale inspection, where a speedier and less memory-intensive solution is highly preferable.

2.3.2 Photogrammetry

In recent years, technological advancements in digital imagery, stereo vision, RGB-Depth (RGB-D) cameras, and image-mapping algorithms have provided a massive scope for photogrammetry in three-dimensional (3D) model reconstruction. Photogrammetry is a mature technology that has existed for over a century [102]. It relies on 'Structure from Motion' (SfM) and image-stitching techniques to capture, and stitch overlapped images to form a 3D model of a targeted scene. A variety of photogrammetric methods have emerged in the last decade that aim to provide a low-cost and high-resolution possibility to real-time 3D scanning and mapping for a large range of applications [103] including building interiors and façades. Three of such photogrammetry methods, i.e. (a) Monocular photogrammetry, (b) Stereophotogrammetry, and (c) RGB-D

photogrammetry are reviewed in the following sub-sections.

2.3.2.1 Monocular Photogrammetry

In 2015, Kaufman et al. [104] presented a technique to produce a 3D model of a static object through a regular DSLR camera by digitally combining multiple photos taken from different angles around that object. The authors achieved this without any complex hardware or software using a two-DoF turntable that captured multiple images at different angles. The images were then filtered by masking them from the background, and a 3D photo-textured mesh image was formed with the help of an image processing software called PhotoScan Pro. The authors managed to produce a detailed and textured 3D model of an object through a single DSLR camera, a simple setup, and user-friendly software. However, this technique was only applicable to small and portable objects that can be placed and rotated on a turntable.

However, with the advancements in computer vision and open-source photogrammetry algorithms, Pizzoli et al. [105] developed a technique to produce dense and accurate point clouds with depth maps through a single moving camera. This probabilistic monocular depth measurement method allowed a real-time 3D mapping of the surroundings. Figure 11 shows a 3D dense map being produced in real-time as it is being scanned through an ordinary camera. The lack of any additional sensor (such as IR depth) helps in low memory usage and faster processing of 3D reconstruction. This feature shows high potential in 3D mapping of large-scale buildings through remotely controlled mobile robot or an unmanned aerial vehicle (drone) with an on-board processor for all the computational tasks. In the context of building inspections, fusing thermal imagery with the camera result (or stitching beforehand) would require more concurrent memory requirement, which will reduce the speed of construction. However, a delayed real-time model reconstruction that requires moderate computational memory and low cost is certainly more applicable and beneficial in large-scale building inspection than a near-instant reconstruction with heavy computation and high cost.
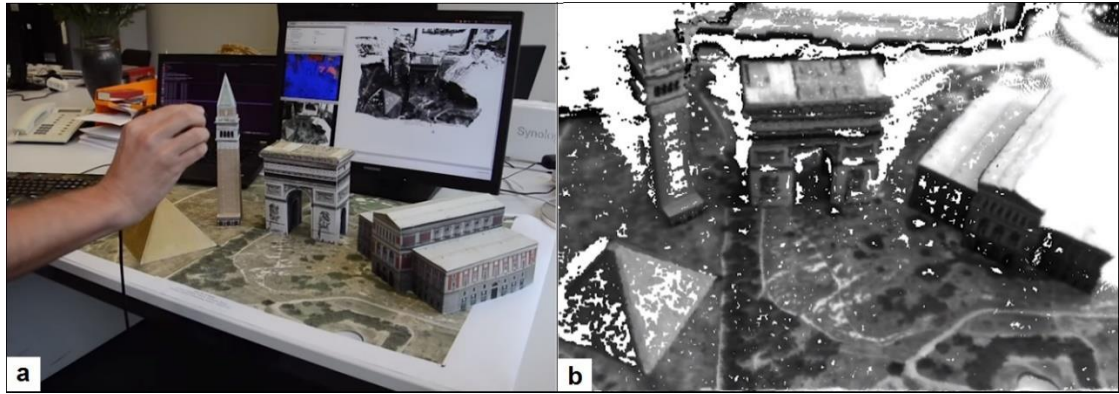
Figure 11 - Dense 3D point clouds and model reconstruction of a building model (a) scanning by hand with (b) real-time results [106]

Similarly, Schöps et al. [107] proposed a smartphone-based real-time monocular model reconstruction technique that performs all its computation through the GPU of the mobile device. This near-instant reconstruction allows the user to visualise the areas that are yet to be reconstructed. Although, the low-resolution (i.e. 320 × 240) of stereo images helps in achieving a low computationally intensive and rapid 3D model reconstruction, building inspection applications would ideally require a denser resolution. Considering the large-scale and outdoor adaptability of this approach, a low-resolution fusion of thermal and RGB images can still produce a comprehensible 3D orthothermogram that can be used for a quick qualitative inspection of building façades before proceeding with an extensive inspection or diagnosis, if necessary.

2.3.2.2 Stereo Photogrammetry

Krutikova et al. [108] investigated a 3D model reconstruction technique through stereo images. A human face was used as an example of a geometrically complex shape to produce its 3D model through two cameras (a small distance apart) that took pictures simultaneously. The distortion in the two images was resolved by locating and aligning two corresponding points of both images. A similar investigation that also aimed to reconstruct the 3D model through stereo images was carried out by Fu et al. [109], which showed more promising results. A novel spatial-temporal stereo-matching algorithm was developed using a space-time speckle projection. The authors' approach is highly time-efficient and can produce multiple 3D models accurately within a second, which shows potential to be applied for a speedy unmanned aerial inspection

of building exteriors.

A high accuracy stereo-based disparity map and 3D surface reconstruction were investigated by Hamzah et al. [111]. The authors introduced an improved stereo-matching algorithm that helped in reducing noise from image data obtained to ensure reliable results from pixel comparison before creating a disparity map. The authors concluded that this algorithm can be applied for 3D surface reconstruction for more accurate mapping through stereo vision images. Similarly, Hadfield et al. [112] presented a top-down approach for a similar stereo reconstruction. Figure 12 shows the output reconstruction of three random places in comparison with the ground truth images. The authors' technique of creating high-quality disparity maps is efficiently applicable in both indoor and outdoor environments.
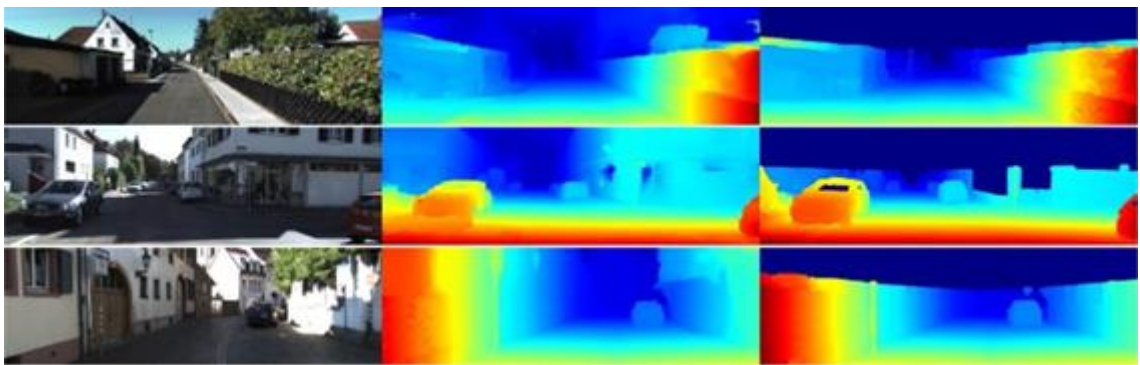
Figure 12 - Examples of the outdoor dataset with actual image (left), the output of investigated reconstruction (middle), and the ground truth reconstruction [112]

2.3.3.3 RGB-D Photogrammetry

Namitha et al. [113] explored 3D reconstruction through the Microsoft Kinect RGB-D sensor [114], [115]. A real-time Kinect Fusion algorithm was used to combine depth maps with the RGB colour information to create 3D point clouds. This allowed the 3D model to be reconstructed in real-time even in darkness. To optimise the use of Kinect sensors, especially for large-scale mapping, Esparza et al. [116] investigated and developed a tool that integrates multiple camera calibration with point cloud using the newer Kinect V2. The novel technique matches multiple 3D points from various Kinect V2 sensors to obtain intrinsic and extrinsic parameters for the cameras (sensors) while attaching the results accurately. This allows a 360-degree field of view for mapping in

real-time (if four Kinect V2 sensors are arranged 90 degrees apart) to reconstruct a 3D model of a room instantly, as shown in Figure 13.

Figure 13 – Point cloud fusion via four Kinect sensors [116]

Similarly, Zollhöfer et al. [118] investigated and analysed in detail the latest techniques for 3D reconstruction using RGB-D cameras. The authors outlined that more than a thousand papers have been published related to 3D RGB-D mapping since the release of the Kinect sensor. After analysing a variety of approaches for multiple scenarios and applications, the authors concluded that despite the developments, a range of challenges remain to be solved or retrofitted. Among these include (1) the need for more efficient methods for geometry optimisation, (2) the potential for applying 3D reconstruction in high-level applications, and (3) integrating machine learning, more specifically deep neural networks, on 3D data for qualitative and quantitative visual analysis to automate 3D reconstruction.

Guclu and Can [119] proposed a real-time 'Simultaneous Localistaion and Mapping' (SLAM) based mapping system through RGB-D sensors for large indoor environments. Through frame-to-frame motion key points filtration and feature matching algorithms, loop closures are performed before a map is produced in real-time using trajectory estimation. A detailed flowchart describing the proposed mapping algorithm is presented in Figure 14. The authors concluded that the framework allows large-scale and complex indoor environments to be mapped in real-time using CPU. Further improvements were suggested to improve the efficiency and speed of mapping includes the integration of deep features and implementation of this system on a Graphical Processing Unit (GPU) instead.
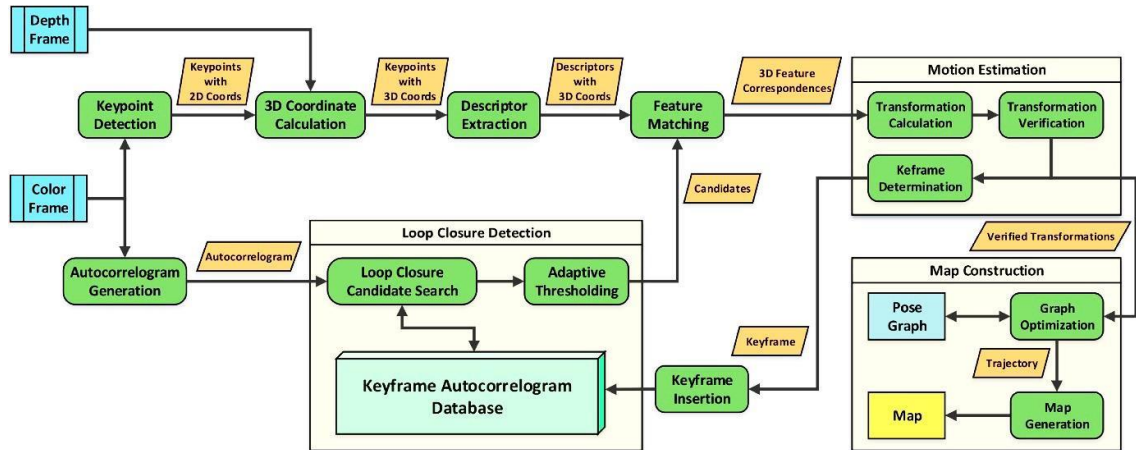
Figure 14 - Detailed RGB-D algorithm for 3D map reconstruction [119]

Although the monocular mapping technique is extremely low cost [120], it generally also requires a lot of post-processing time and high computational requirement [121], except if traded off for a lower resolution model reconstruction, which can be obtained in real-time [107]. While the stereo camera technique significantly reduces most of the heavy computational requirements, they are more applicable in real-time applications [109]. However, stereophotogrammetry is limited by parallax effects (non-matching pairs) in close-ranged mapping and non-planar environments, which causes inaccurate results [122].

This limitation is resolved through the RGB-D sensor that provides depth information along with colour imagery mapped together to produce a high-resolution 3D model. Mapping through RGB-D sensors, such as Kinect [114], not only provides a low-cost solution to 3D mapping but can also replace the need for LiDAR mapping in most applications, including aerial mapping through drones. Concerning building inspections, although none of the recent photogrammetry-based investigations incorporated energy modelling or inspection, some studies [105], [110] showed highly promising features that can be integrated to assist in real-time building energy modelling tasks. Hence, 3D model reconstruction (using photogrammetry techniques) superimposed with thermographic imagery (as discussed next in Section 2.3.3) can enable swift building energy modelling and help fill in these gaps.

2.3.3 Thermographic 3D Modelling

Recent developments towards building information modelling (BIM) have allowed building inspection to be performed non-destructively and time-efficiently. This is achieved through a virtual integration of building geometry during its inspection. Infrared thermography can be fused with point clouds of a building to produce a thermographic 3D model, i.e. an orthothermogram [44]. This orthothermography represents a 3D map of the façade or any building structure along with its thermographic texture (often with radiometric data) that allows defects, such as water leakages, heat losses, etc., to be detected and analysed effectively and remotely. The orthothermogram could be mapped through either laser scanning or photogrammetry.

Lagüela et al. [44], [123], [124] developed a novel framework to automatically map infrared thermal imagery onto point clouds of a building. Image processing was used on thermographic imagery and laser-scanned point clouds to align them to produce a thermographic 3D model. A flowchart outlining the process of creating textured as-built BIM and orthothermogram is shown in Figure 15 and resulting thermographic 3D models are shown in Figure 16. However, this method is not applicable for large buildings or indoor environments due to a lack of autonomy in mapping.
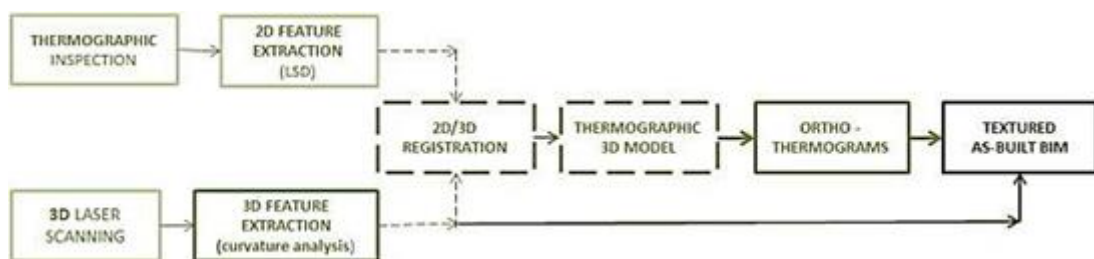
Figure 15 - The process to create 3D orthothermograms for BIM [124]

Figure 16 - Thermal 3D Model (left) and its corresponding RGB 3D Model (right) [124]

Wang et al. [125] outlined a hybrid method for thermal modelling using a LiDAR

system using existing building envelopes. A 3D laser scanner and an IR camera were used to map and produce 3D thermographic models from fixed scans. However, due to the huge amount of concurrent and post-processing with laser scanning, this thermographic 3D modelling approach cannot be applied in real time. This limitation can be addressed and resolved through a less computationally demanding methodology by replacing LiDAR with stereo-depth IR sensors to capture real-time depth maps using stereo photogrammetry, as discussed in Section 2.3.2.

Another similar framework was highlighted by Aguilera et al. [126] that fused point clouds from a 3D laser scanner with IR images to produce thermographic 3D models to study building energy performance. This orthothermogram is generated automatically using a feature extraction method from the registration of multiple IR and thermographic images. The results showed high accuracy in both 3D mapped results (with a point cloud resolution of 10mm) and thermographic and metric information (with 0.1ºC thermal resolution). However, this methodology would be unreasonably time-consuming for a large or complex building.

An indoor mobile robot-based mapping technique was examined by López-Fernández et al. [127] that combined infrared thermography with laser scanning to produce a 3D orthothermogram of indoor environments. A two-wheeled (plus castor) mobile robot was integrated with IMU and wheel odometry to autonomously navigate and scan walls through an IR thermal camera and laser scanner. After data acquisition and image-point cloud registration, a radiometric orthothermogram was produced of an indoor a building as shown from outside in Figure 17. With the advancements in drone surveying as discussed in Section 2.2.3, this inspection methodology can be integrated on a UAV to reconstruct high-resolution 3D thermal models and perform qualitative fault analysis on buildings indoors and exterior façades more accessible.
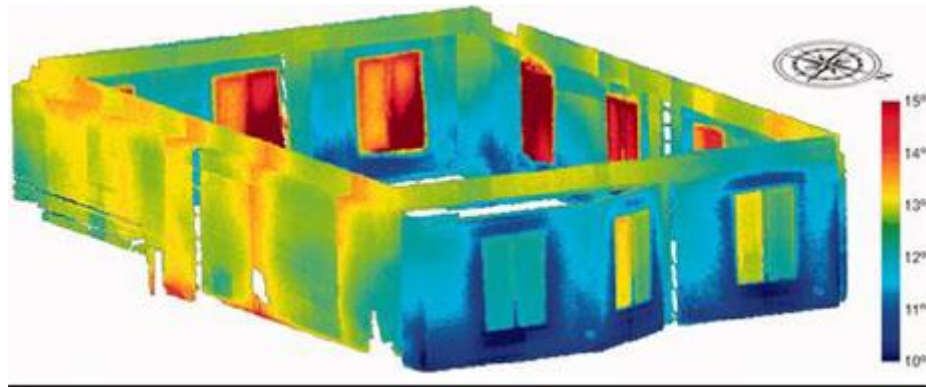
Figure 17 – External view of an indoor orthothermogram of a hall [127]

However, with recent developments in photogrammetric mapping, the 3D modelling technique through laser scanning can be replaced with photogrammetry to provide a more real-time and automated scope to thermographic BIM methodology [128]. Aguilera et al. [129] investigated a method to produce 3D thermal models to inspect building façades without the need for laser scanning. Thermographic images were mapped irrespective of their affine deformations such as scale, rotation, translation, tilt angle, etc. The resulting thermographic 3D model displayed both metric and thermal information. This novel technique allows a remote low-cost thermal inspection with high resolution and accuracy of point clouds (with ground sampling distance (GSD) of 15mm). The authors also highlighted a forthcoming challenge, which is to apply this framework to be performed using an unmanned aerial vehicle (UAV) to enable thermal inspection of the complete building envelope, especially for complex building structures.

Cao et al. [130] studied a real-time approach for thermographic 3D modelling by using an integrated depth and thermal sensor. Using an IR sensor and an RGB-D Kinect sensor [114], the authors implemented camera pose estimation and pixel alignment techniques to produce radiometric thermographic 3D models of the scanned objects (such as a human, chair, mug, etc.). The results present high-resolution radiometric information (±2°C) with a range of 0°C– 400°C. However, apart from a potential addition of mapped RGB imagery, further improvements are needed, especially towards increasing the range of sensing and mapping of walls, where changes in pixel information may be minimal, in order to enable such a framework for building modelling and inspection in real-time.

31

Müller and Kroll [131] also investigated a similar technique that utilised a depth camera, RGB camera, and a thermal camera to produce 3D point clouds texturised with thermal data. The authors performed experiments with a variety of conditions (such as sensing distance, reflections, thermal emissivity, camera movements/speeds, etc.) that could affect the accuracy of thermal 3D reconstruction through a hand-held 3D scanning approach. The results showed that the (1) rapid movement of the camera during mapping, (2) exceeding sensing distance of over 50m, and (3) non-perpendicular thermal sensing, all caused considerable errors and distortions in 3D reconstruction and/or its overlaid thermal representation. Although a close-ranged, slow-paced, normal-to-surface scan, would produce a high-fidelity 3D thermal reconstruction, this technique cannot be applied for building inspections as it will be immensely time-consuming and daunting. Similarly, Sels et al. [132] also achieved highly accurate results of thermal superimposition on 3D-mapped models. The authors used a structured light method (through a fixed projector) and an RGB-Depth camera to produce an accurate 3D reconstruction of various objects. Despite accurate thermographic 3D models, this technique is not applicable in real-time 3D model reconstruction since the structured light method requires stationary (fixed camera) scans for mapping.

A leading-edge development by Vidas and Moghadam [133] back in 2013 highlighted a novel solution to real-time thermal inspections for energy audits. The authors presented a handheld device, called HeatWave, capable of recording thermal and digital imagery while creating a photogrammetric 3D model of the scanned visuals in real-time. The light-weight handheld device consisted of an IR range sensor, RGB camera and a thermal camera and as it maps in real-time it enabled users to view an overlay of thermal highlights of the 3D reconstruction with and without the colour imagery. An example of this is shown in Figure 18. This system is a highly efficient solution to an energy audit of buildings in real time. However, with the limitation of the physical reach of humans, this device is not suitable for thermal inspection of a high-rise exterior of building structures or out-of-reach high indoor areas.
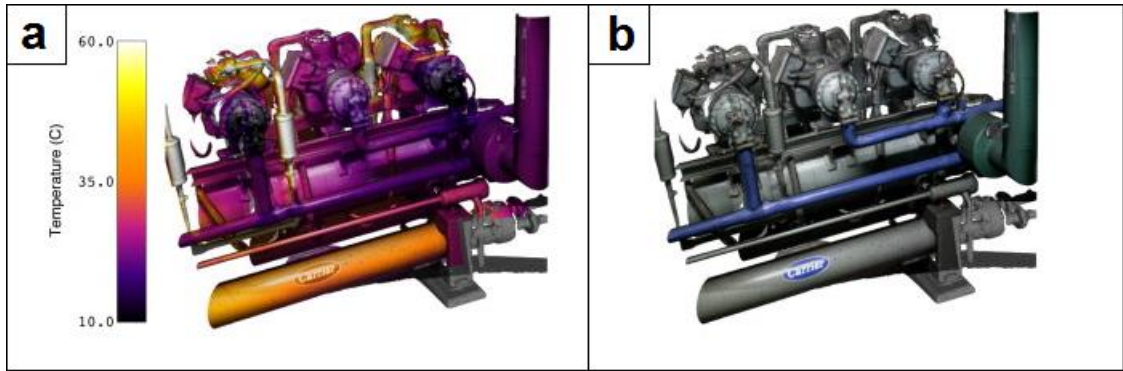
Figure 18 - 3D reconstruction of an HVAC system showing (a) superimposed radiometric data with thermal and only RGB model (b) scanned using HeatWave [133]

Although there has been significant research and advancements in creating 3D thermal models through LiDAR [44], [125]–[127], and an IR depth sensor, such as an RGB-D sensor [130]–[133], none of the techniques showed capability to thermal map and inspect large and complex buildings efficiently in terms of time. Hence, there is an evident need and scope for a non-handheld, aerial and ideally automated photogrammetric approach for a time and cost-efficient real-time building inspection and automated fault diagnosis.

2.4. Heat Recovery and Passive Cooling/Heating Methods

2.4.1 Wind Towers for Natural Ventilation

Wind towers, or wind catchers, have been a traditional architectural design in hot and dry regions such as the Middle East and Egypt [135]. These passive wind catchers, also known as badgirs, are typically designed (or installed) on roofs of buildings to provide natural ventilation and thermal comfort through cool air circulation [136]. The design and concept of such wind towers have evolved over recent decades, mostly by integrating modern technologies and state-of-the-art design strategies to enhance efficiency. Wind tower designs are typically with one-directional, two-directional, or four-directional openings.
Figure 19 shows a rectangular four-directional badgir in Iran.

Figure 19 - A four-directional bagdir (wind catcher) in Yazd, Iran [137]

During the last decade, numerous studies and developments have optimised the design and function of a wind tower. O'Connor et al. [138] investigated the integration of a rotary thermal wheel into a wind tower to improve heat recovery of the wind tower. The authors used a 1:10 scale model for wind tunnel testing and developed a CFD model that was validated with high accuracy. The system was able to raise the incoming airstream temperature by 2°C with a pressure drop of 4.33 Pa across the heat exchanger. The addition of a physical rotary wheel partially obstructed the flow; however, experimental results showed the airflow maintained above the recommended ventilation rates.

Kassir [139] designed and constructed cooling towers to passively cool outdoor courtyards at a University in Riyadh, Saudi Arabia. The dual-tower system leverages evaporative cooling with an automated control system to regulate auxiliary mechanical vents. These power-efficient towers were simulated using CFD and results showed a temperature drop from 46°C ambient to up to 34°C with a cooling capacity of 560kW. However, the design and mechanism of these cooling towers are limited to outdoor use as they rely on a large open space for air circulation. Hence, adapting this technique to cool indoor spaces within buildings would not be viable.

Research conducted by Grosso and Ahmadi [140] reviewed the application of conventional one-channel Iranian wind towers in temperate-hot climates. The authors examined and highlighted key factors that affect the performance of the passive cooling towers, such as their orientation, size, height and geometric design of inlet and outlet openings. This was done through simulation software (called SPERAvent) to assess the energy performance as a function of controlled natural ventilation (CNV). The authors concluded that the traditional Iranian wind towers can reduce cooling energy load by 43% to 61% annually. However, the authors also acknowledged that the cooling performance of such passive wind towers is highly dependent on their architectural design and environmental conditions.

To address this, recent studies focussed heavily on the design of the wind tower to optimise the ventilation and cooling performances. For example, Hughes and Ghani [141] showed through CFD analysis that the addition of a damper on a wind tower helps reduce short circuits and improves performance by 5%. The authors conducted another study [142] to explore the impact on performance with external angles of the wind tower louvres. With the help of eight CFD models to inspect the internal pressure and velocity profile using a range of louvre angles, the authors identified an optimal angle of 35° that provided the best ventilation performance. Hughes and Ghani [143] further investigated the optimal operating range of the angle of control dampers. The authors conducted 19 CFD simulations to conclude that the angle of 45° to 55° provides the highest rate of internal air movement.

Similarly, several numerical and experimental studies explored the geometric characteristics of wind towers to optimise their performances. Dehghan et al. [144] evaluated the ceiling tilt angle, Hoseinnia et al. [145] explored the channel partitioning and Crus-Salas et al. [146] evaluated the optimum cross-sectional shape and size of the wind catchers. Likewise, Alsailani et al. [147] analysed various geometrical structures at the inlet of a wind catcher to assess the effectiveness of ventilation in buildings.

Figure 20 shows three simulations of inlet wind flow that the authors employed to compare a nozzle-shaped inlet and a straight inlet with guide vanes against a reference structure with no modification.

While wind catchers promise natural ventilation and passive cooling, their performance and efficacy are highly dependent on ambient climate conditions [148]. For example, wind towers are least effective during times of minimal wind speeds, unfavourable wind directions, and extreme temperatures. To tackle this limitation, numerous studies focused on integrating various heat transfer devices such as heat pipes to wind towers.
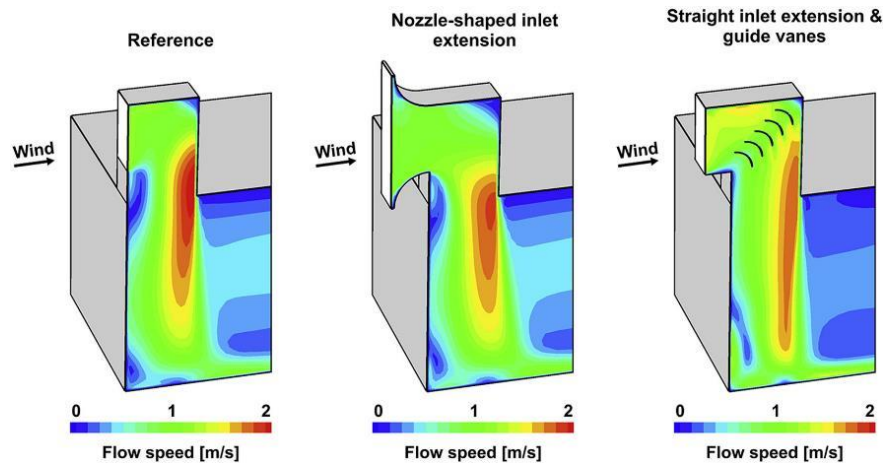
Figure 20 – Comparison of flow simulation across inlet structural designs [147]

2.4.2 Heat Pipe Integration

Heat pipes are passive heat transfer devices that can efficiently transport heat without the need for external power [149]. They consist of a sealed tube containing a working fluid, which evaporates and condenses to transfer heat from the hot end to the cold end [150]. An increasing number of research have employed heat pipes with natural ventilation systems. For example, Chaudhry et al. [151] investigated the passive cooling performance through the integration of heat pipes on a roof-mounted wind tower. The authors performed CFD simulations using ANSYS FLUENT to model with and without the integration of heat pipes. Although the heat pipes reduced the airflow, the minimum required fresh air intake of 10L/s per occupant was achieved. The results showed a passive cooling capacity between 6K to 15K. However, as the study relied on computational analysis, the authors acknowledge that experimental trials are necessary to confirm the efficacy of this system in natural climate conditions.

Similarly, Calautit et al. [152] studied the performance of a uni-directional wind catcher integrated with heat transfer devices (HTDs) as shown in Figure 21. The standard wind

catcher was used to compare the reduction of airflow and the cooling performance with the HTD. The experimental results showed high external wind speeds (of 5m/s) lowered indoor air temperature by 6K, while lower wind speeds (of 2m/s) showed more promising cooling potential as they lowered the temperatures by up to 9.5K. Overall, the proposed method showed as high as 12K of cooling potential, however, due to the addition of HTDs, external wind velocities need to be higher than 1m/s to be able to meet the recommended ventilation rates. As the study was based on wind tunnel testing using a prototype and its CFD validation, the authors acknowledged that full-scale field testing is necessary for further analysis and validation of their results.
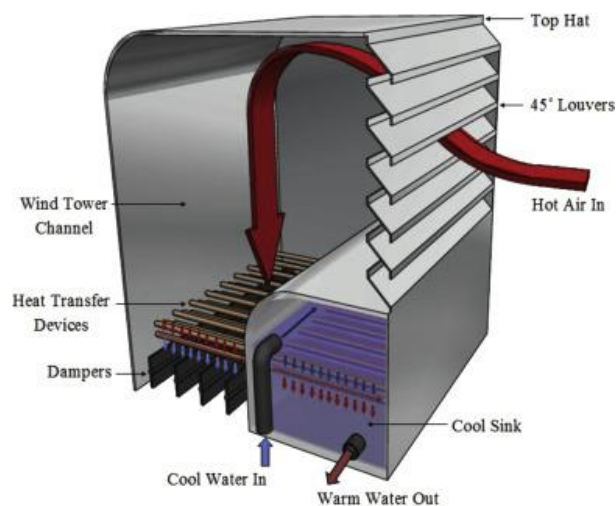
Figure 21 - Uni-directional wind catcher with heat transfer devices (HTDs) [152]

Hughes et al. [153] examined the potential of heat pipes as a means of heat recovery in domestic buildings. The authors used CFD-assisted multiphase flow with heat and mass transfer analysis to investigate an optimum size and geometrical configuration of heat pipes that would facilitate maximum heat transfer with the airflow. The analyses were performed with an inlet air temperature of 283.15K and an initial velocity of 0.25m/s while keeping the working fluid temperature constant at 293K. The simulation results concluded that an equal column pitch and diameter of the pipe deliver the highest rates of heat transfer. The simulation results showed a prospect of precooling air by 15.6°C and recovering 3.3°C. Although experimental tests were not conducted in this study, the experimental data from existing literature helped validate the results that show high prospects for reducing the HVAC loads.

With the promising potential of heat pipes towards heat recovery and passive heating, Calautit et al. [154] explored the integration of heat pipes in a traditional multi-channel wind tower for cold regions. The authors employed the pipes in a vertical arrangement of two layers on each quadrant to pre-warm the incoming fresh air. The study relied on a CAD model for CFD analysis as well as a prototype as shown in Figure 22. The vertical arrangement of heat pipes facilitated high ventilation rates even at low wind speeds of 1m/s and was able to raise the temperature of supply air by 4.5K. However, as the gravity-assisted flow of working fluid creates a thermal gradient across the heat pipes, this system is best suited for cold regions and would not be effective in pre-cooling warm air in hot climates.

(a) 3D CAD View   (b) Prototype Top View
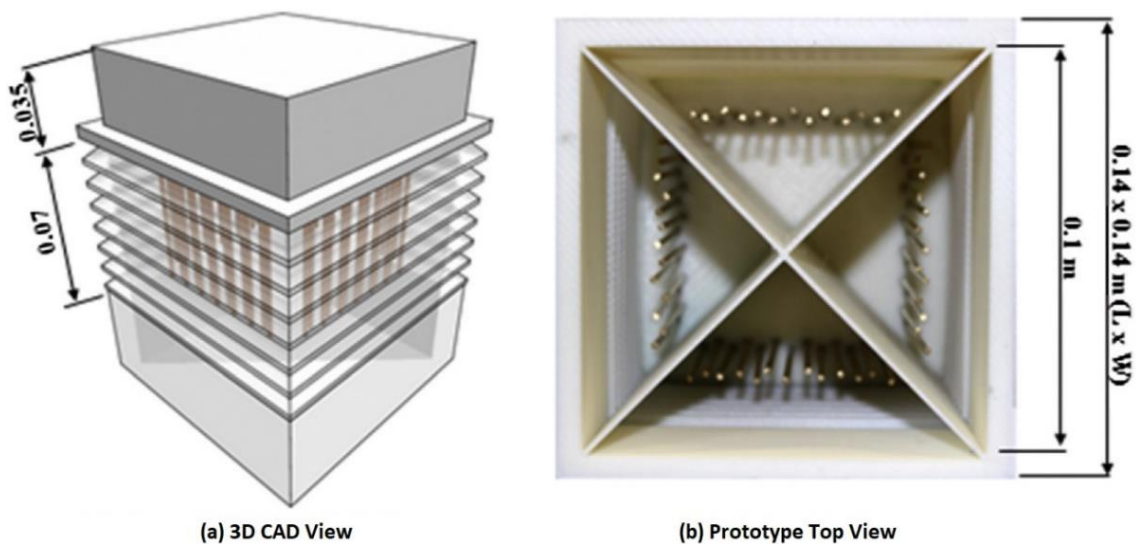
Figure 22 – (a) 3D CAD view and (b) Top view of the prototype with vertical pipes [154]

With the same geometrical specification of the wind tower, Harry et al. [155] investigated the ventilation rates and passive heating performance using heat pipes in a horizontal configuration. A total of 35 pipes were mounted beneath the cross divider of the wind tower in two layers. The authors used CFD simulations and numerical modelling to examine the airflow and heat transfer. The results showed that ventilation rates of 0.1m³/s were maintained at an inlet velocity of 1m/s. The horizontal arrangement of the pipes under the cross-frame facilitated a high rate of heat transfer to passively preheat the incoming air by up to 2.8°C. Though experimental testing was not performed to reflect on the performance with real-world conditions, the study showed promising scope to reducing energy demands. The

authors acknowledged that using seasonal thermal loop, the proposed system can be employed for passive cooling in hot seasons.

Similarly, Liu et al. [156] proposed a solid tube bank heat recovery device for the four-channel wind tower. The authors performed CFD-based wind tunnel simulations to determine the heat transfer performance of the solid tubes that were arranged horizontally in 7 layers in alternating staggered configuration. The study observed reduced air velocities, however, ventilation rates were still above the recommended levels with a minimum distance between the tubes of 60mm and a vertical distance of 25mm. With an initial external airflow velocity of 5.54m/s and average indoor and supply temperatures of 15.75℃ and 24.35 ℃, respectively, the proposed system was able to pre-heat the cold air by 2.44°C. The authors acknowledge that physical experiments are required to validate the CFD results.

2.4.3 Other Passive Cooling Techniques

As many studies examined heating potential through heat recovery using heat transfer devices with passive ventilation, there has been less focus on the cooling methods with natural ventilation for hot climates. Some of the previously discussed studies showed passive cooling prospects [151]–[153] [155], however, they lack experimental validation and are prone to counter-effectiveness in extreme hot climates.

Cooling indoor spaces in arid climatic regions while ensuring adequate ventilation has consistently posed a significant challenge [157]–[159]. Nevertheless, several recent studies have proposed innovative solutions to address this. For example, Ghoulem et al. [160] investigated a passive downdraught evaporative cooling windcatcher for greenhouses in hot climates. An evaporative cooling-based water spray system was proposed. The authors conducted CFD analysis and validated the results using previous experimental data to study the performance of the system against different ambient conditions. The results showed higher efficiency of the system in hotter and drier conditions with indoor temperature drop potential of up to 17.13°C. However, apart from the limited scope of theoretical results to reflect real-world conditions, the proposed oversized system for greenhouses would pose cost, architectural and installation challenges to adapt to existing buildings for indoor space cooling.

Using a similar water spray technique, Foroozesh et al. [161] performed CFD simulations to explore the optimum baffle angle to assess the performance of a one-sided wind catcher. The authors were also able to record a temperature drop of up to 17.4°C with a 60° baffle. Another study with the water spray method by Jafari and Kalantar [162] examined the cooling performance by integrating a solar chimney with the water spray system. The authors conducted CFD analysis of this system on a three-story building model to achieve an indoor temperature reduction of up to 12°C.

Sakhri et al. [163] integrated an Earth-to-air Heat Exchanger (EAHE) along with a solar chimney to the wind catcher to investigate the improvement in thermal comfort in arid regions. In this experimental study, the authors produced a real scale model with temperature, wind speed and humidity sensors. The integration of EAHE helped reduce the temperature by 12°C in summer conditions and raised the outlet temperatures by 9°C in winter conditions. Thanks to the full-scale tests, the proposed passive system showed a promising and reliable cooling alternative. However, integrating a solar chimney and EAHE on a wind catcher poses challenges related to installation and maintenance complexity. Similarly, Benhammou et al. [164] also studied the cooling performance of a wind tower integrated with an EAHE by examining the optimum pipe dimensions among other design parameters of the wind tower. The authors observed maximum cooling of 30.7kWh with a pipe length of 70m and argued that optimising the pipe dimensions produced a higher impact on cooling performance than optimising the wind tower dimensions.

Cai et al. [165] proposed a novel ventilation method with the use of thermoelectric-driven ventilation. This Thermoelectric Ventilated Building Envelope (TVBE) integrated TEMs with passive building envelopes to improve cooling performance and reduce energy loads. Figure 23 shows a schematic of the proposed system. Using numerical analysis and experimental validation, the authors argued the TEM arrangement significantly enhanced the cooling performance and power generation with energy savings of up to 13.1%.
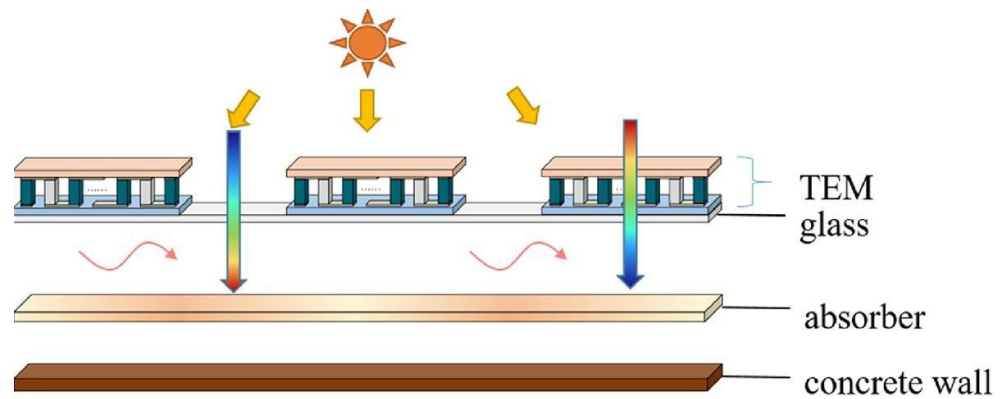
Figure 23 – Schematic diagram of TVBE model [165]

During the last decade, phase change materials (PCMs) have gained significant attention for their potential in passive cooling in buildings [166]. PCMs are substances that absorb or release large amounts of latent heat during phase transitions. This property makes them useful for storing thermal energy as the temperature can be harnessed as they change phase (e.g. from solid to liquid or vice versa). Yang et al. [165] explored PCMs in ceiling panels for passive cooling in buildings. Using CFD modelling validated using full-scale experimental data, the authors analysed various geometric optimisations and design parameters to enhance heat transfer and natural convection. Similarly, Kong et al. [167] proposed a novel double-layer PCM Trombe wall with multiple phase change points to enhance thermal performance in buildings. The authors analysed the system using mathematical models and CFD simulations. The results showed a reduction of average temperature by up to 0.93°C in hot ambient conditions and an increase of temperature by up to 6.6°C in winter conditions.

Likewise, several other studies explored the integration of PCMs for passive cooling in buildings [168]–[174], however, despite their effectiveness, a large number of drawbacks and limitations are involved with PCMs. These include their low thermal conductivity, phase segregation, supercooling tendencies, season adaptability, thermal stability, flammability, and leakage during phase transitions as highlighted by Li et al. [166] in their comprehensive review of phase change materials for passive cooling in building envelopes.

2.4.4 Active-Passive Cooling Techniques

While passive cooling is bound to certain limitations, such as high dependency on specific ambient conditions and reduced efficacy during extremely hot conditions, the integration of active cooling with passive techniques is becoming increasingly common. This active-passive hybrid cooling approach aims to supplement indoor cooling while maintaining required ventilation rates and regulating thermal comfort.

Jafari et al. [175] explored an adsorption cooling technique for wind catchers to provide natural cooling on a 2-storey building. The authors designed a cooling channel with solar adsorption plates installed inside a wind catcher that acts as a chiller for incoming fresh air. The study probed the impact of geometric parameters of the wind catcher and the plates on the cooling performance. The active-passive system could reduce the air temperatures by 10°C to 20°C depending on the ambient conditions. The authors noted that the humidity greatly affected the cooling performance as a reduction of 50% of relative humidity showed a 16.5% reduction in air temperatures. Nevertheless, the study was dependent on numerical analysis did not include a physical testing of the system and may not fully represent actual performance against real-world ambient conditions.

Similarly, Noaman et al. [176] investigated the integration of active solar cooling technology (ASCT) and passive solar design strategies (PSDSs) on façades. The ASCT employed an absorption chiller driven by solar thermal collectors (STCs) while the PSDSs focussed on window-to-wall ratio, glazy types, shading devices, and wall materials. Figure 24 shows the main components of the proposed ASCT system. The authors concluded that the PSDSs helped reduce the cooling demands by 43.5% to 65.7% and maximum efficiency of ASCT was achieved with STC sloped at 30°.
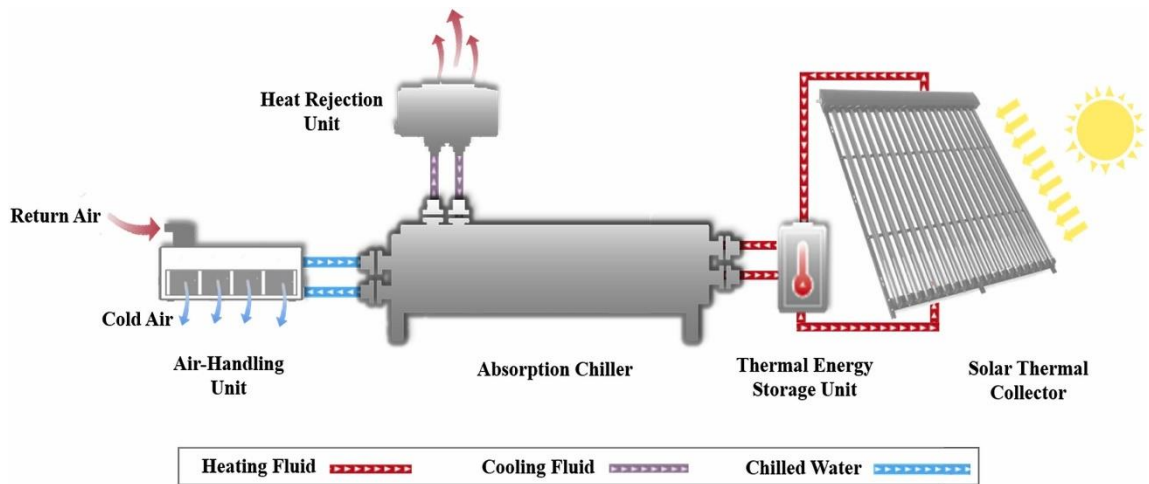
Figure 24 – Components of Active Solar Cooling Technology [176]

Vaseghi et al. [177] performed a numerical assessment of an active-passive ventilation system for a museum building. The authors integrated passive solar radiation heating with an active hot water circulation in spiral pipes. Despite promising results and desired thermal comfort, the study is not only limited to daytime operation and poses high complexity in integration on an existing building roof for indoor cooling.

In a case study on a hostel building in a tropical climate, Shukla et al. [178] examined the energy-saving potential through an active-passive approach. Active systems include Photovoltaic (PV) panels for the roof and EAHE cooling and ventilation system, while passive elements include double-glazing glass for windows, Gypsum plaster for walls, and cool paint for the roof. The authors concluded that the EAHE system significantly reduced the ventilation loads and the overall system helped reduce the cooling load from 285 TR to 186 TR.

Zavrl et al. [179] studied the integration of PCM into the internal walls and ceilings as an active-passive cooling mechanism in buildings. The authors leveraged complete solidification of the PCM at nighttime to provide sufficient cooling during the daytime. The CFD analysis evaluated various inlet air temperature scenarios ranging from 15 to 20°C to examine the energy performance and operational costs. The results showed optimum performance at an inlet temperature of 17°C with 6.34 kWh of cooling energy recovered to be used for daytime. However, the authors acknowledged that (1) this method would still require additional electrical energy for ventilation, and (2) at higher

temperatures, additional cooling options may be needed. Moreover, considering energy consumption and operational costs involved, the authors questioned the practicality of the APS method in comparison to conventional air conditions.

Oropeza-Parez and Østergaard [180] conducted a comprehensive review of active and passive cooling methods for residential dwellings. The following arguments can be drawn from the authors' key findings:

1. The most common active cooling methods apart from conventional air conditioners include evaporative coolers and fans, however, their cooling capacity is less than that of many passive systems.

2. Among the most effective passive cooling methods include passive cooling shelters, phase change materials, and radiant heat barriers, however, these methods require a high level of maintenance or installation cost,

3. Among the low-maintenance and low-cost passive cooling methods include natural ventilation, thermal capacity, shading systems, and heat sinks, however, they are not effective or impactful in extremely hot climatic conditions due to their limited cooling capability.

Hence, existing research has explored a variety of solutions to reduce building energy heating and cooling demands through various active and passive approaches, however, higher cooling performances are often faced with higher maintenance cost or installation complexities. Moreover, natural ventilation wind catchers adversely impact the effectiveness or viability of any passive or active cooling in extremely hot climates.

2.5. Thermoelectric Methods

Thermoelectricity refers to converting heat directly into electricity, or vice versa. Thermoelectric methods present an environmentally friendly, energy-efficient, low-cost and low-maintenance solution towards active cooling. Thermoelectric modules (TEM) are typically used either as (1) Thermoelectric generators (TEGs) that work on Seebeck effect [181] to produce electricity from a temperature difference or as (2) Thermoelectric coolers (TECs) that work on Peltier effect [182] to convert electricity

into a temperature differential to generate cooling. Figure 25 shows the components of a typical TEC (or Peltier) module.
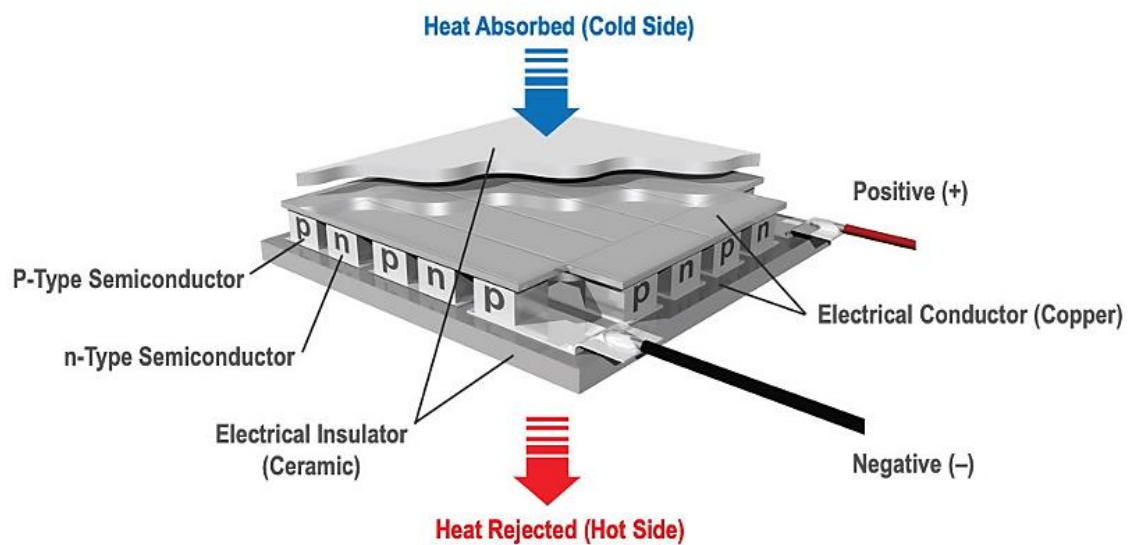
Figure 25 – Inside a thermoelectric module [183]

2.5.1 Common applications of thermoelectric cooling systems

Thermoelectric coolers have increasingly been studied and employed in a variety of applications, as detailed in Figure 26, such as medical for cold chambers, automotive industry for battery thermal management or air-conditioning, computing and telecommunications to cool electronic components. For example, Wiriyasart et al. [184] investigated the integration of TEC to cool a dual processor computer. The authors experimentally tested a TEC-based air cooler module to effectively prevent the CPUs from excessively heating with increasing computer load. The study also emphasised on how different sizes and operating modes of the cooling fans for heat dissipation have a significant effect on the cooling performance. Similarly, Al-Shehri and Saber [185] studied the cooling of computer chips at different heat rates by experimentally evaluating the optimum power requirements. The authors concluded that the cooling performance was not proportional to the input power at a higher current. The results showed that the largest temperature drop occurred when 5.5A of current flowed through the TEC device.
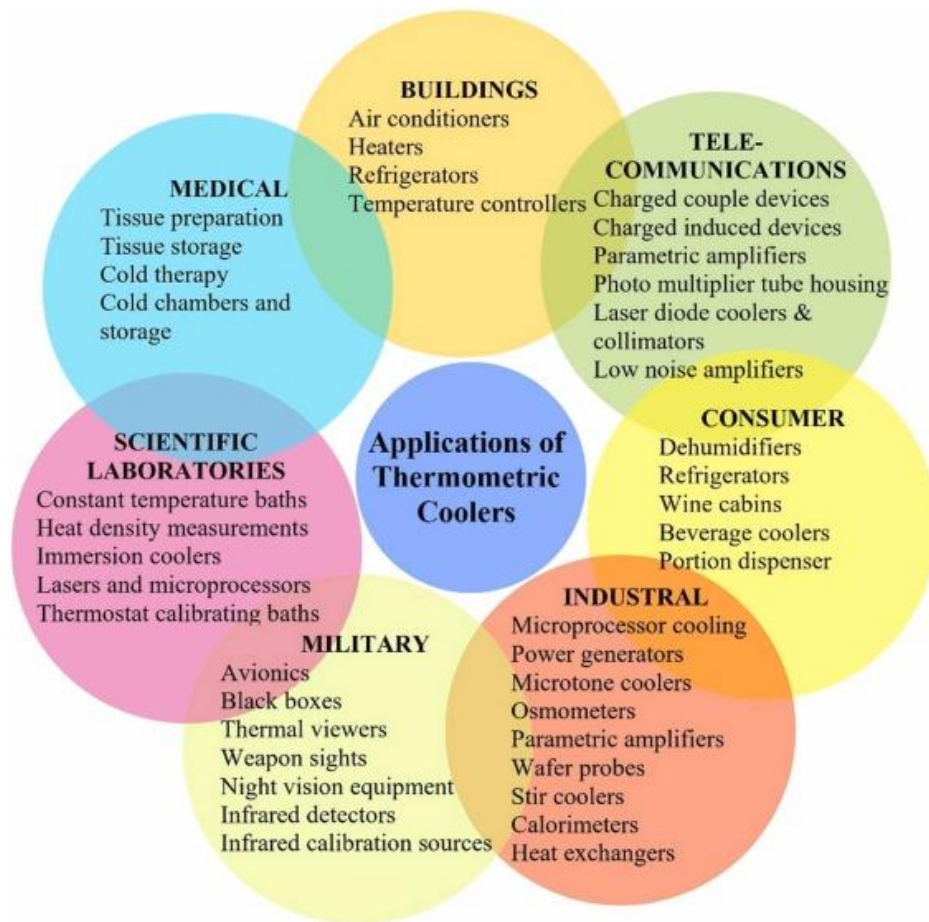
Figure 26 – Examples of common applications of TEC [204]

With the benefits of no moving parts, no working fluid, no operational noise, and compact sizes, thermoelectric coolers present several use cases in automobiles. For example, Luo et al. [186] developed and installed a TEC air-conditioner for a truck cab. This novel eco-friendly cooling system provided thermal comfort with a COP of up to 0.8 at an ambient temperature of 30°C. Likewise, Choi et al. [187] developed a TEC-based temperature-controlled cooling and heating system for a car seat. The authors integrated a control system using temperature sensors to help regulate the car seat temperature. Additionally, heat sinks were installed to dissipate heat and optimise cooling performance.

For medical applications, Alam et al. [188] studied the cooling performance of a solar thermoelectric refrigerator. The authors achieved 0.61 of COP with a 4.1°C reduction in the temperature of the refrigerator cabin. Likewise, leveraging the Peltier effect, Haynes et al. [189] explored the transportation and storage of blood using a TEC

refrigerator. Experimental tests confirmed the effectiveness of the proposed method as temperatures of the blood storage unit were maintained at the desirable range of 1 to 6°C under field conditions. Furthermore, Jiamin et al. [190] reviewed other promising developments using TEC for medical applications including vaccine cooling, cooling of inorganic and organic materials, tissue storage and cold therapy using eco-friendly and reliable thermoelectric refrigeration.

2.5.2 Integration of TECs in buildings for indoor cooling

Recent studies investigated the potential and viability of integrating thermoelectric cooling systems to assist in space cooling in buildings. For example, in a case study on the TEC1-12706 Peltier module, Tian et al. [191] explored the performance and economic aspects of a thermoelectric-assisted air cooler for indoor spaces. The authors highlighted that an increase in input power generated higher cooling capacity but with a reduced coefficient of performance (COP). The cost of cooling through a single TEC module varied between $0.7 to $1.4 kWh depending on ambient conditions, however, an optimum power of 23W was noted where the cost per unit of cooling is minimised. The authors argued that further research is needed to optimise the number of TEC modules for large-scale applications.

Similarly, Parmar et al. [192] developed and examined a Peltier-based air cooler prototype for indoor spaces to help reduce energy demands. The authors focused on analysing heat transfer rates and energy efficiency ratios (EER). The system showed a noticeable improvement in heat capacity, power usage and EER/COP analyses while exhibiting better cooling performance than traditional coolers. However, as a standalone cooler, a variety of challenges exist in terms of the scalability of this system with substantial heat dissipation requirements. Moreover, in extremely hot conditions, this impact of cooling and load reduction would be significantly reduced.

Cheng et al. [193] investigated an innovative energy-saving cooling system by integrating solar cells and TEC modules. As TEC devices require constant heat dissipation, the authors incorporated a water channel to remove heat from both the solar cells and the TECs as shown in Figure 27.

Higher performance was seen with an increased cooling water flow rate. A significant temperature reduction of 16.2°C was observed in the model house used for testing purposes. However, the results may not reflect the real-world parameters and ambient conditions including the size of the room, humidity, and ambient temperatures, particularly in hotter regions. Furthermore, a potential large-scale version of this system would be highly complex and cost-intensive.
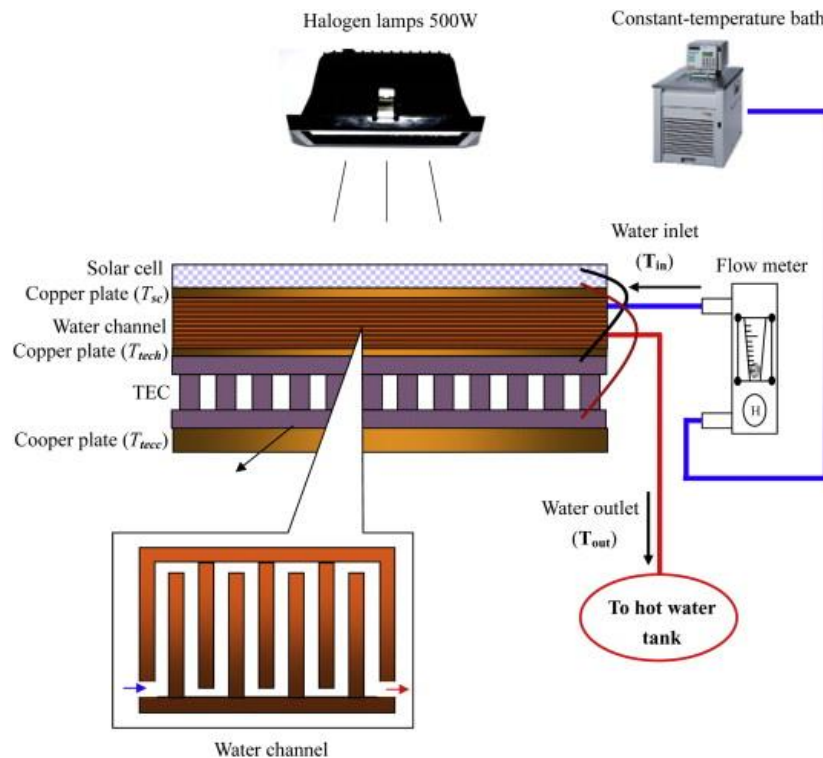
Figure 27 - Experimental setup of Solar-cell TEC cooler [193]

Lv et al. [194] studied sky radiative cooling using a solar photovoltaic-thermoelectric (PV-TE) system. Using mathematical modelling, the authors presented an optimal ratio between photovoltaic and radiative cooling areas for maximum cooling efficiency. The system demonstrated effective cooling power, particularly in temperate climates of mid-latitude regions with low humidity and longer daytime hours. Similarly, Shen et al. [195] examined a novel thermoelectric radiant air-conditioning system (TE-RAC). The authors converted TEC1-12706 modules to operate as radiant panels, which allowed both cooling and heating depending on the direction of the current. At 1.2A of current, the theoretical model showed a COP of 1.77, which was lower than that of a conventional air conditioning system. However, despite the economic viability, a large-scale version of these systems would pose complexities in integration on building roofs.

Additionally, the performance of the system would be significantly reduced in equatorial regions with higher humidity and extreme ambient climates.

Several authors explored the integration of TEC-based cooling and heating on existing building envelopes. For example, Liu et al. [196] experimentally evaluated the cooling and heating performance on a prototype of a thermoelectric building envelope (TBE). The authors inspected the impact of various operating conditions such as outdoor temperatures, power inputs and fan conditions. Key findings of this study include a higher heating efficiency than an auxiliary electric heater and the COP of heating being three times that of cooling. The authors also acknowledged that the performance of the TBE was significantly affected by the outdoor temperature conditions, which could limit its application in certain climates. Similarly, Zuazua-Ros et al. [197] investigated the thermoelectric potential for heating, cooling and ventilation in buildings by examining the viability, strategies and integration. The authors highlighted that (1) the performance of a thermoelectric system is not yet competitive compared to conventional vapour compression systems, (2) the performance of TE systems is highly dependent on the operating conditions, and (3) despite providing comfort conditions, there is a need for improvement in efficiency and effectiveness. Nevertheless, the authors also acknowledged that thermoelectric offers a greener alternative to existing HVAC as it does not use refrigerants and has high durability.

Likewise, Aranguren et al. [198] examined the performance of a thermoelectric cooler-heat pump (TECHP) system integrated with heat pipes for 'nearly zero-energy building' (nZEB) applications. The study focuses on optimising heat transfer against the thermal resistance of heat pipes at different orientations and operational modes. The methodology for both heating and cooling is illustrated in Figure 28. With computational and experimental analysis, the authors concluded that the TECHP system can effectively provide heating and cooling in nZEBs. Despite the limitations, such as environmental sensitivity and integration complexity, the authors acknowledged that the TEC integration with heat pipes in cooling indoor spaces exhibits promising potential towards reducing carbon emissions from buildings.
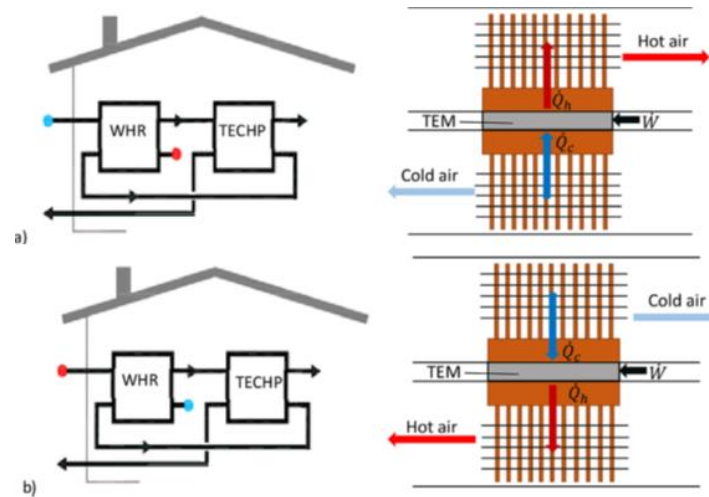
Figure 28 – Operation of TEC cooler-heat pump for (a) winters and (b) summers [198]

A detailed review of solar-powered thermoelectric cooling technologies for nZEBs was carried out by Liu et al. [199] which inspects the viability of TECs for building cooling.

Among the key findings, the authors underlined that:

1. The integration of PV panels and the absence of any mechanical moving parts and refrigerants offers an environmentally friendly alternative to space cooling.

2. Integration of TECs with building walls and windows can actively regulate thermal flux as switching their polarity helps alternate between heating and cooling.

3. TECs benefit from waste heat recovery capabilities that increase overall efficiency.

However, several drawbacks and limitations were also stressed by the authors, such as:

1. TECs and PV systems have a much lower efficiency compared to conventional systems, as previously noted by other authors.

2. TECs are highly sensitive to external environmental conditions like temperature and solar irradiance.

3. Challenges involving the integration of TECs with existing building designs that may require sophisticated control systems for optimal operation.

Finally, the authors concluded that there is a need for further advancements in PV and TEC technologies to make these systems more viable for building applications.

2.6 Summary

The main findings of the comprehensive literature review are summarised below under two categories, i.e. (1) building inspection methods as reviewed in sections 2.2 and 2.3, and (2) active and passive cooling techniques as reviewed in sections 2.4 and 2.5:

2.6.1   Summary of Building Inspection Methods:

1. Emerging practices and developments in image fusion, machine learning, and drones (or UAVs) have shown promising scope and prospects towards improving the efficiency of large-scale inspection in buildings. For example, machine learning has shown impressive results in numerous applications [69]. However, less focus and development are seen towards the use of AI for building or structural inspection as it requires an enormous amount of time and training data [68].

2. Drones provide automated prospects to reduce the time and cost of building energy audits. However, 3D mapping and thermographic surveying require hefty hardware that cuts down their flight time (and overall inspection time) drastically. Hence, employing appropriate inspection methods and equipment (such as image-fusion technique, 3D mapping hardware and algorithm, and fault detection mechanism) is imperative for an efficient drone-based thermal mapping and inspection [27].

3. Among the 3D model reconstruction techniques, 'monocular photogrammetry' showed a highly promising scope for a real-time drone-based 3D mapping task thanks to its minimal hardware and computational processing requirements [200].

4. A thermographic 3D model is generated either by superimposing thermal imagery on a 3D point cloud or by stitching it with photogrammetric results. Point-cloud method inevitably reduces the thermal resolution to that of point clouds, which causes partial omission of useful thermal data. Whereas the stitching method provides a complete thermogram with radiometric details of building envelopes that are useful for BEM and quantitative energy analysis. However, both techniques require extensive computational processing time and hardware [201], [202].

5. Wind towers are not only beneficial for providing adequate ventilation in buildings, but they also offer passive cooling in hot and dry regions. Studies have optimised these structures for better airflow and temperature regulation. However, their effectiveness is heavily influenced by their architectural design, environmental conditions and unfavourable wind speeds and directions [148].

6. Conventional passive cooling techniques, such as evaporative cooling windcatchers, PCMs, and Earth-to-air Heat Exchangers (EAHE) have shown potential in reducing cooling energy loads significantly (43%-61% annually [140]). However, these technologies present various challenges, such as high installation costs and maintenance, and complexity in integration on existing buildings [160], [163], [166].

7. Heat pipes are efficient passive heat transfer devices that are increasingly explored as an integration to roof-mounted wind towers as they demonstrate heat recovery and passive cooling capabilities [203]. However, their stand-alone effectiveness on a wind tower is constrained by the ambient and indoor temperatures. Hence, a gap and an opportunity exist towards integration of active techniques with heat pipes to further leverage their heat transfer capability for improved efficiency.

8. The incorporation of active cooling systems with passive techniques is emerging as a solution to supplement indoor cooling while maintaining necessary ventilation rates. Research in this area explores various methods like adsorption cooling, solar cooling technologies, and photovoltaic systems. However, they face challenges in real-world applications, including cost, installation complexities, and maintenance.

9. Thermoelectric coolers (TECs) have shown promising results in active cooling applications across various industries [198], [204], [205], [205]. Integration of TEC systems in buildings for indoor space cooling is a growing area of research. Despite their eco-friendly, low-noise and low-maintenance qualities, existing solutions struggle with their low efficiencies for large-scale adoption [199]. However, no studies were found that explore an integration of TECs on wind towers with heat pipes as a hybrid solution for cooling, heating, and ventilation.

2.7 Research Gaps

Based on the comprehensive review of building inspection and retrofit techniques to improve building energy consumption, the following gaps were identified:

1. Lack of research and development towards computationally-friendly real-time thermal image fusion and 3D mapping techniques. Existing work heavily relied on image stitching algorithms using feature detection or manual post-processing. Computational demands need to be massively reduced to allow for a drone-assisted fully automated large-scale building inspection system.

2. Limited energy-friendly solutions to provide natural ventilation-assisted cooling and heating for indoor spaces. Natural ventilation often works counter-effectively to cooling or heating needs in extreme temperature zones. Studies lack a versatile and cost-effective solution to green HVAC.

3. No study found that exploits the cooling potential of TECs with the rapid heat transfer properties of heat pipes on wind towers. Such a solar-powered hybrid system that exhibits potential for an energy-friendly, noiseless, no maintenance, and cost-effective resolution to reduce energy demands is yet to be explored.

This research aims to fill the gaps using two novel approaches, i.e. (a) real-time image-fusion method and (b) Peltier-driven cooling technique as defined in Section 1.3 while adhering to the research methodology as described in Section 1.4.

Chapter 3 – Smart Building Inspection and Peltier-driven Cooling Methods

3.1 Introduction

This chapter first details the qualitative approach of this research, i.e. the smart building inspection framework, which proposes a thermal-visible image fusion technique followed by its qualitative proof-of-concept. The preliminary results from the prototype of the proposed fusion module as well as its experimental integration with machine learning models are also presented and discussed.

Secondly, this chapter further presents a retrofit approach using Peltier-driven cooling, which uses thermoelectric conductive cooling of heat pipes to develop a ventilation-assisted active cooling mechanism through wind towers. The specifications, functions, and theoretical insight into the performances of key components and the overall cooling system are discussed. Additionally, integration and assembly of the proposed cooling unit with a 1m x 1m wind tower is described.

3.2 Smart Building Inspection Framework

Existing techniques to superimpose thermal imagery with visible data are computationally intensive with feature detection and image-stitching algorithms typically using stereo or depth cameras. This work proposes an innovative extrinsic image fusion approach to capture and pre-align thermal and visible images with minimal computational time and resources.

Similarly, existing automated fault detection techniques pose several challenges and limitations. For example, (1) the heavy computational time or hardware requirements to first superimpose visible and thermal images, (2) the enormous training data and time required to teach an ML model on the fused (thermal-visible) images, and (3) the ML model would be limited to spot only specified (trained) defects, i.e. incapable of highlighting unseen potential anomalies.

This research integrates the proposed image-fusion method with a hybrid machine learning (deep learning) framework to qualitatively assess its effectiveness to identify building façade anomalies.

3.2.1 Methodology

The proposed methodology is illustrated in Figure 29 that first introduces a lightweight and speedier image fusion technique and then presents a hybrid semi-supervised ML framework that requires minimal training dataset through two supervised ML models (i.e. on separate thermal and visible image sets), which would help train a self-supervised model with their fused images to find pre-trained (labelled) and untrained (pseudo-labelled) defects.
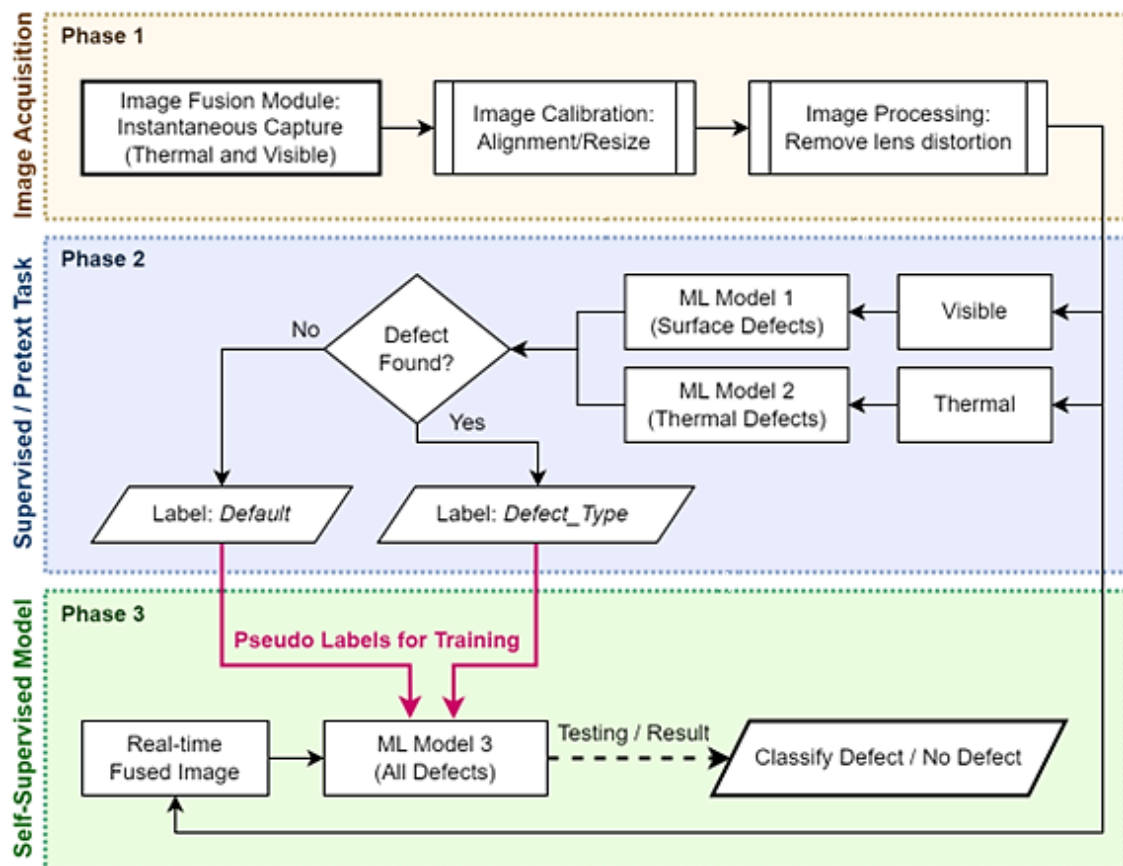
Figure 29 - Proposed framework: Image Acquisition, Supervised / Pretext Task and Self-supervised Model

The process is divided into three phases that occur instantaneously, i.e. (1) Image Acquisition, (2) Supervised Learning or Pretext Task and (3) Self-Supervised Model as detailed in the following sub-sections after camera optics theory.

3.2.2 Camera Optics Theory

The 'image acquisition' (as described in the methodology framework) is where the proposed image fusion module simultaneously captures thermal and visible images. These images originate from different types and specifications of cameras that require image calibration. Thus, it is important to analyse the camera optics and projection theory as the two images may undergo necessary calibrations to align (superimpose) accurately.

The general camera projection matrix of a camera **P** is given by:

$$\mathbf{P} = \mathbf{K}\begin{bmatrix}\mathbf{R}\\\mathbf{t}\end{bmatrix}, \text{ with } \mathbf{K} = \begin{bmatrix} f_x & s & c_x \\ 0 & f_y & c_y \\ 0 & 0 & 1 \end{bmatrix} \tag{3.1}$$

where,

R is the 3x3 rotation matrix representing camera orientation (extrinsic)

t is the transformation vector for representing camera position (extrinsic)

K is the intrinsic parameters matrix that includes:

f_x f_y , the focal length,

c_x c_y , the principal point (optical centre),

s, the skew coefficient

An example of a stereo camera configuration in the cartesian coordinate system is shown in Figure 30 [206]. The left camera (C_1) and the right camera (C_2) both target point **P**, which is projected as p_1 and p_2 on their respective image planes as shown. A near-distant and/or non-planar target scene affects the accuracy of homographic transformation and fusion results, which this paper aims to resolve.
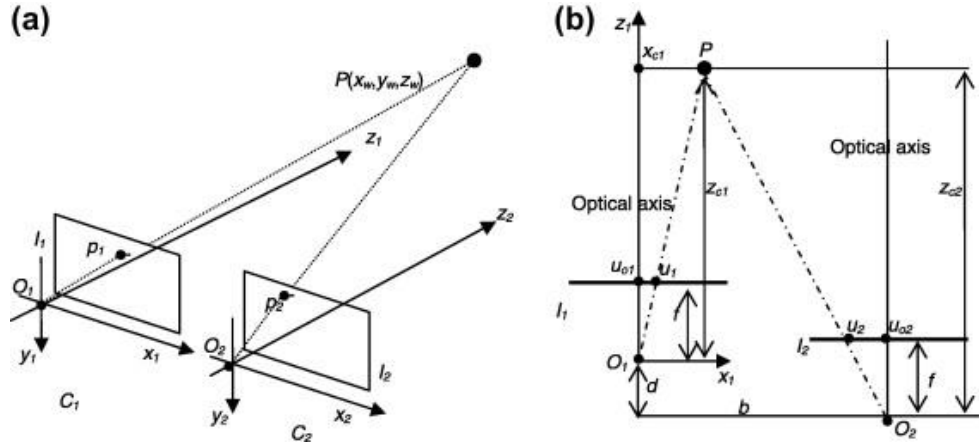
Figure 30 - (a) Stereo camera arrangement (b) optical axes from top view [207]

Since the cameras capture nearly perpendicular from the scene, the skew and lens distortions can be corrected easily through MATLAB or other computational methods. Hence, the skew coefficient, *s*, becomes zero. Moreover, as the optical axes of both cameras are aligned to be coincident during capture, the extrinsic parameters of both cameras can be expressed as:

$$\begin{bmatrix} \mathbf{R} \\ \mathbf{t} \end{bmatrix}_{RGB} = \begin{bmatrix} \mathbf{R} \\ \mathbf{t} \end{bmatrix}_{Thermal} \tag{3.2}$$

Therefore, the RGB-T camera projection matrix **P** can be defined as:

$$\mathbf{P} = \begin{bmatrix} \mathbf{R} \\ \mathbf{t} \end{bmatrix} \left(\mathbf{K_R} + \mathbf{T_{Th}^{-1} K_{Th}} \right) \tag{3.3}$$

where K_R and K_{Th} are the intrinsic matrix of RGB camera and thermal camera respectively, and T^{-1} is the inverse affine transformation of thermal camera from general pose to origin.

3.2.3 Phase 1: Proposed Design and Prototype Development

This process uses an extrinsic thermal-visible image capturing and fusion procedure that helps pre-align the optical axes of both cameras (thermal and visible) to eliminate hefty computational image processing that would be required otherwise for image fusion as illustrated in Figure 31.
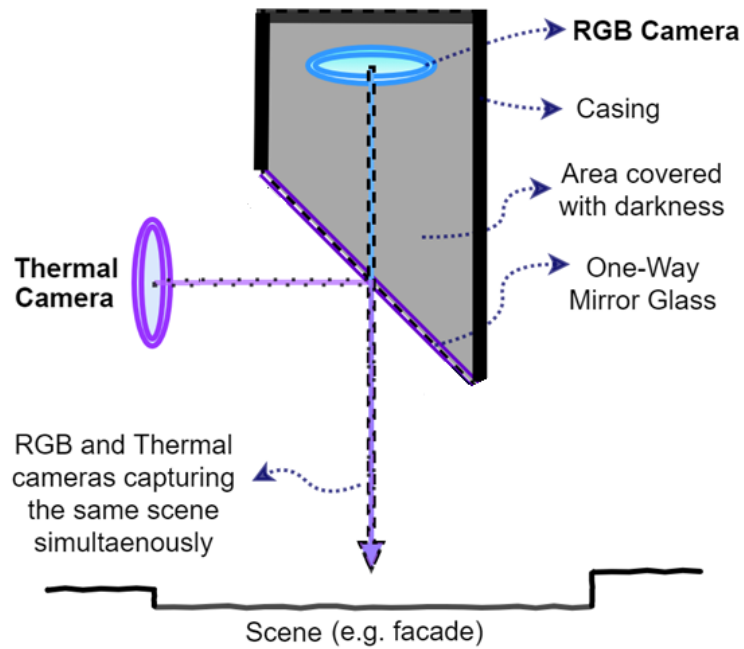
Figure 31 – Image fusion module with coincident axes of thermal and visible cameras

A CAD illustration of this image fusion module and its 3D printed prototype is shown in Figure 32. It is designed to hold a single one-way mirror at a 45° angle with support for a FLIR T640 Thermal imager and a smartphone camera to capture the concurrent thermal and visible images. This image fusion module prototype is used for all data capture for experimentations and validations presented in this paper.
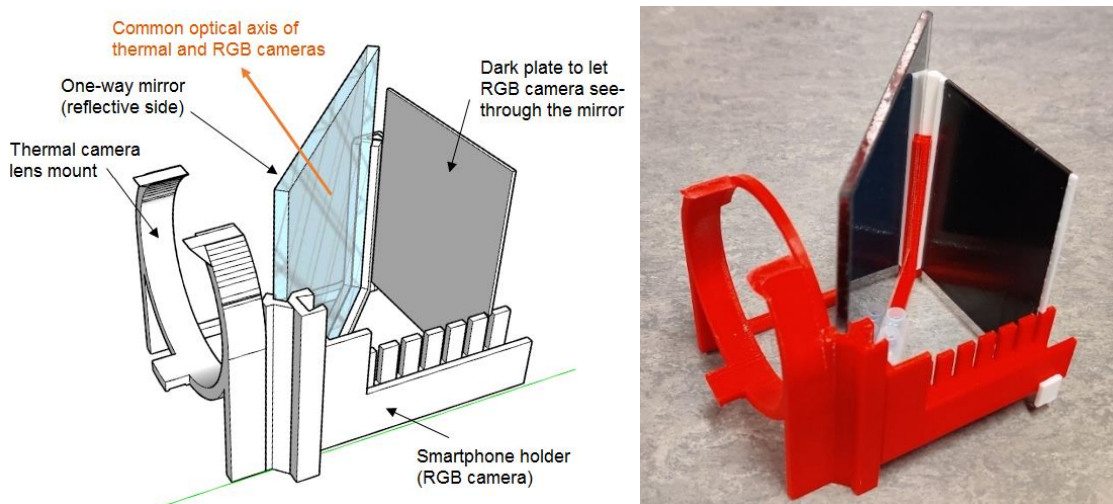
Figure 32 - CAD schematic (left) and a 3D printed prototype of the image fusion module

Figure 33 shows the image fusion module on a tripod stand with both cameras mounted 90° from each other with their optical axes bisected at 45° with the one-way mirror.

Figure 33 – Image fusion module with cameras mounted shown from two angles

This hybrid module (i.e. the image fusion module) promises to benefit in assisting in training machine learning models more accurately to better interpret the fused images in real-time for façade defect detection and identification. Henceforth, the following sub-section describe the integration of two supervised machine learning models to detect visible and thermal defects separately (phase 2).

3.2.4 Phase 2: Supervised Learning / Pretext Task:

This phase takes visible and thermal data from phase 1 as separate image sets. These two channels of corresponding captured images are used to train two independent supervised machine learning models for image classification using regression technique for both, visible façade defects (such as cracks, spalls and moulds) and potential thermal faults (e.g. heat losses and moisture), using 'ML Model 1' (ML1) and 'ML Model 2' (ML2), respectively. Additionally, transfer learning approach is used to reduce training time and data allowing a potential low-powered CPU to handle a relatively simpler fault detection task. This is illustrated in Figure 34.
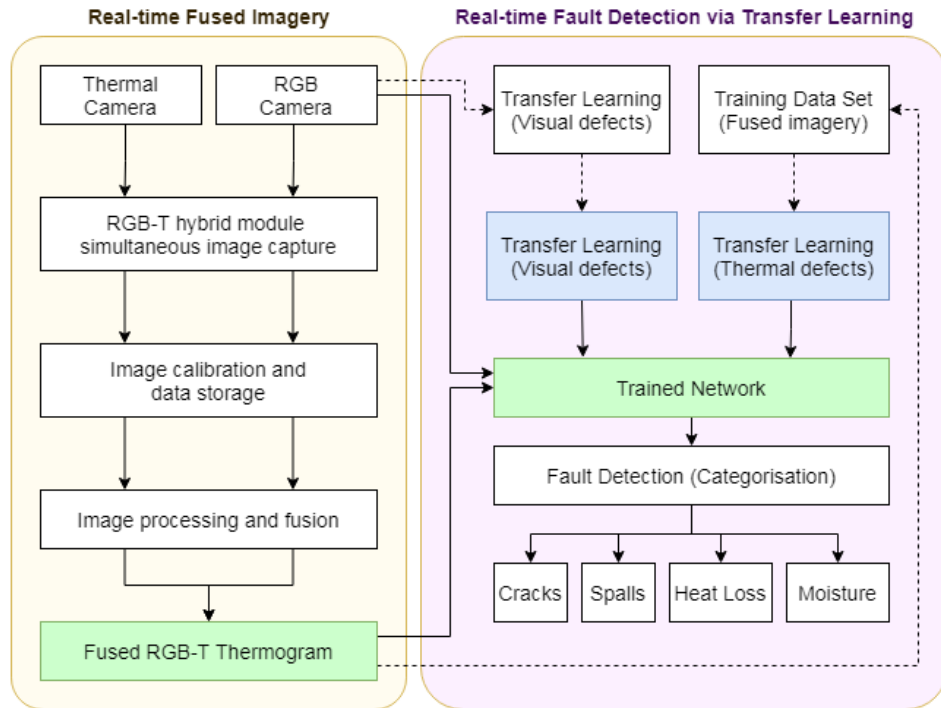
Figure 34 – Fused imagery to Fault Detection via Machine Learning

The results from these ML models are first optimised to provide highly accurate predictions using unseen test data and classify defects on façades against the trained labels (including 'Default' that represents 'no fault'). Once the predictions are reliable, the input images (visible and thermal) are superimposed (fused) to be used for phase 3 as a pretext task to self-train an unsupervised ML model (in a self-supervised fashion) as described section 3.2.5.

3.2.5 Phase 3: Self-Supervised ML Model:

The 'ML Model 3' (ML3) in phase 3 is a provisionally unsupervised model that requires automatic training to function as a self-supervised model (SSL). This is done using a pretext training task with the help of pseudo labels that are extracted from phase 2 as the predictions (results) from the supervised model, including the default state with no fault. Hence, for every matching image set, its visible-thermal fused image is used as an input to train the ML3 on with its corresponding result (category of the defect) as a pseudo label to self-train the model in real-time.

The idea here is to let the SSL ML3 model develop more sense of the overall scene and context through pixel-accurate fused image sets, as opposed to identifying faults

separately or independently from thermal and visible images. This helps provide more meaningful and comprehensive information to the deep learning networks inside ML3 to find patterns that could otherwise be overlooked by both ML1 and ML2 due to a lack of context.

The pretext training task (that comprises ML results and pseudo labels from phase 2) is then tested through a similar downstream task to evaluate and validate the performance of SSL. Once the defect detection accuracy of this self-supervised phase exceeds the accuracy of the supervised models, phase 2 can then (optionally) be withdrawn from the process completely to have a more computationally efficient and simpler system for façade inspection in real time.

3.2.6 3D Thermal Model Reconstruction:

To keep physical hardware and computational processing to a minimum, monocular photogrammetry is used for 3D model reconstruction through an RGB camera. This relies on generating 3D point-clouds from multiple images captured at different angles with overlapping features. This is done through camera calibration and triangulation processes. While this photogrammetry process is generally computationally intensive, a GPU-equipped hardware can perform this 3D model reconstruction in real-time.

As this work leverages a hybrid thermal and visible image capture, generating a 3D thermographic model can be simplified. The raw visible images used to texture the 3D model are replaced with the corresponding twin version of their thermal images post-calibration.

3.2.7 Experimental Validation and Results

The experimental setup, tests, validation and results for all three phases (i.e. Image Acquisition, Supervised Learning / Pretext Task, and Self-Supervised Learning) are presented and discussed in this section.

3.2.7.1 Phase 1 - Image Acquisition: Calibration and Validation

Images captured from two different types of cameras must be calibrated to remove any differences in lens distortions and resolution (or scaling). As this work uses a 3D

printed image fusion module for proof-of-concept with smartphone camera and FLIR 640 mounted on it, the images from both cameras may need further elementary calibrations. The relevant specifications of both cameras (thermal and visible) used in this work are listed in Table 3.

Table 3 - Specifications of thermal and RGB cameras used in this study Imager [208]

Specification	Thermal Camera	RGB Camera
Make	FLIR	LG
Model	T640	G Pro 2
FOV	45°	45°
Resolution	640 x 480	1920 x 1080
Framerate	25 FPS	60 FPS
Range	-40°C - 150°C	-
NEDT	< 30mK	-
Weight	1.3kg	0.172kg

In order to calibrate (i.e. precisely align) the images, two thermoelectric (TEC) devices (also known as Peltier modules) are used that generate heat once powered. These 40mm x 40mm square devices help in this one-time calibration as their captured features are sharp and recognisable by both thermal and visible data.

For calibration purposes, the arrangement of these two TECs is shown in Figure 35 with a front view (left) and top view (right) as they are arranged with a difference of 50mm in depth and to be captured from 30cm.

Figure 35 - TEC modules arrangement shown from front view (left) and top view (right)

The results after calibration of thermal-visible images aim to present a comparison of image fusion against the existing MSX feature [209] of the FLIR T640 Thermal Imager [208], which ensures instantaneous fusion, unlike existing methods as discussed in Section 2.2.

Figure 36 (left) shows the fused image captured through the proposed image fusion module as 50% opacity of the visible image was overlaid on top of its corresponding thermal image, while

Figure 36 (right) shows the Canny edge features [210] produced of the same visible image.
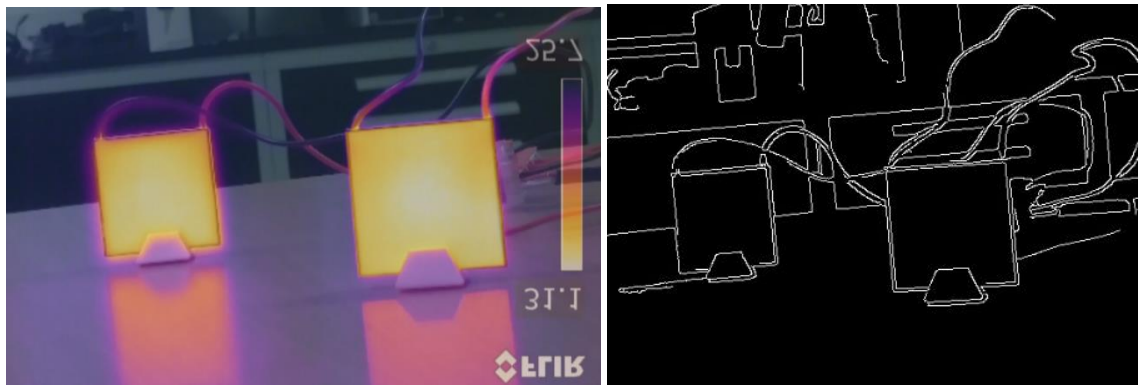
Figure 36 - Superimposed 50% opacity visible over thermal image (left) and Canny edge features of visible (right)

The same scene (with the same subject and same distance) was then captured with FLIR's MSX feature that aims to automatically align the edge features from FLIR's built-in visible image onto its corresponding thermal image shown in
Figure 37 (left). Likewise, for comparison,
Figure 37 (right) shows the results from the image fusion module of this work presented in the same fashion (i.e. superimposing the Canny edge features of the visible image superimposed on the thermal image). The Python programming code using the OpenCV library is shared in Appendix C-1.
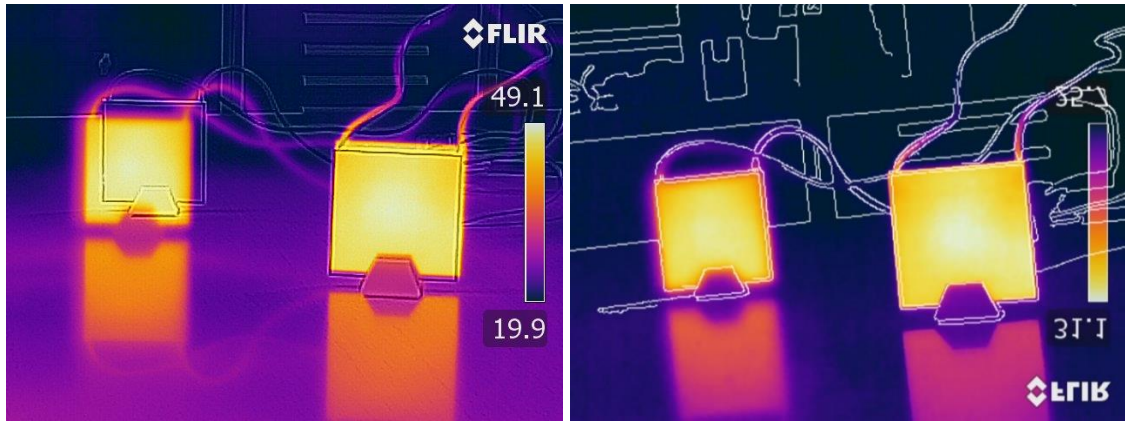
Figure 37 - FLIR MSX Result (left) and result using proposed image fusion method (right)

As seen from the results in

Figure 37, due to the distance (depth) between the two TECs, FLIR MSX failed to correctly align or show both features of TEC accurately. This is due to the inevitable parallax errors from both cameras (and their optical axes) that are physically 48mm apart [208]. On the other hand, the results using the proposed image fusion module (phase 1) showed pixel-level accuracy against the same subject despite the depth between the two objects.

This validates the concept and purpose of the image fusion module and how it helps in seamlessly superimposing stereo images without the need for complex image-stitching computation with feature detection algorithms or any additional IR depth cameras.

3.2.7.2 Phase 2 - Supervised Learning Training Process

The training and testing of the supervised learning models (i.e. visible and thermal images) are presented. For validation purposes, cracks and heat losses are selected as a subject of this study. The same process can be reperformed, replicated and applied for other types of visible and thermal defects.

To ensure the highest reliability and accuracy of the machine learning models, abundant and relevant training data for both visible and thermal image sets are necessary. 20% of this data would be used for testing and validation of the ML models. The machine learning models are first pre-trained with necessary low-level transfer learning knowledge. This allows us to focus on only the relevant training dataset, i.e.

cracks and heat losses. Two classes are used for each set annotated as "Default" and "Cracks" for the visible dataset, and "Default" and "Heat Loss" for the thermal dataset.

The training and testing dataset was obtained from a combination of handpicked relevant images (of cracks and non-cracks) from online publicly available datasets [211], [212] along with first-hand captured through FLIR T640 camera (and its built-in RGB camera) for cracks, non-cracks, heat losses, and regular thermal images of various types of walls both indoors and outdoors. Additionally, for the "Default" image dataset (all the non-defect images), different types of façades were video-recorded, for both visible and thermal, sampled and saved at 1fps. For each annotated class, a total of 10,000 images with 227x227 pixels were used for training (80%) and testing (20%) dataset for visible images, and 1,000 images for thermal images. A batch size of 16 with 50 epochs were used during training at a learning rate of 0.0005. Examples of training datasets for both visible and thermal images are shown in Figure 38 and Figure 39 respectively.

Figure 38 - Examples of training dataset for 'default' and 'cracks' in supervised model
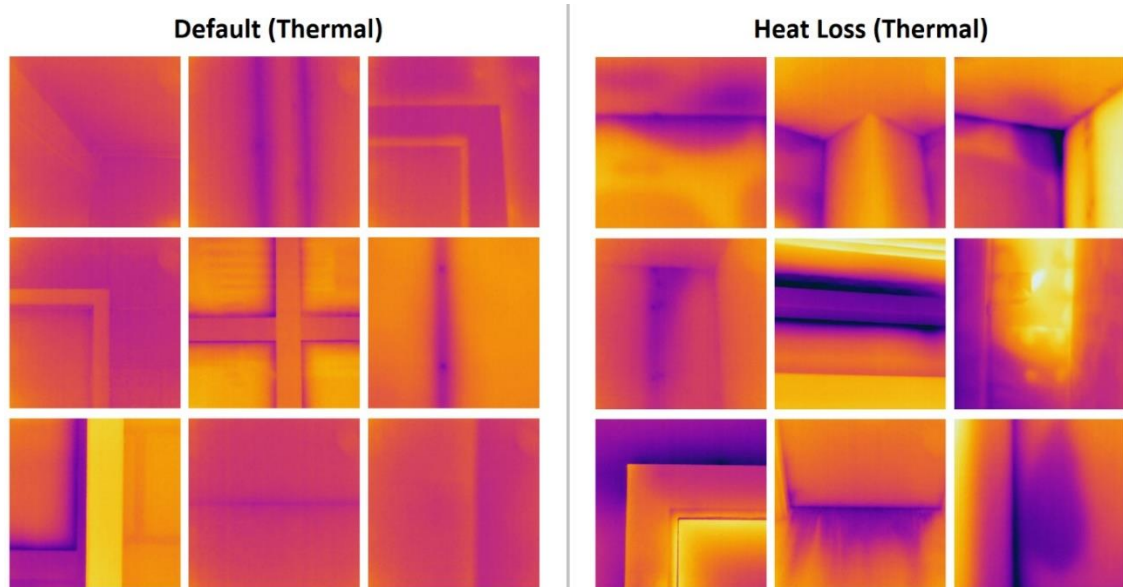
Figure 39 - Examples of thermal dataset for 'default' and 'heat loss' in supervised model

Both training and testing image sets also included visible cracks and thermal faults that are not centred (i.e. they are located close to edges or corners) similar to how they might be captured during an actual survey. This added practice during the ML training process improves the practicality of the ML model [213] and the reliability of inspection results.

Thanks to the abundant and diverse images for cracks (and no cracks) dataset, the training accuracy reached near 100% under 10 epochs, while each epoch took approximately 30 seconds. The loss graph for training and validation for visible ML model is shown in Figure 40.
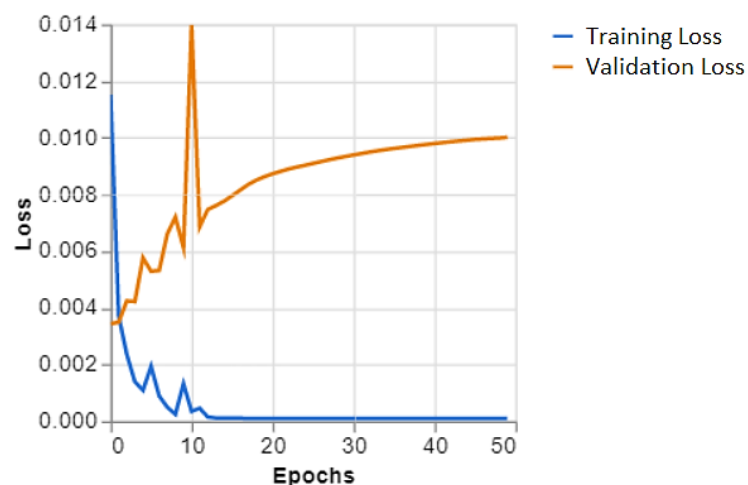
Figure 40 – Training and validation loss graph of ML1

66

3.2.7.3 Phase 3 - Self-Supervised Learning Training and Validation

Self-Supervised Learning (SSL) uses pseudo-labels (that would help to initialise and fine-tune the network weights) during the initial (manual) training process. Once the model is reasonably trained, it will continue to fine-tune itself from the supervised ML model's output to improve accuracy with the fused dataset.

The training and testing dataset comprises visible and thermal fused images captured from both, the image fusion module, as well as from FLIR T640 thermal-visible manually fused images. Examples of training datasets used for phase 3 (self-supervised learning) with two pseudo-labels classes of "Default" and "Heat Loss" are shown in Figure 41.
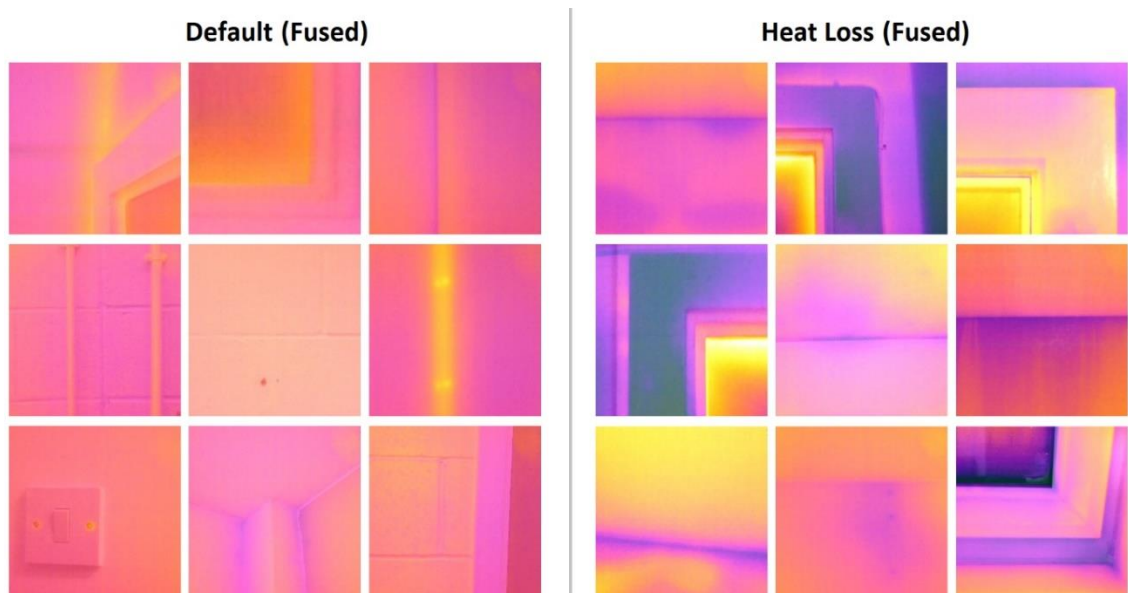
Figure 41 - Examples of fused dataset for 'default' and 'heat loss' used in SSL model

3.2.7.4 Phase 2 and Phase 3 – Results and Validation:

The results of training and validation for both supervised models and the self-supervised model are presented and discussed in this sub-section. Figure 41 shows the training and validation loss graphs of ML2 (thermal only) and ML3 (fused) machine learning models trained for 'Default' and 'Heat Loss' accordingly.
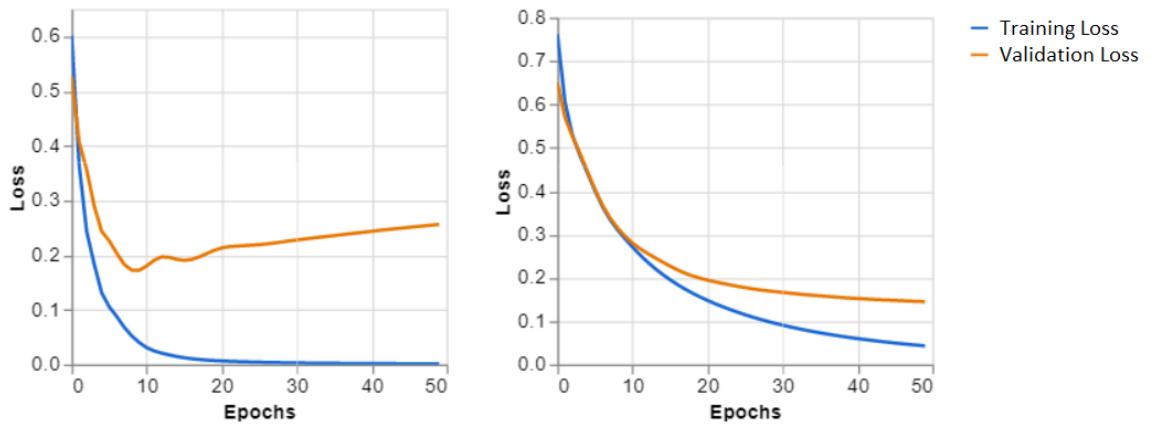
Figure 42 - Training and validation loss graph of ML2 (left) and ML3 (right)

To qualitatively validate the usefulness of deep learning on fused thermal-visible data, several specific examples of walls were captured and handpicked to test on the supervised model (ML2) with thermal-only data. To compare the fault detection accuracy, the same subject was tested on its corresponding fused data (i.e. ML3). In many scenarios where the heat signatures look visibly unusual, ML2 incorrectly predicted these as a thermal fault (heat loss) with high probability.
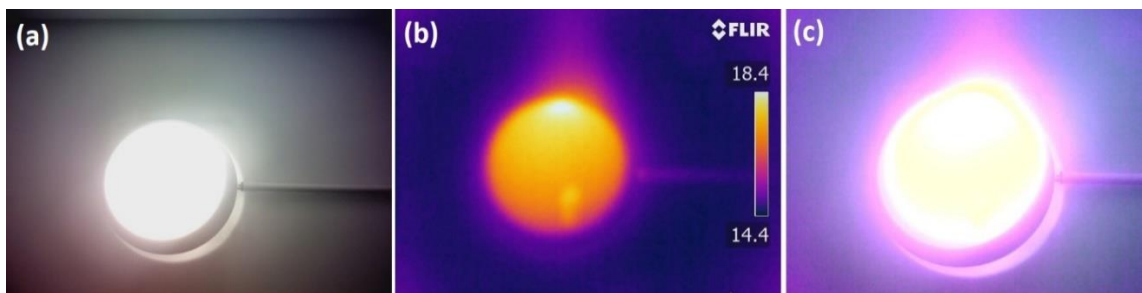
Figure 43 - A wall-mounted lamp as a test subject to compare supervised (thermal only) against self-supervised (fused) ML results

An example of such test subjects captured was a wall-mounted lamp shown in Figure 43, where (a) shows its visible image, (b) shows its thermal image, which is tested with the supervised ML model that classified it as 'heat loss', and (c) is the fused image that is tested with the self-supervised ML model that correctly classified it as 'Default' (i.e. no thermal fault). This validates the need for pixel-level accurate fused imagery for the maximum context of the scenario to assist deep learning model with more meaningful high-level information and predict with much higher accuracy.

3.2.8 Highlights and scope

The results from the image fusion module (phase 1) showed pixel-level accuracy compared to FLIR's built-in MSX feature which is prone to parallax errors and misalignment of edge features. In phase 2, both supervised models were trained with ample datasets and showed high accuracy for cracks and heat-loss detection on unseen data. Fused imagery from phase 1 and the corresponding results of phase 2 was trained and tested on the self-supervised model of phase 3, which detected faults accurately. However, a higher amount of training data and labels as the pretext task would continue to improve the accuracy of the SSL. Once the self-supervised model is trained with acceptable accuracy, the supervised ML models (of phase 2) are no longer actively required and can be bypassed to further improve the speed of inspection, which is ideal for instantaneous and automatic fault detection applications.

This framework provided a novel solution to improve the time and efficiency of building inspections while ensuring minimal hardware and real-time computational processing capacity. This helps reduce cost and human dependencies whilst increasing the accuracy and scalability of such inspections.

3.3 Peltier-driven Cooling Method

This section introduces the proposed Peltier-driven cooling method as an integration with heat pipes for wind towers. First, the design specification, function of key components, control system and power distribution are discussed, which is followed by the assimilation of the proposed method.

3.3.1 Thermoelectric Cooling

Thermoelectric coolers (TECs), also known as Peltier modules, are compact devices with no moving parts that can reduce temperatures to significantly below freezing at zero thermal loads. These environmentally friendly devices work using the Peltier effect [182] that produces a temperature difference across their junctions when an electric current is applied. TECs comprise Bismuth Telluride Elements with 'P' and `N` type semi-conductor properties arranged in a matrix (as shown in Figure 25) that helps

pump heat from one end (i.e. the source) to the other (i.e. the sink). This process is illustrated in

Figure 44, which shows a heat sink attached to a hot junction where the heat is rejected. Furthermore, reversing the polarity of the current switches the hot and cold sides. This property expands the scope of TECs to switch from cooling to heating in winter seasons.
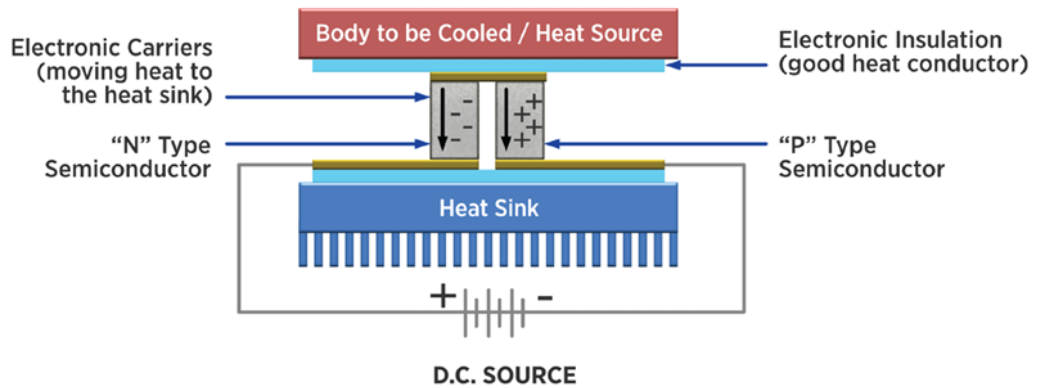
Figure 44 - Working schematic of a Peltier module [183]

Thermoelectric modules are available in a variety of shapes and sizes ranging from as small as 2mm x 2mm to 80mm x 80mm, some of which are shown in Figure 45. Their label provides details on its technical configuration as illustrated in Figure 46.Figure 47

Figure 45 – Examples of different shapes and sizes of TEC modules

Peltier modules are also available in a 'multistage' configuration (as shown on the left in Figure 45) where two layers of the TEMs are cascaded to provide a higher temperature difference by applying double the input power. This provides the ability and scope to enhance the cooling capability in future without affecting the design and assembly of the intended heat pipe integration. However, for this project, a single-layer Peltier module, called the TEC1-12706, is studied and implemented. Performance

charts to compare multistage coolers are presented in Appendix A-1, which also presents the justification for a single-stage TEC for this research.
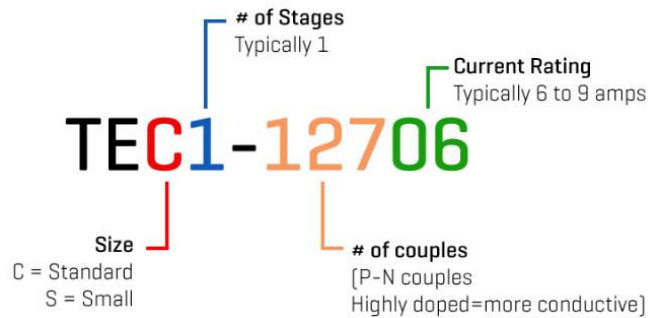
Figure 46 – TEC module label terminology

3.3.2 Specifications of the Cooling Unit Components

This section details the function and specifications of the key components that are employed in the proposed cooling system for wind towers, including the chosen TEC, heat sinks and heat pipes. The control system, assimilation and assembly details are presented in the subsequent sections.

3.3.2.1 Peltier Module

The TEC1-12706 module (shown in Figure 47) was selected for this research primarily due to its balance between operational efficiency and cost-effectiveness to allow affordable scalability. This single-stage device, while offering competitive thermal performance parameters, is the most inexpensive TEC model (£3 per unit) compared to alternative options commercially available. This ensures the scalability and accessibility of the key component in a larger-scale adoption. Additionally, its size (40 x 40 x 3.5mm) and power requirements (12V, 6A) align well with the project's design constraints for an intended solar-powered wind-tower-based system. Furthermore, the TEC1-12706's widespread applications in numerous studies provide a useful benchmark for evaluating its performance, which adds reliability and consistency to the experimental setup. The key specifications of TEC1-12706 are listed in Table 4.
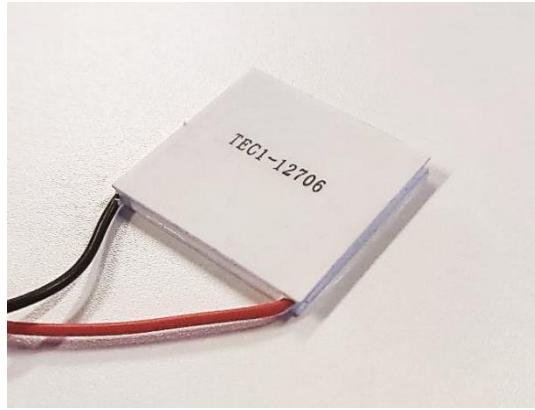
Figure 47 – TEC1-12706 Peltier Module

Table 4 – Specifications of TEC1-12706

Physical Dimensions	40 x 40 x 4 mm
Operating Voltage	12V
Maximum Voltage (V)	15.4V
Maximum Current (A)	6A
Rated Power	72W
Maximum Power	92W
Maximum Temperature	138°C
Maximum Temperature Difference	70°C

A detailed specification of TEC1-12706 module is presented in Appendix A-2.

The efficiency of a cooling system is assessed through its 'Coefficient of Performance' (COP). This dimensionless COP of a TEC is the ratio of the amount of heat removed from the system (i.e. cooling effect) to the work done by the heat pump (TEC) [214] as expressed in equation 3.4 and is typically between 0.3 and 0.7 for single-stage TEC applications.

$$COP = \frac{Q_c}{W_{in}} \quad (3.4)$$

The COP strongly depends on the temperature difference (dT) between the hot and the cold side. This is shown in Figure 48 with a graph of COP vs. normalised current (I/Imax) for dT varying by 10K from 0 to 70K.
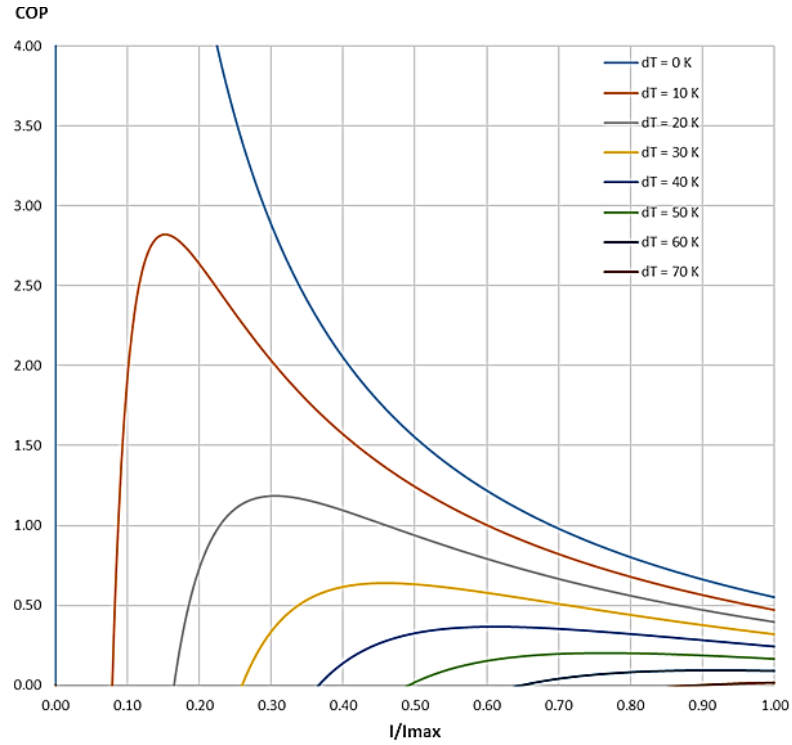
Figure 48 – COP vs Current of a Peltier module for different dT

To calculate the COP using equation 3.4, the heat removed from the TEM (Q_c) and work done by the TEM (W_{in}) can be calculated using equations 3.5 and 3.6 [215], respectively:

$$Q_c = (\alpha_2 - \alpha_1)T_1 I - \gamma(T_c - T_h) - 0.5(I^2)R \qquad (3.5)$$

$$W_{in} = (\alpha_2 - \alpha_1)(T_c - T_h)I + (I^2)R \qquad (3.6)$$

where, α_1 and α_2 are the Seebeck coefficients of the materials (in this case: Bismuth and Telluride), respectively, T_h and T_c are temperatures of the hot side (T_h) and the cold side (T_c) of the TEC, respectively, R is the electrical resistance, I is the electrical current and γ is the effective thermal conductance.

In addition to COP, the 'Figure of Merit' (ZT) [216] is also useful to gauge the cooling efficiency of a TEC. ZT is a dimensionless property that provides a relative assessment of the TEC's thermoelectric conversion efficiency, and it is calculated by:

$$ZT = \frac{S^2 \sigma T}{k} \qquad (3.7)$$

where, S is the effective Seebeck coefficient of the system (TEC), σ is the electrical conductivity, T is the absolute average temperature, and k is the thermal conductivity of the TEC. The Seebeck coefficient (used in equation 3.7) is the measure of an induced thermoelectric voltage due to a temperature difference, which can be calculated by:

$$S = \frac{V}{\Delta T} \tag{3.8}$$

where, V is generally the voltage induced by the temperature difference, and ΔT is the temperature difference between the hot and cold sides of a TEM. However, unlike TEGs, in the application of Peltier cooling, V is the applied voltage across the terminals of the TEC while ΔT is the resulting temperature difference across the TEC module.

3.3.2.2 Heat Sink

The efficiency of a Peltier module (or TEC) is largely dependent on a constant heat dissipation from its hot junction, which includes the pumped heat and the Joule heat. With a lack of effective heat dissipation, the heat from the hot side of the Peltier module transports internally to the warm the cold side and affects the cooling performance. Heat sinks are finned metal devices ideal for heat dissipation as they are made of high thermal conductivity materials (such as aluminium or copper) and have a large surface area to maximise heat transfer with the surroundings. Heat sinks are available in different shapes and sizes as shown in

Figure 49. They are often employed with a noiseless DC CPU fan to facilitate an effective heat transfer with ambient air streamed through their fins.

Figure 49 – Examples of different types of heat sinks

A typical arrangement of the heat sink with the heat-producing device and their respective temperature nomenclatures is shown in Figure 50, where 'junction' refers to the heat source tier inside of a TEC.
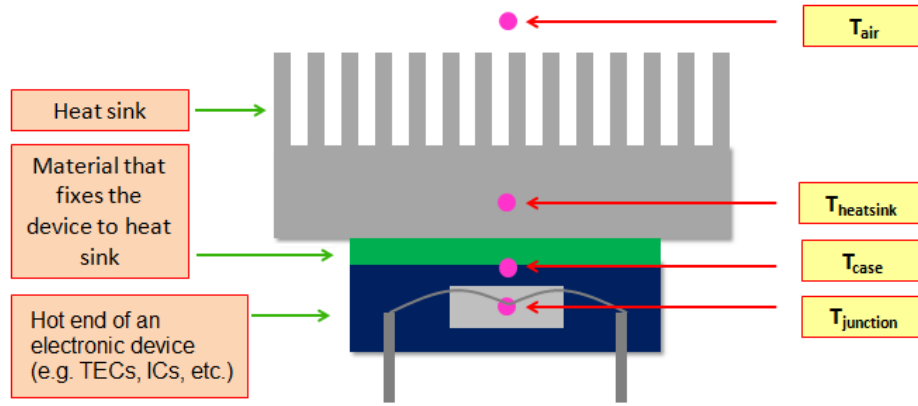
Figure 50 - Typical heat sink assembly and thermal parameters [217]

Between each temperature labelled, there is a thermal resistance (R_{th}). The total power dissipation P_D is given by:

$$P_D = \frac{T_{j\_max} - T_{c\_max}}{R_{th_{jc}} + R_{th_{ch}} + R_{th_{ha}}}$$ (3.9)

where, T_{j_max} and T_{c_max} are maximum temperatures at the junction and the case (e.g. thermal pad), respectively, while R_{th_jc}, R_{th_ch} and R_{th_ha} are thermal resistance from junction-to-case, case-to-heatsink, and heatsink-to-air, respectively.

Heat sink selection is primarily based on the thermal resistance required by the component (i.e. the Peltier device). As both the heat sink and thermal paste possess high thermal conductivity, R_{th_ch} is virtually zero. Secondly, as T_{j_max} represents the hot end temperature as measured from the surface of the TEC, R_{th_jc} can be neglected (or assumed zero). Hence, to calculate the required thermal resistance of the heat sink ($R_{th_{ha}}$), equation 3.9 can be re-arranged and simplified as:

$$R_{th\_ha} = \frac{T_{j\_max} - T_{c\_max}}{P_D}$$ (3.10)

where, T_{j_max} = 138°C and $P_D \approx 12$W as per the specifications of TEC1-12706, T_{c_max} is set to be 70°C as a desired hot end temperature of the TEC for effective cooling, while R_{th_jc} and R_{th_ch} are equal to 0°C/W as explained above. Hence, using equation 3.10 to solve for the maximum required limit of thermal resistance $R_{th_{ha}}$ for the heatsink:

$$R_{th\_ha} = \frac{138 - 70}{12} = 5.67°C/W \tag{3.11}$$

Equation 3.11 provides the thermal resistance based on the heat dissipation of one TEC. As per the assembly design for wind tower (which is later detailed in Section 3.3.5) a total of six TECs shall be attached to one larger heatsink. Hence, the total thermal resistance for six TECs can be obtained by:

$$R_{th_{total}} = \frac{T_{j\_max} - T_{c\_max}}{P_{D_{Total}}} = \frac{138 - 70}{6 \times 12} \approx 0.9°C/W \tag{3.12}$$

Hence, an aluminium heat sink of 300 x 86 x 40 mm is chosen with a thermal resistance of $0.8°C/W$ under forced air flow, which is less than the maximum thermal resistance calculated in equation 3.12. This heatsink would dissipate heat effectively from up to six TECs (to cool six heat pipes) with the help of an active air flow using a 0.1A 12V CPU fan. The heatsink and the fan are shown in Figure 51.
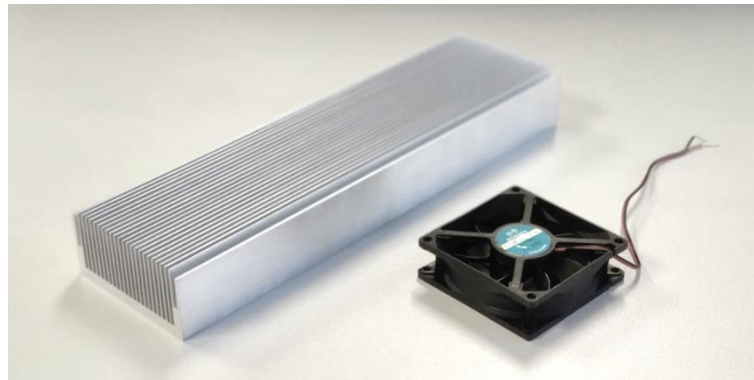
Figure 51 - Heatsink (left) and 12VDC CPU fan (right)

3.3.2.3 Heat Pipe

Heat pipes are devices that leverage the principles of phase change and capillary action to transport heat with high thermal efficiency. These heat pipes are charged with working fluid (e.g. water) that is sealed under a vacuum condition [218]. Their shells are made of materials with high thermal conductivity such as copper or aluminium. The heat transfer inside the heat pipe occurs passively when heat absorption occurs at its evaporator section, where the working fluid vaporises. This vapour then travels along the length of the pipe rapidly to the cooler end of the pipe (i.e. condenser), where it releases the heat and converts back into liquid. This liquid then travels back to the

evaporator region through capillary action with the help of a wick structure that surrounds the inner walls of the pipe. This continuous cycle effectively allows a heat pipe to transfer heat over considerable distances with minimal temperature drop.

Figure 52 shows the schematic of the internal working of a heat pipe.
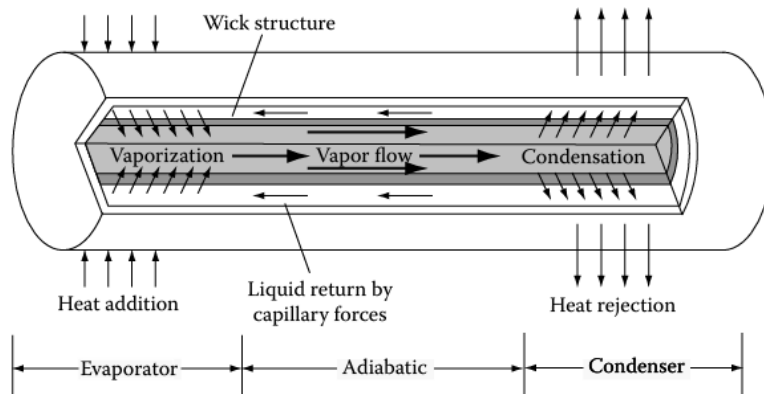
Figure 52 – Schematic of the working of a heat pipe [219]

An aluminium-coated copper heat pipe of 15mm diameter and 1m length is selected for this research. The length of 1 meter aims to leverage the large surface area that will be in contact with the flow of air through wind tower. A Peltier module is to be fastened to the centre of the pipe, ensuring that the module's cold side is in contact with the pipe firmly. With the rapid heat circulation ability of the heat pipe allows an even distribution of cooling evenly across the length of the pipe. Heat absorption in the centre produces heat to transport from either end towards the centre as illustrated in

Figure 53. A total of 35 of these TEC integrated pipes are to be used for one wind tower. Details on the assembly with the wind tower is provided in Section 3.3.5 and the attachment with the TEC module is described in Section 3.3.3.
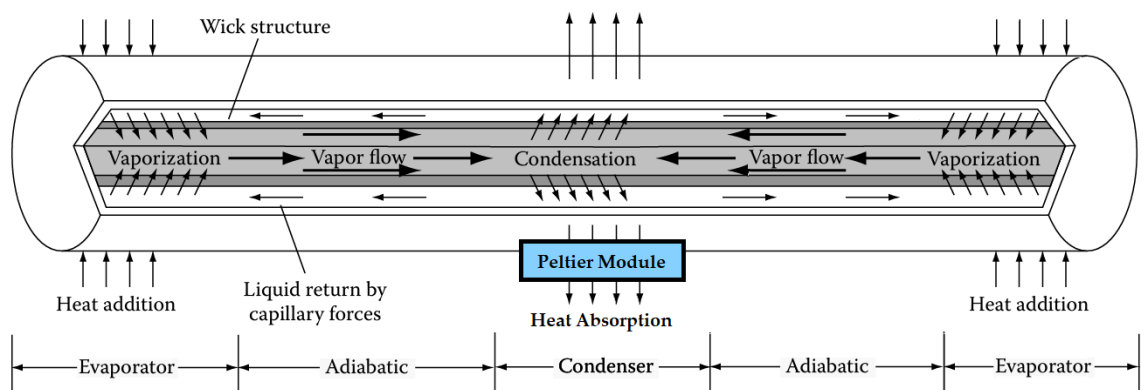
Figure 53 – Revised working of heat pipe with integration of Peltier module

Likewise, reversing the direction of current on the TEC would switch from cooling to heating mode, where heat will be added in the centre of the pipe and rejected from each end in contact with the air flow. The conductive heat transfer Q_{cond} is given by:

$$Q_{cond} = -k \cdot A \cdot \frac{dT}{dx} \tag{3.13}$$

where, k is the thermal conductivity, A is the cross-sectional area, and dT/dx is the temperature gradient along the length of the heat pipe.

3.3.3 Assimilation of the Cooling Unit

This section provides an overview of the proposed cooling system including integration with wind tower, the process of cooling, and the practical benefits of this method.

3.3.3.1 Integration with the wind tower

The thermoelectric cooling approach using heat pipes is designed to be installed on a multi-channel wind tower situated on the roof of a building. It operates on the principle of warm wind entering the tower and interacting with actively cooled arrays of heat pipes, which cools the fresh air entering the room. This cooler air descends into the room while expelling warmer, stale air through the tower's leeward side. The process is illustrated in Figure 54. The detailed assembly process of the cooling unit and its attachment to the wind tower is later presented in section 3.3.5.
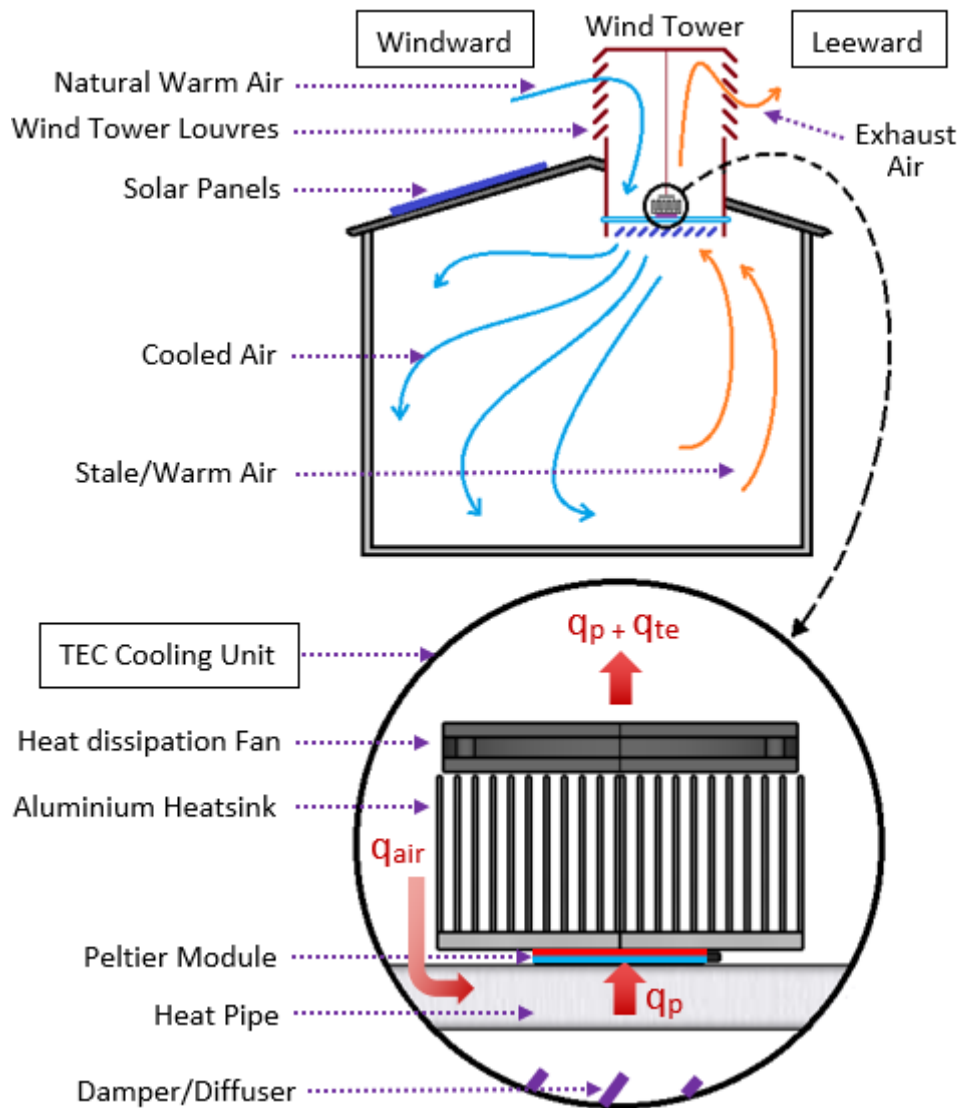
Figure 54 – Integration of TEC cooling unit on wind tower

3.3.3.2 Cooling mechanism and heat recovery

The active cooling is primarily achieved through the thermoelectric (TEC1-12706) modules, which are powered by solar panels. These compact TECs are sandwiched between the heat pipe (in contact with the TEC's cold side) and a heat sink (against the TEC's hot side). The heat pipes play a key role in cooling the incoming warm air through the wind tower. As the TECs absorb heat from the heat pipes, their large surface area helps to collect heat from the incoming air (q_{air}) thereby cooling the air before it enters the room. This heat travels internally through the heat pipe to the condenser (TEC) region (q_p) where it gets pumped to the hot side of the TEC. In addition to q$_p$, the heat generated by the electrical work done by the TEC (q_{te}), known as Joule heating, is

also accumulated. The heat sink assisted by a 1.2W fan facilitates the dissipation of this heat to ensure optimal cooling performance of the TEC. Moreover, the air exiting through the wind tower further assists in heat dissipation of the heat sinks aiding TECs' efficiency.

The hot end of the TEC can additionally be used for waste heat recovery for other applications such as water heating. However, in the context of Peltier-driven cooling in this research, heat recovery primarily refers to recovering heat from the ambient environment to enhance the efficiency of the cooling processes. In other words, the proposed system extracts and utilises heat from the incoming air to facilitate the TEC-integrated heat pipe's heat absorption process as described in section 3.3.2.3.

A damper system is situated beneath the heat pipes and is designed to control the volume flow rate of air, which helps in regulating thermal comfort within the room. The distribution of power from the solar panels to the thermoelectric modules and the damper, along with the comprehensive control system, is elaborated in section 3.3.4.

Furthermore, a notable feature of this method is its ability to switch between cooling and heating modes. By switching the polarity of the current to the TECs, the direction of heat flux is reversed, enabling the system to heat the room. This dual functionality offers a versatile, energy-efficient and all-season thermal comfort solution to reducing HVAC-related energy loads. Though, despite the heating potential, the primary focus and the scope of this research is on evaluating the system's cooling capabilities.

3.3.4 Heat load and convection

The convective heat load (Q) to cool the ambient air through the actively cooled heat pipes is given by:

$$Q = hA(T_{ambient} - T_{cold}) \tag{3.14}$$

where, h is the convective heat transfer coefficient in W/m²K, A is the surface area of the heat pipes in m², T_{cold} and $T_{ambient}$ refers to the heat pipe and ambient temperatures, respectively.

The overall cooling capacity (Q_c) of the cooling unit is given by:

$$Q_c = \dot{m}c_p(T_{indoor} - T_{ambient}) \qquad (3.15)$$

where, $\dot{m}$ is the air mass flow rate in kg/s, c_p is the specific heat capacity of air in kJ/kg, T_{indoor} and $T_{ambient}$ refers to the indoor and ambient temperatures, respectively. This heat removal rate is dependent on the cooling power and efficiency of the TEC modules.

3.3.5 Control System and Power Distribution

3.3.5.1 Control System and Hardware

The purpose of a control system in an active-passive cooling system is to regulate thermal comfort inside the room autonomously while allowing users to have an all-in-one intuitive UI for manual controls. However, in the context of this research, the incorporation of a control system aims to allow (1) real-time data monitoring remotely (of temperatures, power consumption, CO2, etc) and (2) manual controls for cooling, heating, and louvre angles remotely.

The two control devices used are (1) Control4 [220] that is a commercially available home automation system with capabilities of integrating controls for home appliances wirelessly through mobile app or tablet, and (2) ESP32 [221] Development board that is an open-source programmable microcontroller device capable of interfacing custom sensors and actuators wirelessly. Details on these hardware devices are shared in Appendix B-1 along with their specifications.

Figure 55 – ESP32 Microcontroller and its integration with Control4 UI

Figure 55 shows Control4 and ESP32 integration to allow a home automation system to automate the TEC cooling and wind tower airflow (damper) using an intuitive UI potentially integrated with existing HVAC systems. Additionally, a CO_2 sensor unit (SCD40) also capable of sensing temperatures and humidity was integrated with two ESP32 boards as shown in Figure 56. These boards were programmed for (1) wireless data monitoring and (2) App-based controls for the dampers. The programming of both boards is shared in Appendix C-2.
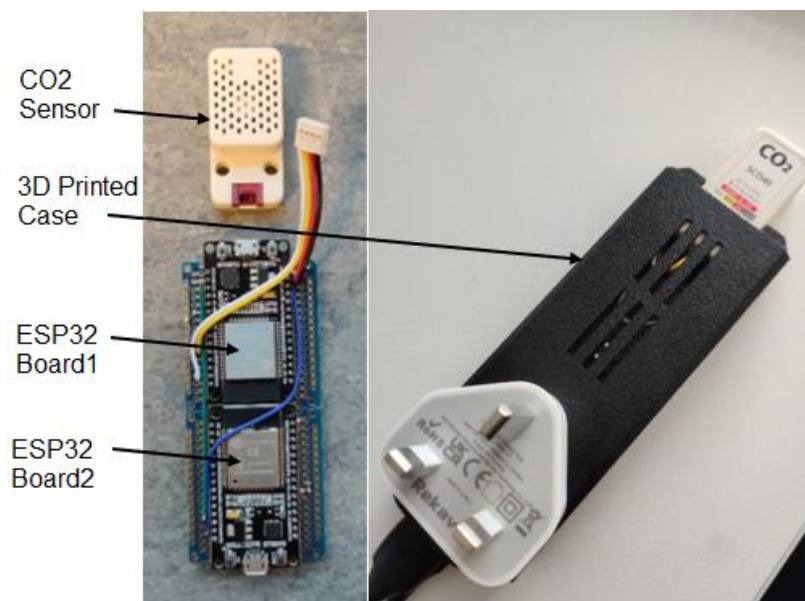
Figure 56 – ESP32 boards connected with CO_2 sensor with casing

A control system flowchart illustrating the integration of sensors, control devices, actuators, user interface, communications and storage protocol is presented in

Figure 57. Furthermore, app screenshots for sensor data logging, UI control, and ESP32 programming are shared in Appendix B-2.
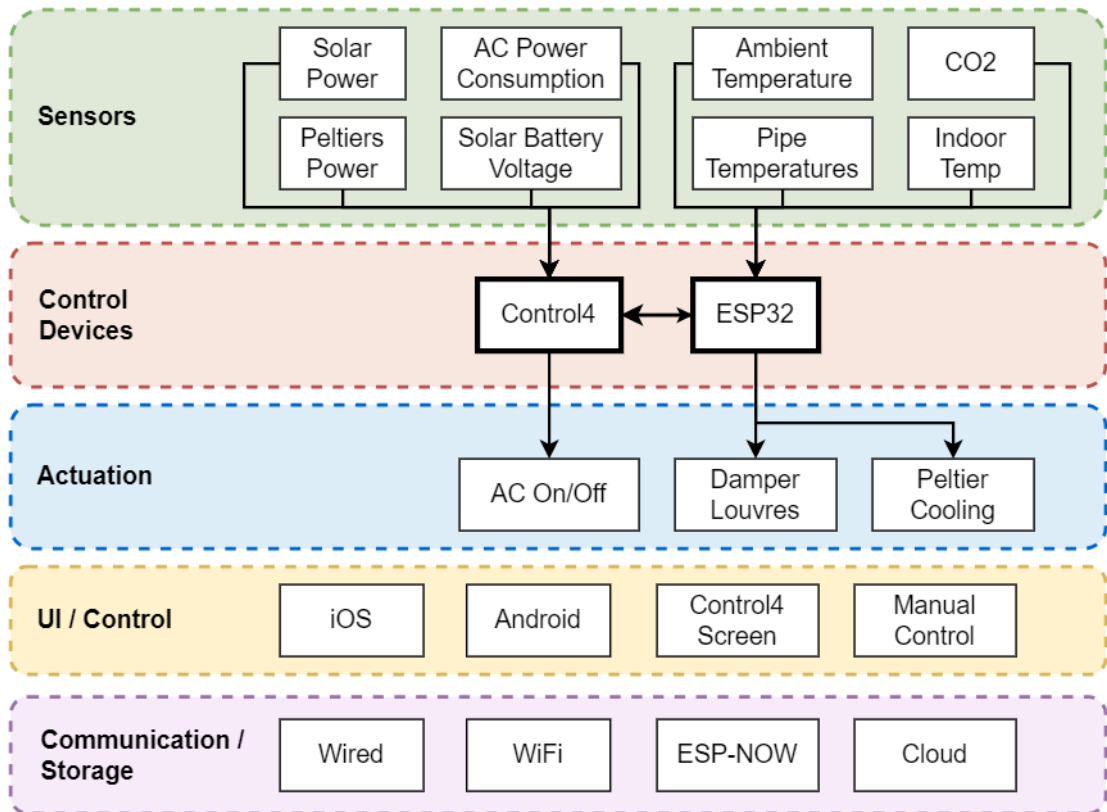
Figure 57 – Integrated Control System Flowchart

3.3.5.2 Power Distribution and Management

The practical adoption of this passive-active cooling system on building roofs would ideally use solar power management including 12V solar panels with a minimum of 1280W, a 60A charge controller and a 200Ah or higher battery storage to regulate the power. However, for the purpose of experimental testing, two external power supplies of 12V 30A (360W) each are used to power the TEC system. Additionally, two 12V to 6V buck converters are used to limit the voltage to 6V to the TECs. Through preliminary tests, cooling of one heat pipe using 6V consumes 12W of power, which equates to a total of 420W of power consumption for the whole thermoelectric cooling system.

Figure 58 – 12V 30A External Power Supply (left) and 12V-6V Buck converter (right)

Despite the rated voltage of 12V of the TEC1-12706, the 12V to 6V voltage converters aim to improve the efficacy of the cooling operation in terms of power management. The reduction of input power by half is not equivalent to reducing the cooling capacity by half as the COP of TECs with dT of less than 40K is always higher at half of the maximum current as seen from Figure 48. However, detailed experimental analysis is presented in Chapter 5 Section 5.4.4 to practically validate this principle by investigating the optimum cooling potential of heat pipes against varied power inputs.

The external power supply and the waterproof 30A buck converters used for this research are shown in

Figure 58. These voltage converters also help in powering the control devices (i.e. the ESP32 boards) and the damper actuator (i.e. the 6V Servo). A flowchart schematic of the power distribution of the overall system is illustrated in Figure 59.
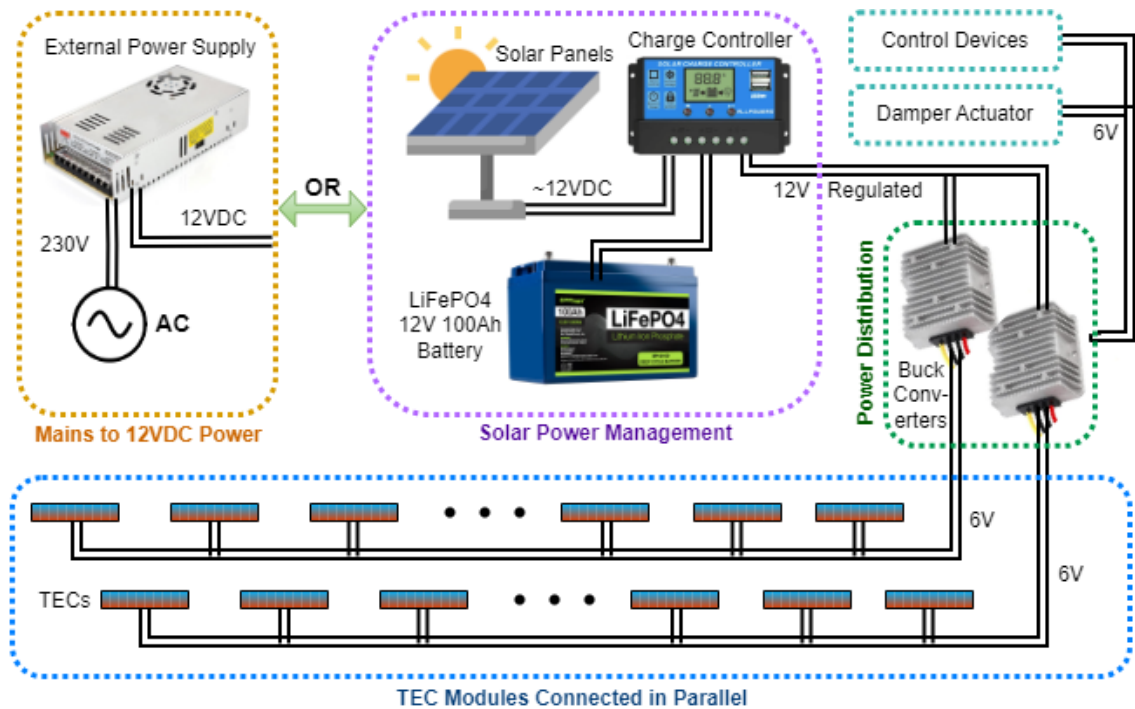
Figure 59 – Flowchart to illustrate the power distribution system

3.3.6 Assembly of the cooling unit

3.3.6.1 Bill of Materials

The bill of materials and their specifications and quantities required to assemble a cooling unit for one wind tower are detailed in Table 5. Items 1 to 4 were discussed in detail in section 3.3.2. The remaining required items include thermal paste and 3D-printed brackets.

The use of thermal paste significantly improves the thermal contact between the hot surface of the TEC with the heat sink, as well as the cold surface of the TEC with the heat pipe. This minimises thermal resistance with the TEC junctions and ensures efficient heat dissipation, which corresponds to optimal cooling performance. The 3D-printed brackets are designed strategically to firmly sandwich the TEC in between the heat pipe and heat sink with adequate compression force to ensure high thermal contact. The 3D-printed spacers are used to allow a 50mm distance between each heat pipe.

85

Table 5 – Bill of materials of the TEC cooling unit

	Item	Image	Specification	Qty for 1 WT
1	Aluminium Heatsink		Dimensions: 310x80x35mm	6
2	Peltier Module (TEC)		Type: TEC1-12706 Dimensions: 40x40x3mm	35
3	Heat pipe		Aluminium coated copper heat pipe Dimensions: 1000mm length, 15mm diameter	35
4	Heat dissipation fan		12V, 0.2A, 80x80x25mm	12
5	Thermal paste		Thermal conductivity >= 70W/mK 20g	1
6	Heat pipe to Heatsink Clamps		3D Printed (PLA)	70
7	Spacers		3D Printed (PLA)	60

3.3.6.2 Assembly process:

The assembly process of the TEC cooling unit for the wind tower using the components detailed in Table 5 is illustrated in Figure 60 followed by its step-by-step instructions.
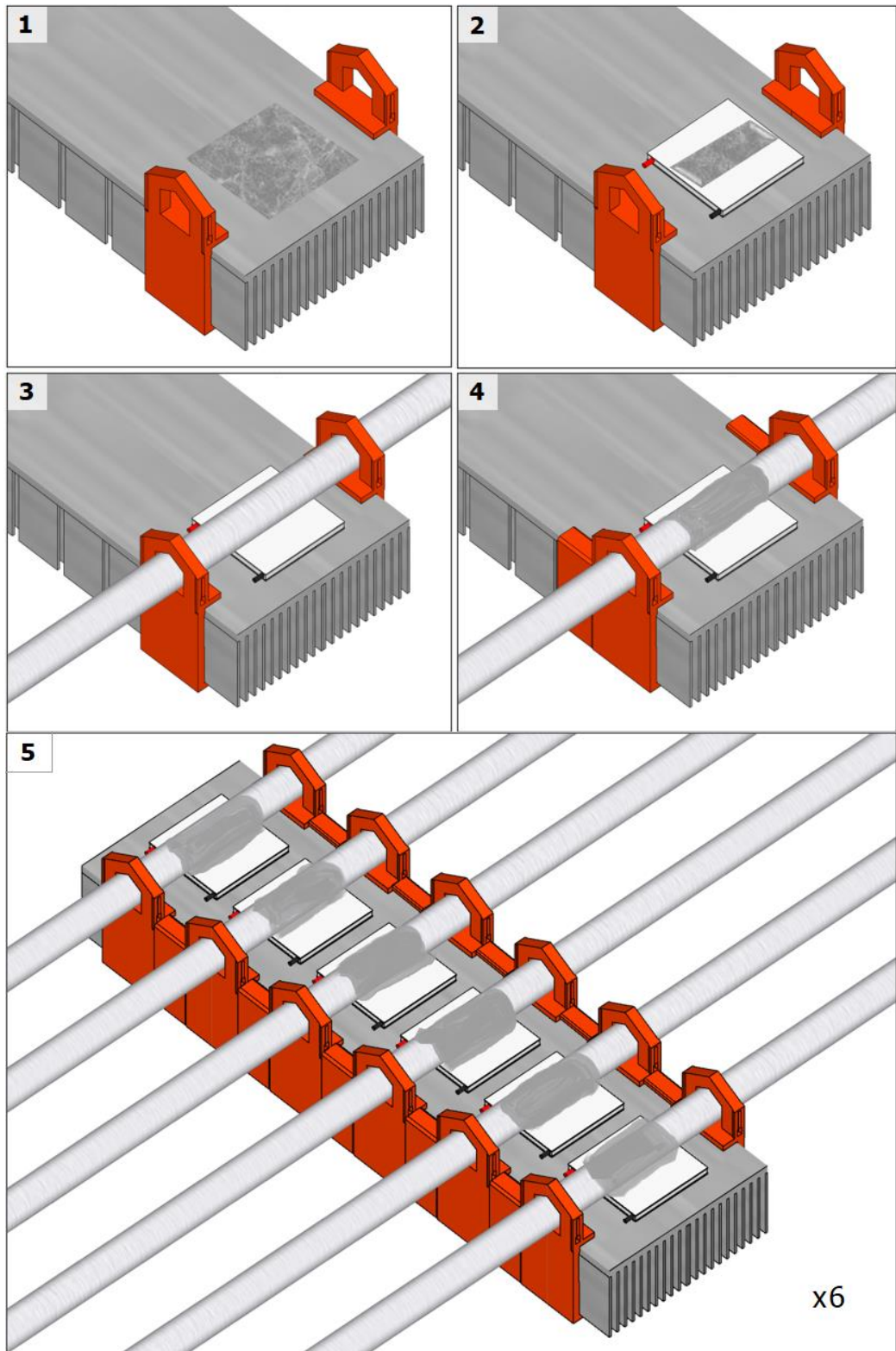
Figure 60 - Assembly process of the TEC cooling unit

1. Two heat pipe clamps are aligned on opposite sides of the heat sink. A thin layer of thermal paste is spread in the centre to optimise the thermal contact with the surface of the TEC module.

2. A TEC is placed and pressed in the centre over the thermal paste such that the hot side is in contact with the heat sink. A thick blob of thermal paste is laid on the top side of TEC for effective thermal contact with the heat pipe's curved surface.

3. The heat pipe is then slid through the clamp holes ensuring that the heat pipe extrusion from both sides of the heat sink is equidistant.

4. Additional thermal paste is spread over the curved surface of the heat pipe to enhance thermal contact and conductivity with the cold side of the TEC. Lastly, one spacer is added beside each clamp to complete the assembly of one heat pipe.

5. Likewise, the above steps are repeated to assemble a total of six heat pipes on one heat sink. For a wind tower of 1m x 1m base area, six of these assemblies are required that are to be arranged in two layers of TEC-cooled heat pipes.

Additionally, the CPU fan is fastened on the finned face of the heatsink. This is done to ensure necessary heat dissipation from the hot side of TECs to enhance cooling performance. It is to be noted that in hot climatic regions with extremely high ambient temperatures, two fans may be necessary to dissipate heat effectively. A complete assembly of six heat pipes is shown in

Figure 61 from both sides with two fans installed.
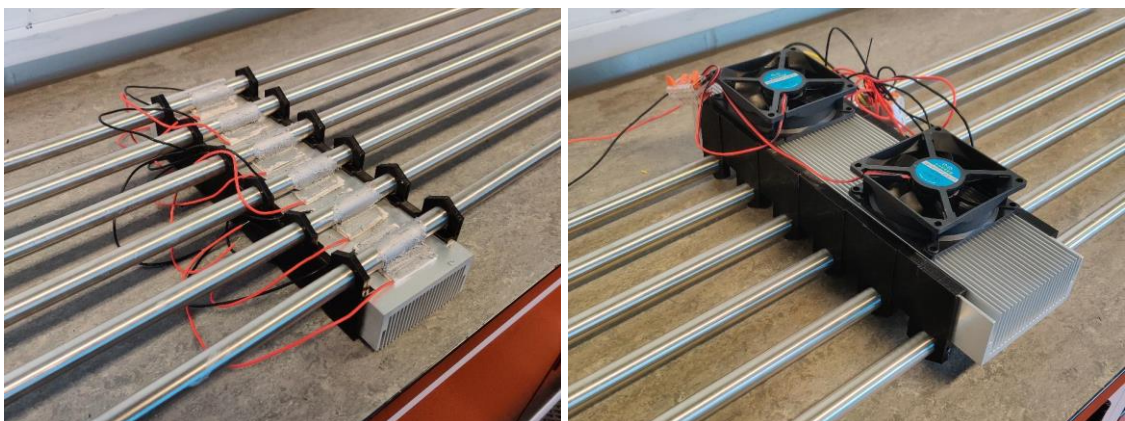
Figure 61 – Heat pipe assembly with TEC and heat sink (left) and fan attachment (right)

The design of the complete cooling unit as an add-on to a 1m x 1m wind tower base consists of a total of 35 heat pipes arranged in two layers. This is enclosed using a 1m x 1m x 0.2m aluminium frame that is illustrated in Figure 62 as 3D CAD drawing. Fully

assembled photos of a full-scale model of this modular cooling unit are shown in section 4.3.5 which further shows the heat pipes' attachment to the frame.
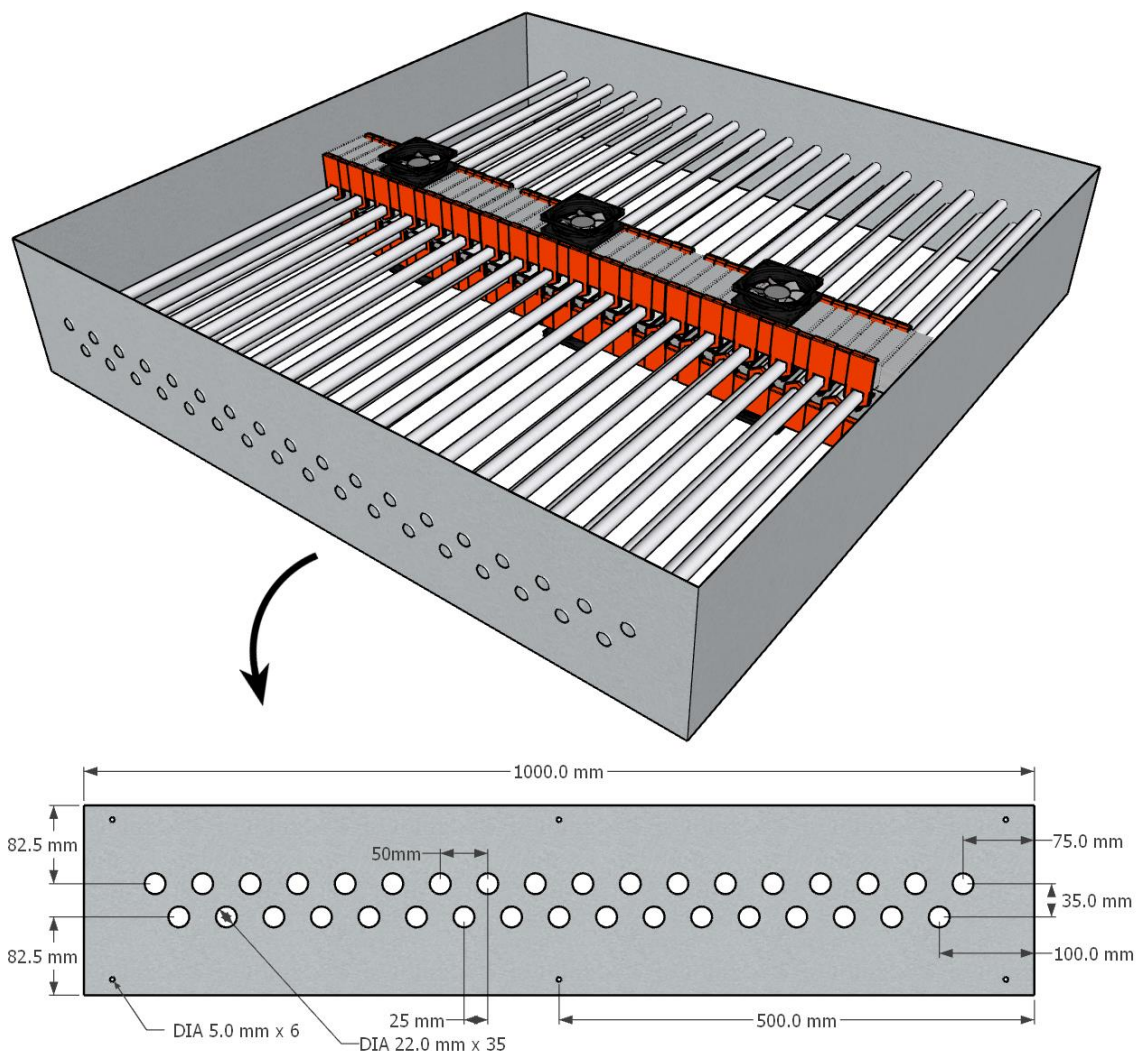
Figure 62 – Modular TEC cooling unit and outer frame specifications

3.3.6.3 Integration with Wind Tower

A modern multi-channel four-quadrant wind tower is selected for this research with 1m x 1m x 1.2m design as previously studied by John et al. [154] and Harry et al. [155].

Figure 63 shows the louvres arrangement of this 1.5mm thick aluminium sheet metal wind tower designed for building roofs.
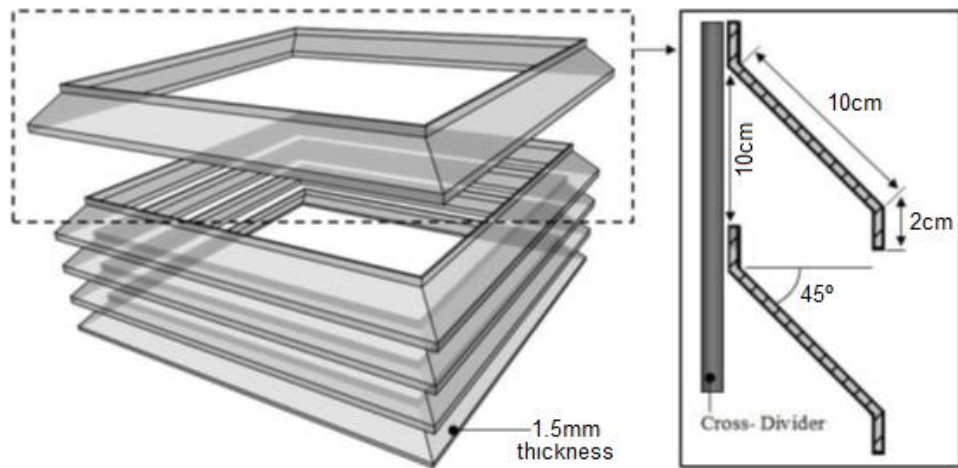
Figure 63 – Wind tower louvres

Additionally, a 1m x 1m damper is installed beneath the wind tower to regulate the air volume flow rate based on the control system as discussed already in Section 3.3.4. A high torque (60kg/cm) metal gear 6V DC servo is selected to actuate the damper louvre. The servo used and its attachment with the damper is shown in Figure 64.
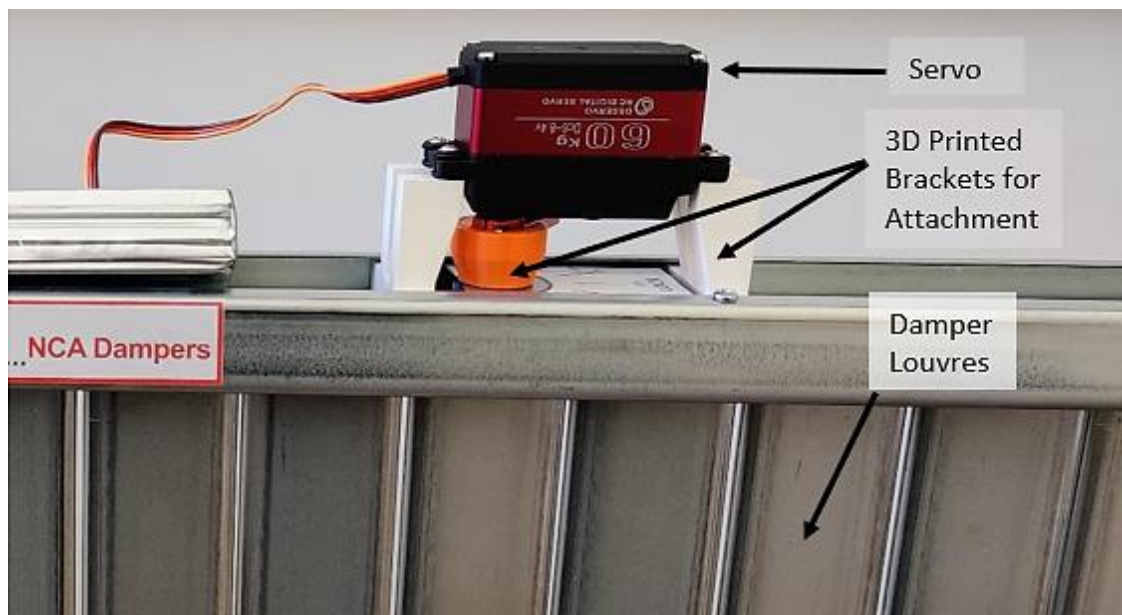
Figure 64 – Servo and Damper

The assembly of the damper and cooling unit with the four-sided wind tower along with an X-ray view of a fully assembled 3D CAD model is shown in Figure 65.
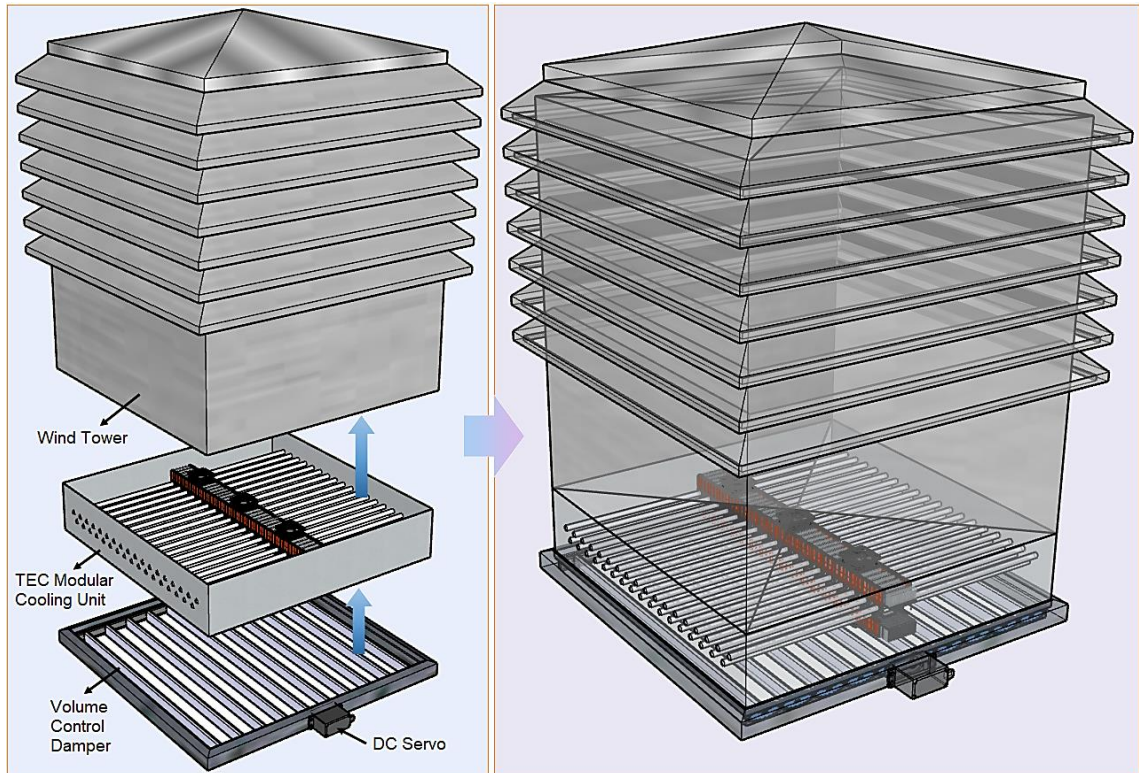
Figure 65 – Damper, Cooling Unit, and Wind Tower Integration

3.4. Summary

This chapter first detailed a qualitative approach that presents an image fusion technique to efficiently map thermal and visible data in real-time. This was achieved by integrating a custom-designed image fusion module to align the optical axes of thermal and visible cameras. The results from the prototype of the module showed high accuracy with minimal hardware and a time-efficient approach to superimpose thermal and visible images. Additionally, qualitative evaluation of the fused results on machine learning models and 3D thermal reconstruction showed promising scope for a large-scale computationally friendly building inspection solution.

Secondly, this chapter presented the Peltier-driven cooling method integrated with heat pipes for wind towers, detailing design specifications, functions of key components, control system, power distribution, and assembly processes. The TEC1-12706 Peltier module was selected due to its high cooling potential at low power consumption and scope for scalability due to its cost-effectiveness.

Thermoelectric coolers are generally less efficient than other existing cooling technologies, however, the proposed method leverages the thermal efficiencies of heat pipes to collect heat from a much larger surface area to cool the warm air as it passes through wind towers. This heat travels rapidly through the heat pipe and is absorbed by the TEC. A finned block of aluminium heat sink assisted with a low-power fan then dissipates this actively pumped heat from the TEC's hot side including the internal Joule heating. The exhaust air exiting the room through the wind tower further helps in heat dissipation of the heat sinks allowing TECs to perform efficiently.

The next chapter details experimental and simulation methodology followed by results and validation to evaluate and optimise the parameters that influence the performance of this Peltier-driven cooling method.

Chapter 4 – Experimental and Simulation Methodology

4.1. Introduction

This chapter discusses the experimentation methods, followed by simulation and validation methodology, for the Peltier-driven cooling system. SolidWorks software and its Computational Fluid Dynamics (CFD) add-on called 'Flow Simulation' was used for 3D modelling and CFD analysis.

Section 4.2 defines the methodology for all experiments and associated CFD simulations. Section 4.3 details the experimental setup, methods, and instruments used for each experiment. Section 4.4 introduces the CFD model and simulation methodology to replicate the experimentation using CFD analysis for cross-validation.

4.2 Experimentation Methodology Framework

A total of five physical experiments were performed, including four CFD simulations. A chronological list of physical experiments and their purpose is summarised as follows:

1. **Experiment 1: Proof of Concept and Ambient Temperature Impact** – This includes a preliminary set of conduction tests to observe the Peltier-driven cooling and heat absorption rate across the length of two heat pipes. Additionally, the impact of ambient temperatures on the cooling effect is also evaluated.

2. **Experiment 2: Natural Convection – Power Impact** – This set of experiments studies the impact of input voltage (and power consumption) of the TEC on the steady-state temperatures and rate of change of these temperatures on the surface of the heat pipes under natural convection (i.e. ambient room conditions).

3. **Experiment 3: Coefficient of Performance and Heat Transfer Rate Validation** – The coefficient of performance (COP) is evaluated against a range of input power to the TECs. The heat transfer rate for TEC in the computational model is then defined to analyse the wind-assisted steady-state temperature of the pipe on the CFD model. This helps simplify the computational model to have an active (negative) heat

transfer rate on the surface of the pipe to replicate the TEC cooling provided. The resulting temperatures are validated with experimentation results.

4. **Experiment 4: Forced Convection – Velocity Impact and Validation** – Once the optimum power is defined from experiment 2, the trials under forced convection are conducted to replicate the real-world effect of wind over an actively cooled pipe. The relation between wind speed and the resulting steady-state temperatures of the pipe is studied. These experiments further help validate the results of CFD analysis performed on a matching computational setup.

5. **Experiment 5**: **Cooling Unit – Air Mass Impact and Validation** – As the results of experiments and simulations of single-pipe cooling are in harmony with each other for varied power input and wind speeds, a true-scale heat exchanger (the cooling unit) with 35 actively cooled pipes is then tested against air mass flowrate and wind speeds. An equivalent CFD analysis is performed to investigate the results.

Additionally, the successful validations of the experimental and CFD results enabled a scope for further optimisations on the cooling performances. Post-validation CFD analyses were applied on a true-scale wind tower model to examine and optimise the cooling inside a room through various augmentation techniques using the validated cooling mechanism, which is described in section 4.4.3. A flowchart summarising all the experiments and their corresponding CFD analysis is illustrated in Figure 66.
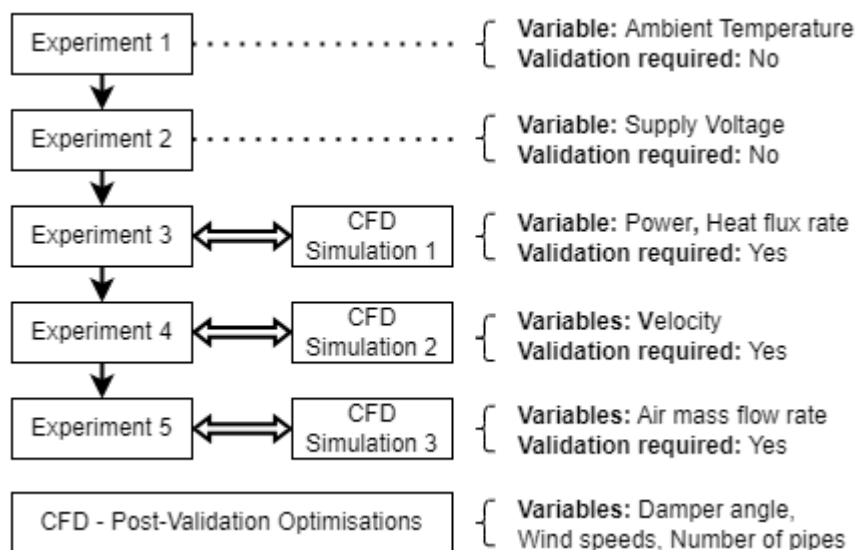
Figure 66 – Experimental and Simulation Methodology Outline

4.3. Experimental Setup

The experimental setup and methods for each experiment are detailed in this section.

4.3.1 Experiment 1 – Proof of Concept and Ambient Temperature Impact

4.3.1.1 Experiment 1a – Proof of Concept: Conduction Cooling of Heat Pipe

The aim of experiment 1a is to investigate the temperature drop in heat pipe surfaces through TEC-based conductive cooling as a proof of concept. Two vacuum-sealed 1m aluminium-coated copper heat pipes are utilised to assess heat absorption along their length through active cooling from one end. The cold side of this TEC is in contact with both pipes and the hot side is attached to the metal block at the bottom of the heat sink. The heat sink used for these preliminary trials (of experiment 1a) possesses a much larger heat dissipation capacity than required. This is done to observe the temperature drop using the proposed Peltier-driven method at the peak heat pump capacity of the TEC. This heat sink uses 8 copper heat pipes that transport heat effectively from the hot end of the TEC to the fan-assisted aluminium fins for efficient heat dissipation as shown in Figure 67.
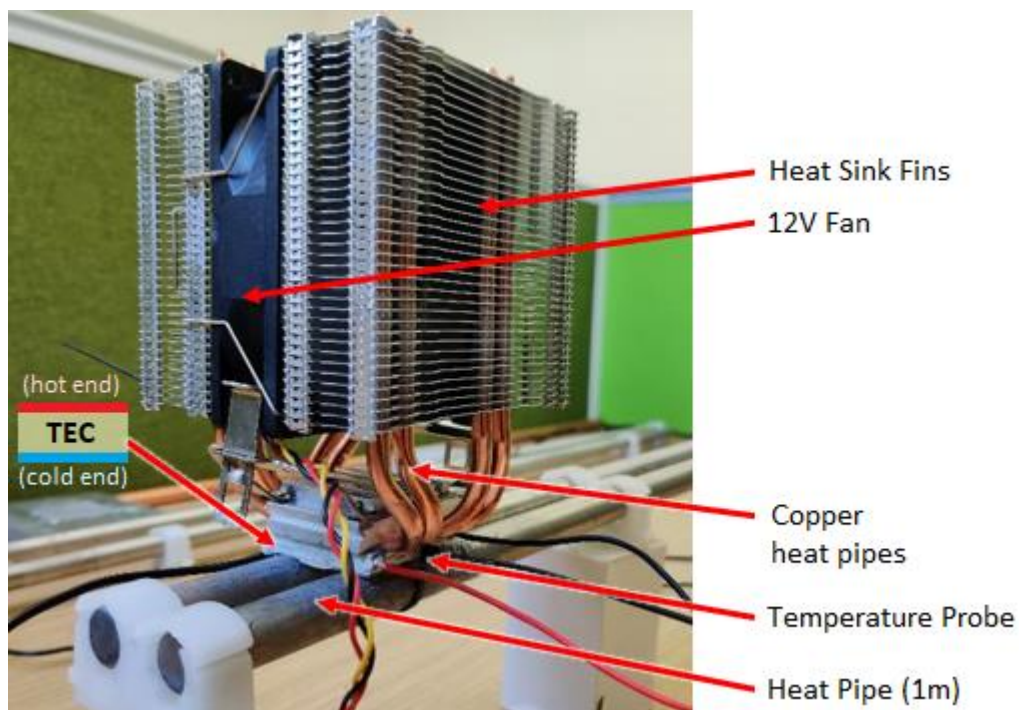
Figure 67 – Heat sink for Experiment 1

A single TEC1-12706 Peltier module is utilised to cool two heat pipes simultaneously using a 12V 30A power supply. Five DS18B20 digital temperature sensors are used to measure the pipe surface temperatures at the centre and opposite end of each pipe, and the cold surface of the TEC module as shown in the overall arrangement in Figure 68.
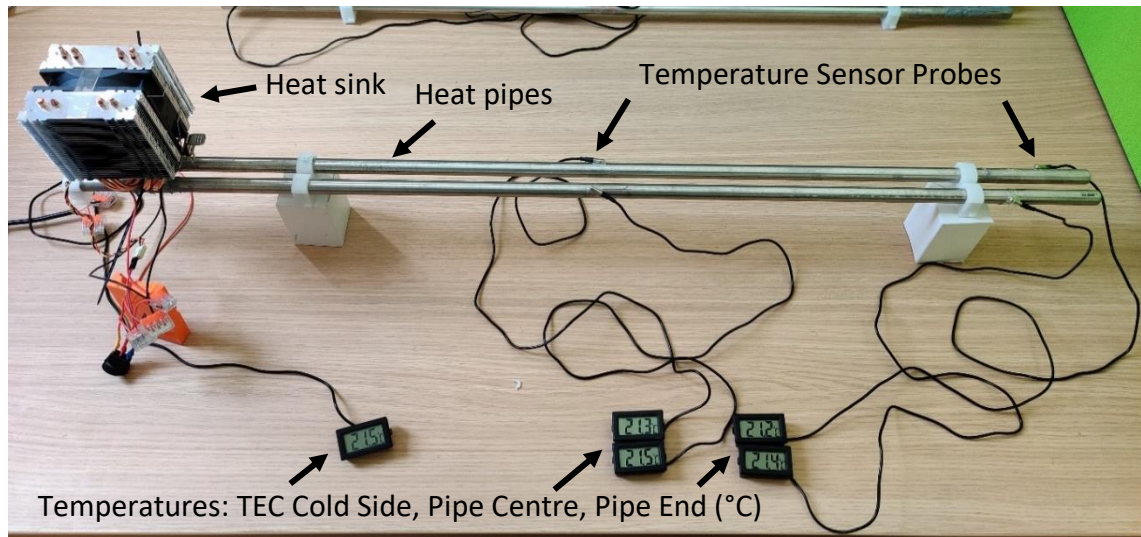
Figure 68 – Experiment 1 – Preliminary Cooling Test

The large heat sink (with excessive heat dissipation capacity) adds to the complexity of the design from a potential large-scale perspective. An adequately sized heat sink with minimum required thermal resistance was studied and selected in section 3.3.2.2, which will be used for all subsequent experiments.

Similarly, the position of the TEC module at one end of the pipe for this preliminary test (experiment 1a) was to observe the distribution (and rate of decrease) of temperatures across the full length of the pipe. All forthcoming experimentations and simulations will have the TEC device mounted in the centre of the pipe for quicker and more efficient heat transfer (across the length of the pipe) and potential ease of installation.

4.3.1.2 Experiment 1b – Impact of Ambient Temperature on Heat Pipe Cooling

This set of experiments examines the difference in steady-state temperature drop of pipe surface at different ambient temperatures. Two separate TEC modules are used to cool both pipes. A total of 7 temperature sensors are used such that three probes are attached at different locations (both ends and one at the centre) on each heat pipe.

Additionally, the ambient temperature is also measured. The power consumption, i.e. the voltage input and total current drawn is measured using a standard DC clamp meter. The experimental setup with centred TEC and a compact heat sink is shown in Figure 69 with a close-up of its TEC assembly in Figure 70.
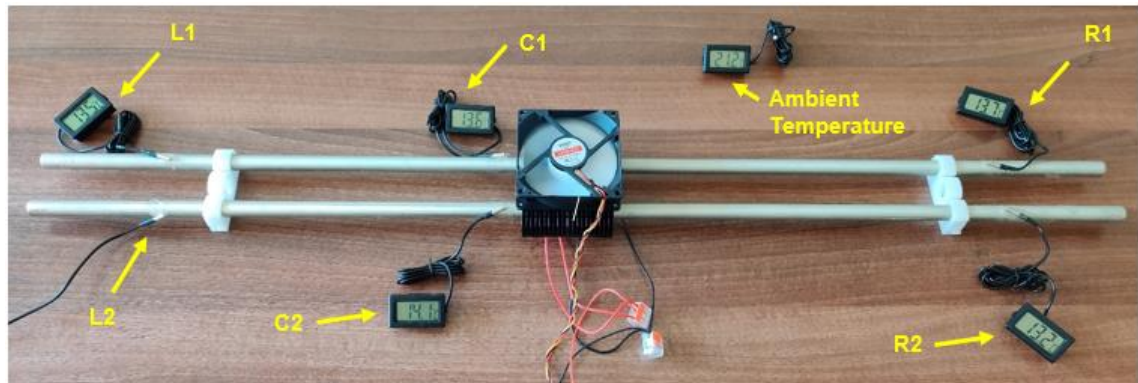
Figure 69 – Experiment 1b – Simplified set-up with centred TEC and compact heat sink
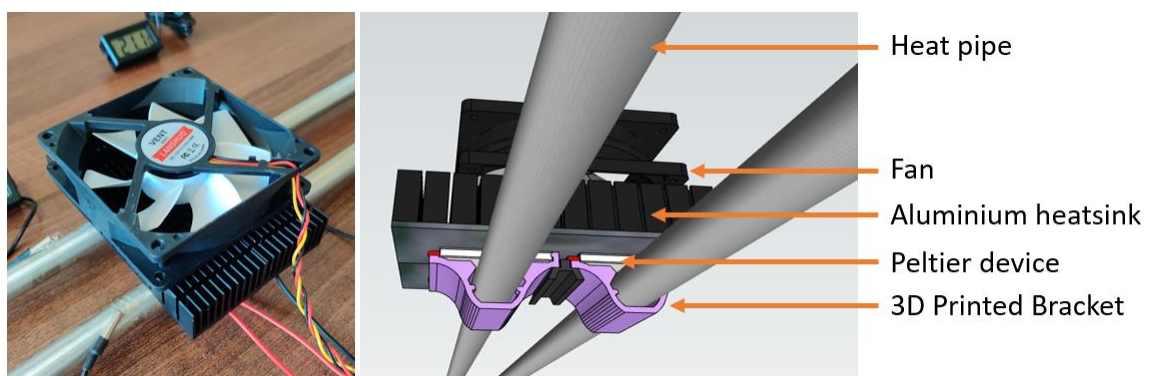
Figure 70 – Experiment 1b – TEC, heat sink and heat pipes

Experiment 1b aims to (1) examine the transient response of the temperature drop, (2) identify the steady state time constant, (3) confirm the even distribution of temperatures at all points on both pipes and (4) investigate the impact of ambient temperatures on the TEC-assisted heat pipe performance.

4.3.2. Experiment 2 – Natural Convection – Power impact on cooling

A high-power input (using 12V) inevitably constitutes higher energy consumption, which may pose operational challenges from a scalability perspective. Moreover, as highlighted in section 3.3.2, the COP of a TEC is bound to decrease as the current

approaches maximum rating. Hence, it is imperative to study the cooling performances with a lower set of input voltages to find an optimum range of voltage input to the TEC.

Experiment 2 aims to investigate the temperature drop (from ambient to steady state) of a single TEC attached to a single pipe against voltage input of 5V, 6V, 7.5V, 9V and 12V. The resulting power consumption by the cooling unit (TEC and fan combined) at these voltages are then measured using an energy clamp meter.

A 20A 300W step-down buck converter is used to regulate the voltage output for each experiment (except 12V where the 12V power supply is used directly). This step-down converter (shown in Figure 71) has voltage and current adjustment potentiometers, where the current is set to maximum and only voltage is adjusted.
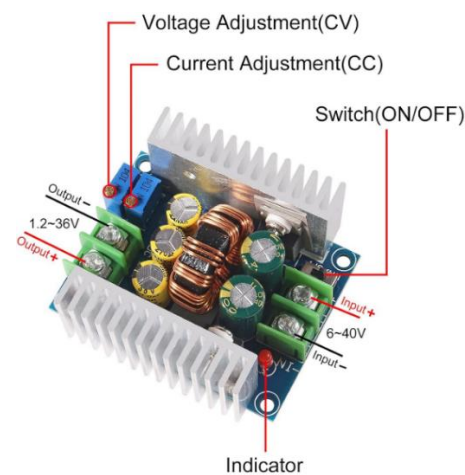
Figure 71 – Adjustable step-down buck converter

To further enhance the thermal connection of the TEC's cold side with the heat pipe, the TEC (for this experiment) is mounted diagonally to have more contact with the surface of the pipe.
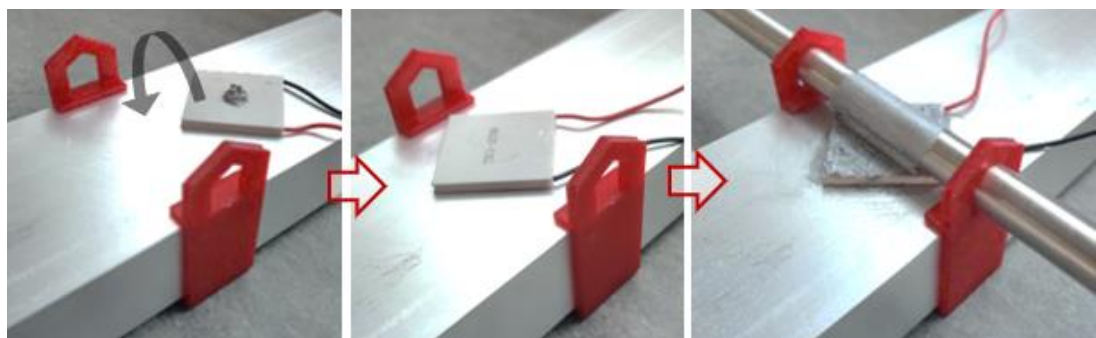
Figure 72 – Heatsink TEC and pipe assembly with thermal paste

An adequate amount of thermal paste (as a blob) is poured at the centre of the hot side of the TEC before flipping it on the heat sink as shown in

Figure 72. Next, the TEC is pressed firmly onto the heat sink and the heat pipe is slid through the 3D-printed brackets before spreading additional thermal paste over the pipes with the cold side of the TEC. Finally, two fans are mounted using zip-ties and the heat pipe is installed with four temperature sensors evenly placed along the length in addition to the ambient temperature (T_{amb}) sensor as shown in Figure 73.
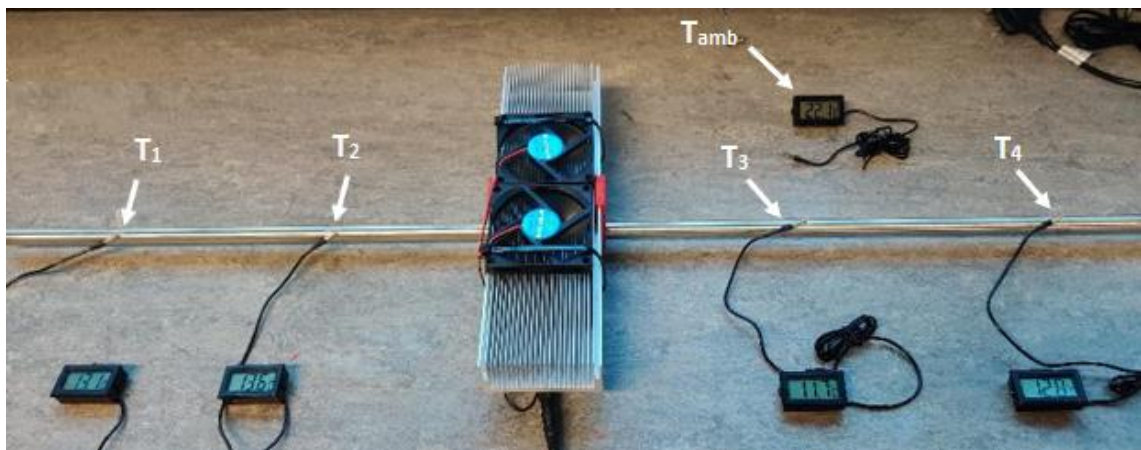
Figure 73 – Experiment 2 – Single pipe set-up

4.3.3. Experiment 3 – Coefficient of Performance and Heat Transfer Rate Validation

The preliminary experiments to study the impact on temperature drop against varying ambient temperatures (experiment 1) and power input (experiment 2) helped confirm that (1) higher ambient temperatures are beneficial for the cooling performance of the system, and (2) higher power input reduces the efficiency of the cooling system, which is also validated by the Coefficient of Performance (COP) charts of a TEC operation as discussed in section 3.3.2.1.

Hence, it is important to identify the power input with the optimum COP of the proposed cooling system. To calculate and examine the COP, a complete set of assembly of six heat pipes (as detailed in section 3.3.5) is prepared. In addition to the procedure followed in experiment 2 to adjust the voltage input to vary from 5V to 12V, a temperature sensor probe is attached to the heat sink to measure the collective hot

end temperature of the TECs whilst heat dissipation. The experimental setup for this investigation is shown in Figure 74.
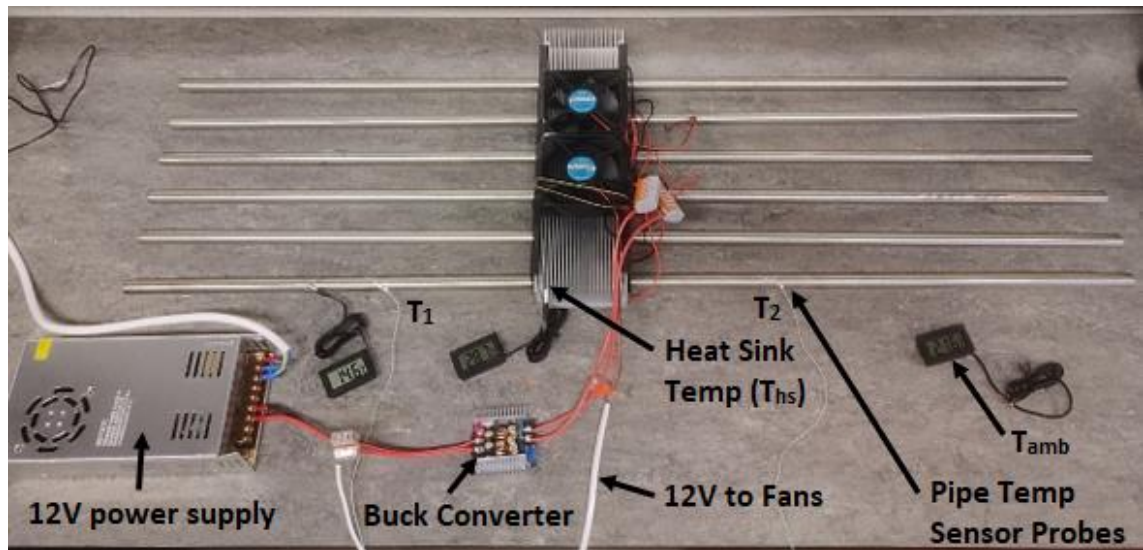
Figure 74 – Experimental setup of experiment 3

The voltages are then varied to observe the steady state average temperature of the pipes, the heat sink temperature and the current (to obtain power consumption) with 5V, 6V, 7.5V, 9V and 12V. This set of experiments is repeated twice, first with a single fan, and then a dual fan configuration (as in Figure) to examine the impact on cooling performance (using COP) and heat dissipation. The ambient temperature of 21.5°C and fan voltage of 12V are maintained throughout.

For precise data logging at each configuration and voltage setting, a Pico Technology TC-08 temperature sensor data logger. The apparatus with two PTFE insulated thermocouple sensor probes are used as shown in Figure 75.

Figure 75 – Pico TC-08 Temperature Data Logger

Experiment 3 further studies the heat flux of pipe required by the computational model to accurately represent the active cooling response of the physical set-up. Its computational methodology is presented in section 5.5.3. The actively cooled pipe (at 6V) is subjected to a fixed 1.2m/s air flow (manually adjusted through voltage regulation) to study the impact of the resulting steady state temperature of the pipe compared to the steady state at natural convection. This allows a comparative study in computational analysis (CFD) by adjusting the heat transfer rate of the surface of the pipe to examine the transient response of both experimental and CFD results at 1.2m/s. The heat transfer rate that accurately reflects the experimental transient response and steady-state pipe temperature at 1.2m/s is then noted. The set-up for airflow and velocity regulation is detailed in the next experiment in section 4.3.4.

4.3.4. Experiment 4 – Forced Convection – Velocity impact and validation

All previous experiments were performed under natural convection (indoor room conditions). In a real-world scenario, especially inside a wind tower, the heat pipes will be subjected to varying wind speeds that are expected to impact steady-state temperatures as the pipes would then be exposed to a quicker heat transfer rate of ambient temperatures.
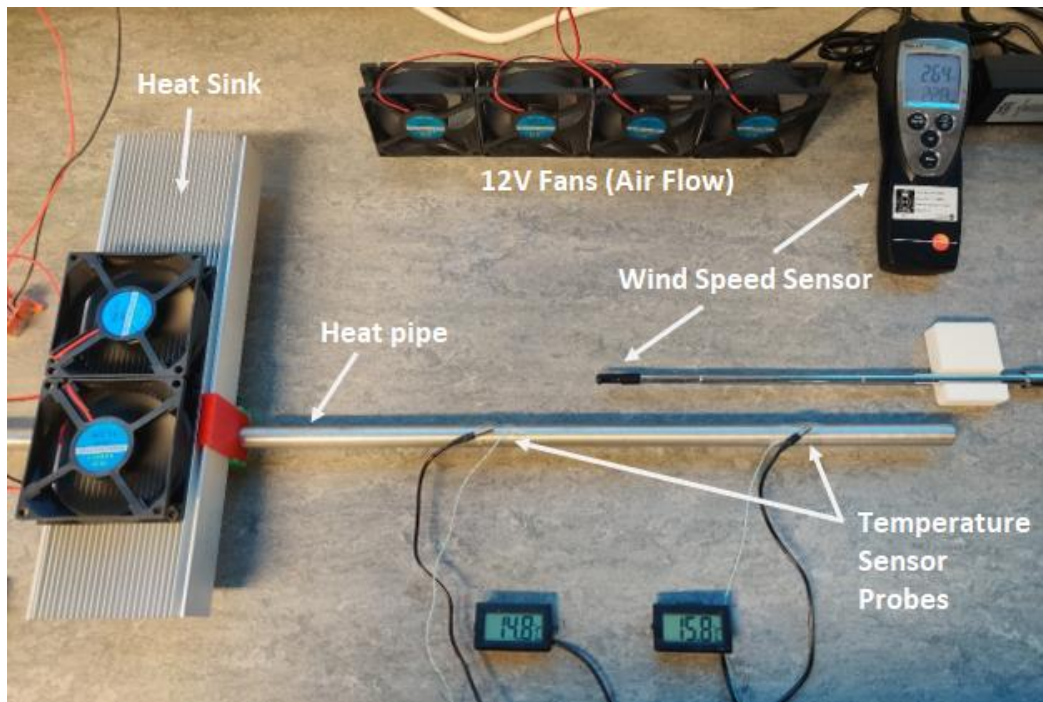
Figure 76 - Experimental setup for forced convection

To precisely measure this, an experimental setup for forced convection was prepared with an array of four 12V DC fans replicating wind, a wind speed sensor, and temperature probe sensors to measure the pipe surface temperatures. The voltage of the fans was regulated using the buck converter (Figure 71) to vary the wind speeds. This setup is shown in Figure 76.

Experiment 4 conducts a series of trials of active cooling with varying wind speeds from 0.1m/s to 3m/s to validate the heat transfer rate used in CFD analysis by simulating the computational model with the corresponding wind speeds. This validation is highly crucial as it defines the accuracy of the CFD results related to the impact of pipe temperatures against wind before a larger scale model is tested (in experiment 5).

The fans were found to produce unwanted turbulence and inconsistent airflow. While this may reflect real-world conditions, for the aim and purpose of this experiment, it was necessary to streamline the airflow to accurately measure temperatures at specific wind speeds. Therefore, the fans were covered with fine mesh netting to diffuse the air and reduce turbulence as shown in Figure 77. The experiments and results without netting were discarded, i.e. all results in this thesis include measurements with netting.
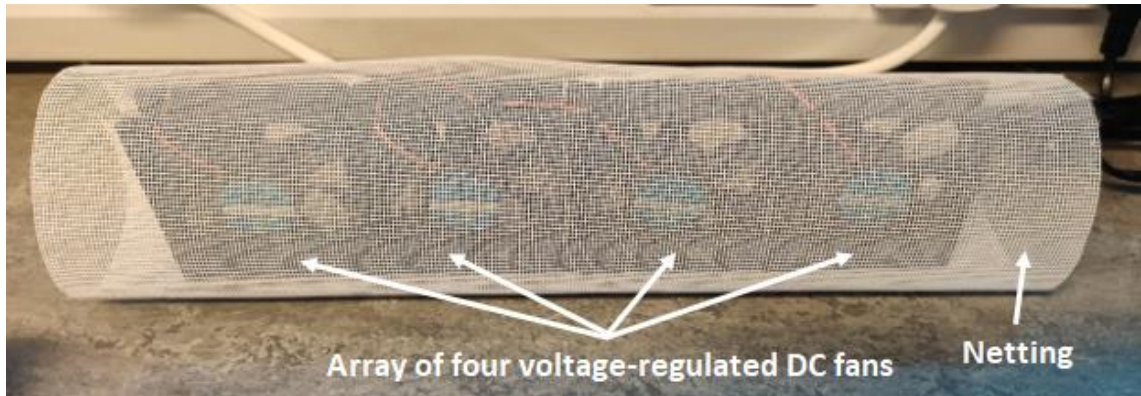
Figure 77 – Airflow of Experiment 4 diffused using fine netting

The Testo 425 anemometer is used in this experiment as a wind speed sensor (as seen in the experimental set-up in

Figure 76). This hot-wires thermal anemometer is suited for low airflow velocities (0 to 20m/s) with a resolution of 0.01m/s for wind and 0.1°C for temperatures. The instrument (shown in Figure 78) can measure spontaneous as well as averaged air flow speeds making it an ideal choice for this experiment.

The probe was positioned 2cm before the heat pipe in line with the stream of air to measure the air speeds accurately around the surface of the pipe. The voltage of the fans was adjusted to regulate the speeds. Once the desired speed was noted, the probe was removed before the TECs were powered to begin measurements. This was done to ensure that the anemometer probe did not influence the wind speeds around the pipe.

Figure 78 – Testo 425 Anemometer

This experiment not only investigates the impact of wind velocities on the actively cooled heat pipe temperatures but also allows the cooling heat transfer rate of the CFD model (derived through experiment 3) to be further validated across varying wind speeds. The corresponding computational model and simulations of this experiment are detailed in section 4.4.1.

4.3.5. Experiment 5 - Cooling Unit – Air mass impact and validation

Validation of the results from experiment 4 allows the development and examination of a full-scale prototype against varying air mass flow rates in a confined environment. In this experiment the temperatures 'below' the pipes are measured, i.e. the air temperature as it transfers heat to the actively cooled pipes. This would help in predicting the actual cooling impact of this system. Hence, experiment 5 aims to study the temperature reduction of supplied air as it passes through 35 cooled pipes arranged in two layers.

The electrical set-up of this full-scale prototype comprised of two external 12V power supplies, four buck converters (Figure 71), four 0-25V DC sensor modules to ensure voltage output is consistent, and four MOSFET 5V to 36V 30A modules to enable wireless and timed switching of TECs.
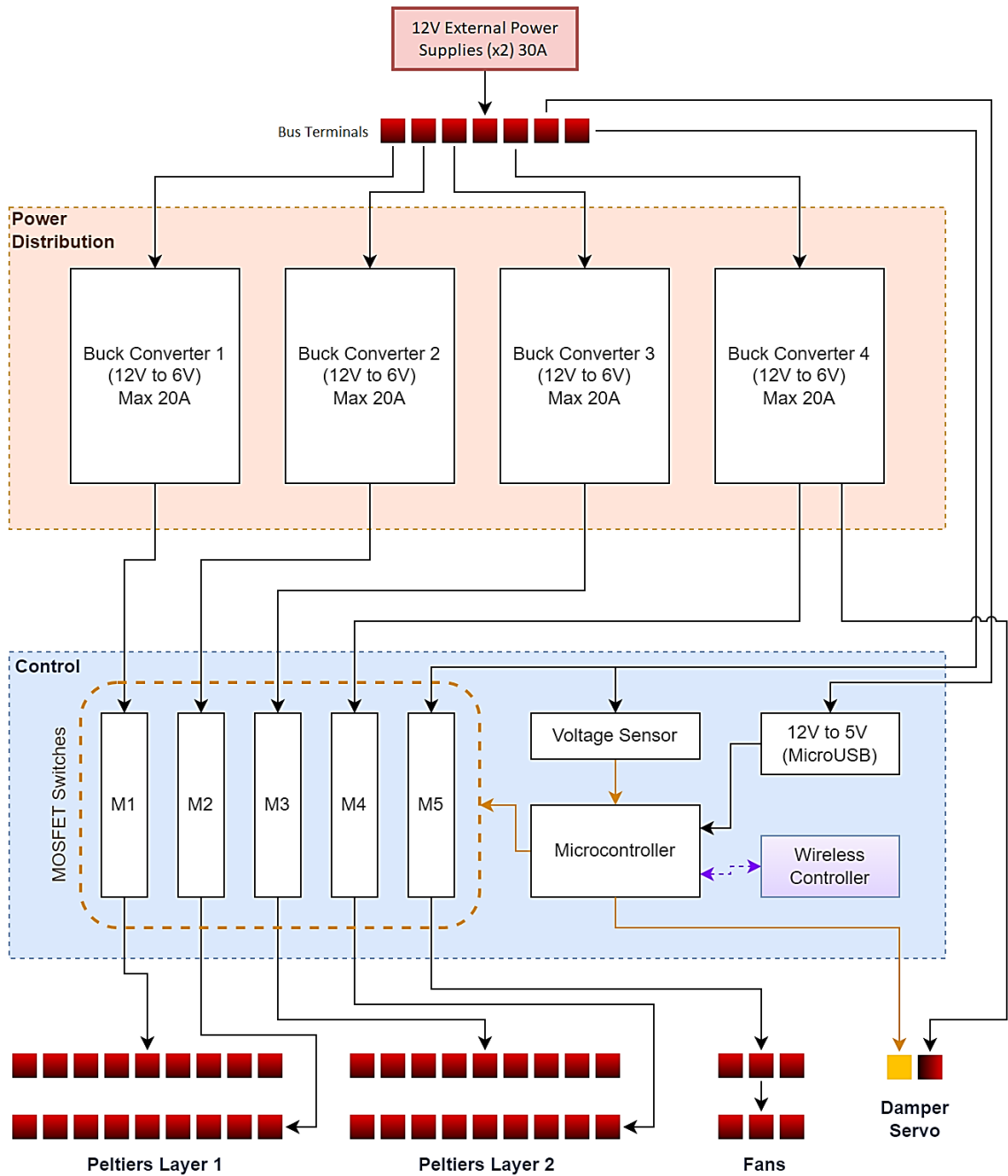
Figure 79 – Control system and power distribution for experiment 5

The fans are powered at 12V voltage throughout to ensure adequate heat dissipation.
The control system including the electrical power distribution is illustrated in

Figure 79. The MOSFET and voltage sensor modules are shown in Figure 80.
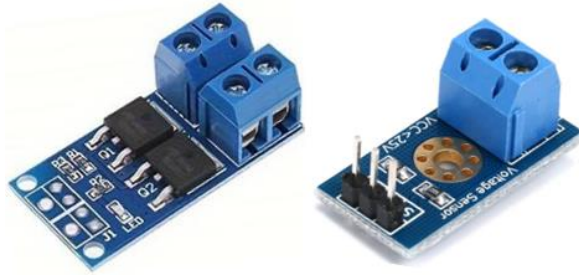
Figure 80 – MOSFET switch module (left) and Voltage sensor module (right)

An aluminium frame of 1m x 1m x 0.2m was constructed according to the modular design of the cooling unit. The frame with 35 holes of 22mm diameter cutouts (for heat pipes) is shown in Figure 81.

Figure 81 – Aluminium frame for full-scale prototype

The assembled cooling unit with a total of 35 heat pipes and TECs, 6 aluminium heat sink blocks, and 6 fans for heat dissipation is shown in Figure 82.

Figure 82 – Fully assembled prototype of the TEC cooling unit for experiment 5

The confined wind tunnel testing facility to test the TEC cooling unit prototype was provided by the BRE Group [222], an organisation in the UK that provides industrial testing facilities for research projects with published standards. A test rig was designed to accurately integrate an 'X-Frame' to create a four-quadrant at the inner section of the 1m x 1m duct and a TEC cooling unit underneath it. The testing system was equipped with a variety of measurement units including air flow, bulk air temperatures, fresh air temperatures (inlet), multiple points of measurements of temperature immediately after the cooling unit, and the exhaust temperatures.
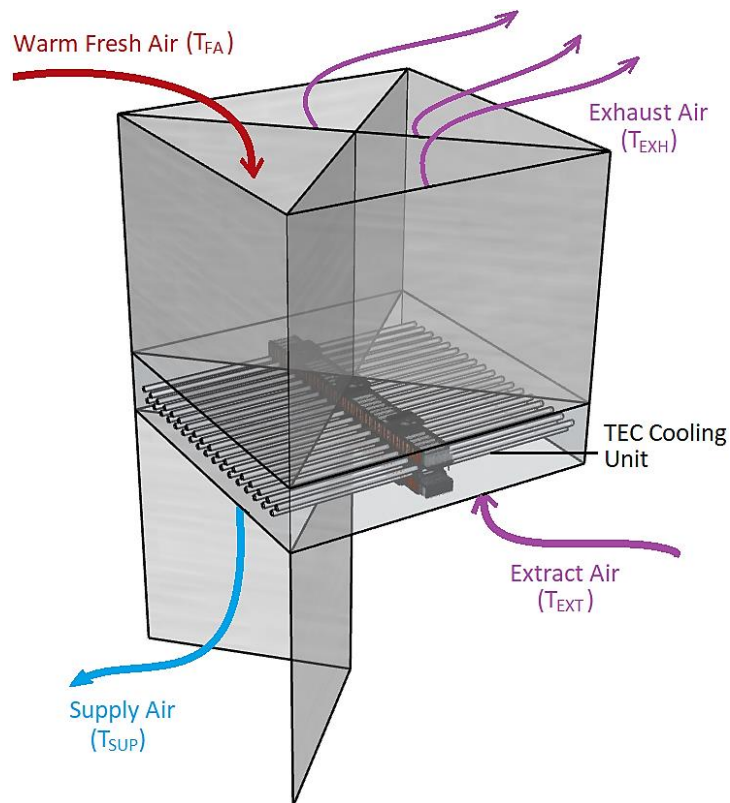
Figure 83 – Air flow through the quadrants

A controlled mass flow rate of air is pushed through one of the upwind channels to replicate horizontal wind entering a wind tower through the windward region. As this air exchanges heat with the actively cooled pipes, it exits through the bottom channel as the supply air as shown in Figure 83. The extracted air passes through any of the remaining three quadrants and is drawn up as exhaust air. The rig designed to hold this X-frame and the cooling unit comprised of a plenum under the cooling unit to replicate the room before the air is extracted to the leeward section of the cooling as shown in Figure 84 and Figure 85.

Figure 84 – Four-quadrant section (left) and the cooling unit underneath (right)

Figure 85 – Windward inlet for regulated air supply (left) and extract air system (right)

Table 6 shows the test parameters for 'Experiment 5'. The supply air temperature (T_{SUP}) is measured for each trial.

Table 6 – Test Matrix for Experiment 5

Experiment	Fresh Air Temperature, T_{AIR} (°C)	Average Air Speed before heat exchanger, v (m/s)	Airflow rates, $\dot{m}$ (L/s)
5a	25	0.2, 0.3, 0.4, 0.8, 1.2	50, 75, 100, 200, 300
5b	30	0.2, 0.3, 0.4, 0.8, 1.2	50, 75, 100, 200, 300
5c	35	0.2, 0.3, 0.4, 0.8, 1.2	50, 75, 100, 200, 300

4.4 CFD Simulation Methodology

Computational Fluid Dynamics (CFD) helps in integrating numerical methods and solving complex algorithms related to fluid flow computationally. This helps in examining flow and thermal patterns that are either time-consuming, expensive and/or impractical to study experimentally. For this research, the SolidWorks 2022 software is used for all CAD modelling as well as CFD simulation and analyses through the 'Flow Simulation' addon.

Developing and analysing a full-scale wind tower integrated CFD model involves many variables that can result in inaccuracies in real-world observation due to environmental conditions and discrepancies in computational constraints. Hence, it is imperative to (1) break down the complexity of the system into simpler and isolated studies, and (2) validate the CFD results of these simpler systems with experimental tests.

To achieve a reliable CFD model of a potential full-scale cooling mechanism using actively cooled heat pipes with passive ventilation through a wind tower, a single-pipe model is first examined and validated for its impact against the wind. Once validated, a full-scale cooling unit model is validated from a full-scale experimental prototype. A successful validation of the full-scale model would then allow for a variety of optimisations to further enhance the cooling capability of the proposed mechanism.

Figure 86 shows a summary of the CFD methodology used in this research.
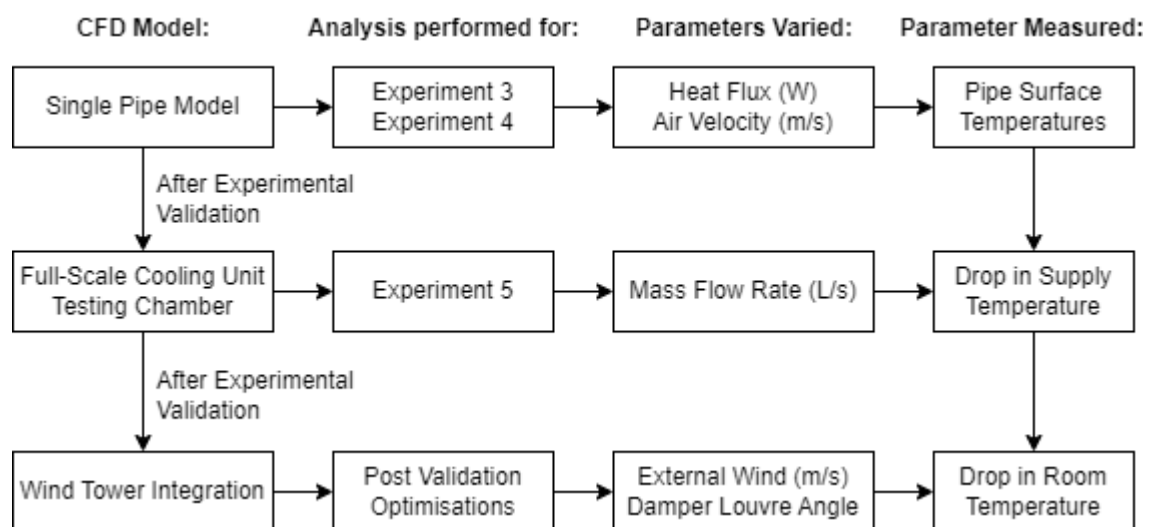
Figure 86 – Summarised Methodology of CFD Analyses in this Thesis

4.4.1. Single Pipe CFD Model (Experiments 3 and 4)

The framework for the process and purpose of CFD analysis used for experiments 3 and 4 is described below:

1. First, a physical experiment is conducted (as detailed in section 4.3.3) using 6V to observe the rate of change of temperature, steady-state temperature, and steady-state time to cool one heat pipe as forced convection with fixed (1.2m/s) of airflow.

2. An identical pipe of 15mm diameter and 1m length is modelled (as shown in

Figure 87) to simulate through CFD using the same boundary conditions and input parameters using a constant heat transfer rate of -3W.

3. Multiple trials of these simulations were conducted by varying the heat transfer rate from -3W to -7W and the transient response was observed.

4. The experimental results (transient response graph) of pipe surface temperatures are then merged with the experimental results. This allows the selection of the heat transfer rate that best matches and reflects the actual heat transfer rate in practice.

5. The selected cooling power is then extensively examined by validating against a set of corresponding experimental and CFD trials on varied wind speeds from 0.1m/s to 3m/s to gauge the accuracy and consistency of the CFD heat transfer rate. This allows replicating a full-scale heat exchanger using the validated heat transfer rate (or corresponding heat flux) for experiment 5.
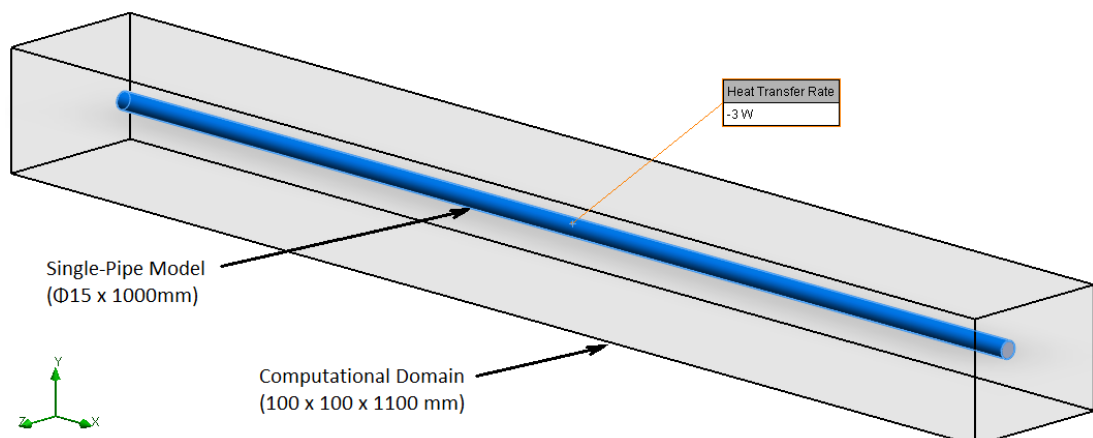
Figure 87 – Single-pipe model for CFD

Figure 88 shows the SolidWorks Flow Simulation process that was followed to set up the CFD model for single-pipe analyses.
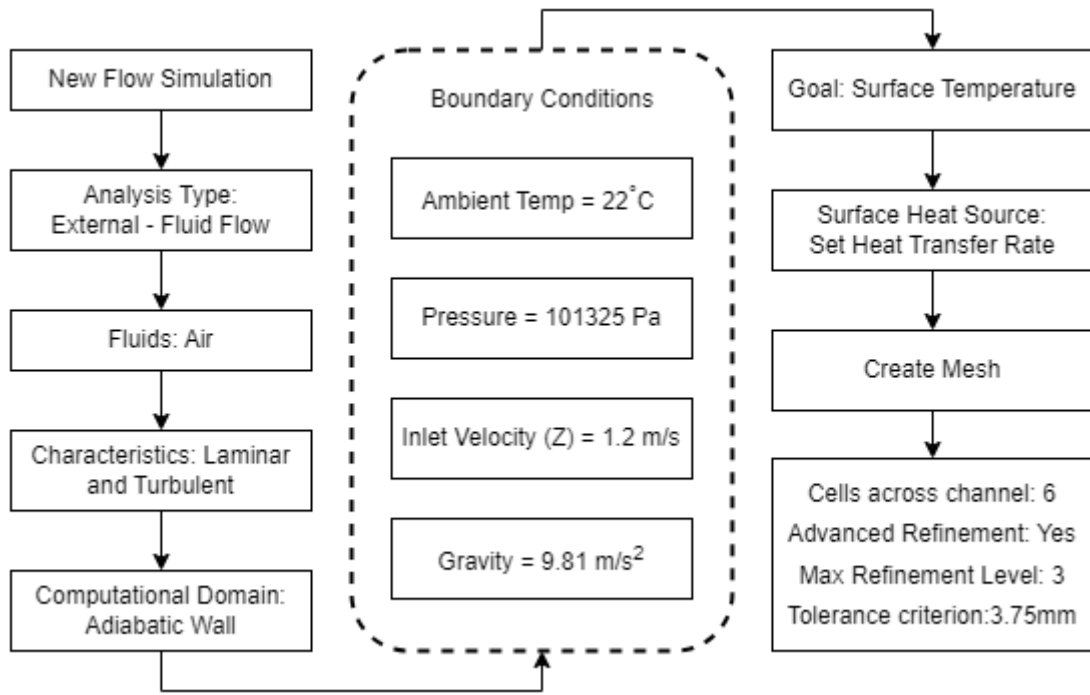
Figure 88 – SolidWorks Flow Simulation Set-up Process

The mesh around the pipe was adjusted with an advanced refinement (sub-division) level of 3 for an accurate computational heat transfer during simulations. Details on mesh selection are further explained in section 4.4.2. The results of the single-pipe CFD analyses are presented in section 5.5.3.

4.4.2. Full-scale Prototype CFD Model: Experiment 5

The process in Figure 88 was used to create a new CFD set-up to recreate and computationally model the experimental set-up of 'Experiment 5' as detailed in section 4.3.5. In this case, the boundary conditions include the 'inlet mass flow rate' (of air) that was varied with each set of experiments using the test set from 50L/s (0.06125kg/s) to 300L/s (0.36kg/s) of mass flow. Figure 89 shows the final CAD assembly prepared for CFD to validate experiment 5 results. The four-channel duct is identical to the experimental wind tunnel rig with one channel used for fresh air (inlet)

allowing the remaining three quadrants to exhaust the extracted air. The heat exchanger (cooling unit) with 35 pipes arranged in two layers is placed under the X-Frame leading to an enclosed chamber (room) of 3m x 2.5m x 2.5m.
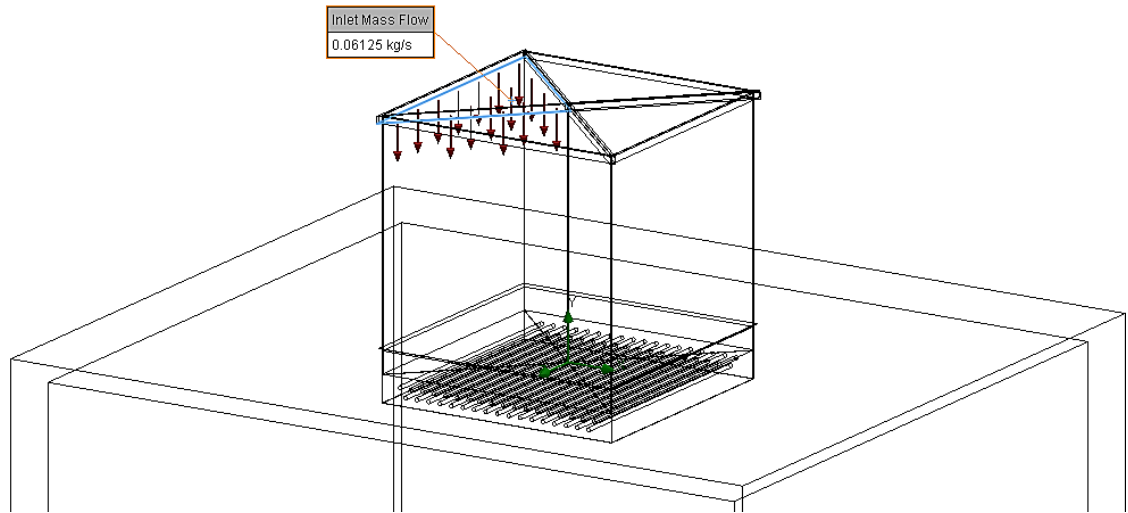
Figure 89 – CFD Model with inlet fresh air mass flow rate

A global mesh was set for the overall model with automatic refinement and a maximum refinement level of 3 to have a favourable balance between the accuracy of results and the processing time of the simulation. This mesh refinement is ideal for the walls of the ducts and inside the room where the complexity of computation (thermal, velocities, etc.) is minimal. However, it is imperative to gauge and apply an appropriate mesh for the pipe surfaces. For example, if the finest sub-divided mesh resolution is roughly equal to the diameter of the pipe, the computational results will be highly inaccurate. Similarly, the gap between the pipes is also a key consideration in defining the mesh refinement. Hence, a local mesh was added only around the pipes of the inlet (windward) quadrant as shown in Figure 90. The figure also shows the locations of the measurement probes added for fresh air temperature (T_{AIR}) as well as for temperatures below the pipes (T_{BP}).
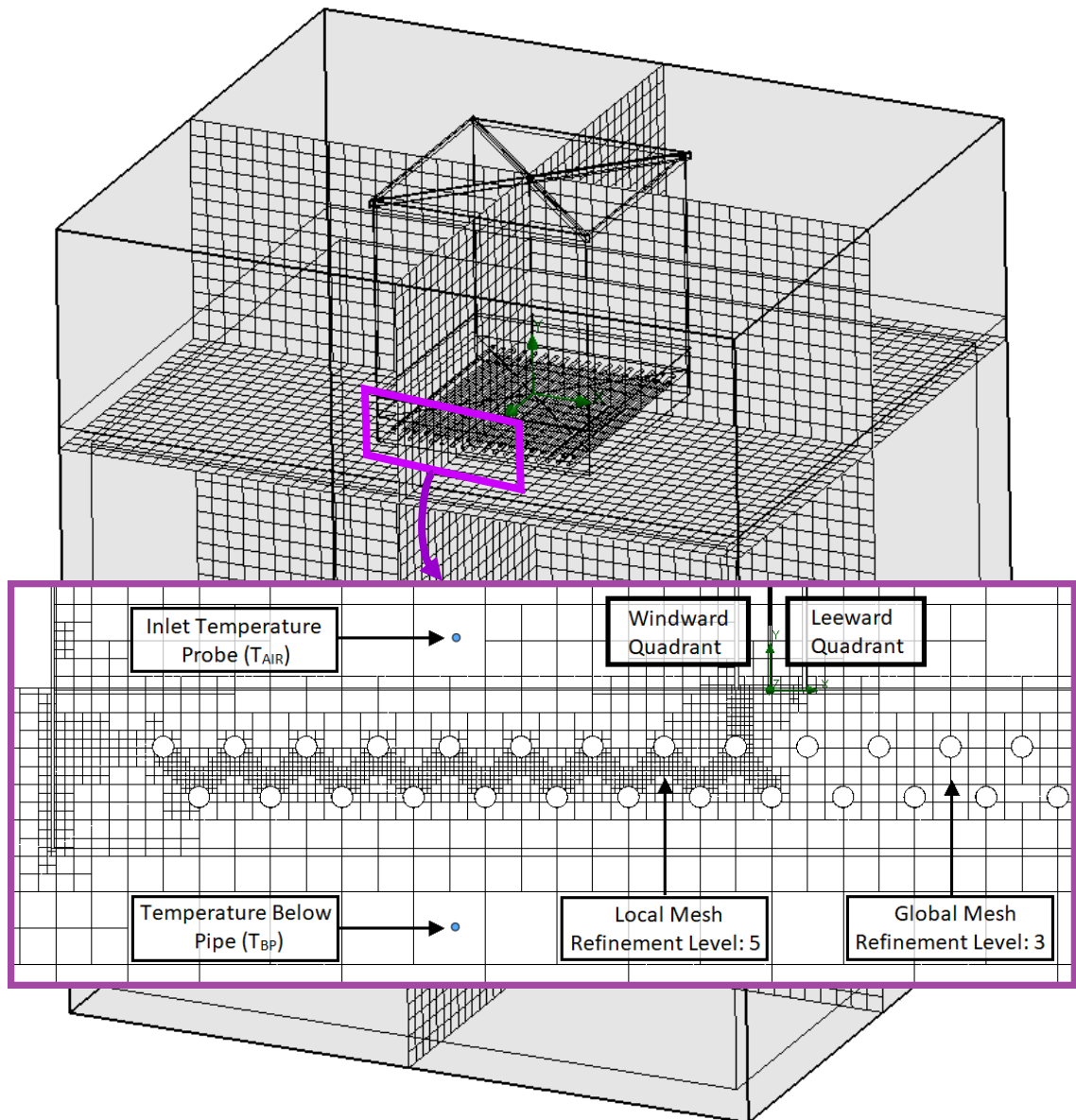
Figure 90 – Temperature probes and mesh assignment

4.4.3. Wind Tower and Room Model (Post-Validation Optimisations)

Once the CFD model of the full-scale cooling unit is validated against the experimental results in 'Experiment 5', the CFD model is upgraded to include a true-scale wind tower model instead of the testing duct. The specifications of this four-channel wind tower are the same as detailed in Chapter 3 section 3.3.5. The room dimensions (3 x 2.5 x

2.5m) are unchanged. The cooling unit is actively cooled using a -5W heat transfer rate in the CFD model as shown in

Figure 91.
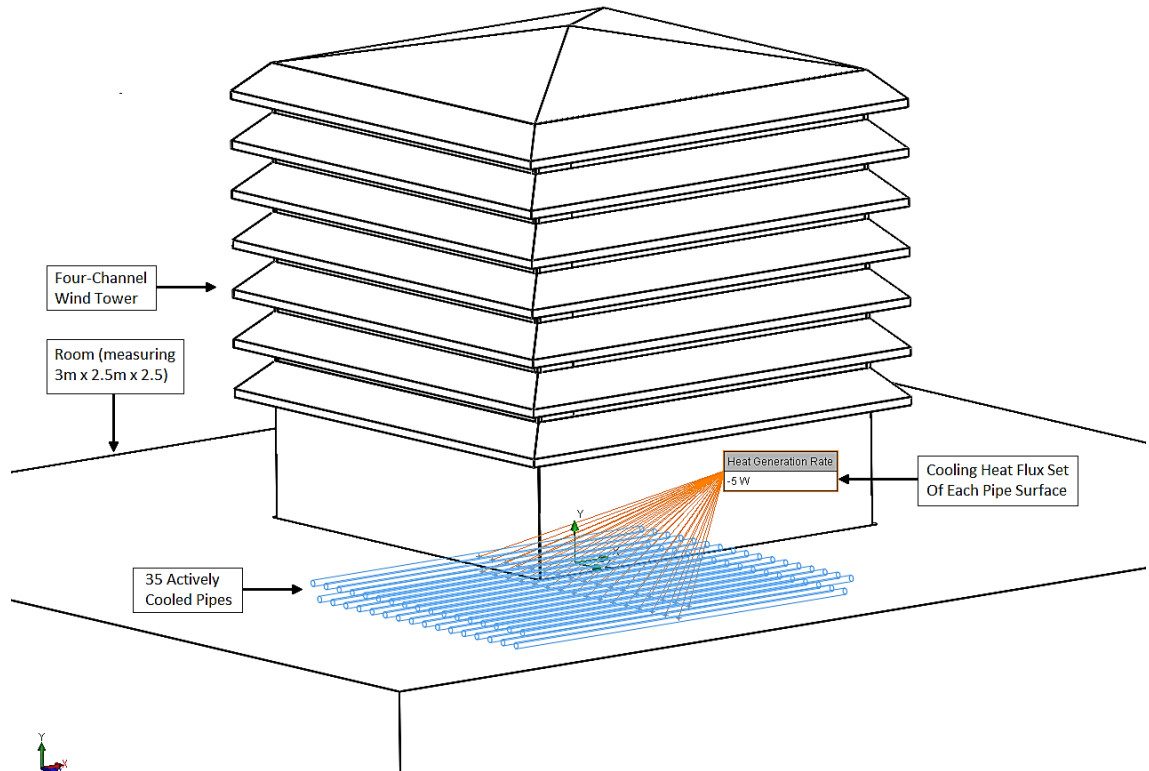
Figure 91 – Wind Tower Integration to the CFD Model

The post-validation CFD experiments aim to explore and propose various performance augmentation techniques to enhance the cooling capabilities of the validated Peltier-driven cooling mechanism for improved indoor cooling impact.

These augmentation techniques will be simulated using the wind tower model to accurately mimic the response to external wind velocities. For example, the boundary conditions of previous simulations actively forced the inlet air streams through the heat exchanger (cooled pipes). The integration of the wind tower model aims to leverage the external and internal pressure differential to deliver a more realistic stream of air, especially as it enters the windward quadrant and passes through the heat exchanger with a transitional and dynamic airflow. A 3D meshed illustration of this CFD model with the wind tower is shown in Figure 92 and a 2D cross-section of the meshes around the wind tower louvres and the pipes are illustrated in Figure 92.
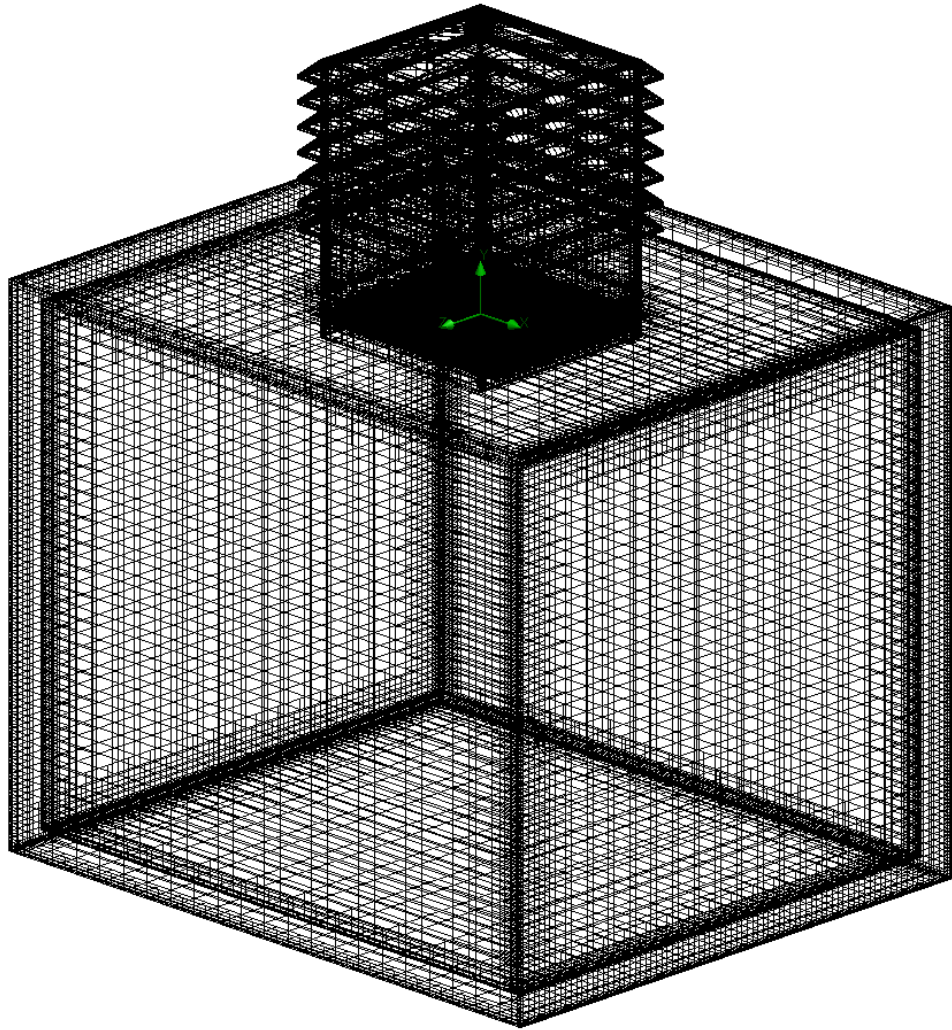
Figure 92 – 3D Mesh of Wind Tower Integrated CFD Model
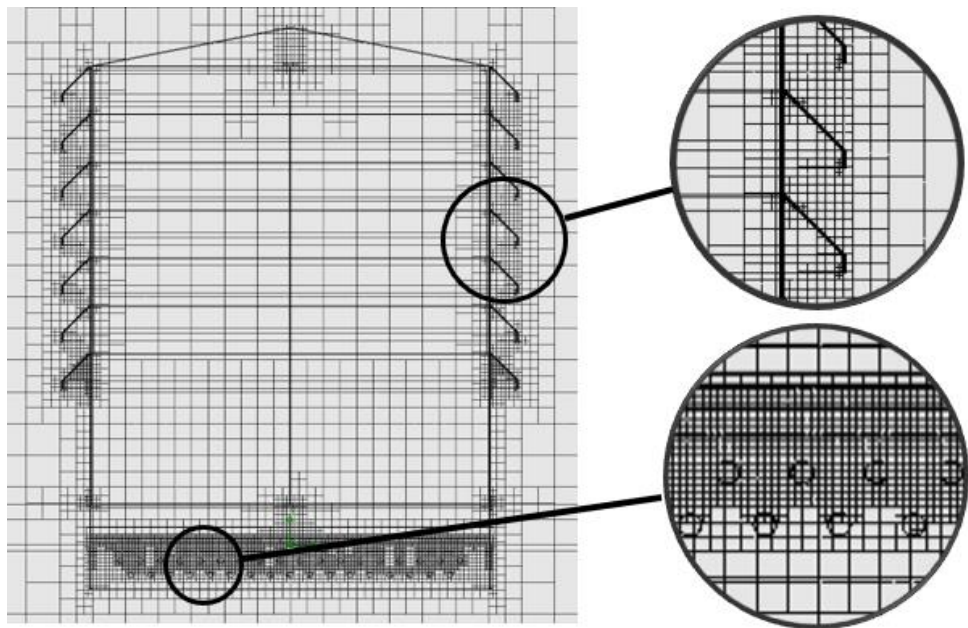
Figure 93 – 2D mesh cross-section of Wind Tower

The measurement probes that are used for CFD analysis for velocity and temperature (fluid) are placed at the inlet quadrant (i.e. the East quadrant). The velocity probe is 60mm to measure the speed of air before it enters the heat exchanger and compares it with the external wind speed. The temperature probe is located 30mm after the pipes.

The three performance augmentation techniques that were proposed and explored are:

1. Damper Before The Heat Exchanger:

As both experimental and CFD results of 'Experiment 5' showed higher temperature drop with lower velocities, another configuration is explored which includes a damper before (above) the pipes as shown in Figure 94. This damper (shown in 30° configuration) utilises the louvre angle that helps regulate the wind flow. This is particularly useful in lowering the high wind speeds to ensure increased residence time with the pipes and allow more heat exchange to occur before the wind enters the room. The figure also shows two probes to measure temperatures and velocities before and after the heat exchanger.
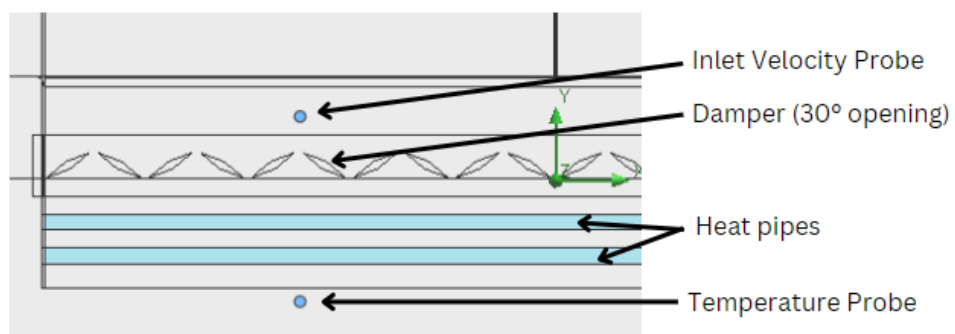
Figure 94 - Arrangement of damper and measurement probes

2. Three Layer Pipe Arrangement

In addition to the damper configuration, adding another layer of actively cooled pipes is also examined. A total of three layers of Peltier-driven cooling pipes (as opposed to two) can significantly enhance the cooling performance inside the room. The arrangement of these 53 pipes is shown as a cross-section of the wind tower in Figure 95.
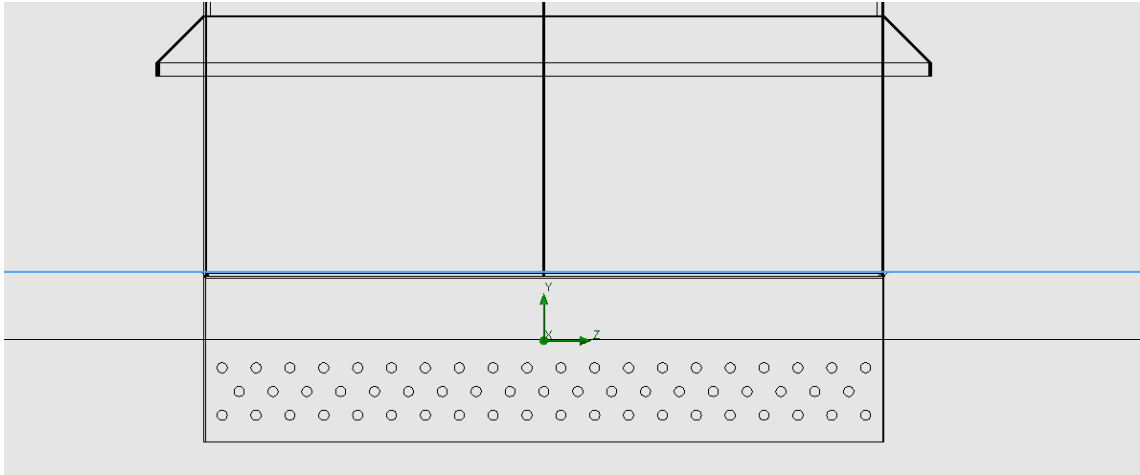
Figure 95 – Three-layered configuration of actively cooled pipes

3. Fan Integration for Improved Ventilation

The inclusion of another layer of pipes caused a significant drop in the volume flow rate of fresh air, hence reducing the ventilation rates. To restore a higher ventilation rate with lower wind velocities, an addition of a layer of thin axial 12V noiseless fans is proposed to regulate the airflow into the room at low external wind speeds. Comair Rotron MCH3 DC Mid-speed axial fans were integrated into the CFD model as shown through a section-cut view in Figure 96.
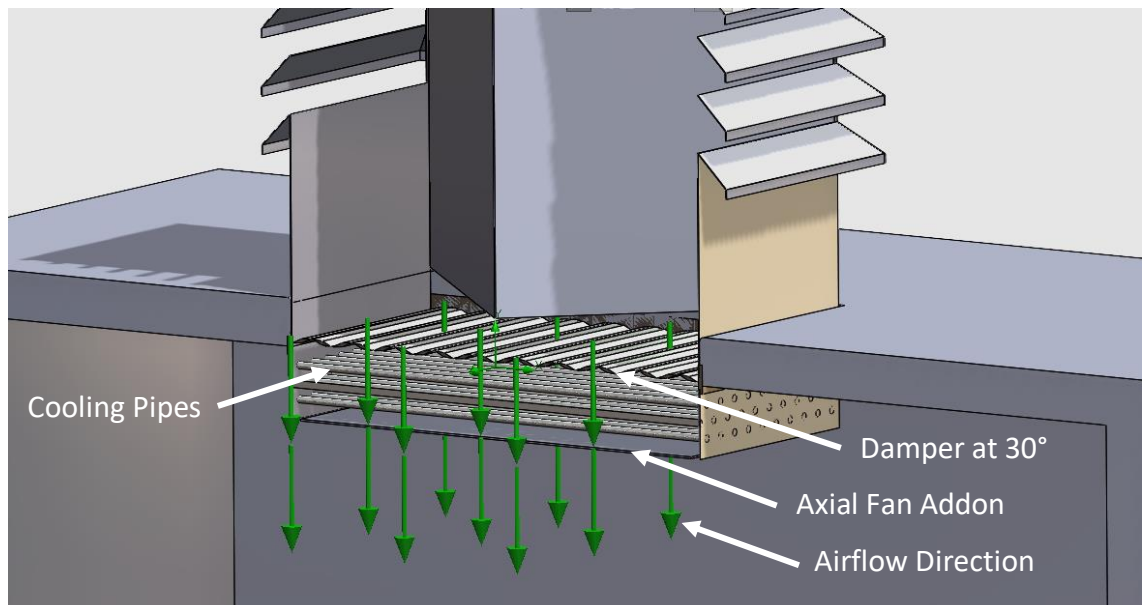
Figure 96 – Fan integration below the pipes

5. Chapter 5 – Results and Validation

5.1 Introduction

This chapter presents and discusses the results obtained from the physical experimentation and the CFD simulations as described in Chapter 4. The results of each experiment are detailed chronologically with validation where necessary (e.g. for experiments 3, 4 and 5) as previously outlined in section 4.2. This framework of results and validation is further summarised in section 6.2.

The five experiments are followed by an additional set of post-validation optimisations (labelled as 'PVO'), which is investigated through CFD simulations to further enhance the indoor cooling potential of the proposed Peltier-driven cooling mechanism when integrated into a wind tower.

5.2 Results and Validation Framework

The breakdown of experiments is done strategically to evaluate the impact of each relevant physical variable (such as ambient temperature, power input, wind speed, etc) on the cooling performance parameters (such as pipe surface temperature drop, time to reach steady state, indoor temperatures, efficiency, etc). The results of experimentation compared to computational analysis may show discrepancies due to inconsistent ambient conditions.

To ensure that the cooling potential as produced from CFD analysis would reflect a real-world scenario, it is critical to first examine and validate the CFD results through experimentation results discretely. This helps narrow down the individual factors affecting the resulting parameters. This is done for experiments 3, 4 and 5 as they play a crucial role in identifying the correlation of computational heat transfer rate and wind velocities on the pipe surface temperatures and the effective heat transfer with the air passing through the pipes. Table 7 outlines the physical input variables and parameters examined for each experiment along with the section numbers that direct to their experimental setup and results in this thesis.

Table 7 – Experiments and Validation Outline

| | Experiments | | | | | |
	Exp 1	Exp 2	Exp 3	Exp 4	Exp 5	PVO
Input variables	T_{amb}	P_i	$P_i, \dot{Q}_{CFD}$	v, v_{CFD}	$\dot{m}, T_s$	θ, v_{CFD}
Parameters to examine	ΔT_p , t_{ss}	ΔT_p , t_{ss}	ΔT_p, COP	ΔT_p	T_{bp}	T_{bp} , ΔT_r
Physical experiment	✓	✓	✓	✓	✓	-
CFD simulation	-	-	✓	✓	✓	✓
Validation required	-	-	✓	✓	✓	-
Thesis Section (Setup/Results)	4.3.1/5.3	4.3.2/5.4	4.3.3/5.5	4.3.4/5.6	4.3.5/5.7	4.4.3/5.8

Among the nomenclatures used in Table 7, T_{amb} is the ambient temperature, P_i is the power input, v is the air/wind velocity, $\dot{Q}$ is the heat transfer rate, $\dot{m}$ is the air mass flow rate, T_s is the temperature, θ is the angle of the damper louvres, ΔT_p is the change in pipe surface temperature, t_{ss} is the time taken for temperatures to reach a steady-state, COP is the coefficient of performance of the overall system, T_{bp} is the temperature below the pipes, ΔT_r is the change in temperature inside the room, and 'PVO' refers to the post-validation optimisations through CFD simulations.

5.3 Experiment 1: Proof of concept and ambient temperature impact

5.3.1. Proof of Concept

The preliminary results present a proof-of-concept of Peltier-based conductive cooling of heat pipes as discussed in the experimental setup in section 4.3.3.1. The measured data of this experiment is shown in Table 8 and the temperature sensor reading at steady state is shown in Figure 97.

Table 8 – Experiment 1 – Preliminary Experimental Results

Ambient Temperature (°C)	21.5°C
TEC Cold Side Temperature (°C)	-5°C
Average Pipe Temperature (°C)	11.5°C
Measured current (I)	4.5A
Voltage (V)	12V
Power consumption (W)	54W
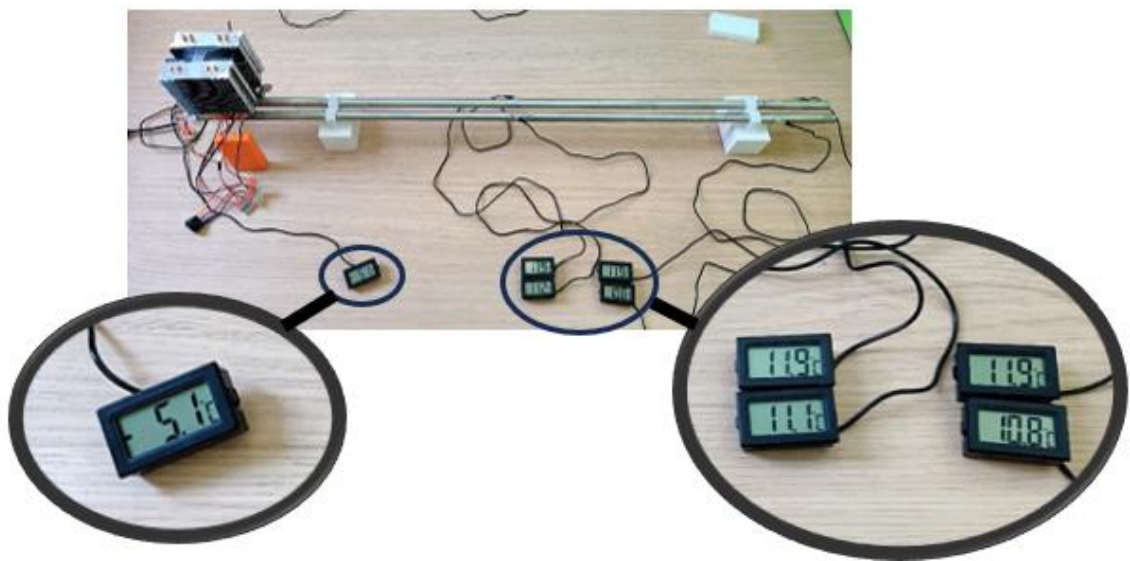
Figure 97 – Experiment 1a – Temperatures at steady state

Hence, with 54W of power through the TEC to cool two heat pipes with ample heat dissipation, the cold side of the TEC reached -5°C and the heat pipes attained a steady state average temperature of 11.5°C along their length. This temperature drop of 10°C below ambient level indicates significant potential for further research and development.

It is to be noted that preliminary trials also included varying the angle of the pipes at various inclines (from 0° to 60°). However, this approach was discarded as it produced temperature gradients along the length of the pipes (with higher temperatures at higher elevations as expected), which would not benefit the planned integration of pipes with a potential multi-channel wind tower. The horizontal heat pipes showed

optimum and consistent cooling performance along the length of the pipes via Peltier-driven cooling.

Moreover, due to the use of a large heat sink and cold side temperatures reaching below freezing temperatures (i.e. -5°C), a thick layer of ice was formed in less than an hour underneath the TEC as seen in Figure 98.
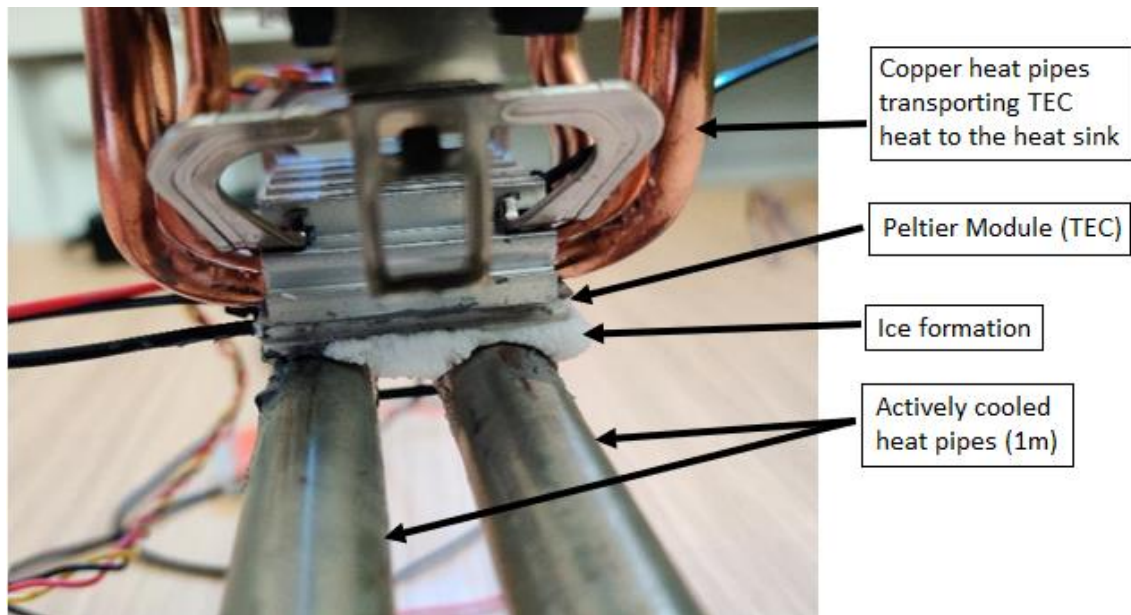
Figure 98 – Ice formation underneath the TEC

There are several reasons for ice to accumulate at the cool end of the TEC, such as:

1. Excessive Heat Transfer: This occurs when the rate of the heat pump is higher than the heat absorption capacity of the load.

2. Over-performing Heat Sink: This happens when the hot side of the TEC is effectively cooled at a much greater power than the rate of the heat pump.

In this case, the second reason is applicable as a much higher capacity heat sink was (purposely) employed to examine the cooling effect. As the dT_{max} of TEC1-12706 is 70°C as discussed in section 3.3.3, an actively cooled hot side would inevitably reduce the cold side temperatures to below zero under optimum conditions, leading to freezing moisture from the air to form ice.

However, despite the substantial cooling capability and favourable preliminary results, several negative implications of this ice formation must be addressed, such as:

1. Inefficiency: The ice acts as an insulator, reducing the efficiency of the Peltier module over time as it builds up. Besides, the formation of ice univocally indicates that the system is over-performing by trying to cool past the pipe's heat absorption capacity.

2. Water Damage: As the ice melts, the water would potentially cause damage to the TECs or the electrical connections, or cause unwanted dribbles inside the room.

Hence, the heatsink selection plays a critical role in mitigating the above implications and preventing the system from over-cooling as well as under-cooling than required. In other words, it is imperative to identify the appropriate system parameters for optimum cooling performance. Thus, chapter 3 section 3.3.5 detailed the process of heat sink selection and a suitable heat sink was chosen based on the required heat dissipation.

The initial experimental results presented a promising proof of concept of the proposed Peltier-driven cooling of heat pipes. However, it is to be noted that the preliminary testing in indoor conditions and its results also raised several questions. For example, what would be the impact of ambient temperatures, power input, and wind velocities on the cooling performance? The subsequent experiments aim to answer these through diverse experimentations and computational modelling and simulations.

5.3.2 Transient Response with Active Cooling

The cooling performances under normal indoor conditions are first examined. To further improve the efficacy of active cooling, the experimental setup (as detailed in section 4.3.1.2) now has the TEC positioned in the centre of the heat pipes with an adequate active heat dissipation arrangement with an aluminium heatsink and a 12V fan.

The results from the experimental setup are presented in the graph in Figure 99, which shows the transient response of the pipes' surface temperatures recorded in the first 20 minutes of powering the TECs and heat dissipation fan at 12V. The measurements were logged every 30 seconds. The ambient temperature and the initial temperature of the heat pipes were recorded as 22°C. The experiment concluded once a steady state was achieved for all pipe temperatures.
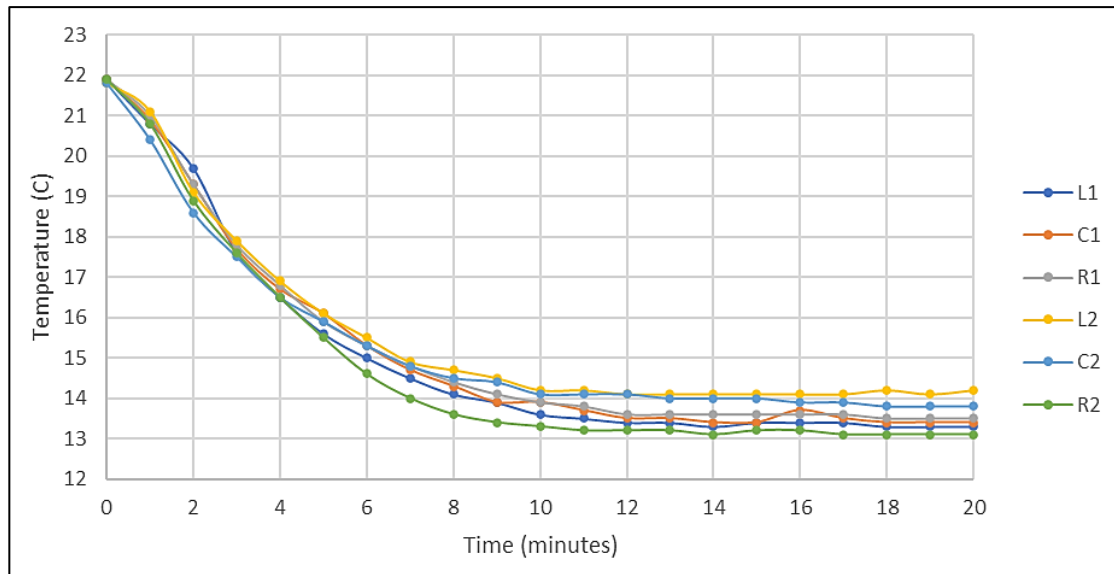
Figure 99 – Experiment 1b transient response of pipe temperature

From the above graph, the legends' alphabets L, C and R refer to the Left, Centre and Right temperature probes for both Pipe1 and Pipe2 as illustrated previously in Figure 69. The results from the transient response confirm the following:

1) Despite the cooling source being in the centre, the temperatures remain even across the whole length of both heat pipes. Hence, for future experiments in the subsequent sections, an 'average temperature' (T_{AVG}) will be used when referring to the mean temperature of each heat pipe.

2) The change in temperature occurs during the first 12 minutes, after which the temperatures reach a steady state. This steady state time (t_{ss}) and the steady state temperatures (T_{ss}) slightly vary with ambient temperature as discussed later.

3) Approximately 8°C of temperature change (ΔT) was observed on both pipes.

5.3.3 Ambient Temperature Impact

In theory, based on the principles of both convective and conductive heat transfer, any increase or decrease in ambient temperature should reflect proportionally to the surface temperature of the pipe, in order to preserve the temperature differential (ΔT). However, both, the TECs (that are equipped with active heat dissipation) as well as the heat pipes (that leverage high temperatures to operate effectively), are likely to be affected by the ambient temperatures.

The experiment is now repeated at different ambient temperatures, i.e. to observe the rate of change and maximum reduction in pipe surface temperatures (ΔT) at various constant surrounding temperatures. A total of five independent experiments at ambient temperatures of 22°C, 25.3°C, 28°C, 31°C, and 33.8°C were conducted. The results shown in Figure 100 collectively present the transient response of the average temperatures of heat pipes for each experiment vs time.
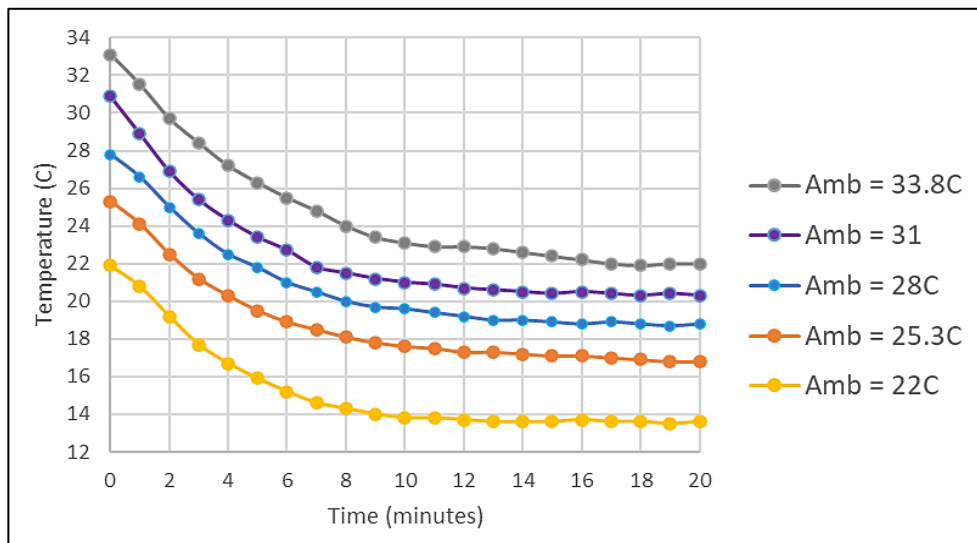
Figure 100 – Pipe Surface Temperatures vs Ambient Temperatures

The results show a common trend in the rate of drop in temperatures with time, which also maintains a similar time taken (12-14 minutes) to reach the steady state temperature irrespective of the ambient temperature. However, to assess the impact of ambient temperatures on the cooling performance, a graph of the absolute temperature difference (ΔT) of pipes is plotted against each experiment's ambient temperature as shown in Figure 101.

The results indicate that the performance of the Peltier-driven heat pipe cooling operation improves in response to higher ambient temperatures, i.e. from ΔT of 8°C at 22°C of ambient temperature, the system is capable of dropping the temperatures of heat pipes by up to 12°C when the ambient temperature climbs up to 34°C. This provides a favourable benefit in extreme climates where enhanced cooling efficiencies are crucial.
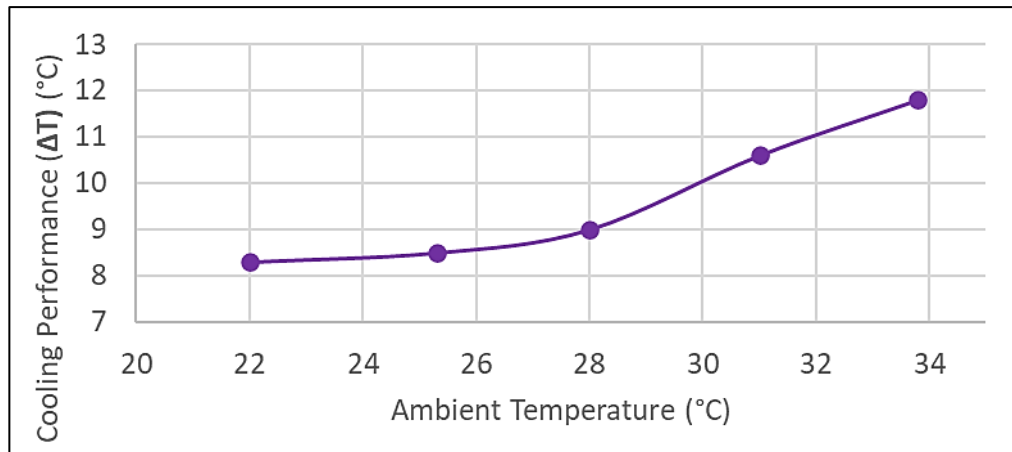
Figure 101 – Absolute Temperature Difference vs Ambient Temperatures

This improvement in cooling at higher temperatures is essentially due to the working mechanism of the heat pipes whilst constant conductive cooling by the TECs. When the ambient temperature rises, the working fluid within the heat pipe becomes more effective at transferring heat internally. This is further aided by the active heat absorption from the centre of the pipe enhancing the thermal circulation and phase change efficiency inside the pipes.

5.4. Experiment 2: Natural convection – Power impact on cooling

As experiment 1 confirmed that both heat pipes showed identical surface temperatures consistent across the length of the pipe, only a single pipe is studied to simplify the measurements. This section examines the impact of input power (regulated by input voltage) on the absolute temperature drop (ΔT_p) of the pipe surface temperatures.

5.4.1. Cooling performance vs Power input

Experiment 1 presented the transient response and temperature drop (ΔT_p) across the heat pipes' surface against different ambient temperatures but fixed power input (P_i) using 12V. This section will examine the performance of heat pipes' surface temperatures under natural convection against P_i ranging from 5V to 12V. This would help measure the efficiency of the resulting cooling performance.

The objective of 'Experiment 2' is to vary the power input with discrete values of 5V, 6V, 7.5V, 9V and 12V, and for each test observe its (a) transient response, (b) steady state temperatures, and (c) the current consumption through the TEC. The ambient temperatures (and initial pipe surface temperatures) are maintained at around 22°C. Temperatures were recorded at four points (two on each side of the TEC) every 30 seconds for 20 minutes. Transient response with four temperature points measured across the length of the heat pipe are shown in Figure 102 for 5V and 12V as a comparison.
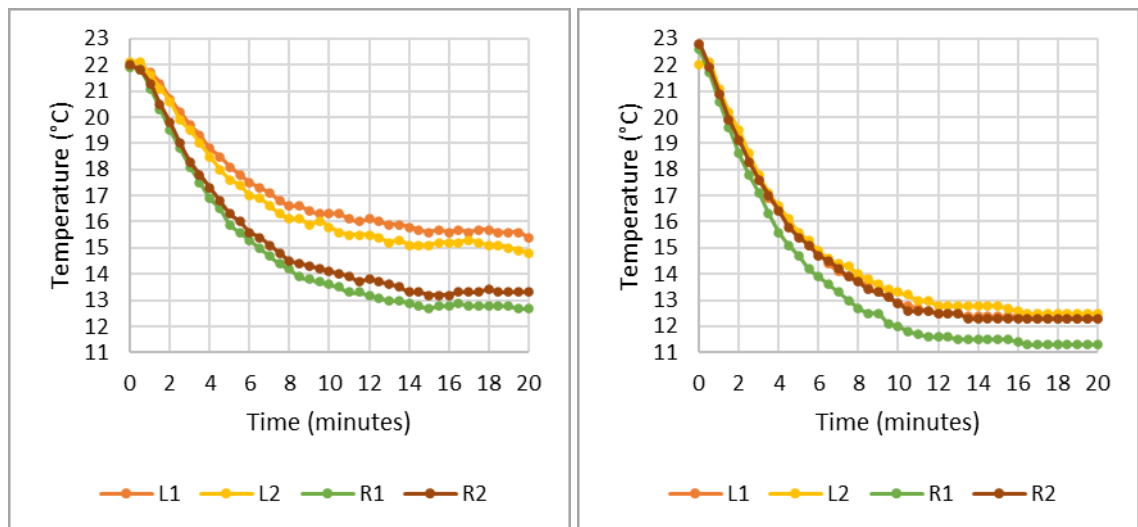
Figure 102 – Pipe surface temperature with 5V input (left) vs 12V input (right)

The results show around 2°C further reduction in temperatures using 12V input compared to 5V. A noticeable difference between the steady-state temperatures of the left and the right side of the pipe is also observed on the 5V chart. This suggests that lower heat absorption power reduces the phase change effectiveness of the heat pipe.
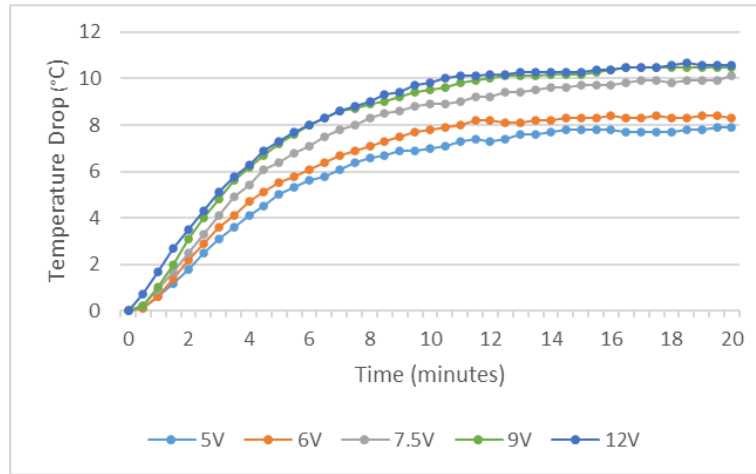
Figure 103 – Experiment 2 – Absolute temperature drop vs Time for varied input voltage

The collective graphs of the average temperature drop (i.e. absolute change in temperature) of the pipe surface for each of the five voltage inputs are shown in Figure 103. Next, a summary of results with the average temperature of the pipe surface and power consumption for each input voltage is shown in Table 9.

Table 9 – Experiment 2 results against varied input voltage

Input Voltage	T_{amb}	ΔT_{avg}	I (A)	P_i (W)
5V	21.5	7.9	1.4	7.0
6V	21.6	8.3	1.5	9.0
7.5V	22.7	10.1	1.8	13.5
9V	22.0	10.6	2.3	20.7
12V	22.8	10.7	3.4	40.8

This shows that the temperature drop is proportional to the power consumption. However, the performance correlation is not linear. As the proposed system is to be solar-powered, it is essential to identify the optimum value of power requirements.

5.4.2. Optimum voltage input based on power consumption

Figure 104 summarises the average temperature drop of the pipe surface (ΔT_{AVG}) and power consumption (P_i) against each voltage input tested. As observed from the two

graphs, voltage input above 7.5V induces saturation towards the cooling performance as the temperature drop reaches a plateau with increasing power consumption.
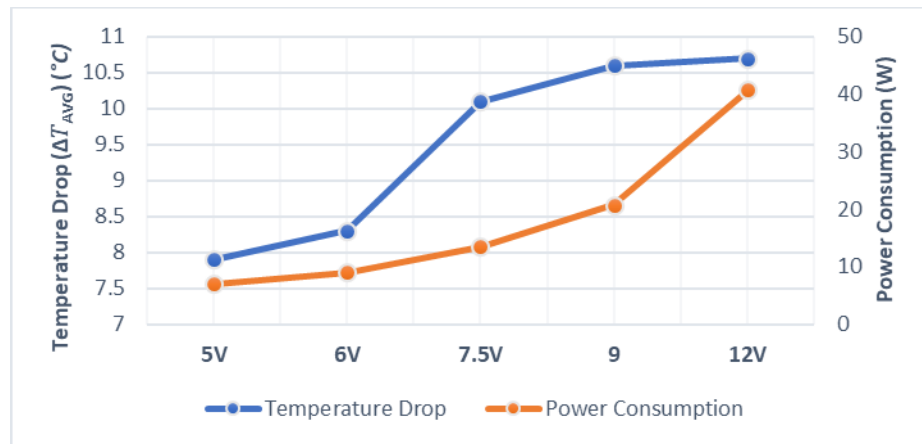
Figure 104 - Temperature drop (°C) and Power consumption (W) against voltage input

This potential limit of ΔT_{AVG} occurs as the rate of heat extraction by the TEC reaches the rate of convective heat transfer from ambient to the pipe surface due to natural convection. This is where the temperatures stabilise. The graph in Figure 104 suggests that 7.5V is the most effective input voltage with a considerable reduction in pipe temperatures with relatively low power consumption. However, it is to be noted that (1) these results do not consider the heat losses and efficiency of the cooling system, and (2) the experiment was conducted on a single pipe with minimal heat dissipation needs. To find the optimum input power, a full set of six heat pipes against a single and dual fan system needs to be examined for an overall COP at each voltage input, which is investigated in Experiment 3.

Furthermore, the desired input power would depend on the climate conditions and cooling demands. For example, temperate regions would more likely require lesser power with better efficiency to provide the necessary cooling, as compared to hotter regions that would demand a higher cooling capacity (with higher input power) despite the lower efficiency.

Thermoelectric devices are capable of both heating and cooling (with switching current polarity). Although space heating (by heating the pipes) is not in the scope of this thesis, the preliminary experiments (so far) were performed for both cooling and

heating by switching the polarity of the TECs using the same experimental setup. The results of 'Experiment 2' in the heating mode are presented in Appendix D-1.

5.5. Experiment 3: COP and Heat Transfer Rate Validation

This section first evaluates the Coefficient of Performance (COP) of the TEC-driven heat pipe cooling mechanism on a six-pipe set-up and then examines the computational heat transfer rate that would reflect the experimental results of a single-pipe.

The COP and efficiency through a TEC-based system depend on several factors, which include the quality of the TEC, the operating conditions, and the efficiency of heat dissipation from the hot side. Typically, the efficiency of a thermoelectric cooling device ranges from 5% to 15% [223]. This limited cooling efficiency is due to several factors. Firstly, the heat pump by the TEC generates a significant amount of heat on the hot side. Despite active heat dissipation, some heat travels back internally to the cold side. Additionally, a large amount of energy is lost due to the internal electrical resistance of the TEC (i.e. Joule heating). Consequently, the remaining energy that absorbs heat at the cold side of the TEC is used for effective cooling, i.e. the conductive cooling of pipes.

5.5.1. Optimum voltage input based on COP

Previously, preliminary results of experiment 2 evaluated the temperature reduction response through varying input voltages and the associated power consumption. However, the results did not account for the cooling efficiency of the system. Hence, this experiment aims to find the optimum input voltage based on a suitable balance between the COP of the system as well as temperature reduction capacity. This is investigated for an assembly of six heat pipes utilising the full capacity of the chosen heat sink and analysing configurations using a single and dual fan arrangement as detailed in the experimental setup in section 4.3.3.

The results of 'Experiment 3' (Figure 74) are presented in Table 10. This includes the readings from pipe surface temperatures (averaged) as T_p, the absolute temperature drop (ΔT) from an ambient temperature of 21.5°C, the heat sink temperatures (T_{hs})

whilst heat dissipation, the power consumption (as a product of supplied voltage and measured current) and the COP for both single and dual fan usage.

Table 10 – Experiment 3 Results – Temperatures, Power Consumption and COP

	5V		6V		7.5V		9V		12V	
No. of Fans:	1	2	1	2	1	2	1	2	1	2
T_p (°C)	14.5	15.2	13.8	14.5	13.5	14.0	13.6	13.7	13.9	13.5
ΔT (°C)	7.0	6.3	7.7	7.0	8.0	7.5	7.9	7.8	7.6	8.0
T_{hs} (°C)	27.0	23.6	29.6	26.0	32.3	28.2	36.5	30.6	37.8	33.1
I (A)	3.3	6.0	3.4	6.9	3.8	8.8	4.2	10.5	3.6	10.6
P (W)	16.5	28.5	20.4	41.4	28.5	66.0	37.8	94.5	43.2	127.2
COP	0.41	0.57	0.42	0.55	0.29	0.32	0.21	0.18	0.15	0.08

The COP in the results is based on the overall cooling mechanism (of the six heat pipe assemblies) calculated using the T_p, T_{hs} through equation 3.4 for both single-fan and dual-fan configurations. It is critical to consider and visualise the correlations between the temperature drop, power consumption and COP against each voltage input.

Figure 105 shows the pipe surface temperatures and heatsink temperatures against the voltage input to compare the response for both configurations, i.e. with one fan and two fans for heat dissipation.
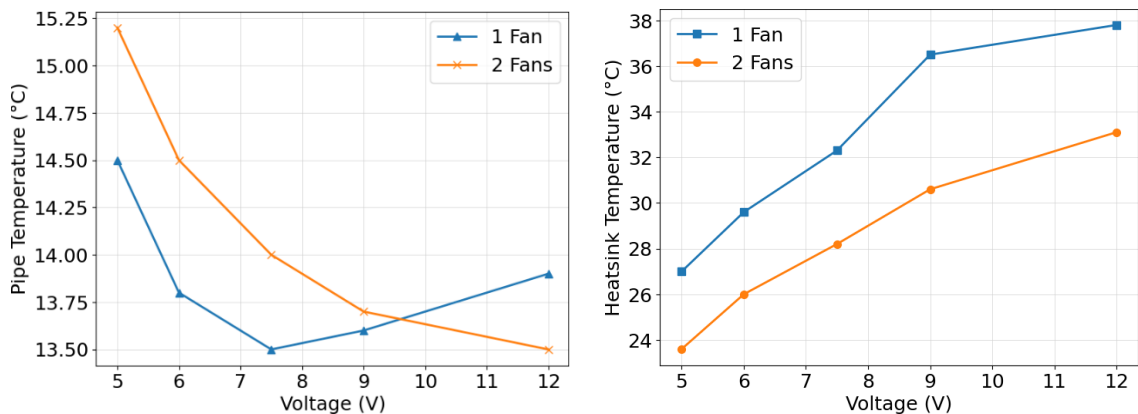
Figure 105 – Pipe Temperature (left) and Heatsink Temperature (right) vs Voltage

As seen from the pipe temperature chart (left), the single fan configuration shows slightly better cooling performance at lower voltages, however, at 12V power the

single fan is unable to adequately meet the heat dissipation needs. Whereas a dual fan system shows a reliable heat dissipation. The same observation is confirmed from the heatsink chart (right) where the temperatures of the heatsink with one fan are consistently higher than the dual fan while elevating further at higher input voltages.
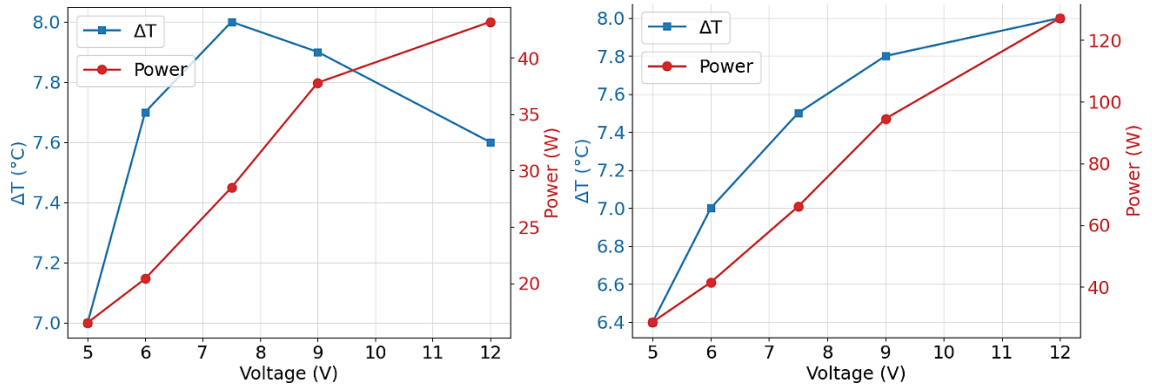
Figure 106 – ΔT and Power vs Voltage graphs with one fan (left) and two fans (right)

Figure 106 shows the absolute temperature drop of single fan (left) and dual fan (right) configurations alongside the power consumption for each voltage input. The single fan configuration shows a decrease in temperature drop at higher voltage despite consuming higher power. This is due to the energy losses (as heat), which are inevitably higher with an under-performing heat dissipation system. Nevertheless, compared to the dual fan system, the single fan provides a much better cooling capability at voltages between 6V to 9V. Figure 107 compares the absolute change in temperatures of heat pipes and heat sink temperatures alongside power consumption vs. voltage input in both fan configurations.
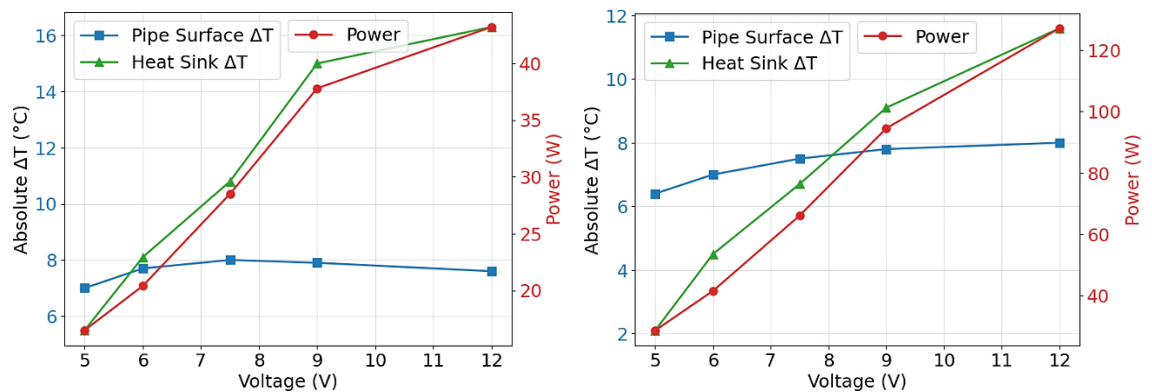
Figure 107 – Absolute ΔT of Pipe and Heatsink with one fan (left) and two fans (right)

The heatsink temperatures proportionally follow the power consumption in both configurations of fans. However, the intersection of the absolute change in temperature of the pipe and heatsink suggests that the temperature drop of the pipe exceeds the rise in temperature of the heat sink for voltages under 6V for the one-fan configuration and under 8V for the two-fan configuration.

Figure 108 compares ΔT and COP of the two configurations to assess the pipe cooling alongside cooling efficiencies.
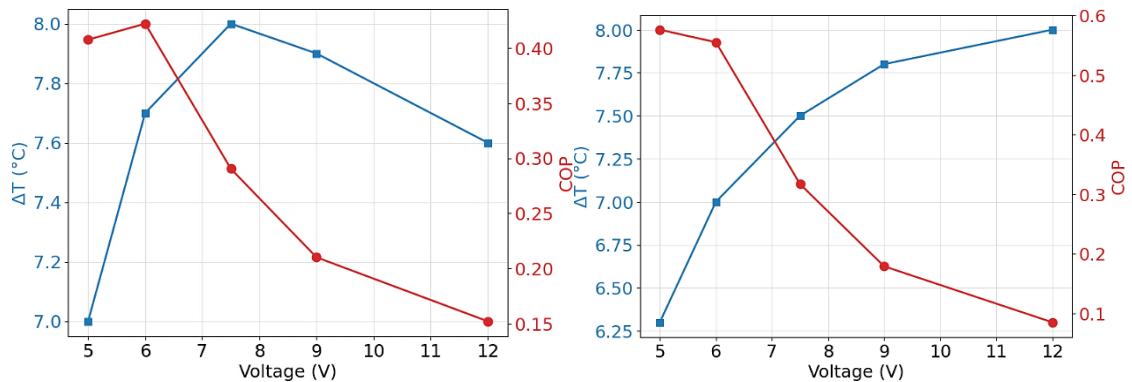
Figure 108 - ΔT and COP vs Voltage with one fan (left) and two fans (right)

The COP of the cooling system is notably high (i.e. above 0.4) between 5V and 6V before dropping significantly at 7.5V for both fan configurations. This suggests that despite the higher temperature drop at 7.5V, the cooling performance is significantly reduced. In other words, at 7.5V, much higher energy is wasted (in heat) to achieve a slightly larger drop in pipe temperatures compared to 6V. Moreover, although 5V shows the highest COP of 0.57 in the two-fan configuration, the pipe temperature drop is the lowest (i.e. 6.3°C).

This confirms that for the TEC1-12706 modules using the proposed design and mechanism of conductive cooling of heat pipes:

1. the optimum voltage input is 6V, which delivers a COP above 0.4. This lower voltage than the rated TEC voltage not only shows high cooling efficiencies, but due to the lower power consumption, the system becomes more suitable in a potential solar-powered cooling application.

2. the ideal fan configuration depends on the practical application and requirements. For example, at 6V, and in the context of this research, one fan configuration is sufficient to provide a temperature drop in pipes of 7°C with low power consumption and high cooling efficiencies. However, if an application demands a much larger temperature reduction of pipes, then a 12V input with two fans can drop the pipe temperatures by 8°C or higher depending on the ambient conditions.

5.5.2. Preliminary Convection Trial Results

Once the conductive cooling performances are optimised with the concluded set of parameters, the next step is to examine the effect of wind over the pipes as described in section 4.3.3. A preliminary convection test was conducted to observe the impact of this forced convection on the heat transfer with pipes. A stream of wind is blown over a single heat pipe via an array of 12V CPU fans with regulated power to adjust the speed (at 1.2m/s) using the experimental set-up of Figure 76. To compare the influence of the convective heat transfer rate of the airflow on the pipes, a similar experiment is repeated with no airflow. The transient response comparing both experimental results, i.e. the average pipe temperatures at 1.2m/s and natural convection, is shown in Figure 109.
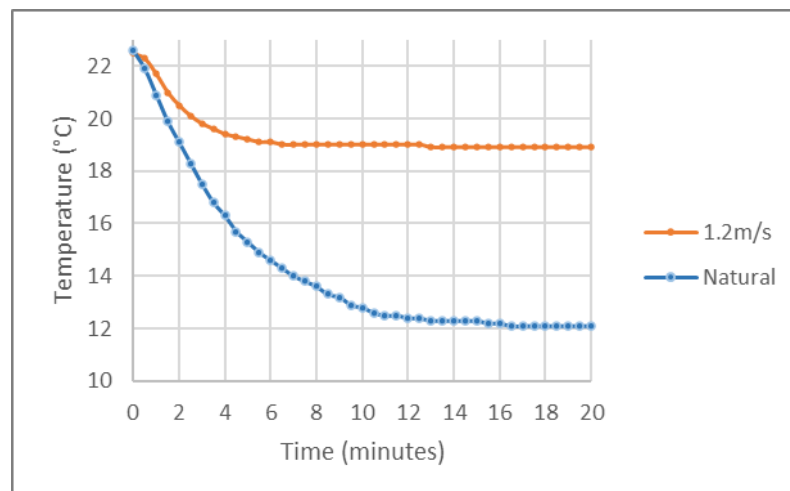
Figure 109 – Experimental comparison between natural and forced convection

The average pipe surface temperature vs time graph shows that the steady-state temperature with 1.2m/s wind speed attains 19°C as opposed to 12°C at natural indoor

conditions. Moreover, the rate of decline of the temperatures was rapid with the airflow reaching a steady state in 6 minutes compared to 14 minutes without wind.

This transient response with 1.2m/s will be used to investigate and validate the CFD trials on a corresponding computational model of a single-pipe model.

5.5.3 CFD results and validation for single-pipe heat transfer rate

The surface temperature remains consistent along the length of the heat pipe during Peltier-driven conductive cooling as confirmed in Experiment 1. This allows for a simplification in modelling the heat pipe for CFD simulation by applying a constant heat transfer rate (heat flux) on the entire pipe surface. This section explores the viability of this simplified model with necessary validation.

A constant negative heat transfer rate on the surface of the pipe is applied to reflect the heat removed from the pipe (that is removed through the TEC in practice). This CFD analysis aims to identify an accurate heat transfer rate that conforms to the experimental data obtained in section 5.5.2.

The simulation results for the single-pipe study are based on the following CFD boundary conditions and experimental parameters:

Inlet velocity v (Experimental and CFD) = 1.2m/s

Ambient Temperature T_{amb} (Experimental and CFD) = 22°C

Initial Pipe Surface Temperature T_p (Measured and CFD) = 22.5°C

Input power to TEC (experimental) P_i, = 9W (6V input, 1.5A measured consumption)

Input heat transfer rate on pipes surface (CFD) $\dot{Q}_{CFD}$ = Varied from -3W to -7W.

Figure 110 shows a surface plot of the pipe at a steady state while it is actively cooled using a -7W of active heat transfer rate and a 22°C of air is blown over it at 1.2m/s. The windward section of the pipe surface absorbs most of the heat while the leeward remains colder, which helps in cooling the stagnant air cavities that are expected to descend due to gravity.
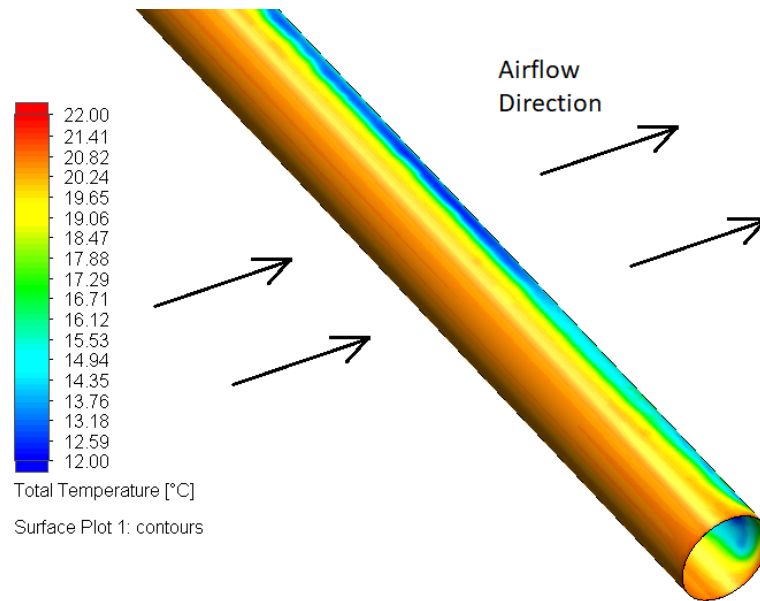
Figure 110 – Pipe surface temperature plot during single-pipe active cooling

A cut plot with temperature contours and velocity vectors of air around the actively cooled pipe is shown in Figure 111.
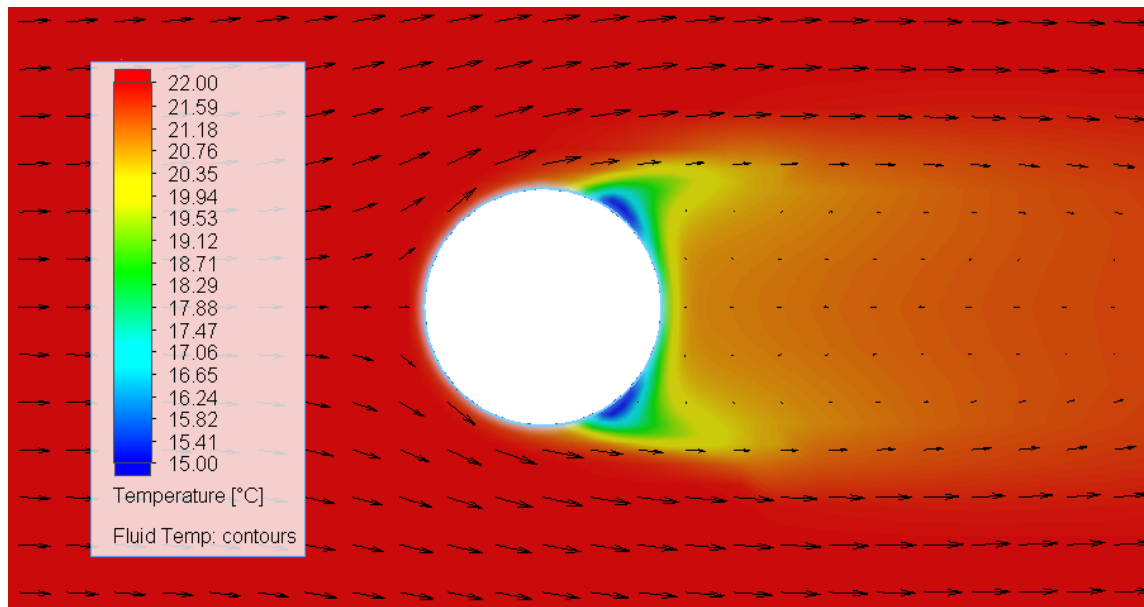
Figure 111 – Single pipe temperature cut plot

Figure 112 shows the CFD results using the transient response of the pipes subjected to active cooling using a heat transfer rate between 3W to 7W (Note: These parameters are input as negative values in the CFD model to denote heat removal from the pipe, i.e. cooling). In the same figure, the experimental transient response of the pipe

temperatures with 1.2m/s of forced convection (from section 5.5.2) is also included for comparison.
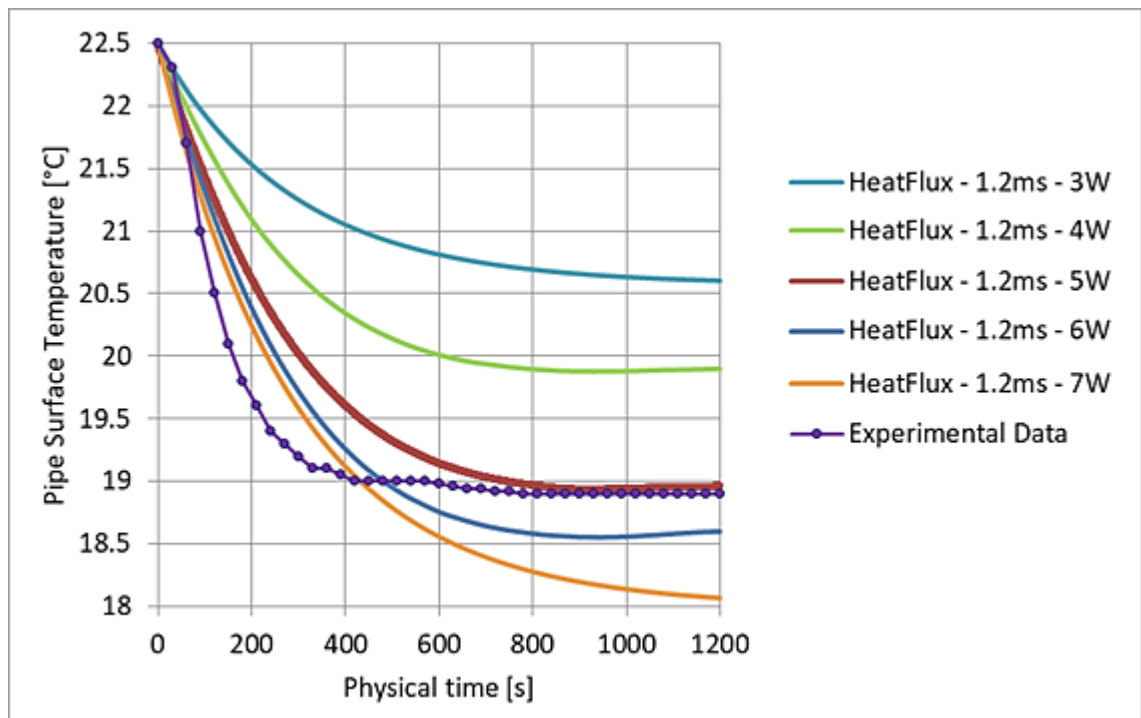
Figure 112 - Heat transfer rate validation with experimental data

From the trials of heat transfer rate between 3W to 7W, the transient response of the CFD results with 5W of heat transfer rate with 1.2m/s of airflow accurately corresponds and correlates to the steady state temperature (18.9°C) of the pipe surface of the experimental result at 1.2m/s. Nevertheless, this requires further validation with a wider range of experimental trials using different wind speeds to observe the steady state temperatures of corresponding CFD trials. This set of experiments (both CFD and experimental) and their validation are presented in the next section.

Additionally, while the steady state of the experimental response matches that of -5W heat flux, a noticeable deviation that is observed between the two corresponding line graphs is the rate at which the temperature drops during the transient phase. This is because the computational simulations typically model heat transfer via conduction and convection without including the effects of phase change. As the studied system uses heat pipes, the phase change (i.e. evaporation and condensation of the working fluid inside the heat pipe) is a key element that accelerates the heat transfer.

From the simulation of -5W of the heat transfer rate of the pipe, a heat flux of -106.1W/m² and the average heat transfer coefficient of 48.0W/m²K were measured.

5.6. Experiment 4: Forced convection – Velocity impact and validation

5.6.1. Experimental Results

To adjust the wind speed, the voltage of the fans is regulated and the velocity around the pipes is measured (as described in section 4.3.4). The ambient temperatures were maintained at 23°C and the velocity was varied from 0.1m/s up to 3m/s and the steady state surface temperatures of the heat pipe were measured for each discrete airflow. The TECs were powered at 6V for each test. The graph of pipe temperature vs wind speed is shown in Figure 113.
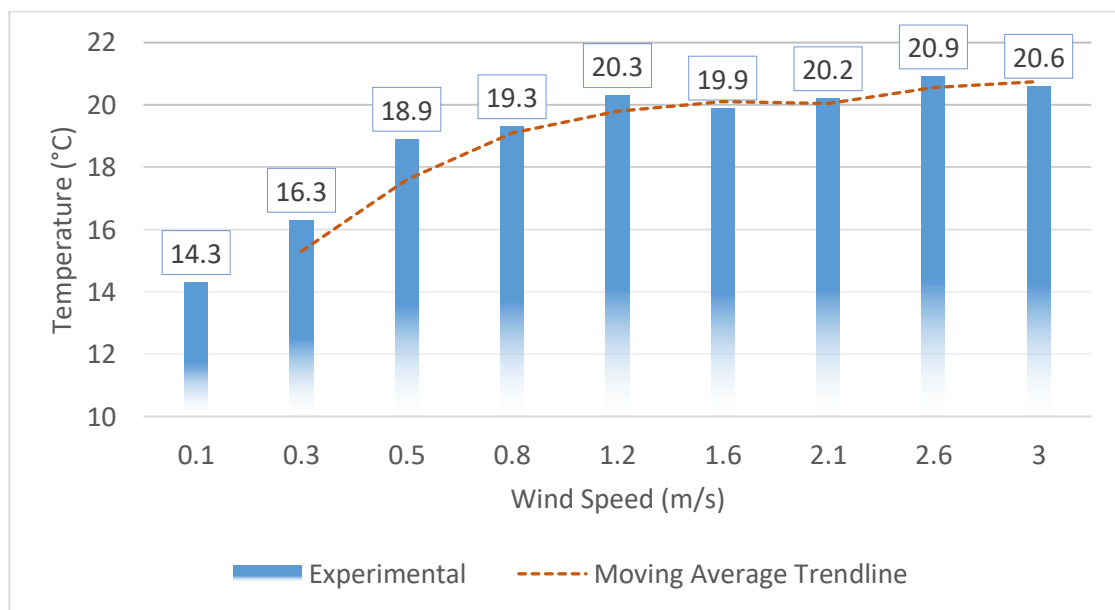
Figure 113 –Pipe surface temperatures vs. velocity at ambient temperature of 23°C

The results show that as the wind speeds increase, the steady-state temperatures are higher. However, the moving average (red dashed trendline) in Figure 113 indicates that wind speeds above 1.2m/s have negligible impact on the temperatures, while lower velocities observed significantly better cooling. This confirms that TEC-assisted conductive cooling is more dominant to affect the surface temperatures than the convective heat transfer from the ambient airflow at lower wind speeds.

5.6.2. CFD Results and Validation

From the CFD trials of 'Experiment 3' a 5W of heat flux was chosen due to its closest correlation with the actual (experimental) efficiency of the cooling system. Hence, a range of CFD simulations were performed using the 5W heat flux of the pipe surface to match the test scenarios against the same wind velocities and a constant ambient temperature of 23°C as set for the experimental trials. Table 11 shows the test set and the results of both CFD and experimental trials, which is followed by Figure 114 which presents the result as a bar chart.

Table 11 – Experimental and CFD results of 'Experiment 4'

Set	Wind (m/s)	Ambient Temp (°C)		Pipe Surface Temp (°C)	
		EXP	CFD	EXP	CFD
A	0.1	23.0	23.0	14.3	10.7
B	0.3	23.1	23.1	16.3	15.8
C	0.5	22.9	22.9	18.9	17.6
D	0.8	23.3	23.3	19.3	19.4
E	1.2	23.6	23.6	20.3	19.7
F	1.6	23.1	23.1	19.9	20.4
G	2.1	23.3	23.3	20.2	21.0
H	2.6	23.2	23.2	20.9	21.1
I	3.0	22.9	22.9	20.6	21.0
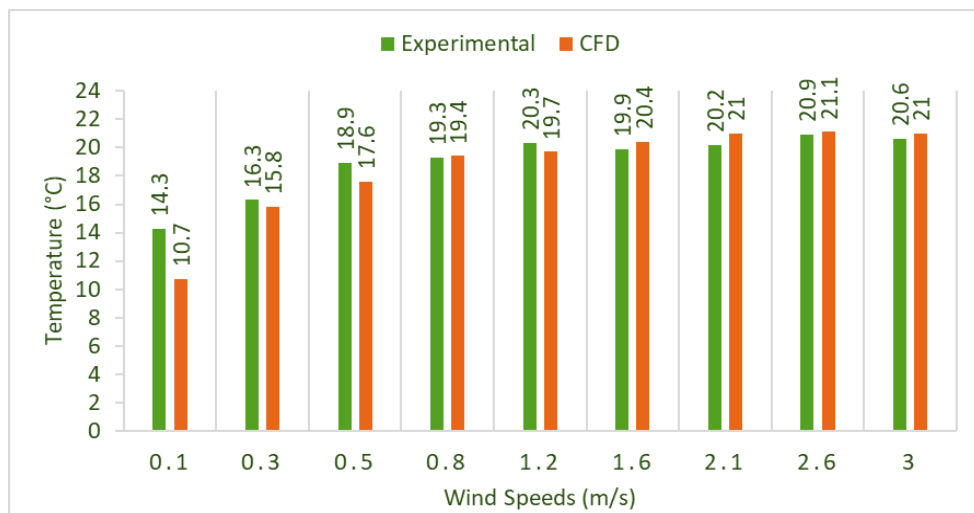
Figure 114 – Experimental vs CFD pipe surface temperatures vs. velocity

The forced convection experiments against discrete wind speeds from 0.1m/s to 3m/s from both experimental and CFD trials exhibit a consistent and analogous correlation.

139

Both results demonstrate a rising steady state temperature of the actively cooled pipe with minimal discrepancies. To highlight the errors between the results, a relative percentage error is calculated against each trial as shown in Figure 115.
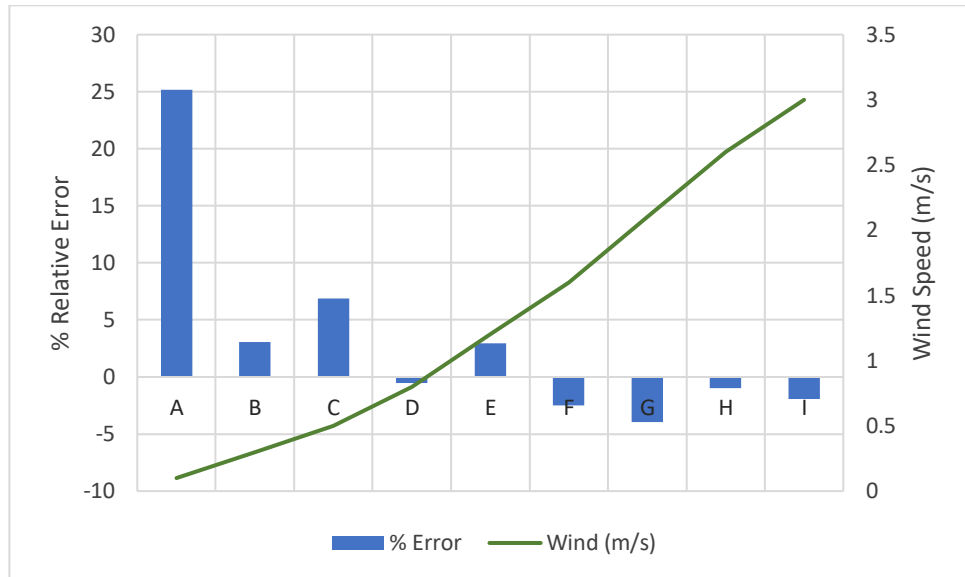
Figure 115 – Relative percentage error in experimental and CFD trials

The errors are generally seen within a 5% range, especially for higher velocities. This accuracy validates the CFD approach to use a (negative) heat flux as an active cooling mechanism to reflect the TEC-assisted conductive cooling of the heat pipes.

However, the only outlier as seen in Figure 114 and Figure 115 is the 25% error in the steady state temperature of the CFD-based temperature of 10.3°C at 0.1m/s as compared to an actual temperature of 14.3°C measured at the same wind speed. The primary factor affecting the discrepancies at extremely low speed is likely due to environmental conditions. In the CFD simulations, the supply air stream a consistent and laminar, whereas in the experimental test, the airflow is inevitably turbulent around the pipe, particularly at lower airflows, which could easily affect the heat transfer rate.

It is important to note that this experiment was conducted on a single pipe. In a full-scale version of the proposed cooling system with two layers of pipes, the wind speed is expected to drop considerably after the first layer of pipe, allowing better temperature drops on the lower layer(s) of heat pipes. This effect is better visualised through the cut plots of CFD simulations in the subsequent sections.

5.7 Experiment 5: Heat Exchanger Unit – Air mass impact and validation

This section presents the results of the full-scale prototype of the cooling unit through a custom-designed wind supply-and-extraction compatible rig to examine the cooling of supply air through the actively cooled pipes. A corresponding CFD model replicating a similar set-up was simulated, analysed and validated against the experimental data.

5.7.1. Experimental Results

In the experimental trials, the air mass flow rate of the fresh air was varied between 50L/s to 300L/s. The steady-state temperatures recorded comprised of temperature of fresh air, supply air, extract air and exhaust air. Table 12 presents the change in temperatures between fresh air and supply air as well as exhaust and extract for an ambient temperature of 35°C. A complete set of raw results are shared in Appendix D-2, while the graph of temperature difference (of fresh air and supply air), i.e. ΔT_{AIR} against ambient temperatures ΔT_{amb} for each flow rate is shown in Figure 116.

Table 12 – Temperature differences recorded against increasing flow rates

Air Flow Rate (L/s)	50	75	100	200	300
ΔT_{AIR} (T_{SUP}-T_{FA}) (°C)	-3.62	-2.94	-1.64	-0.83	-0.87
ΔT_{AIR} (T_{EXH}-T_{EXT}) (°C)	2.36	2.01	2.62	3.21	2.61
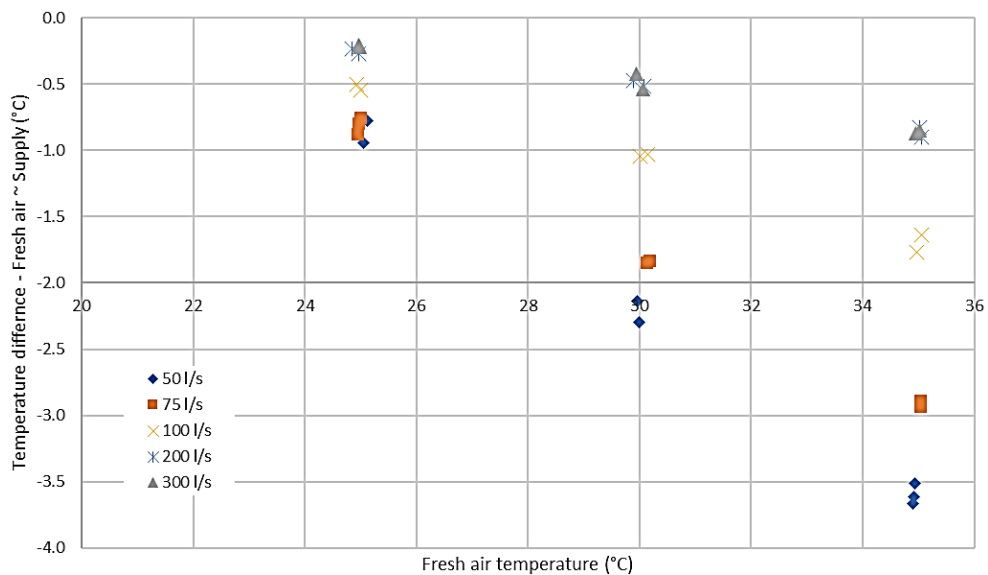
Figure 116 – Temperature drop vs Fresh air temperature

The temperature drop (cooling) against the fresh air was observed to be greater with a lower rate of flow. A maximum of 3.66°C of temperature drop was recorded at a flow rate of 50L/s when the inlet temperature was approximately 35°C. However, based on the setup, the system acts like a volume displacement system, where the air is pushed and extracted from the exhaust leaving less time for heat transfer with the pipes. In real-world conditions, the temperature drops are likely to improve as the constant flow pressure over the cooling system limits the time for heat transfer to occur between the air and the surface of the heat pipes.

The results also show that at higher temperatures, more temperature drop was observed, which confirms the preliminary results of 'Experiment 1' against ambient temperatures. This is due to the increase in performance in heat pipes at higher temperature differentials, which is beneficial in extremely hot climates where the heat pipes would capitalise on larger temperature differentials for rapid heat extraction.

5.7.2. CFD Simulations

The simulations of the full-scale CFD model of Experiment 5 (as discussed in section 4.4.2) are presented here to visualise the temperature and velocity contours inside the model. Figure 117 shows the duct cut plot of velocity streams as 50L/s of air is pushed through the pipes from the inlet (left) quadrant.
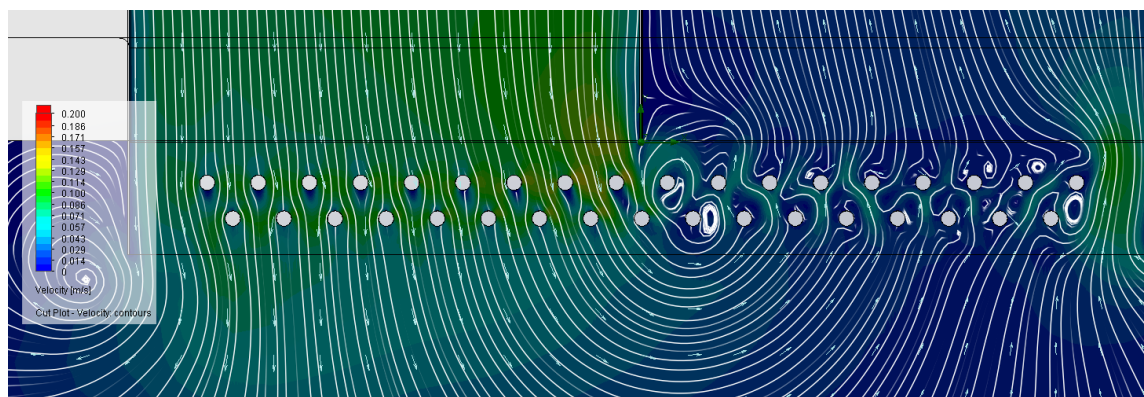
Figure 117 – Velocity streamlines around the pipes

The inlet velocity streamlines (left) show a consistent and laminar airflow around the pipes as compared to the exhaust quadrant(s) where the stream is slightly disturbed due to the convergence of velocity vectors from a distributed air in the plenum.

Furthermore, the air speed is reduced as the cut plot shows only one quadrant, whereas the air exits from a total of three quadrants combined.

Figure 118 shows the temperature cut plot with velocity vectors of the duct at 2.5 seconds after the simulation commenced to observe the effect of the drop in temperatures of air around and below the pipes.
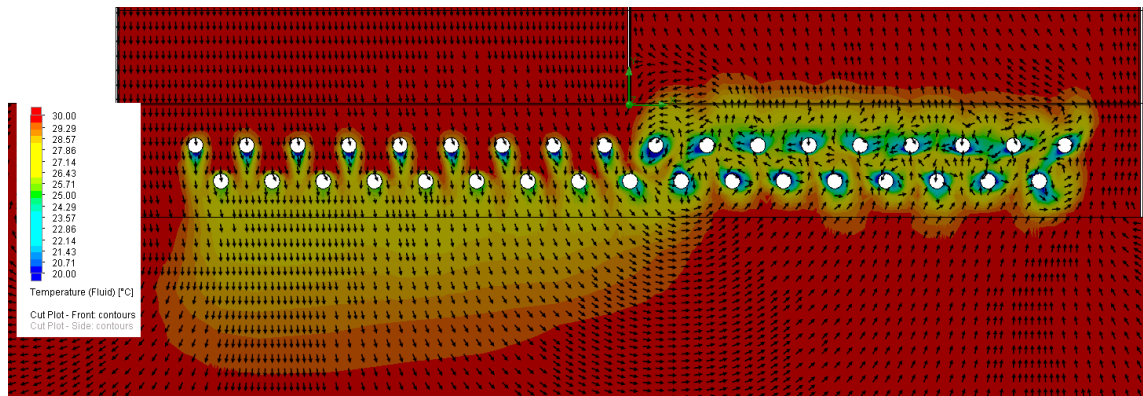
Figure 118 – Cut plot showing temperature contour around the pipes

5.7.3 CFD Results and Validation

The results of the CFD analyses of 'Experiment 5' (as detailed in section 4.3.5) are presented here. An air flow rate of 50, 75, 100, 200 and 300 L/s was used at the inlet quadrant to measure the temperature of air after the heat exchanger (cooling unit). A combined transient response of these temperatures below pipes against an ambient temperature of 35C is shown in Figure 119
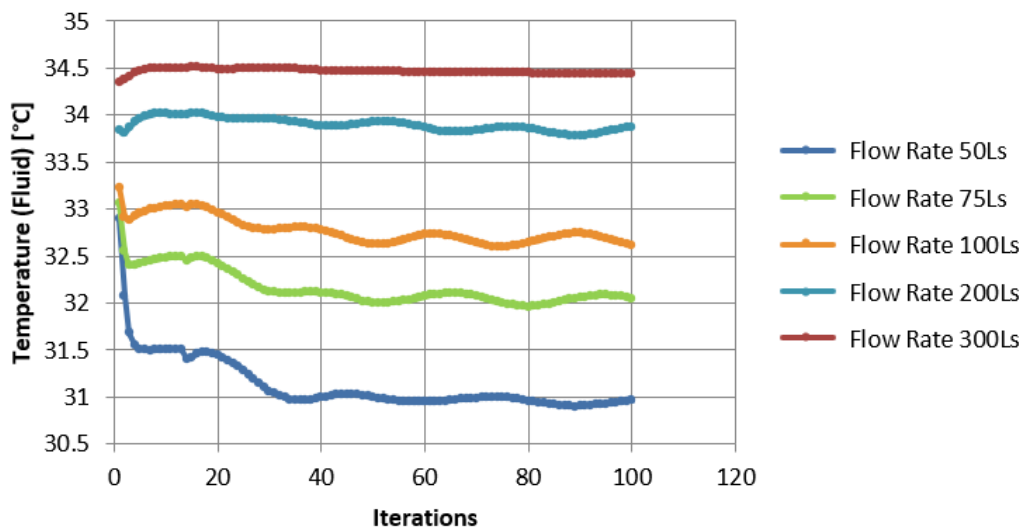
Figure 119 – Transient response of temperature below pipes for varied air flow rates

The experimental and CFD results are now compared and validated. Figure 120 shows the graph of temperature below pipes vs. each air flow rate tested at an ambient temperature of 35°C.
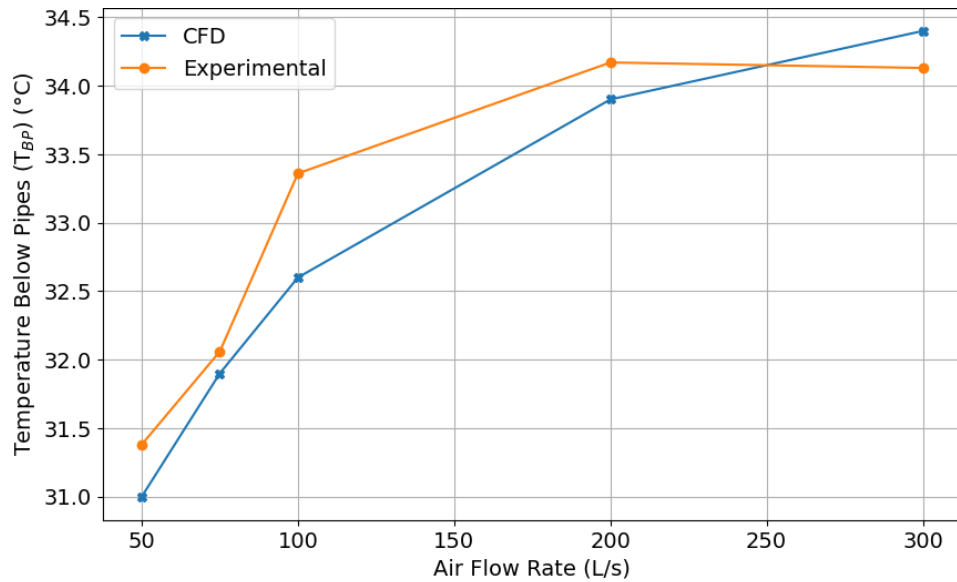
Figure 120 – Experimental and CFD results for 50Ls to 300Ls (Experiment 5)

Results show a consistent correlation of temperature drops against varying air flow rates. As seen, a higher air flow rate resulted in a negligible drop in air temperature in both CFD and experimental trials, while a low air flow rate (50L/s) showed considerable cooling. The percentage error between the experimental and CFD results (with the experimental as a reference) is shown in

Figure 121.
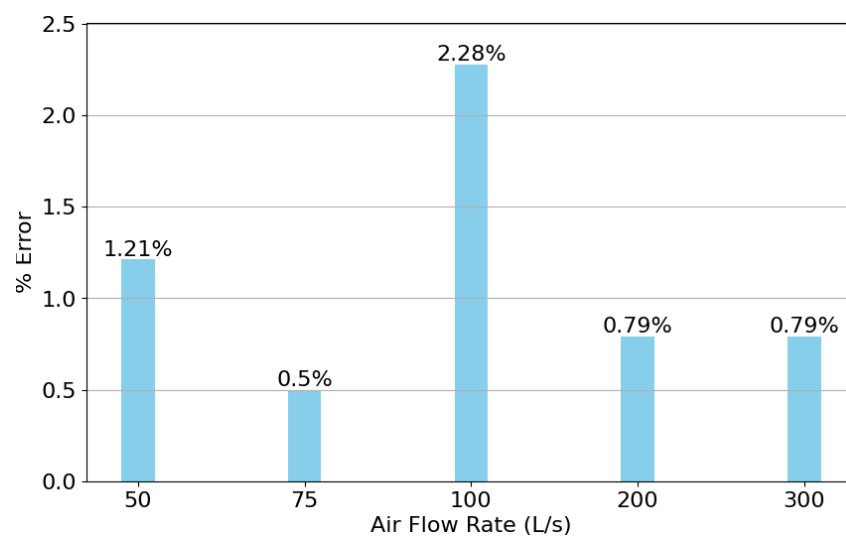
Figure 121 – Percentage error between experimental and CFD results

The minimal errors with an average of 1.11% discrepancies between the experimental and CFD results successfully validate the CFD model to computationally replicate a Peltier-driven heat pipe cooling mechanism. This enables further optimisations to be explored to enhance the cooling capability of this system.

Furthermore, the full-scale experimentation relied on an artificially blustered air mass flow rate through the inlet quadrant, which mimics a volume displacement system and lacks the needed natural air circulation before and around the cooled pipes. In other words, the experimental approach of using confined channels for supply and extraction oversimplified the system and reduced the dynamic thermal interaction between the pipes and the stream of air. Hence, the next section explores cooling optimisations using a wind tower integrated CFD model with the validated cooling mechanism.

5.8 Post-Validation Optimisation: Proposed Augmentations

This section evaluates the impact of each augmentation technique that was described in section 4.4.3. The CFD analyses simulate a combined external and internal CFD model with a wind tower comprising the TEC cooling unit to examine transient indoor temperature reduction against external wind flow and high ambient temperatures.

Figure 122 shows a cut plot illustrating the velocity contours as 1.5m/s of external wind enters the room and passes through the pipes.
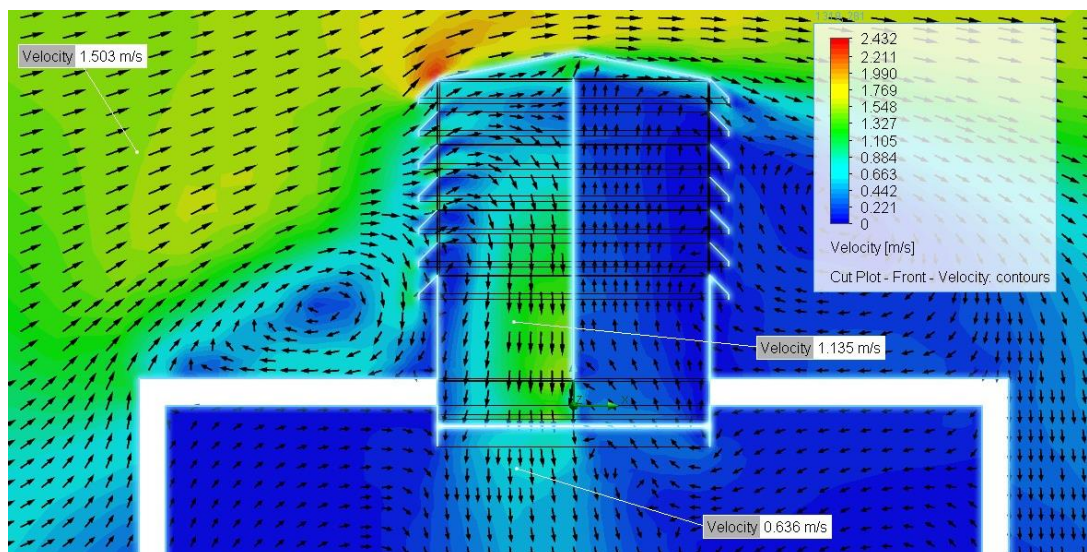
Figure 122 – Velocity contours cut plot of wind tower

Three velocity probes are shown, i.e. the external wind speeds, the velocity before the pipes, and the speed of air as it enters the room. The speed decreases by 24% as it reaches the pipes, and further decreases by 44% as it enters the room. However, even the reduced speeds often require further diffusion for the comfort of the occupants, which is done via diffusers or volume control dampers underneath the opening of the wind tower. Figure 123 shows the temperature gradient of flow trajectories of air through the wind tower model.
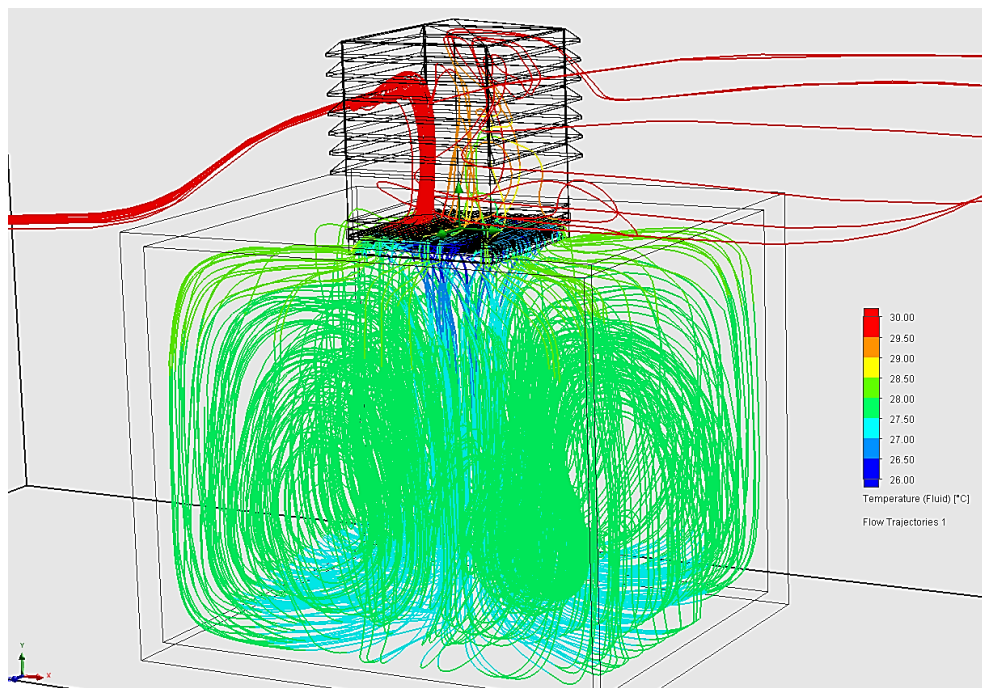
Figure 123 – Flow Trajectory of Temperature at 1m/s wind speed

Thanks to the 35 actively cooled pipes at -5W of heat transfer rate, the ambient 30°C of external wind at 1.5m/s cools by up to 4°C as it enters the room. This causes a temperature drop of 3°C as 27°C of air that circulates inside the room passively before it exists through the leeward quadrant of the wind tower.

Similarly, a variety of simulations with varying ambient temperatures and wind speeds confirmed that the indoor room temperatures are generally 75% of the temperatures below the pipes with a steady state time of 1 hour for the room size 3m x 2.5m x 2.5m.

However, the insignificant temperature drop is primarily due to the less residence time of air around the actively cooled pipes. In this section, a variety of techniques are

proposed to leverage the cooling capability of the pipes with a more effective heat transfer from the ambient air at the inlet quadrant(s).

5.8.1 Regulated Damper Integration before Heat Exchanger

The placement of the damper before the heat exchanger aims to enhance the cooling by (1) increasing the residence time of warm air with the pipes, and (2) developing turbulence around the pipes to promote the effective exchange of heat before the air enters the room. CFD simulations were performed using an ambient temperature of 30°C at 1m/s wind speed to compare cooling capability in both configurations, i.e. without a damper and with a damper before the pipes. Figure 124 shows the CFD results of the velocity contour plot at steady-state with 1m/s inlet wind velocities for both configurations: with and without damper. The addition of dampers substantially reduces the wind speeds before interacting with the actively cooled pipes, hence increasing the residence time significantly.
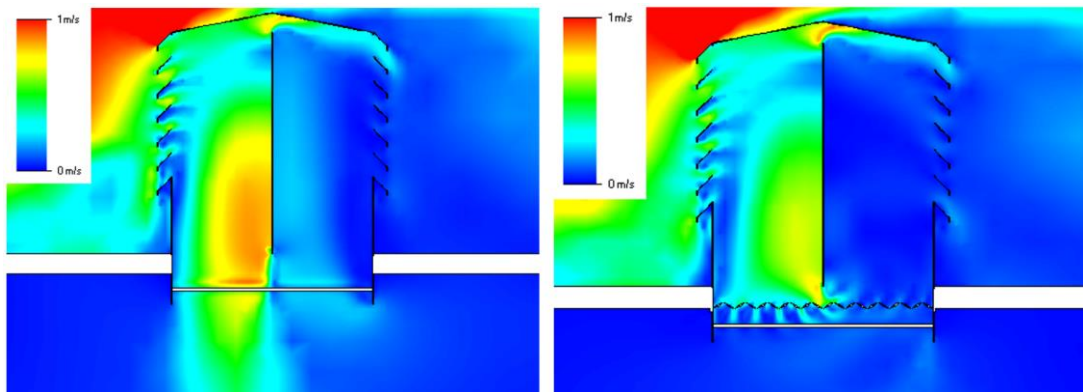
Figure 124 - Velocity contour plots with (right) and without damper (left)

Figure 125 shows the turbulence contour plot at steady state of CFD results with 1m/s inlet wind velocities for both configurations: with and without damper. As observed, massive turbulence occurs around the heat pipes causing a better heat transfer to take place before wind enters the room.
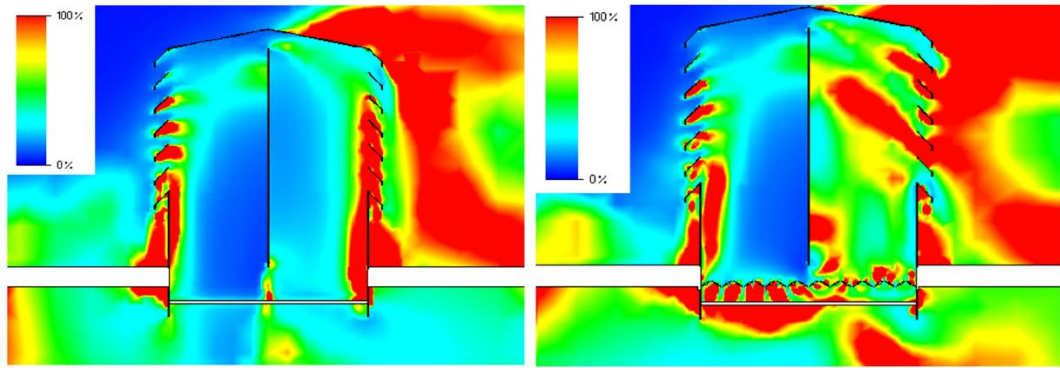
Figure 125 - Turbulence contour plot with (right) and without damper (left)

Figure 126 shows the temperature contour plot at steady state of CFD results with 1m/s inlet wind velocities for both configurations: with and without damper. The temperature on the right side is colder as the exhaust room temperature proceeds to exit the wind tower which further cools the air.

Additionally, an envelope of concentrated cold region forms at the exhaust region of the heat pipes especially at the damper configuration (right). This colder air gradually descends into the room contributing to the overall cooling effect.
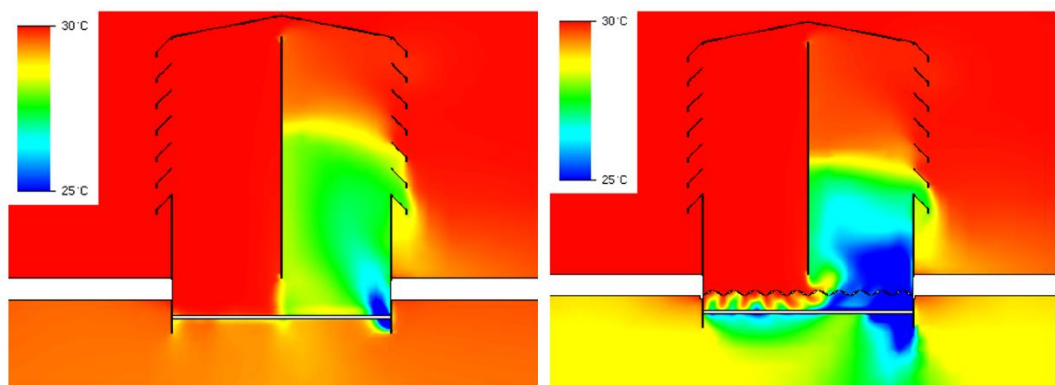
Figure 126 - Fluid temperature contour plot with (right) and without damper (left)

Figure 127 shows the average indoor temperature drop with 1m/s of external wind speeds and 28°C ambient temperature with the dampers (at 60° opening) and without the damper. A significant drop in temperatures is seen with the addition of a damper before the cooling unit.
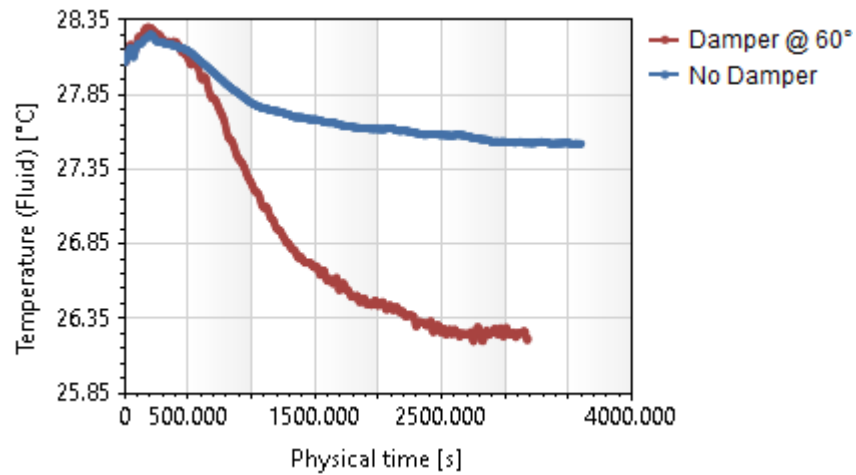
Figure 127 – Indoor temperature drop with damper at 60° and without damper

The damper's opening angle and the external wind speeds play an important role in the resulting temperature drops. Hence, a variety of CFD simulations were conducted to assess the impact of the louvre angle of the damper on the temperature drop against varying wind speeds. The angle (θ) was varied from 0° to 90° opening as a trial set of {0, 15, 30, 45, 60, 90} against the external wind from 0.25m/s to 5m/s with a trial set of {0.25, 0.5, 1, 2, 3, 5} to observe the average temperature below the pipes that enters the room. Figure shows an interpolated 3D surface plot result from these trials using a consistent ambient temperature of 28°C.
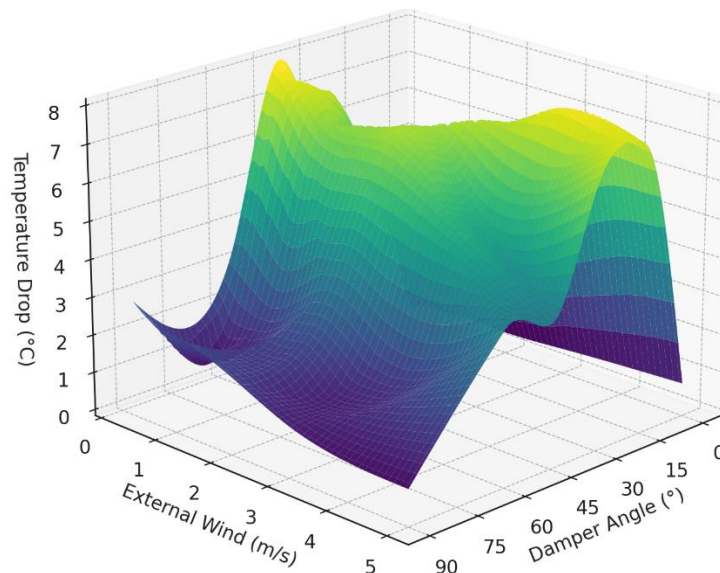
Figure 128 – 3D surface plot to gauge temperature drops against angle and wind

A maximum temperature drop of up to 8°C (below the pipes) was observed in multiple trials. The opening angle of damper louvers is generally optimum between 15° and 45°

but they vary with external wind speeds. For example, at lower wind speeds, a higher opening (45°) of louvres is beneficial for the temperature drop, whereas with increasing wind speeds (at 5m/s), a smaller louvre angle (15°) is recommended. This regulation of damper angles against speed can easily be achieved from the control system described in Chapter 3 Section 3.3.4.1 with an integration of a wind speed sensor/anemometer.

5.8.2 Additional Layer of Actively Cooled Pipes

The added layer of actively cooled pipes aims to further improve the cooling performance. Figure 129 compares the transient response of indoor temperature drops with 3m/s external wind speed at 28°C of ambient temperatures without a damper.
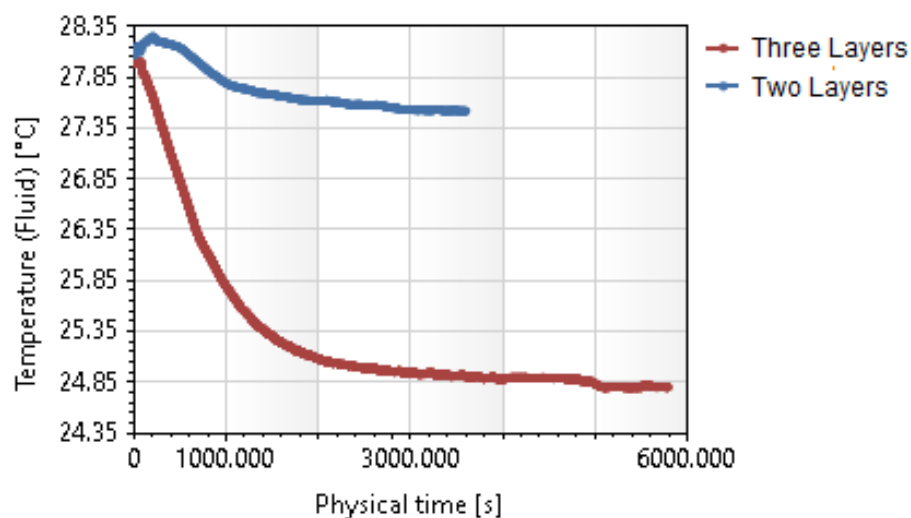
Figure 129 – Two Layers vs Three Layers Average Indoor Temperature Comparison

The results affirm a notable impact in cooling with an additional layer of pipes from 27.5°C average steady state room temperature distribution with two pipes compared to a 24.8°C of steady state indoor temperatures. The first two layers of cooled pipes that are offset by 25mm to encompass the vertical stream of air essentially aid in pre-cooling the air considerably before it reaches the third layer.

Furthermore, the speed of the air is reduced with a slight increase in turbulence, both factors favouring an effective heat transfer as confirmed by previous results. The effectiveness of cooling by the third layer of pipes is hence significantly enhanced.

However, the rate of ventilation is significantly reduced with an extra layer of pipes with a measured inlet volume flow rate of 4.5L/s with 1 m/s of external wind speeds (without a damper). With a damper with a 30° louvre angle and a three-pipe configuration, despite a massive temperature drop below the pipes (up to 10°C), the velocity under the pipe is observed to be virtually zero as shown in Figure 130. This is addressed with the third augmentation technique using DC fan integration.
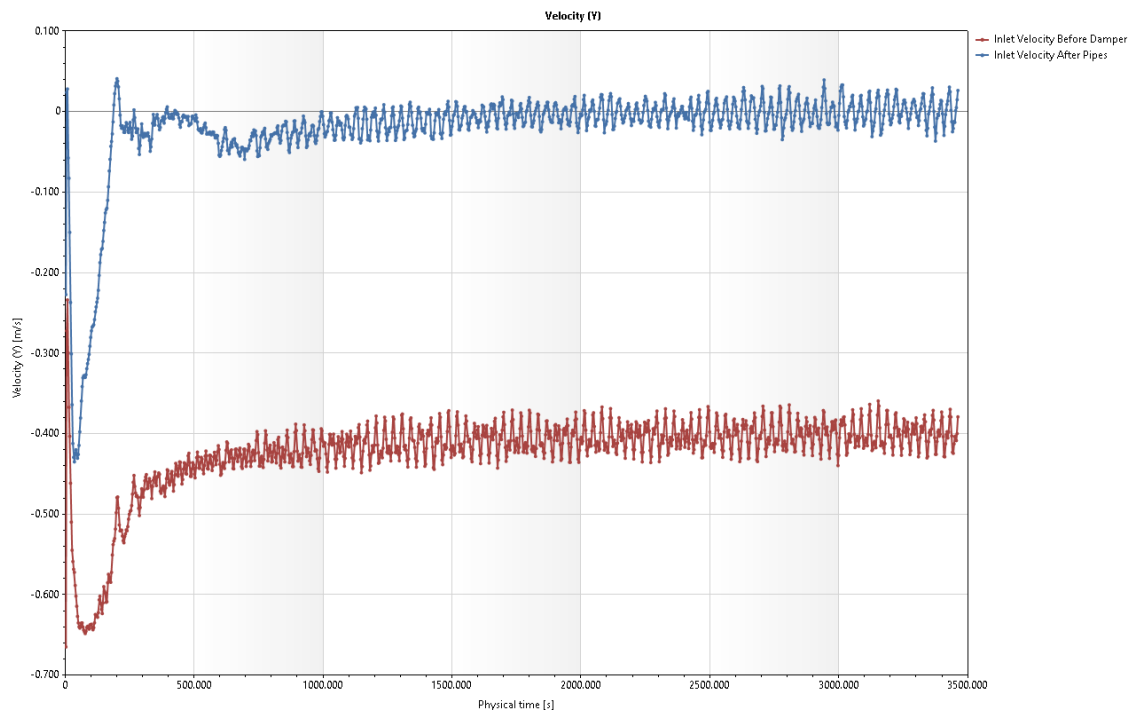
Figure 130 – Velocity after pipes compared to velocity before damper with 1m/s wind

5.8.3. Impact of Fan Integration

The fan model aims to redevelop the speed to ensure the necessary ventilation rates inside the room. However, this augmentation is proposed in combination with the damper integration which first ensures a reduction in temperature that creates an envelope of low speeds of slightly turbulent air and induces substantial drop in temperatures. The axial fan pushes the cool air into the room, which could be further regulated with the number of occupants as needed. Figure 131 shows the cut plot of temperature contour with fan integration along with damper at 15° of louvre angle. A significant drop of up to 5°C is observed inside the room against an ambient temperature of 28°C with external wind speeds of 2m/s.
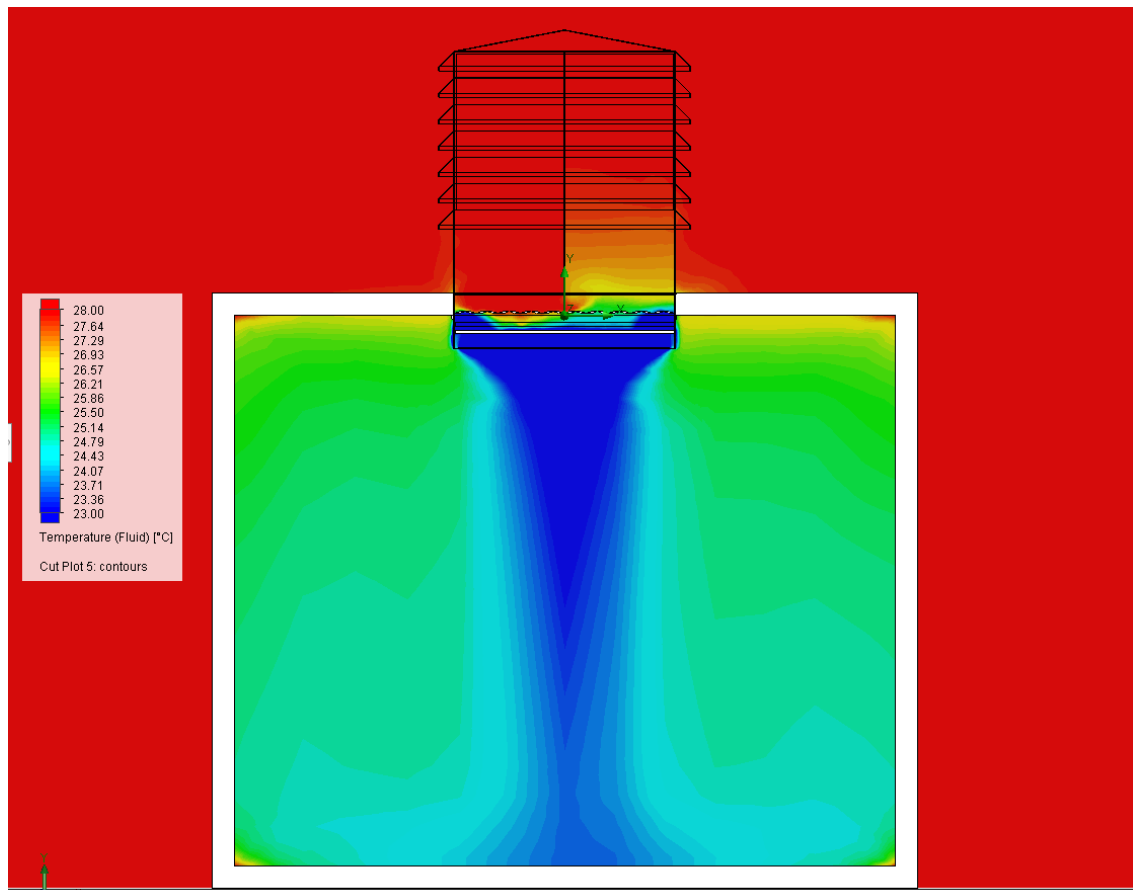
Figure 131 – Cut plot Temperature Contour Mid-plane through Wind Tower and Room

A volume flow rate of fresh air into the room was computed to be 0.0479m3/s, i.e. 47.9L/s. This ensures a safe ventilation rate for up to 9 people (based on BS5952 standards) with external wind speeds of as low as 0.5m/s. Higher wind speeds would further increase the ventilation rates while maintaining the temperature drop thanks to the regulated damper integration.

To evaluate the impact of each augmentation technique on the average room temperatures, results from each augmentation technique including some of their combinations are shown collectively in Figure 132. The damper louvre angles were based on the external wind speeds selected from the optimal angles as seen in Figure 128.

The maximum indoor cooling was achieved with a 'damper' and '3 pipe layers' integration with up to 8°C of temperature drop at 1m/s of external wind speeds, while all three augmentations combined results in 7.5°C. As the wind speed rises, the damper and three layers of pipe continue to maintain the highest cooling performance

compared with other combinations. Hence, the maximum cooling capacity (obtained through equation 3.15) with a ventilation rate of 47.9L/s and a temperature drop of 8°C equates to 474W.
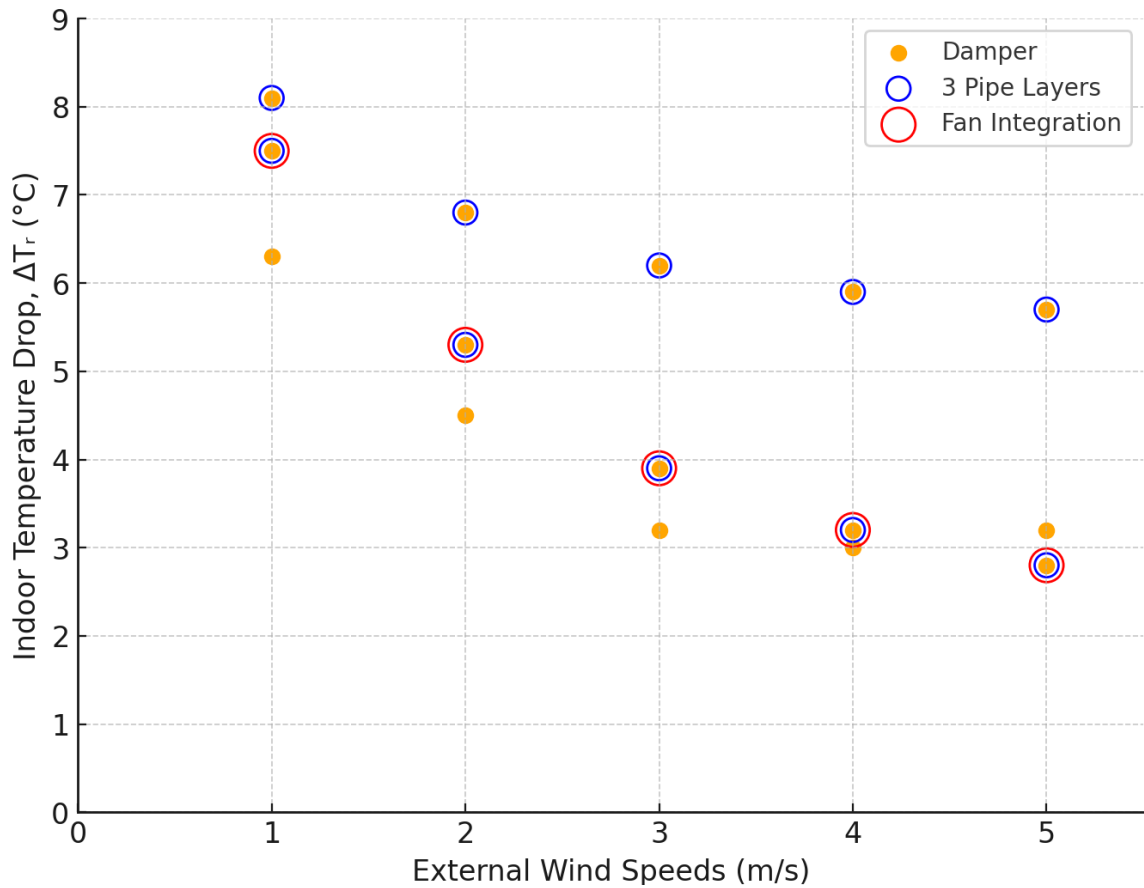
Figure 132 – Collective results of indoor temperature drop for each augmentation

Furthermore, it is observed that the combination of damper and three-layered pipes achieves a temperature reduction consistently exceeding 5°C even under high external wind speeds of 5m/s. Although the integration of fan affects the indoor cooling performance at higher wind speeds, it can be integrated using an automated control system to significantly enhance ventilation rates at lower external wind speeds. This ensures regulated thermal comfort with adequate natural ventilation and improved indoor cooling performance of above 7°C at wind speeds of up to 1m/s.

Chapter 6 - Conclusions and Future Scope

6.1 Introduction

As defined in Chapter 1, the overall aim of this research was to reduce energy consumption in buildings by first developing smart inspection methods, and then providing an energy efficient mechanism to integrate active cooling with passive ventilation to regulate thermal comfort. This chapter presents the conclusions from both qualitative (i.e. image fusion for building inspections) and quantitative (i.e. Peltier-driven cooling mechanism) studies in this research.

6.2 Research Conclusions

The conclusions are divided into five categories based on the research objectives defined in Chapter 1 Section 1.3. The research conclusions are followed by each of the restated objectives in quotations:

1. "Conduct a comprehensive review of existing works on building inspection techniques as well as active and passive cooling methods to identify gaps in the literature";

   A critical review of existing literature was conducted in this research in Chapter 2. The review addressed a total of 132 papers, which evaluated the following areas: (a) Building inspections, (b) 3D model reconstruction, (c) Heat recovery and cooling methods, and (d) Thermoelectric methods. The review highlighted the lack of computationally friendly and time-effective techniques to perform building inspections. The use of existing hefty hardware and software for thermal fusion prevents the inspection from being miniaturised for large-scale aerial automated fault detection. Secondly, several retrofit techniques exist that provide passive and active cooling solutions to reduce energy consumption and provide thermal comfort, such as evaporative cooling windcatchers, phase change materials, and earth-to-air heat exchangers. However, these technologies present cost and maintenance challenges. Wind towers provide passive cooling with natural

ventilation, however, their effectiveness is heavily influenced by environmental conditions such as wind speeds and directions, and high ambient temperatures. A research gap exists to provide environmentally friendly and adequate cooling in hot and dry climates alongside natural ventilation through wind towers.

2. "Develop an instantaneous, extrinsic method to superimpose thermal and visible images, aimed at reducing computational and hardware demands, and qualitatively evaluate its effectiveness in building inspection applications;"

A real-time image capture method was proposed in Chapter 3 that aligns the optical axes of thermal and visible cameras using a two-way mirror at 45° to pre-fuse the imagery extrinsically. The preliminary results showed pixel-level accuracy in image fusion without the need for image stitching or feature detection algorithms. Furthermore, an automatic fault detection framework was proposed that would use this technique to identify heat losses in buildings with a comprehensive context of the scene (façade) through the information from both thermal and visible imagery in real-time. This was qualitatively tested and showed promising results. Future scope using its miniaturised version includes drone-assisted unmanned fault detection and identification mechanism with a capability of monocular photogrammetry using the pre-aligned axes for a fused thermal 3D model reconstruction in real-time.

3. "Integrate and examine conductive cooling of heat pipes with TECs and assess their cooling potential through physical experiments;"

Chapter 3 proposes a Peltier-driven heat pipe cooling mechanism that aims to provide effective heat absorption from the heat pipes through conduction with the cold side of the TEC. In Chapter 4, Section 4.3 described the experimental methodology to evaluate the cooling performance of the TEC-driven conduction of heat pipes. The experiments explored the assessment of pipe surface temperature drops, steady state time, steady state temperatures against varying ambient temperatures, and the impact of input power and wind velocities on the cooling of the pipes. Chapter 5 details the results of these experiments, which highlights that

(a) the cooling performance improves with higher ambient temperatures due to the heat pipe thermal loop mechanism leveraging high temperature differentials, (b) at natural convection, the TECs can drop the temperatures of the pipes by 10°C, (c) an optimum COP (0.55) occurs at 6V of power to the TECs with a practical balance between a high degree of cooling (ΔT_p = 8°C) with minimal heat losses, and (d) wind causes higher convective heat transfer, which increases the steady state temperature of the pipes. Wind speeds above 1.2m/s showed steady heat transfer with the actively cooled pipes. Moreover, this study evaluated the optimum heat dissipation for maximum TEC efficiency. The heat sink's thermal resistance was 0.9°C/W for six TECs. The COP was measured with single and dual fan configurations at various voltages. It was noted that increasing voltage to 12V and adding a second fan resulted in a negligible improvement in cooling, with a gain of 0.5°C.

4. "Assemble a full-scale prototype of a TEC cooling unit to validate CFD analyses for Peltier-driven convective cooling under varying external wind speeds;"

A full-scale prototype of the TEC-driven heat pipe cooling mechanism was designed, assembled and modelled in CAD for CFD analyses. Using the results of forced convection on a single-pipe, a corresponding CFD model of a single-pipe was analysed and validated for the resulting pipe surface temperature. This allowed a full-scale model of 35 pipes to be tested and validated. The preliminary results showed a temperature drop of air 3.66°C at 50L/s of flow rate which validated the CFD model based on the full-scale prototype. The results indicated that lower velocities allow significantly higher heat transfer with enhanced cooling. A wind tower model was integrated to simulate real-world external wind into the inlet quadrant. The natural wind streams entering with a speed of 1.5m/s lowers down to 1.1m/s as it reaches the cooling unit, which produces a temperature drop of 4°C below the pipes.

5. "Investigate optimisation strategies through the proposed TEC-based cooling in passive wind towers to enhance cooling capabilities in hot climates, aiming to

achieve an indoor temperature reduction of at least 5°C below the ambient temperature;"

With the promising results and successful validation after completion of objective number 4, three augmentation techniques were proposed and examined to further enhance the cooling capability of the TEC-driven cooling mechanism, including:

i)   integration of damper before the cooled pipes, which helped in reducing the speed of the air while creating turbulence around the pipes that helped increase the residence time of air with the pipes. This approach also enabled louvre angle regulation (that can be automated) based on external wind speeds to optimise the heat transfer (temperature reductions) of the air through the pipes. This produced a significant improvement in cooling of air with temperature drops (from ambient) of up to 8°C below the pipes, which is equivalent to 6°C of cooling (ΔT_r) inside the room.

ii)   integration of an additional layer of pipe, which significantly enhanced the cooling. A combined integration of three layers of pipe and damper showed the highest indoor temperature drops of up to 8°C at 1m/s of wind speeds, which lowers to 5.7°C at 5m/s of external wind speeds. However, the additional layer reduced the air flow rate into the room, which is necessary for adequate ventilation.

iii) integration of axial fans, which restored the ventilation rates at low external wind speeds while maintaining high indoor temperature reductions when integrated in combination with the damper and three layers of pipe. The results with all three augmentations combined showed a drop in indoor temperatures of 7.5°C at 1m/s of external wind speeds.

6.3 Contribution to Knowledge and Accomplishments

Through the work conducted in this thesis, the following key contributions to knowledge were accomplished:

1. A novel thermal-visible image fusion technique was presented that pre-aligns the thermographic and visible camera imagery to eliminate the need for any additional hardware or post-processing, except a pre-defined initial calibration. This technique presents pixel-level accuracy (once calibrated) and eliminates parallax errors. This work qualitatively confirmed the viability and accuracy of this method.

2. An innovative integration of environmentally friendly thermoelectric coolers to conductively cool passive heat pipes for air cooling is an original study and promises massive scope in reducing HVAC energy demands in buildings. This solar power compatible Peltier-driven system benefits from an easy switch from cooling to heating mode by reversing the polarity of the current, which provides an all-season versatility.

3. With a low power consumption of under 600W, the wind tower integrated cooling mechanism can provide up to 8°C indoor temperature reduction with 474W of cooling capacity and fresh air ventilation to ensure thermal comfort with the recommended air quality. This presents scope to eliminate the need for conventional heaters/coolers in temperate regions or reduce HVAC demands in polar/tropical regions. Hence, this work delivered a promising and impactful prospect for reducing CO_2 gas emissions from buildings.

4. As a result of this PhD project, one international peer-reviewed paper and two conference papers have been published. Furthermore, a poster describing the image-fusion method was presented at the international conference (ICEC 2021) which led to the best poster award [224].

6.4 Future Work

In addition to the proposed augmentation techniques to enhance indoor cooling performances as explored and computationally evaluated in section 5.8, the following implementations are suggested for future research:

1. Thanks to the hardware and software simplicity of the thermal-fused image capture mechanism, the fusion module shall be miniaturised and installed on a

drone (UAV) that can handle the computation in real-time using a memory-efficient, low-power edge computing [225] using TinyML [226] to assist in a large-scale automated building inspection task.

2. Due to the round shape and smooth texture of heat pipes, heat transfer from ambient air was not fully utilised by the entire surface of the pipes. The convective cooling could be enhanced greatly through an integration of fins with the pipes.

3. Although warm air from the heat sink rises and exists through the exhaust quadrants, some of this warm air could be mixed with the inlet fresh air at the inlet quadrant influencing the cooling capability. An ideal system would implement exhaust channels for an effective dissipation of the hot air from the heat sink.

4. The inevitable high temperature at the hot side of the TEC is currently being dissipated through heat sinks. This excess heat, instead of being wasted, can be effectively recycled through a heat recovery unit to be utilised for other heating requirements within the building.

References

[1]   "AR5 Synthesis Report: Climate Change 2014 — IPCC." Accessed: Feb. 17, 2023. [Online]. Available: https://www.ipcc.ch/report/ar5/syr/

[2]   S. C. Doney, V. J. Fabry, R. A. Feely, and J. A. Kleypas, "Ocean acidification: the other CO2 problem," *Ann Rev Mar Sci*, vol. 1, pp. 169–192, 2009, doi: 10.1146/ANNUREV.MARINE.010908.163834.

[3]   N. G. M. L. US Department of Commerce, "Global Monitoring Laboratory - Carbon Cycle Greenhouse Gases".

[4]   P. Friedlingstein *et al.*, "Global Carbon Budget 2021," *Earth Syst Sci Data*, vol. 14, no. 4, pp. 1917–2005, Apr. 2022, doi: 10.5194/ESSD-14-1917-2022.

[5]   C. P. Morice *et al.*, "An updated assessment of near-surface temperature change from 1850: the HadCRUT5 dataset".

[6]   "Buildings – Analysis - IEA." Accessed: Feb. 10, 2023. [Online]. Available: https://www.iea.org/reports/buildings

[7]   "Why The Building Sector? – Architecture 2030." Accessed: Feb. 13, 2023. [Online]. Available: https://architecture2030.org/why-the-building-sector/

[8]   "Heating and cooling | Energy." Accessed: Apr. 21, 2020. [Online]. Available: https://ec.europa.eu/energy/topics/energy-efficiency/heating-and-cooling_en?redir=1

[9]   "Revised Energy Performance of Buildings Directive (EPBD) – Policies - IEA." Accessed: Feb. 22, 2023. [Online]. Available: https://www.iea.org/policies/3296-revised-energy-performance-of-buildings-directive-epbd

[10]   "Energy efficient buildings | Energy." Accessed: Sep. 24, 2019. [Online]. Available: https://ec.europa.eu/energy/topics/energy-efficiency/energy-efficient-buildings_en?redir=1

[11]   Y. Li, S. Kubicki, A. Guerriero, and Y. Rezgui, "Review of building energy performance certification schemes towards future improvement," *Renewable*

and Sustainable Energy Reviews, vol. 113, p. 109244, Oct. 2019, doi: 10.1016/j.rser.2019.109244.

[12]   "Roadmap for Energy-Efficient Buildings and Construction in ASEAN Timelines and actions towards net zero-carbon buildings and construction", Accessed: Feb. 10, 2023. [Online]. Available: www.iea.org/t&c/

[13]   "Space Cooling: Energy demand," 2017. [Online]. Available: www.citylab.com/work/2012/06/cities-might-not-exist-without-air-conditioning/2399/.

[14]   "Global net zero commitments." Accessed: Feb. 23, 2023. [Online]. Available: https://commonslibrary.parliament.uk/global-net-zero-commitments/

[15]   "Energy performance of buildings directive | Energy." Accessed: Apr. 21, 2020. [Online]. Available: https://ec.europa.eu/energy/topics/energy-efficiency/energy-efficient-buildings/energy-performance-buildings-directive_en?redir=1

[16]   K. O'Neill and D. Gibbs, "Sustainability transitions and policy dismantling: Zero carbon housing in the UK," *Geoforum*, vol. 108, pp. 119–129, Jan. 2020, doi: 10.1016/J.GEOFORUM.2019.11.011.

[17]   P. de Wilde, "Ten questions concerning building performance analysis," *Build Environ*, 2019, doi: 10.1016/j.buildenv.2019.02.019.

[18]   J. Alencastro, A. Fuertes, A. Fox, and P. De Wilde, "The impact of defects on energy performance of buildings: Quality management in social housing developments," in *Energy Procedia*, Elsevier Ltd, Feb. 2019, pp. 4357–4362. doi: 10.1016/j.egypro.2019.01.784.

[19]   B. F. Spencer, V. Hoskere, and Y. Narazaki, "Advances in Computer Vision-Based Civil Infrastructure Inspection and Monitoring," *Engineering*, vol. 5, no. 2, pp. 199–222, Apr. 2019, doi: 10.1016/J.ENG.2018.11.030.

[20]   C. Koch, K. Georgieva, V. Kasireddy, B. Akinci, and P. Fieguth, "A review on computer vision based defect detection and condition assessment of concrete

and asphalt civil infrastructure," *Advanced Engineering Informatics*, vol. 29, no. 2, pp. 196–210, Apr. 2015, doi: 10.1016/J.AEI.2015.01.008.

[21]   C. Z. Dong and F. N. Catbas, "A review of computer vision–based structural health monitoring at local and global levels," *Struct Health Monit*, vol. 20, no. 2, pp. 692–743, Mar. 2021, doi: 10.1177/1475921720935585/ASSET/IMAGES/LARGE/10.1177_14759217209355 85-FIG2.JPEG.

[22]   A. Kirimtat and O. Krejcar, "A review of infrared thermography for the investigation of building envelopes: Advances and prospects," *Energy and Buildings*. 2018. doi: 10.1016/j.enbuild.2018.07.052.

[23]   "Infrared cameras for Building thermography." Accessed: Sep. 24, 2023. [Online]. Available: https://www.infratec.co.uk/thermography/industries-applications/building-thermography/

[24]   Y. Tan, S. Li, H. Liu, P. Chen, and Z. Zhou, "Automatic inspection data collection of building surface based on BIM and UAV," *Autom Constr*, vol. 131, p. 103881, Nov. 2021, doi: 10.1016/J.AUTCON.2021.103881.

[25]   K. Chen, G. Reichard, X. Xu, and A. Akanmu, "Automated crack segmentation in close-range building façade inspection images using deep learning techniques," *Journal of Building Engineering*, vol. 43, p. 102913, Nov. 2021, doi: 10.1016/J.JOBE.2021.102913.

[26]   H. T. Mustafa, J. Yang, H. Mustafa, and M. Zareapoor, "Infrared and visible image fusion based on dilated residual attention network," *Optik (Stuttg)*, vol. 224, p. 165409, Dec. 2020, doi: 10.1016/J.IJLEO.2020.165409.

[27]   M. H. Shariq and B. R. Hughes, "Revolutionising building inspection techniques to meet large-scale energy demands: A review of the state-of-the-art," *Renewable and Sustainable Energy Reviews*, vol. 130, p. 109979, Sep. 2020, doi: 10.1016/J.RSER.2020.109979.

[28]   N. Asim *et al.*, "Sustainability of Heating, Ventilation and Air-Conditioning (HVAC) Systems in Buildings—An Overview," *International Journal of Environmental*

Research and Public Health 2022, Vol. 19, Page 1016, vol. 19, no. 2, p. 1016, Jan. 2022, doi: 10.3390/IJERPH19021016.

[29]   M. González-Torres, L. Pérez-Lombard, J. F. Coronel, I. R. Maestre, and D. Yan, "A review on buildings energy information: Trends, end-uses, fuels and drivers," *Energy Reports*, vol. 8, pp. 626–637, Nov. 2022, doi: 10.1016/J.EGYR.2021.11.280.

[30]   F. Jomehzadeh *et al.*, "A review on windcatcher for passive cooling and natural ventilation in buildings, Part 1: Indoor air quality and thermal comfort assessment," *Renewable and Sustainable Energy Reviews*, vol. 70, pp. 736–756, Apr. 2017, doi: 10.1016/J.RSER.2016.11.254.

[31]   "ASHRAE Releases Updated Versions of Standards 62.1 and 62.2." Accessed: Sep. 21, 2023. [Online]. Available: https://www.ashrae.org/about/news/2019/ashrae-releases-updated-versions-of-standard-62-1-and-62-2

[32]   "Indoor Air Quality (TG 12/2022)." Accessed: Sep. 22, 2023. [Online]. Available: https://www.bsria.com/uk/product/n5XVpr/indoor_air_quality_tg_122022__a15d25e1/

[33]   "Guide B2: Ventilation and ductwork (2016) | CIBSE." Accessed: Sep. 22, 2023. [Online]. Available: https://www.cibse.org/knowledge-research/knowledge-portal/guide-b2-ventilation-and-ductwork-2016

[34]   M. Liu, C. Jimenez-Bescos, and J. K. Calautit, "Passive heat recovery wind tower: Assessing the overheating risk in summertime and ventilation heat loss reduction in wintertime," *Sustainable Energy Technologies and Assessments*, vol. 58, p. 103310, Aug. 2023, doi: 10.1016/J.SETA.2023.103310.

[35]   J. K. Calautit, D. O'Connor, and B. R. Hughes, "Determining the optimum spacing and arrangement for commercial wind towers for ventilation performance," *Build Environ*, vol. 82, pp. 274–287, Dec. 2014, doi: 10.1016/J.BUILDENV.2014.08.024.

[36] H. Montazeri and R. Azizian, "Experimental study on natural ventilation performance of one-sided wind catcher," *Build Environ*, vol. 43, no. 12, pp. 2193–2202, Dec. 2008, doi: 10.1016/J.BUILDENV.2008.01.005.

[37] H. Mahon, D. Friedrich, and B. Hughes, "Wind tunnel test and numerical study of a multi-sided wind tower with horizontal heat pipes," *Energy*, vol. 260, p. 125118, Dec. 2022, doi: 10.1016/J.ENERGY.2022.125118.

[38] M. Liu, C. Jimenez-Bescos, and J. Calautit, "CFD investigation of a natural ventilation wind tower system with solid tube banks heat recovery for mild-cold climate," *Journal of Building Engineering*, vol. 45, p. 103570, Jan. 2022, doi: 10.1016/J.JOBE.2021.103570.

[39] J. K. Calautit, D. O'Connor, and B. R. Hughes, "A natural ventilation wind tower with heat pipe heat recovery for cold climates," *Renew Energy*, vol. 87, pp. 1088–1104, Mar. 2016, doi: 10.1016/J.RENENE.2015.08.026.

[40] A. A. Bagasi, J. K. Calautit, and A. S. Karban, "Evaluation of the Integration of the Traditional Architectural Element Mashrabiya into the Ventilation Strategy for Buildings in Hot Climates," *Energies 2021, Vol. 14, Page 530*, vol. 14, no. 3, p. 530, Jan. 2021, doi: 10.3390/EN14030530.

[41] R. Aridi, J. Faraj, S. Ali, T. Lemenand, and M. Khaled, "Thermoelectric Power Generators: State-of-the-Art, Heat Recovery Method, and Challenges," *Electricity 2021, Vol. 2, Pages 359-386*, vol. 2, no. 3, pp. 359–386, Sep. 2021, doi: 10.3390/ELECTRICITY2030022.

[42] J. Gołębiowska and M. K. Widomski, "Numerical Assessment of the Experimental Thermoelectric Cooling System Effectiveness," *Journal of Ecological Engineering*, vol. 23, no. 12, pp. 99–110, Dec. 2022, doi: 10.12911/22998993/154845.

[43] M. Fox, D. Coley, S. Goodhew, and P. De Wilde, "Thermography methodologies for detecting energy related building defects," *Renewable and Sustainable Energy Reviews*. 2014. doi: 10.1016/j.rser.2014.07.188.

[44] S. Lagüela, J. Armesto, P. Arias, and J. Herráez, "Automation of thermographic 3D modelling through image fusion and image matching techniques," *Autom Constr*, 2012, doi: 10.1016/j.autcon.2012.05.011.

[45] M. Fox, S. Goodhew, and P. De Wilde, "Building defect detection: External versus internal thermography," *Build Environ*, 2016, doi: 10.1016/j.buildenv.2016.06.011.

[46] E. Barreira, R. M. S. F. Almeida, and M. Moreira, "An infrared thermography passive approach to assess the effect of leakage points in buildings," *Energy Build*, 2017, doi: 10.1016/j.enbuild.2017.02.009.

[47] W. Cai, X. Wen, S. Wang, and L. Wang, "A real-time detection method of building energy efficiency based on image processing," *J Vis Commun Image Represent*, 2019, doi: 10.1016/j.jvcir.2019.02.032.

[48] A. M. Paterson, G. R. Dowling, and D. A. Chamberlain, "Building inspection: Can computer vision help?," *Autom Constr*, 1997, doi: 10.1016/S0926-5805(97)00031-9.

[49] B. F. Spencer, V. Hoskere, and Y. Narazaki, "Advances in Computer Vision-Based Civil Infrastructure Inspection and Monitoring," *Engineering*. 2019. doi: 10.1016/j.eng.2018.11.030.

[50] C. Xu, J. Xie, G. Chen, and W. Huang, "An infrared thermal image processing framework based on superpixel algorithm to detect cracks on metal surface," *Infrared Phys Technol*, 2014, doi: 10.1016/j.infrared.2014.08.002.

[51] R. A. Galantucci and F. Fatiguso, "Advanced damage detection techniques in historical buildings using digital photogrammetry and 3D surface anlysis," *J Cult Herit*, 2019, doi: 10.1016/j.culher.2018.09.014.

[52] S. Gallardo-Saavedra, L. Hernández-Callejo, and O. Duque-Perez, "Technological review of the instrumentation used in aerial thermographic inspection of photovoltaic plants," *Renewable and Sustainable Energy Reviews*. 2018. doi: 10.1016/j.rser.2018.05.027.

[53]   J. L. Liardon, L. Hostettler, L. Zulliger, K. Kangur, N. S. Gujja Shaik, and D. A. Barry, "Lake imaging and monitoring aerial drone," *HardwareX*, 2018, doi: 10.1016/j.ohx.2017.10.003.

[54]   I. Gomes *et al.*, "What's a picture really worth? On the use of drone aerial imagery to estimate intertidal rocky shore mussel demographic parameters," *Estuar Coast Shelf Sci*, 2018, doi: 10.1016/j.ecss.2018.08.020.

[55]   D. R. A. Almeida *et al.*, "Monitoring the structure of forest restoration plantations with a drone-lidar system," *International Journal of Applied Earth Observation and Geoinformation*, 2019, doi: 10.1016/j.jag.2019.03.014.

[56]   D. Zorbas, L. Di Puglia Pugliese, T. Razafindralambo, and F. Guerriero, "Optimal drone placement and cost-efficient target coverage," *Journal of Network and Computer Applications*, 2016, doi: 10.1016/j.jnca.2016.08.009.

[57]   P. Urbanová, M. Jurda, T. Vojtíšek, and J. Krajsa, "Using drone-mounted cameras for on-site body documentation: 3D mapping and active survey," *Forensic Sci Int*, 2017, doi: 10.1016/j.forsciint.2017.10.027.

[58]   N. M. Kumar, K. Sudhakar, M. Samykano, and V. Jayaseelan, "On the technologies empowering drones for intelligent monitoring of solar photovoltaic power plants," in *Procedia Computer Science*, 2018. doi: 10.1016/j.procs.2018.07.087.

[59]   Y. Liu, X. Chen, J. Cheng, H. Peng, and Z. Wang, "Infrared and visible image fusion with convolutional neural networks," *https://doi.org/10.1142/S0219691318500182*, vol. 16, no. 3, May 2018, doi: 10.1142/S0219691318500182.

[60]   H. T. Mustafa, J. Yang, H. Mustafa, and M. Zareapoor, "Infrared and visible image fusion based on dilated residual attention network," *Optik (Stuttg)*, vol. 224, p. 165409, Dec. 2020, doi: 10.1016/J.IJLEO.2020.165409.

[61]   H. Li and X. J. Wu, "DenseFuse: A fusion approach to infrared and visible images," *IEEE Transactions on Image Processing*, vol. 28, no. 5, pp. 2614–2623, May 2019, doi: 10.1109/TIP.2018.2887342.

[62] J. Ma, Y. Ma, and C. Li, "Infrared and visible image fusion methods and applications: A survey," *Information Fusion*, vol. 45, pp. 153–178, Jan. 2019, doi: 10.1016/J.INFFUS.2018.02.004.

[63] N. Wang, X. Zhao, P. Zhao, Y. Zhang, Z. Zou, and J. Ou, "Automatic damage detection of historic masonry buildings based on mobile deep learning," *Autom Constr*, vol. 103, pp. 53–66, Jul. 2019, doi: 10.1016/j.autcon.2019.03.003.

[64] Y. Narazaki, V. Hoskere, T. A. Hoang, Y. Fujino, A. Sakurai, and B. F. Spencer, "Vision-based automated bridge component recognition with high-level scene consistency," *Computer-Aided Civil and Infrastructure Engineering*, 2019, doi: 10.1111/mice.12505.

[65] J. K. Chow *et al.*, "Automated defect inspection of concrete structures," *Autom Constr*, vol. 132, p. 103959, Dec. 2021, doi: 10.1016/J.AUTCON.2021.103959.

[66] K. Chen, G. Reichard, X. Xu, and A. Akanmu, "Automated crack segmentation in close-range building façade inspection images using deep learning techniques," *Journal of Building Engineering*, vol. 43, p. 102913, Nov. 2021, doi: 10.1016/J.JOBE.2021.102913.

[67] Y. Guo *et al.*, "Deep learning-based fault diagnosis of variable refrigerant flow air-conditioning system for building energy saving," *Appl Energy*, 2018, doi: 10.1016/j.apenergy.2018.05.075.

[68] Y. Zhao, T. Li, X. Zhang, and C. Zhang, "Artificial intelligence-based fault detection and diagnosis methods for building energy systems: Advantages, challenges and the future," *Renewable and Sustainable Energy Reviews*. 2019. doi: 10.1016/j.rser.2019.04.021.

[69] W. Kim and S. Katipamula, "A review of fault detection and diagnostics methods for building systems," *Sci Technol Built Environ*, 2018, doi: 10.1080/23744731.2017.1318008.

[70] E. Lucchi, "Applications of the infrared thermography in the energy audit of buildings: A review," *Renewable and Sustainable Energy Reviews*. 2018. doi: 10.1016/j.rser.2017.10.031.

[71]   C. Eschmann, C. M. Kuo, C. H. Kuo, and C. Boller, "Unmanned aircraft systems for remote building inspection and monitoring," in *Proceedings of the 6th European Workshop - Structural Health Monitoring 2012, EWSHM 2012*, 2012.

[72]   J. Seo, L. Duque, and J. Wacker, "Drone-enabled bridge inspection methodology and application," *Autom Constr*, 2018, doi: 10.1016/j.autcon.2018.06.006.

[73]   S. Yang, S. A. Scherer, X. Yi, and A. Zell, "Multi-camera visual SLAM for autonomous navigation of micro aerial vehicles," *Rob Auton Syst*, 2017, doi: 10.1016/j.robot.2017.03.018.

[74]   M. Gao, X. Xu, Y. Klinger, J. Van Der Woerd, and P. Tapponnier, "High-resolution mapping based on an Unmanned Aerial Vehicle (UAV) to capture paleoseismic offsets along the Altyn-Tagh fault, China," *Sci Rep*, 2017, doi: 10.1038/s41598-017-08119-2.

[75]   A. G. Entrop and A. Vasenev, "Infrared drones in the construction industry: Designing a protocol for building thermography procedures," in *Energy Procedia*, 2017. doi: 10.1016/j.egypro.2017.09.636.

[76]   E. Ciampa, L. De Vito, and M. R. Pecce, "Practical issues on the use of drones for construction inspections", doi: 10.1088/1742-6596/1249/1/012016.

[77]   K. Chen, G. Reichard, and X. Xu, "Opportunities for Applying Camera-Equipped Drones towards Performance Inspections of Building Facades".

[78]   P. Kilabanur *et al.*, "Use of UAVs for Technical Inspection of Buildings within the BRAIN Massive Inspection Platform," *IOP Conf Ser Mater Sci Eng*, vol. 471, no. 2, p. 022008, Feb. 2019, doi: 10.1088/1757-899X/471/2/022008.

[79]   J. Seo, L. Duque, and J. Wacker, "Drone-enabled bridge inspection methodology and application," *Autom Constr*, vol. 94, pp. 112–126, Oct. 2018, doi: 10.1016/J.AUTCON.2018.06.006.

[80]   A. Khaloo, D. Lattanzi, K. Cunningham, R. Dell'Andrea, and M. Riley, "Unmanned aerial vehicle inspection of the Placer River Trail Bridge through image-based 3D

modelling," *https://doi.org/10.1080/15732479.2017.1330891*, vol. 14, no. 1, pp. 124–136, Jan. 2017, doi: 10.1080/15732479.2017.1330891.

[81]   S. Jung *et al.*, "Toward Autonomous Bridge Inspection: A framework and experimental results," *16th International Conference on Ubiquitous Robots (UR)*, pp. 208–211, 2019.

[82]   N. Bolourian and A. Hammad, "LiDAR-equipped UAV path planning considering potential locations of defects for bridge inspection," *Autom Constr*, vol. 117, p. 103250, Sep. 2020, doi: 10.1016/J.AUTCON.2020.103250.

[83]   G. Morgenthal *et al.*, "Framework for automated UAS-based structural condition assessment of bridges," *Autom Constr*, vol. 97, pp. 77–95, Jan. 2019, doi: 10.1016/J.AUTCON.2018.10.006.

[84]   D. Ribeiro, R. Santos, A. Shibasaki, P. Montenegro, H. Carvalho, and R. Calçada, "Remote inspection of RC structures using unmanned aerial vehicles and heuristic image processing," *Eng Fail Anal*, vol. 117, p. 104813, Nov. 2020, doi: 10.1016/J.ENGFAILANAL.2020.104813.

[85]   A. Ellenberg, A. Kontsos, F. Moon, and I. Bartoli, "Bridge deck delamination identification from unmanned aerial vehicle infrared imagery," *Autom Constr*, vol. 72, pp. 155–165, Dec. 2016, doi: 10.1016/J.AUTCON.2016.08.024.

[86]   Y. Tan, G. Li, R. Cai, J. Ma, and M. Wang, "Mapping and modelling defect data from UAV captured images to BIM for building external wall inspection," *Autom Constr*, vol. 139, p. 104284, Jul. 2022, doi: 10.1016/J.AUTCON.2022.104284.

[87]   A. G. Entrop and A. Vasenev, "Infrared drones in the construction industry: designing a protocol for building thermography procedures," *Energy Procedia*, vol. 132, pp. 63–68, Oct. 2017, doi: 10.1016/J.EGYPRO.2017.09.636.

[88]   K. Gopalakrishnan, H. Gholami, A. Vidyadharan, A. Choudhary, and A. Agrawal, "CRACK DAMAGE DETECTION IN UNMANNED AERIAL VEHICLE IMAGES OF CIVIL INFRASTRUCTURE USING PRE-TRAINED DEEP LEARNING MODEL," *International Journal for Traffic and Transport Engineering*, vol. 8, no. 1, pp. 1–14, 2018, doi: 10.7708/ijtte.2018.8(1).01.

[89]   K. Chaiyasarn, A. Buatik, and S. Likitlersuang, "Concrete crack detection and 3D mapping by integrated convolutional neural networks architecture," *https://doi.org/10.1177/1369433220975574*, vol. 24, no. 7, pp. 1480–1494, Dec. 2020, doi: 10.1177/1369433220975574.

[90]   D. Liu, J. Chen, D. Hu, and Z. Zhang, "Dynamic BIM-augmented UAV safety inspection for water diversion project," *Comput Ind*, vol. 108, pp. 163–177, Jun. 2019, doi: 10.1016/J.COMPIND.2019.03.004.

[91]   C. Luo *et al.*, "Autonomous detection of damage to multiple steel surfaces from 360° panoramas using deep neural networks," *Computer-Aided Civil and Infrastructure Engineering*, vol. 36, no. 12, pp. 1585–1599, Dec. 2021, doi: 10.1111/MICE.12686.

[92]   B. Jalil, G. R. Leone, M. Martinelli, D. Moroni, M. A. Pascali, and A. Berton, "Fault Detection in Power Equipment via an Unmanned Aerial System Using Multi Modal Data," *Sensors 2019, Vol. 19, Page 3014*, vol. 19, no. 13, p. 3014, Jul. 2019, doi: 10.3390/S19133014.

[93]   H. Su, J. Ma, R. Zhou, and Z. Wen, "Detect and identify earth rock embankment leakage based on UAV visible and infrared images," *Infrared Phys Technol*, vol. 122, p. 104105, May 2022, doi: 10.1016/J.INFRARED.2022.104105.

[94]   T. Rakha and A. Gorodetsky, "Review of Unmanned Aerial System (UAS) applications in the built environment: Towards automated building inspection procedures using drones," *Automation in Construction*. 2018. doi: 10.1016/j.autcon.2018.05.002.

[95]   T. L. Garwood, B. R. Hughes, D. O'Connor, J. K. Calautit, M. R. Oates, and T. Hodgson, "A framework for producing gbXML building geometry from Point Clouds for accurate and efficient Building Energy Modelling," *Appl Energy*, 2018, doi: 10.1016/j.apenergy.2018.04.046.

[96]   H. Son, S. Lee, and C. Kim, "Automated 3D Model Reconstruction to Support Energy-efficiency," in *Procedia Engineering*, 2016. doi: 10.1016/j.proeng.2016.04.046.

[97] S. Ochmann, R. Vock, R. Wessel, and R. Klein, "Automatic reconstruction of parametric building models from indoor point clouds," *Computers and Graphics (Pergamon)*, 2016, doi: 10.1016/j.cag.2015.07.008.

[98] S. Ochmann, R. Vock, and R. Klein, "Automatic reconstruction of fully volumetric 3D building models from oriented point clouds," *ISPRS Journal of Photogrammetry and Remote Sensing*, 2019, doi: 10.1016/j.isprsjprs.2019.03.017.

[99] Z. Song, S. Tang, F. Gu, C. Shi, and J. Feng, "DOE-based structured-light method for accurate 3D sensing," *Opt Lasers Eng*, 2019, doi: 10.1016/j.optlaseng.2019.02.009.

[100] C. Park, P. Moghadam, S. Kim, A. Elfes, C. Fookes, and S. Sridharan, "Elastic LiDAR Fusion: Dense Map-Centric Continuous-Time SLAM," in *Proceedings - IEEE International Conference on Robotics and Automation*, 2018. doi: 10.1109/ICRA.2018.8462915.

[101] H. El-Din Fawzy, "3D laser scanning and close-range photogrammetry for buildings documentation: A hybrid technique towards a better accuracy," *Alexandria Engineering Journal*, vol. 58, no. 4, pp. 1191–1204, Dec. 2019, doi: 10.1016/j.aej.2019.10.003.

[102] P. Tang, S. Vick, J. Chen, and S. German Paal, "Surveying, Geomatics, and 3D Reconstruction," in *Infrastructure Computer Vision*, Elsevier, 2020, pp. 13–64. doi: 10.1016/b978-0-12-815503-5.00002-4.

[103] I. Colomina and P. Molina, "Unmanned aerial systems for photogrammetry and remote sensing: A review," *ISPRS Journal of Photogrammetry and Remote Sensing*. 2014. doi: 10.1016/j.isprsjprs.2014.02.013.

[104] J. Kaufman, A. E. W. Rennie, and M. Clement, "Single camera photogrammetry for reverse engineering and fabrication of ancient and modern artifacts," in *Procedia CIRP*, 2015. doi: 10.1016/j.procir.2015.01.073.

[105] M. Pizzoli, C. Forster, and D. Scaramuzza, "REMODE: Probabilistic, monocular dense reconstruction in real time," in *Proceedings - IEEE International*

Conference on Robotics and Automation, 2014. doi: 10.1109/ICRA.2014.6907233.

[106] "REMODE: Probabilistic, Monocular Dense Reconstruction in Real Time - YouTube." Accessed: Apr. 21, 2020. [Online]. Available: https://www.youtube.com/watch?v=QTKd5UWCG0Q

[107] T. Schöps, T. Sattler, C. Häne, and M. Pollefeys, "Large-scale outdoor 3D reconstruction on a mobile device," *Computer Vision and Image Understanding*, 2017, doi: 10.1016/j.cviu.2016.09.007.

[108] O. Krutikova, A. Sisojevs, and M. Kovalovs, "Creation of a Depth Map from Stereo Images of Faces for 3D Model Reconstruction," in *Procedia Computer Science*, 2016. doi: 10.1016/j.procs.2017.01.159.

[109] K. Fu, Y. Xie, H. Jing, and J. Zhu, "Fast spatial–temporal stereo matching for 3D face reconstruction under speckle pattern projection," *Image Vis Comput*, 2019, doi: 10.1016/j.imavis.2019.02.007.

[110] T. Pire, T. Fischer, G. Castro, P. De Cristóforis, J. Civera, and J. Jacobo Berlles, "S-PTAM: Stereo Parallel Tracking and Mapping," *Rob Auton Syst*, 2017, doi: 10.1016/j.robot.2017.03.019.

[111] R. A. Hamzah, A. F. Kadmin, M. S. Hamid, S. F. A. Ghani, and H. Ibrahim, "Improvement of stereo matching algorithm for 3D surface reconstruction," *Signal Process Image Commun*, 2018, doi: 10.1016/j.image.2018.04.001.

[112] S. Hadfield, K. Lebeda, and R. Bowden, "Stereo reconstruction using top-down cues," *Computer Vision and Image Understanding*, 2017, doi: 10.1016/j.cviu.2016.08.001.

[113] N. Namitha, S. M. Vaitheeswaran, V. K. Jayasree, and M. K. Bharat, "Point Cloud Mapping Measurements Using Kinect RGB-D Sensor and Kinect Fusion for Visual Odometry," in *Procedia Computer Science*, 2016. doi: 10.1016/j.procs.2016.06.044.

[114] "Kinect XBOX." Accessed: Apr. 21, 2020. [Online]. Available: https://www.xbox.com/en-US/kinect

[115] Z. Zhang, "Microsoft kinect sensor and its effect," *IEEE Multimedia*. 2012. doi: 10.1109/MMUL.2012.24.

[116] D. M. Córdova-Esparza, J. R. Terven, H. Jiménez-Hernández, and A. M. Herrera-Navarro, "A multiple camera calibration and point cloud fusion tool for Kinect V2," *Sci Comput Program*, 2017, doi: 10.1016/j.scico.2016.11.004.

[117] Y. Liu, M. Zhu, and H. Zhang, "Processed RGB-D Slam Using Open-Source Software," in *Proceedings - 2017 IEEE International Conference on Computational Science and Engineering and IEEE/IFIP International Conference on Embedded and Ubiquitous Computing, CSE and EUC 2017*, 2017. doi: 10.1109/CSE-EUC.2017.115.

[118] M. Zollhöfer *et al.*, "State of the art on 3D reconstruction with RGB-D cameras," *Computer Graphics Forum*, 2018, doi: 10.1111/cgf.13386.

[119] O. Guclu and A. B. Can, "k-SLAM: A fast RGB-D SLAM approach for large indoor environments," *Computer Vision and Image Understanding*, 2019, doi: 10.1016/j.cviu.2019.04.005.

[120] A. Jalandoni, I. Domingo, and P. S. C. Taçon, "Testing the value of low-cost Structure-from-Motion (SfM) photogrammetry for metric and visual analysis of rock art," *J Archaeol Sci Rep*, vol. 17, pp. 605–616, Feb. 2018, doi: 10.1016/j.jasrep.2017.12.020.

[121] F. Bandini *et al.*, "Unmanned Aerial System (UAS) observations of water surface elevation in a small stream: Comparison of radar altimetry, LIDAR and photogrammetry techniques," *Remote Sens Environ*, vol. 237, p. 111487, Feb. 2020, doi: 10.1016/j.rse.2019.111487.

[122] F. Dornaika and R. Chung, "Mosaicking images with parallax," *Signal Process Image Commun*, vol. 19, no. 8, pp. 771–786, Sep. 2004, doi: 10.1016/j.image.2004.06.008.

[123] S. Lagüela, L. Díaz-Vilariño, J. Armesto, and P. Arias, "Thermographic 3D models as the foundation for Building Information Models," 2012. doi: 10.21611/qirt.2012.180.

[124] S. Lagüela, L. Díaz-Vilariño, J. Martínez, and J. Armesto, "Automatic thermographic and RGB texture of as-built BIM for energy rehabilitation purposes," *Autom Constr*, 2013, doi: 10.1016/j.autcon.2012.12.013.

[125] C. Wang, Y. K. Cho, and M. Gai, "As-Is 3D thermal modeling for existing building envelopes using a hybrid LIDAR system," in *Journal of Computing in Civil Engineering*, 2013. doi: 10.1061/(ASCE)CP.1943-5487.0000273.

[126] D. González-Aguilera, P. Rodriguez-Gonzalvez, J. Armesto, and S. Lagüela, "Novel approach to 3D thermography and energy efficiency evaluation," *Energy Build*, 2012, doi: 10.1016/j.enbuild.2012.07.023.

[127] L. López-Fernández, S. Lagüela, D. González-Aguilera, and H. Lorenzo, "Thermographic and mobile indoor mapping for the computation of energy losses in buildings," *Indoor and Built Environment*, 2017, doi: 10.1177/1420326X16638912.

[128] M. Solla and B. Riveiro, *Non-Destructive Techniques for the Evaluation of Structures and Infrastructure*. 2016. doi: 10.1201/b19024.

[129] D. González-Aguilera, S. Lagüela, P. Rodríguez-Gonzálvez, and D. Hernández-López, "Image-based thermographic modeling for assessing energy efficiency of buildings façades," *Energy Build*, 2013, doi: 10.1016/j.enbuild.2013.05.040.

[130] Y. Cao *et al.*, "Depth and thermal sensor fusion to enhance 3D thermographic reconstruction," *Opt Express*, 2018, doi: 10.1364/oe.26.008179.

[131] A. Ordonez Muller and A. Kroll, "Generating High Fidelity 3-D Thermograms with a Handheld Real-Time Thermal Imaging System," *IEEE Sens J*, 2017, doi: 10.1109/JSEN.2016.2621166.

[132] S. Sels *et al.*, "A CAD matching method for 3D thermography of complex objects," *Infrared Physics and Technology*. 2019. doi: 10.1016/j.infrared.2019.04.014.

[133] S. Vidas and P. Moghadam, "HeatWave: A handheld 3D thermography system for energy auditing," *Energy Build*, 2013, doi: 10.1016/j.enbuild.2013.07.030.

[134] H. González-Jorge, S. Lagüela, P. Krelling, J. Armesto, and J. Martínez-Sánchez, "Single image rectification of thermal images for geometric studies in façade inspections," *Infrared Phys Technol*, 2012, doi: 10.1016/j.infrared.2012.05.003.

[135] A. R. Dehghani-Sanij, M. Soltani, and K. Raahemifar, "A new design of wind tower for passive ventilation in buildings to reduce energy consumption in windy regions," *Renewable and Sustainable Energy Reviews*, vol. 42, pp. 182–195, Feb. 2015, doi: 10.1016/J.RSER.2014.10.018.

[136] M. Liu, C. Jimenez-Bescos, and J. K. Calautit, "Passive heat recovery wind tower: Assessing the overheating risk in summertime and ventilation heat loss reduction in wintertime," *Sustainable Energy Technologies and Assessments*, vol. 58, p. 103310, Aug. 2023, doi: 10.1016/J.SETA.2023.103310.

[137] M. N. Bahadori and A. Dehghani-Sanij, *Wind Towers: Architecture, Climate and Sustainability*. Springer, 2014.

[138] D. O'Connor, J. K. Calautit, and B. R. Hughes, "A study of passive ventilation integrated with heat recovery," *Energy Build*, vol. 82, pp. 799–811, Oct. 2014, doi: 10.1016/J.ENBUILD.2014.05.050.

[139] R. M. Kassir, "Passive downdraught evaporative cooling wind-towers: A case study using simulation with field-corroborated results," *Building Services Engineering Research and Technology*, vol. 37, no. 1, pp. 103–120, Jan. 2016, doi: 10.1177/0143624415603281/ASSET/IMAGES/LARGE/10.1177_01436244156032 81-FIG9.JPEG.

[140] M. Grosso and M. Ahmadi, "Potential cooling energy reduction by a one-channel wind tower: case study modelling in south-Mediterranean climate,"

International Journal of Ventilation, vol. 15, no. 3–4, pp. 267–287, Oct. 2016, doi: 10.1080/14733315.2016.1214397.

[141] B. R. Hughes and S. A. A. A. Ghani, "Investigation of a windvent passive ventilation device against current fresh air supply recommendations," *Energy Build*, vol. 40, no. 9, pp. 1651–1659, Jan. 2008, doi: 10.1016/J.ENBUILD.2008.02.024.

[142] B. R. Hughes and S. A. A. A. Ghani, "A numerical investigation into the effect of Windvent louvre external angle on passive stack ventilation performance," *Build Environ*, vol. 45, no. 4, pp. 1025–1036, Apr. 2010, doi: 10.1016/J.BUILDENV.2009.10.010.

[143] B. R. Hughes and S. A. A. Abdul Ghani, "A numerical investigation into the effect of windvent dampers on operating conditions," *Build Environ*, vol. 44, no. 2, pp. 237–248, Feb. 2009, doi: 10.1016/J.BUILDENV.2008.02.012.

[144] A. A. Dehghan, M. K. Esfeh, and M. D. Manshadi, "Natural ventilation characteristics of one-sided wind catchers: experimental and analytical evaluation," *Energy Build*, vol. 61, pp. 366–377, Jun. 2013, doi: 10.1016/J.ENBUILD.2013.02.048.

[145] S. M. Hosseinnia, H. Saffari, and M. A. Abdous, "Effects of different internal designs of traditional wind towers on their thermal behavior," *Energy Build*, vol. 62, pp. 51–58, Jul. 2013, doi: 10.1016/J.ENBUILD.2012.10.058.

[146] M. V. Cruz-Salas, J. A. Castillo, and G. Huelsz, "Effect of windexchanger duct cross-section area and geometry on the room airflow distribution," *Journal of Wind Engineering and Industrial Aerodynamics*, vol. 179, pp. 514–523, Aug. 2018, doi: 10.1016/J.JWEIA.2018.06.022.

[147] M. Alsailani, H. Montazeri, and A. Rezaeiha, "Towards optimal aerodynamic design of wind catchers: Impact of geometrical characteristics," *Renew Energy*, vol. 168, pp. 1344–1363, May 2021, doi: 10.1016/J.RENENE.2020.12.053.

[148] J. K. Calautit, D. O'Connor, D. SNM. Nasir, P. Sofotasiou, B. Hughes, and S. Shahzad, "Numerical Analysis of a Wind Catcher Assisted Passive Cooling Technology," Jun. 2015, doi: 10.15445/02012015.27.

[149] H. N. Chaudhry, B. R. Hughes, and S. A. Ghani, "A review of heat pipe systems for heat recovery and renewable energy applications," *Renewable and Sustainable Energy Reviews*, vol. 16, no. 4, pp. 2249–2259, May 2012, doi: 10.1016/J.RSER.2012.01.038.

[150] L. L. Vasiliev, "Heat pipes in modern heat exchangers," *Appl Therm Eng*, vol. 25, no. 1, pp. 1–19, Jan. 2005, doi: 10.1016/J.APPLTHERMALENG.2003.12.004.

[151] H. N. Chaudhry, J. K. Calautit, and B. R. Hughes, "Computational analysis of a wind tower assisted passive cooling technology for the built environment," *Journal of Building Engineering*, vol. 1, pp. 63–71, Mar. 2015, doi: 10.1016/J.JOBE.2015.03.004.

[152] J. K. Calautit, B. R. Hughes, and S. S. Shahzad, "CFD and wind tunnel study of the performance of a uni-directional wind catcher with heat transfer devices," *Renew Energy*, vol. 83, pp. 85–99, Nov. 2015, doi: 10.1016/J.RENENE.2015.04.005.

[153] B. R. Hughes, H. N. Chaudhry, and J. K. Calautit, "Passive energy recovery from natural ventilation air streams," *Appl Energy*, vol. 113, pp. 127–140, Jan. 2014, doi: 10.1016/J.APENERGY.2013.07.019.

[154] J. K. Calautit, D. O'Connor, and B. R. Hughes, "A natural ventilation wind tower with heat pipe heat recovery for cold climates," *Renew Energy*, vol. 87, pp. 1088–1104, Mar. 2016, doi: 10.1016/J.RENENE.2015.08.026.

[155] H. Mahon, D. Friedrich, and B. Hughes, "Wind tunnel test and numerical study of a multi-sided wind tower with horizontal heat pipes," *Energy*, vol. 260, p. 125118, Dec. 2022, doi: 10.1016/J.ENERGY.2022.125118.

[156] M. Liu, C. Jimenez-Bescos, and J. K. Calautit, "Passive heat recovery wind tower: Assessing the overheating risk in summertime and ventilation heat loss

reduction in wintertime," *Sustainable Energy Technologies and Assessments*, vol. 58, p. 103310, Aug. 2023, doi: 10.1016/J.SETA.2023.103310.

[157] Z. Shaikh and H. N. Chaudhry, "Energy Modelling and Indoor Air Quality Analysis of Cooling Systems for Buildings in Hot Climates," *Fluids 2018, Vol. 3, Page 77*, vol. 3, no. 4, p. 77, Oct. 2018, doi: 10.3390/FLUIDS3040077.

[158] A. Velashjerdi Farahani, J. Jokisalo, N. Korhonen, K. Jylhä, R. Kosonen, and S. Lestinen, "Performance assessment of ventilative and radiant cooling systems in office buildings during extreme weather conditions under a changing climate," *Journal of Building Engineering*, vol. 57, p. 104951, Oct. 2022, doi: 10.1016/J.JOBE.2022.104951.

[159] T. Ahmed, P. Kumar, and L. Mottet, "Natural ventilation in warm climates: The challenges of thermal comfort, heatwave resilience and indoor air quality," *Renewable and Sustainable Energy Reviews*, vol. 138, p. 110669, Mar. 2021, doi: 10.1016/J.RSER.2020.110669.

[160] M. Ghoulem, K. El Moueddeb, E. Nehdi, F. Zhong, and J. Calautit, "Analysis of passive downdraught evaporative cooling windcatcher for greenhouses in hot climatic conditions: Parametric study and impact of neighbouring structures," *Biosyst Eng*, vol. 197, pp. 105–121, Sep. 2020, doi: 10.1016/J.BIOSYSTEMSENG.2020.06.016.

[161] J. Foroozesh *et al.*, "CFD modeling of the building integrated with a novel design of a one-sided wind-catcher with water spray: Focus on thermal comfort," *Sustainable Energy Technologies and Assessments*, vol. 53, p. 102736, Oct. 2022, doi: 10.1016/J.SETA.2022.102736.

[162] S. Jafari and V. Kalantar, "Numerical simulation of natural ventilation with passive cooling by diagonal solar chimneys and windcatcher and water spray system in a hot and dry climate," *Energy Build*, vol. 256, p. 111714, Feb. 2022, doi: 10.1016/J.ENBUILD.2021.111714.

[163] N. Sakhri, A. Moussaoui, Y. Menni, M. Sadeghzadeh, and M. H. Ahmadi, "New passive thermal comfort system using three renewable energies: Wind catcher,

solar chimney and earth to air heat exchanger integrated to real-scale test room in arid region (Experimental study)," *Int J Energy Res*, vol. 45, no. 2, pp. 2177–2194, Feb. 2021, doi: 10.1002/ER.5911.

[164] M. Benhammou, B. Draoui, M. Zerrouki, and Y. Marif, "Performance analysis of an earth-to-air heat exchanger assisted by a wind tower for passive cooling of buildings in arid and hot climate," *Energy Convers Manag*, vol. 91, pp. 1–11, Feb. 2015, doi: 10.1016/J.ENCONMAN.2014.11.042.

[165] Y. Cai, X. Y. Huang, J. W. He, Y. X. Huang, and F. Y. Zhao, "Investigation of thermoelectric ventilated building envelope for simultaneously passive cooling and energy savings: Critical analysis and parametric characteristics," *Energy Build*, vol. 297, p. 113421, Oct. 2023, doi: 10.1016/J.ENBUILD.2023.113421.

[166] C. Li, X. Wen, W. Cai, H. Yu, and D. Liu, "Phase change material for passive cooling in building envelopes: A comprehensive review," *Journal of Building Engineering*, vol. 65, p. 105763, Apr. 2023, doi: 10.1016/J.JOBE.2022.105763.

[167] X. Kong, J. Li, M. Fan, W. Li, and H. Li, "Study on the thermal performance of a new double layer PCM trombe wall with multiple phase change points," *Solar Energy Materials and Solar Cells*, vol. 240, p. 111685, Jun. 2022, doi: 10.1016/J.SOLMAT.2022.111685.

[168] P. J. Ong *et al.*, "Integration of phase change material and thermal insulation material as a passive strategy for building cooling in the tropics," *Constr Build Mater*, vol. 386, p. 131583, Jul. 2023, doi: 10.1016/J.CONBUILDMAT.2023.131583.

[169] E. Zavrl, U. Tomc, M. El Mankibi, M. Dovjak, and U. Stritih, "Parametric study of an active-passive system for cooling application in buildings improved with free cooling for enhanced solidification," *Sustain Cities Soc*, vol. 99, p. 104960, Dec. 2023, doi: 10.1016/J.SCS.2023.104960.

[170] A. Castell and M. M. Farid, "Experimental validation of a methodology to assess PCM effectiveness in cooling building envelopes passively," *Energy Build*, vol. 81, pp. 59–71, Oct. 2014, doi: 10.1016/J.ENBUILD.2014.06.011.

179

[171] V. Vinayaka Ram, R. Singhal, and R. Parameshwaran, "Energy efficient pumpable cement concrete with nanomaterials embedded PCM for passive cooling application in buildings," *Mater Today Proc*, vol. 28, pp. 1054–1063, Jan. 2020, doi: 10.1016/J.MATPR.2019.12.356.

[172] C. Piselli, M. Prabhakar, A. de Gracia, M. Saffari, A. L. Pisello, and L. F. Cabeza, "Optimal control of natural ventilation as passive cooling strategy for improving the energy performance of building envelope with PCM integration," *Renew Energy*, vol. 162, pp. 171–181, Dec. 2020, doi: 10.1016/J.RENENE.2020.07.043.

[173] X. Sun, Y. Zhang, K. Xie, and M. A. Medina, "A parametric study on the thermal response of a building wall with a phase change material (PCM) layer for passive space cooling," *J Energy Storage*, vol. 47, p. 103548, Mar. 2022, doi: 10.1016/J.EST.2021.103548.

[174] H. Kitagawa, T. Asawa, T. Kubota, and A. R. Trihamdani, "Numerical simulation of radiant floor cooling systems using PCM for naturally ventilated buildings in a hot and humid climate," *Build Environ*, vol. 226, p. 109762, Dec. 2022, doi: 10.1016/J.BUILDENV.2022.109762.

[175] A. P. Haghighi, S. H. Pakdel, and A. Jafari, "A study of a wind catcher assisted adsorption cooling channel for natural cooling of a 2-storey building," *Energy*, vol. 102, pp. 118–138, May 2016, doi: 10.1016/J.ENERGY.2016.02.033.

[176] D. S. Noaman, S. A. Moneer, N. A. Megahed, and S. A. El-Ghafour, "Integration of active solar cooling technology into passively designed facade in hot climates," *Journal of Building Engineering*, vol. 56, p. 104658, Sep. 2022, doi: 10.1016/J.JOBE.2022.104658.

[177] M. Vaseghi, M. Fazel, and A. Ekhlassi, "Numerical investigation of solar radiation effect on passive and active heating and cooling system of a concept museum building," *Thermal Science and Engineering Progress*, vol. 19, p. 100582, Oct. 2020, doi: 10.1016/J.TSEP.2020.100582.

[178]   A. K. Shukla, A. K. Yadav, and R. Prakash, "Active and passive methods for cooling load reduction in a tropical building: A case study," *Energy Convers Manag*, vol. 293, p. 117490, Oct. 2023, doi: 10.1016/J.ENCONMAN.2023.117490.

[179]   E. Zavrl, U. Tomc, M. El Mankibi, M. Dovjak, and U. Stritih, "Parametric study of an active-passive system for cooling application in buildings improved with free cooling for enhanced solidification," *Sustain Cities Soc*, vol. 99, p. 104960, Dec. 2023, doi: 10.1016/J.SCS.2023.104960.

[180]   I. Oropeza-Perez and P. A. Østergaard, "Active and passive cooling methods for dwellings: A review," *Renewable and Sustainable Energy Reviews*, vol. 82, pp. 531–544, Feb. 2018, doi: 10.1016/J.RSER.2017.09.059.

[181]   M. Ebrahimi, "Thermoelectric generator," *Power Generation Technologies*, pp. 575–598, Jan. 2023, doi: 10.1016/B978-0-323-95370-2.00015-6.

[182]   M. Hong, S. Xu, M. Li, and Z. G. Chen, "Fundamentals of thermoelectrics," *Advanced Ceramics for Energy Storage, Thermoelectrics and Photonics*, pp. 259–281, Jan. 2023, doi: 10.1016/B978-0-323-90761-3.00007-3.

[183]   "Thermoelectric Handbook | The World Leader in Thermal Management Solutions." Accessed: Oct. 02, 2023. [Online]. Available: https://lairdthermal.com/thermal-technical-library/handbooks/thermoelectric-handbook

[184]   S. Wiriyasart, C. Hommalee, and P. Naphon, "Thermal cooling enhancement of dual processors computer with thermoelectric air cooler module," *Case Studies in Thermal Engineering*, vol. 14, p. 100445, Sep. 2019, doi: 10.1016/J.CSITE.2019.100445.

[185]   S. Al-Shehri and H. H. Saber, "Experimental investigation of using thermoelectric cooling for computer chips," *Journal of King Saud University - Engineering Sciences*, vol. 32, no. 5, pp. 321–329, Jul. 2020, doi: 10.1016/J.JKSUES.2019.03.009.

[186] Q. Luo, Y. Wang, and P. Zhang, "A novel thermoelectric air-conditioner for a truck cab," *2010 International Conference on Advances in Energy Engineering, ICAEE 2010*, pp. 178–181, 2010, doi: 10.1109/ICAEE.2010.5557585.

[187] H. S. Choi, S. Yun, and K. il Whang, "Development of a temperature-controlled car-seat system utilizing thermoelectric device," *Appl Therm Eng*, vol. 27, no. 17–18, pp. 2841–2849, Dec. 2007, doi: 10.1016/J.APPLTHERMALENG.2006.09.004.

[188] N. Alam, M. Salman Ali, S. Sajid, D. Sharma, and Z. Hasan, "Experimental investigation and analysis of cooling performance of solar thermoelectric refrigerator," *Solar Energy*, vol. 263, p. 111892, Oct. 2023, doi: 10.1016/J.SOLENER.2023.111892.

[189] D. H. Haynes and W. P. Monaghan, "Blood storage and transport in the field using a portable thermoelectric refrigerator: assessment of potential use.," *Mil Med*, vol. 149, no. 4, pp. 184–188, 1984, doi: 10.1093/milmed/149.4.184.

[190] J. Ding, W. Zhao, W. Jin, C. an Di, and D. Zhu, "Advanced Thermoelectric Materials for Flexible Cooling Application," *Adv Funct Mater*, vol. 31, no. 20, p. 2010695, May 2021, doi: 10.1002/adfm.202010695.

[191] M. W. Tian, F. Aldawi, A. E. Anqi, H. Moria, H. S. Dizaji, and M. Wae-hayee, "Cost-effective and performance analysis of thermoelectricity as a building cooling system; experimental case study based on a single TEC-12706 commercial module," *Case Studies in Thermal Engineering*, vol. 27, p. 101366, Oct. 2021, doi: 10.1016/J.CSITE.2021.101366.

[192] N. Parmar, N. Sharma, A. Arora, D. Goyal, and D. Buddhi, "Hybrid thermoelectric air cooler for building cooling," *Mater Today Proc*, vol. 69, pp. 309–316, Jan. 2022, doi: 10.1016/J.MATPR.2022.08.540.

[193] T. C. Cheng, C. H. Cheng, Z. Z. Huang, and G. C. Liao, "Development of an energy-saving module via combination of solar cells and thermoelectric coolers for green building applications," *Energy*, vol. 36, no. 1, pp. 133–140, Jan. 2011, doi: 10.1016/J.ENERGY.2010.10.061.

[194] S. Lv, Y. Ji, Z. Qian, W. He, Z. Hu, and M. Liu, "A novel strategy of enhancing sky radiative cooling by solar photovoltaic-thermoelectric cooler," *Energy*, vol. 219, p. 119625, Mar. 2021, doi: 10.1016/J.ENERGY.2020.119625.

[195] L. Shen, F. Xiao, H. Chen, and S. Wang, "Investigation of a novel thermoelectric radiant air-conditioning system," *Energy Build*, vol. 59, pp. 123–132, Apr. 2013, doi: 10.1016/J.ENBUILD.2012.12.041.

[196] X. Liu *et al.*, "Experimental performance evaluation of a convective thermoelectric building envelope for building heating and cooling," *Energy Build*, vol. 273, p. 112376, Oct. 2022, doi: 10.1016/J.ENBUILD.2022.112376.

[197] A. Zuazua-Ros, C. Martín-Gómez, E. Ibañez-Puy, M. Vidaurre-Arbizu, and Y. Gelbstein, "Investigation of the thermoelectric potential for heating, cooling and ventilation in buildings: Characterization options and applications," *Renew Energy*, vol. 131, pp. 229–239, Feb. 2019, doi: 10.1016/J.RENENE.2018.07.027.

[198] P. Aranguren, S. DiazDeGarayo, A. Martínez, M. Araiz, and D. Astrain, "Heat pipes thermal performance for a reversible thermoelectric cooler-heat pump for a nZEB," *Energy Build*, vol. 187, pp. 163–172, Mar. 2019, doi: 10.1016/J.ENBUILD.2019.01.039.

[199] Z. Liu, L. Zhang, G. Gong, H. Li, and G. Tang, "Review of solar thermoelectric cooling technologies for use in zero energy buildings," *Energy Build*, vol. 102, pp. 207–216, Sep. 2015, doi: 10.1016/J.ENBUILD.2015.05.029.

[200] S. K. Filippelli, M. A. Lefsky, and M. E. Rocca, "Comparison and integration of lidar and photogrammetric point clouds for mapping pre-fire forest structure," *Remote Sens Environ*, vol. 224, pp. 154–166, Apr. 2019, doi: 10.1016/j.rse.2019.01.029.

[201] A. López, J. M. Jurado, C. J. Ogayar, and F. R. Feito, "An optimized approach for generating dense thermal point clouds from UAV-imagery," *ISPRS Journal of Photogrammetry and Remote Sensing*, vol. 182, pp. 78–95, Dec. 2021, doi: 10.1016/J.ISPRSJPRS.2021.09.022.

[202] A. Ramón, A. Adán, and F. Javier Castilla, "Thermal point clouds of buildings: A review," *Energy Build*, vol. 274, p. 112425, Nov. 2022, doi: 10.1016/J.ENBUILD.2022.112425.

[203] J. Kaiser Calautit, B. Richard Hughes, and S. Abdul Ghani, "Integration and Application of Passive Cooling Within a Wind Tower," pp. 160–167, 2014, Accessed: Mar. 16, 2023. [Online]. Available: https://eprints.whiterose.ac.uk/

[204] S. H. Zaferani, M. W. Sams, R. Ghomashchi, and Z. G. Chen, "Thermoelectric coolers as thermal management systems for medical applications: Design, optimization, and advancement," *Nano Energy*, vol. 90, p. 106572, Dec. 2021, doi: 10.1016/J.NANOEN.2021.106572.

[205] D. Zhao and G. Tan, "A review of thermoelectric cooling: Materials, modeling and applications," *Appl Therm Eng*, vol. 66, no. 1–2, pp. 15–24, May 2014, doi: 10.1016/J.APPLTHERMALENG.2014.01.074.

[206] W. Chen, L. Cao, Z. Wu, and S. Huang, "A stereo range computation method using thermal infrared and visible cameras," *Infrared Phys Technol*, vol. 62, pp. 115–123, Jan. 2014, doi: 10.1016/j.infrared.2013.11.003.

[207] M. H. Shariq and B. R. Hughes, "Real-time pixel-level fusion of colour and thermal (RGB-T) imagery via extrinsic optical alignment: Scope for automating building inspections," *Proceedings of the International Conference on Evolving Cities*, Feb. 2021, doi: 10.55066/PROC-ICEC.2021.30.

[208] "FLIR T640 Thermal Imager Specifications," 2011, Accessed: Nov. 22, 2022. [Online]. Available: https://5.imimg.com/data5/MZ/LK/NB/SELLER-85638771/high-performance-thermal-imaging-camera.pdf

[209] "What is MSX®? | Teledyne FLIR." Accessed: Dec. 28, 2022. [Online]. Available: https://www.flir.co.uk/discover/professional-tools/what-is-msx/

[210] J. Canny, "A Computational Approach to Edge Detection," *IEEE Trans Pattern Anal Mach Intell*, vol. PAMI-8, no. 6, pp. 679–698, 1986, doi: 10.1109/TPAMI.1986.4767851.

[211] A. Sharma, "Structural Defects Network (SDNET) 2018 | Kaggle." Accessed: Dec. 26, 2022. [Online]. Available: https://www.kaggle.com/datasets/aniruddhsharma/structural-defects-network-concrete-crack-images

[212] A. Pandian, "Surface Crack Detection | Kaggle." Accessed: Dec. 26, 2022. [Online]. Available: https://www.kaggle.com/datasets/arunrk7/surface-crack-detection

[213] H. Xu, X. Su, Y. Wang, H. Cai, K. Cui, and X. Chen, "Automatic Bridge Crack Detection Using a Convolutional Neural Network," *Applied Sciences 2019, Vol. 9, Page 2867*, vol. 9, no. 14, p. 2867, Jul. 2019, doi: 10.3390/APP9142867.

[214] A. F. AbdelGawad, "Experimental Study of a Thermoelectric-(Vapor Compression) Hybrid Domestic Refrigerator," *Fourteenth International Conference of Fluid Dynamics (ICFD14), 2-3 April 2021, Fairmont Nile City Hotel, Cairo, Egypt*, Jan. 2021, Accessed: Dec. 07, 2023. [Online]. Available: https://www.academia.edu/48707863/Experimental_Study_of_a_Thermoelectric_Vapor_Compression_Hybrid_Domestic_Refrigerator

[215] R. A. Ibikunle, M. A. Akintunde, I. F. Titiladunayo, and A. A. Adeleke, "Estimation of coefficient of performance of thermoelectric cooler using a 30 W single-stage type," *International Review of Applied Sciences and Engineering*, vol. 13, no. 2, pp. 124–132, Sep. 2021, doi: 10.1556/1848.2021.00322.

[216] L. E. Bell, "Cooling, Heating, Generating Power, and Recovering Waste Heat with Thermoelectric Systems," *Science (1979)*, vol. 321, no. 5895, pp. 1457–1461, Sep. 2008, doi: 10.1126/SCIENCE.1158899.

[217] "Heat Sink Thermal Resistance Calculation Easy Explanation | ElectronicsBeliever." Accessed: Nov. 30, 2023. [Online]. Available: https://electronicsbeliever.com/heat-sink-thermal-resistance-calculation-easy-explanation/

[218] D. A. Reay, P. A. Kew, and R. J. McGlen, "Heat transfer and fluid flow theory," *Heat Pipes*, pp. 15–64, Jan. 2014, doi: 10.1016/B978-0-08-098266-3.00002-9.

[219] B. Zohuri, *Heat Pipe Design and Technology: A Practical Approach*, First Edition. CRC Press, 2011.

[220] "OS 3 | Control4." Accessed: Dec. 07, 2023. [Online]. Available: https://www.control4.com/os3

[221] "ESP32 Resources | Espressif Systems." Accessed: Dec. 07, 2023. [Online]. Available: https://www.espressif.com/en/products/socs/esp32/resources

[222] "BRE Group - World leaders in built environment research and development." Accessed: Dec. 20, 2023. [Online]. Available: https://bregroup.com/

[223] N. Wang *et al.*, "High Efficiency Thermoelectric Temperature Control System with Improved Proportional Integral Differential Algorithm Using Energy Feedback Technique," *IEEE Transactions on Industrial Electronics*, vol. 69, no. 5, pp. 5225–5234, May 2022, doi: 10.1109/TIE.2021.3082462.

[224] "ICEC 2021 Gallery | Evolving Cities." Accessed: Feb. 02, 2023. [Online]. Available: https://evolvingcities.org/icec-2021-gallery/#:~:text=Next-,Award%20winners

[225] S. Asutkar, C. Chalke, K. Shivgan, and S. Tallur, "TinyML-enabled edge implementation of transfer learning framework for domain generalization in machine fault diagnosis," *Expert Syst Appl*, vol. 213, p. 119016, Mar. 2023, doi: 10.1016/J.ESWA.2022.119016.

[226] P. P. Ray, "A review on TinyML: State-of-the-art and prospects," *Journal of King Saud University - Computer and Information Sciences*, vol. 34, no. 4, pp. 1595–1623, Apr. 2022, doi: 10.1016/J.JKSUCI.2021.11.019.

Appendix

Appendix A: Thermoelectric Cooling – Performance and Specifications

Appendix A-1: Multistage Thermoelectric Coolers

Multistage TECs are a stack of one or more Peltier modules. Each layer cools the hot side of the layer above it, allowing the top layer to reach a much lower temperature than a single TEC could achieve on its own. However, multistage TECs should be used only when a single stage module does not meet temperature control requirements.

Figure A1 depicts shows (1) the ΔT vs. Normalized Power input (Pin/Pmax) and (2) the ΔT vs. COP graphs to compare a single and multistage TEC performance. These charts help identify if the application demands for a cascaded TEC as they show the operational ΔT range of multiple stages. A dual-stage cascade should be considered between a ΔT of 40°C and 65°C, while a ΔT above 65°C may require a 3 or even higher stage module. As this research deals with ΔT of less than 40°C, a single stage module meets the requirements.
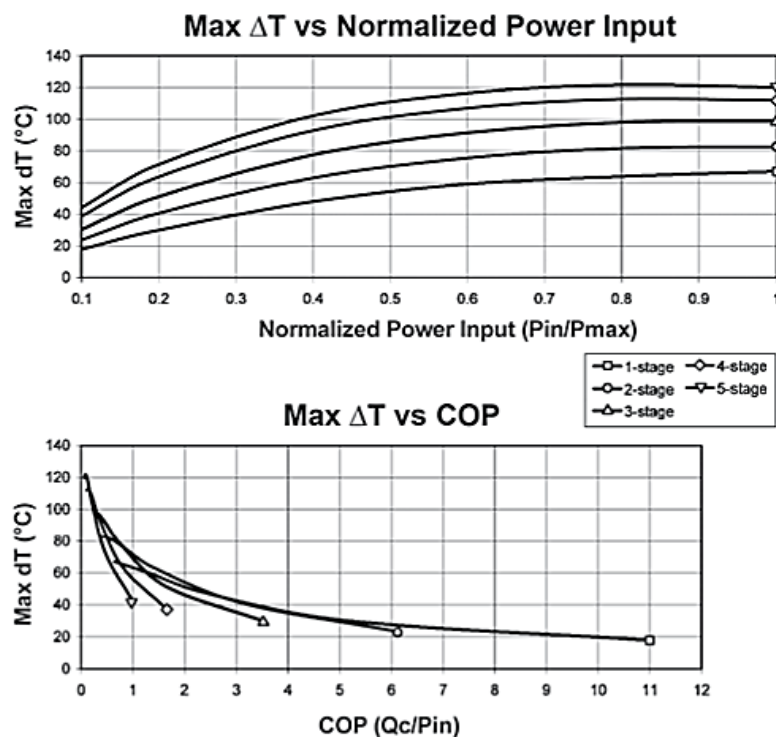

Figure A1 – Multistage Temperature Differential

Appendix A-2: Specifications and Performance Charts of TEC1-12706

Detailed specifications of TEC1-12706 Peltier Module are presented in Table A1.

Table A1 – Specifications of TEC1-12706 Peltier Module

PRODUCT SPEC.	DATA
Temp. of Hot Surface(℃)	30
△Tmax(°C)	⩾65
Qmax (W)	⩾51
Imax (A)	6
Vmax (VDC)	15,4
AC resistance（room temp.: 25℃）(ohm)	2.07±0.1
width and tolerance (mm)	40±0.5
length and tolerance (mm)	40±0.5
thickness and tolerance (mm)	3.7±0.1
flatness and tolerance (mm)	⩽0.05
parallelization and tolerance (mm)	⩽0.05
Solder(℃)	138

Charts for the cooling power and applied voltage against current are shown in Figure A2, while charts for the heating power and Coefficient of Performance (COP) vs. current (I) are shown in Figure A3.

The cooling power (Qc) refers to the amount of heat energy the TEC can remove from its cold side. The graph shows as the current increases the Qc increases; however, the cooling efficiency reduces with higher current as more internal heat is generated that opposes the effectiveness of cooling at higher power.

Whereas the heating power (Qh), which is also non-linear like Qc, increases at a higher rate with increasing current. This is due to the addition of internal heat produced with higher electrical power that helps the hot side get hotter more effectively.

The voltage and current are proportional and obeys Ohm's law from 0 to 6A of current for each temperature drop observed. This suggests that the resistance within the semiconductors of the TEC is stable with the increasing power.
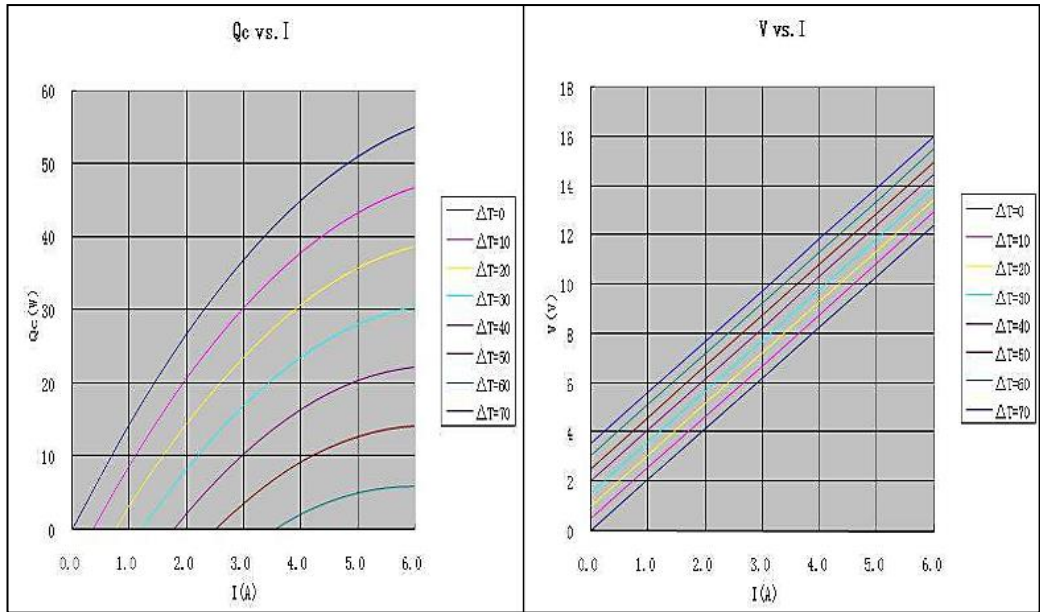
Figure A2 – Qc vs I and V vs I charts for TEC1-12706 Module
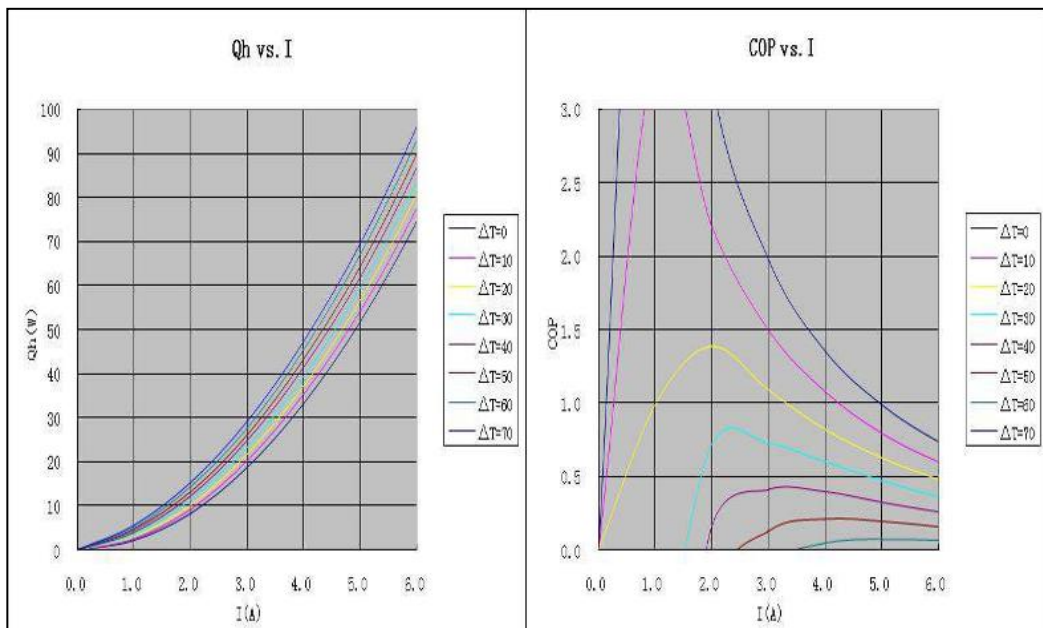
Figure A3 – Qh vs I and COP vs I charts for TEC1-12706

The Coefficient of Performance (COP) vs Current (I) shows that at lower currents, the TEC operates significantly more efficiently for lower temperature drops. The COP varies depending on the thermal loads (maximum temperature difference). In all scenarios, the COP declines after the peak with increasing current as the rate of electrical power (and its resulting heat produced) exceeds the rate of heat that can be moved.

Appendix B: Control Systems

Appendix B-1: Control4 and ESP32 Hardware

The Control4 hardware (as referred to in Section 3.3.4) used to test an integrated control system is called the Control4 C4-EA3. The device is shown in Figure B1 and its datasheet is presented Figure B2 [220]. Likewise, the Wroom-32 model was used to program ESP32 development board. The ESP32 microcontroller device and its specifications are shown in Figure B3. The specifications of ESP8266 board, another microcontroller device by Espressif, which is installed with the actuation of dampers and the cooling unit are similar to the specifications of the ESP32.
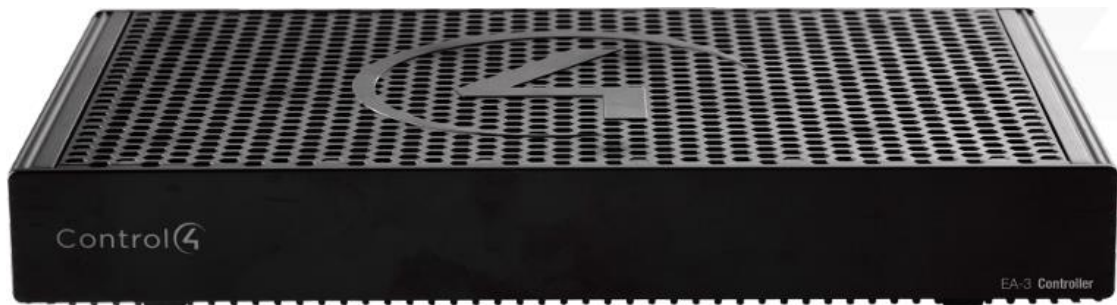
Figure B1 – Control4 EA3 Controller Device

Control	
IR out	6 IR out—5V 27mA max output, 1 IR blaster—front
IR capture	1 IR receiver—front; 20-60 kHz
Serial out	3 serial out (shared with IR out 1-3)
Contact	1 contact sensor—2V-30VDC input, 12VDC 125mA maximum output
Relay	1 relay—AC: 36V, 2A maximum voltage across relay; DC: 24V, 2A maximum voltage across relay
Power	
Power requirements	100-240 VAC, 60/50 Hz or PoE+
Power consumption	Max: 25W, 85 BTUs/hour; Idle: 13W, 44 BTUs/hour

Figure B2 – Datasheet of Control4 C4 EA3 [220]

FEATURES

- ESP32-WROOM-32 contains two low-power Xtensa® 32-bit LX6 microprocessors
- 448 KBytes ROM for booting and core functions
- 520 KBytes on-chip SRAM
- WiFi: 802.11 b/g/n/d/e/i/k/r (802.11n up to 150 Mbps)
- Bluetooth v4.2 BR/EDR and BLE specification
- Wi-Fi mode Station/softAP/SoftAP+station/P2P
- Security WPA/WPA2/WPA2-Enterprise/WPS

- IPv4, IPv6, SSL, TCP/UDP/HTTP/FTP/MQTT
- Interfaces: SD-card, UART, SPI, SDIO, I2C, LED PWM, Motor PWM, I2S , IR, GPIO, capacitive touch sensor, ADC, DAC, Hall sensor, temperature sensor
- Operating temperature -40 + 85C
- Operating voltate: 2.2-3.6V
- Consumption: 80 mA typ
- Dimensions: 18 mm x 20 mm x 3 mm

Figure B3 – ESP32 Wroom-32 device and specifications [221]

Appendix B-2: User Interface for Controls and Monitoring

Figure B4 show screenshots of the App created using Espressif's Rainmaker library [221] on ESP32 Wroom-32 development board. This Android app allows wireless control of dampers and TEC cooling, along with sensor data monitoring of indoor temperature and CO2 levels. This provides opportunity to add additional sensors (e.g. outdoor temperature, wind speeds and directions, etc.) to automate the cooling and damper angles to regulate the thermal comfort. However, such features are beyond the scope of this research.

Figure B4 - App screenshots showing sensor data and UI Controls

191

Appendix B-2: User Interface for Controls and Monitoring

Figure B4 show screenshots of the App created using Espressif's Rainmaker library [221] on ESP32 Wroom-32 development board. This Android app allows wireless control of dampers and TEC cooling, along with sensor data monitoring of indoor temperature and CO2 levels. This provides opportunity to add additional sensors (e.g. outdoor temperature, wind speeds and directions, etc.) to automate the cooling and damper angles to regulate the thermal comfort. However, such features are beyond the scope of this research.
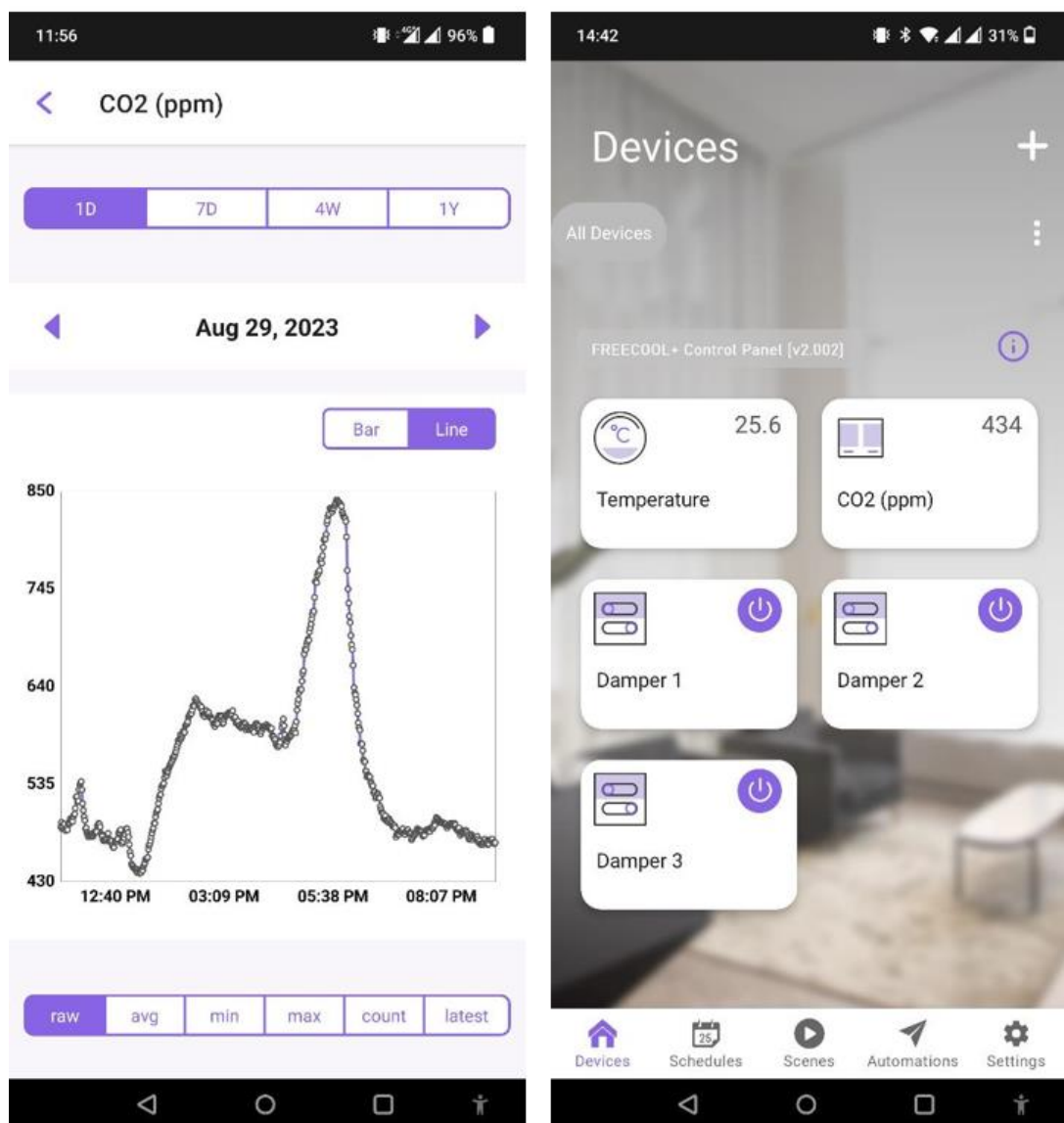

Figure B4 - App screenshots showing sensor data and UI Controls

Appendix C: Programming

Appendix C-1: OpenCV Image-Fusion Programming

Programming codes using OpenCV library to (1) fuse visible (RGB) and thermal imagery with initial calibration for preliminary test, and (2) the integration of Canny edge detection is shared below:

```python
# imageFusion.py : Using hybrid module, fuses images.

import cv2
import numpy as np

#Calibration (x,y)
xcal = 7 #5.5
ycal = -28 #-17

img = cv2.imread('Data/rgb1.jpg', 1)

img = img[:,520:-520]
img = cv2.resize(img, (640, 480))
img = cv2.flip(img, 1)

M = np.float32([[1, 0, xcal], [0, 1, ycal]])
img = cv2.warpAffine(img, M, (img.shape[1], img.shape[0]))

img2 = cv2.imread('Data/IR1.jpg', 1)
img2 = cv2.resize(img2, (664, 498))
img2 = img2[9:-9,12:-12]

dst = cv2.addWeighted(img, 0.5, img2, 1, 0)
dst = dst[:int(ycal),int(xcal):]
cv2.imshow('Blended Image',dst)

img_arr = np.hstack((img, img2))
cv2.imshow('Input Images',img_arr)
cv2.imwrite('Blended1.jpg', dst)

# CannyEdge.py : Integrating Canny Edge Features

img_gray = cv2.cvtColor(img, cv2.COLOR_BGR2GRAY) # Convert to graycsale
# Blur the image for better edge detection
img_blur = cv2.GaussianBlur(img_gray, (3,3), 0)

# Canny Edge Detection
edges = cv2.Canny(image=img_blur, threshold1=200, threshold2=1)
# Display Canny Edge Detection Image
cv2.imshow('Canny Edge Detection', edges)
cv2.imwrite('CannyEdgeRGBP1.jpg', edges)
cv2.waitKey(0)
cv2.destroyAllWindows()
```

Programming codes for the two ESP32 boards and one of the receiving ESP8266 boards are shared below. Board 1 deals with CO2 and Temperature sensors and integrates the control UI with the Rainmaker App. This board also receives App-based user actions, which it sends to board 2 through serial communication. Board2 uses ESP-NOW protocol to send wireless data to the wind tower, which contains receiving nodes as ESP8266 devices to actuate the damper. Arduino IDE software was used for programming.

ESP32_Board_1.ino :

```
// Including Relevant Libraries
#include "RMaker.h"    //Rainmaker App Library
#include "WiFi.h"
#include "WiFiProv.h"
#include <SimpleTimer.h>   //Timer library
#include <wifi_provisioning/manager.h>
#include "esp_rmaker_scenes.h"   //Rainmaker App Scheduling Service
#include <HardwareSerial.h>    //Serial communication
#include "SparkFun_SCD4x_Arduino_Library.h" //CO2 Sensor
#include <Wire.h>    //Serial library
SCD4x mySensor;

HardwareSerial Unit1(2);

#define DEFAULT_Temperature 0
#define DEFAULT_CO2 0

// BLE Credentials (For the Rainmaker App)
const char *service_name = "Controller";
const char *pop = "DD";

bool cloud = false;
bool wifi_connected = 0;
int damper1 = 90;
int damper2 = 90;
int damper3 = 90;
int timer30 = 0;
int p1 = 0;
int p2 = 0;
int p3 = 0;
bool switch_state = true;
static uint8_t gpio_reset = 15;
```

193

```cpp
//--------- Declaring Devices ----------//

static TemperatureSensor temperature("Temperature");
static Device CO2("CO2 (ppm)", "custom.device.co2");

//static Switch my_switch("Relay", &relay);
static Switch my_switch1("Damper 1"); // Adding Damper1 device
static Switch my_switch2("Damper 2"); // Adding Damper2 device
static Switch  my_switch3("Damper 3"); // Adding Damper3 device

void sysProvEvent(arduino_event_t *sys_event)
{
  switch (sys_event->event_id) {
    case ARDUINO_EVENT_PROV_START:
#if CONFIG_IDF_TARGET_ESP32
      Serial.printf("\nProvisioning Started with name \"%s\" and PoP
\"%s\" on BLE\n", service_name, pop);
      printQR(service_name, pop, "ble");
#else
      Serial.printf("\nProvisioning Started with name \"%s\" and PoP
\"%s\" on SoftAP\n", service_name, pop);
      printQR(service_name, pop, "softap");
#endif
      break;
    case ARDUINO_EVENT_WIFI_STA_CONNECTED:
      Serial.printf("\nConnected to Wi-Fi!\n");
      wifi_connected = 1;
      delay(100);
      break;
    case ARDUINO_EVENT_PROV_CRED_RECV: {
        Serial.println("\nReceived Wi-Fi credentials");
        Serial.print("\tSSID : ");
        Serial.println((const char *) sys_event-
>event_info.prov_cred_recv.ssid);
        Serial.print("\tPassword : ");
        Serial.println((char const *) sys_event-
>event_info.prov_cred_recv.password);
        break;
      }
    case ARDUINO_EVENT_PROV_INIT:
      wifi_prov_mgr_disable_auto_stop(10000);
      break;
    case ARDUINO_EVENT_PROV_CRED_SUCCESS:
      Serial.println("Stopping Provisioning!!!");
      wifi_prov_mgr_stop_provisioning();
      break;
  }
}
```

```cpp
void write_callback(Device *device, Param *param, const param_val_t val,
void *priv_data, write_ctx_t *ctx)
{
  const char *device_name = device->getDeviceName();
  const char *param_name = param->getParamName();
  Serial.printf("Received value = %d for %s - %s\n", val.val.i,
device_name, param_name);
  if (strcmp(device_name, "Damper 1") == 0)
  {
    if(strcmp(param_name, "Power") == 0) {
    Serial.printf("Received value = %s for %s - %s\n", val.val.b? "true"
: "false", device_name, param_name);
    switch_state = val.val.b;
    (switch_state == false) ? p1 = 1 : p1 = 90;
    param->updateAndReport(val);}
  }
  if (strcmp(device_name, "Damper 2") == 0)
    {
    if(strcmp(param_name, "Power") == 0) {
    Serial.printf("Received value = %s for %s - %s\n", val.val.b? "true"
: "false", device_name, param_name);
    switch_state = val.val.b;
    (switch_state == false) ? p2 = 1 : p2 = 90;
    param->updateAndReport(val);}
  }

    if (strcmp(device_name, "Damper 3") == 0)
  {
    if(strcmp(param_name, "Power") == 0) {
    Serial.printf("Received value = %s for %s - %s\n", val.val.b? "true"
: "false", device_name, param_name);
    switch_state = val.val.b;
    (switch_state == false) ? p3 = 1 : p3 = 90;
    param->updateAndReport(val);}
  }
  param->updateAndReport(val);

}


void setup()
{
  pinMode(gpio_reset, INPUT_PULLUP);

  Serial.begin(115200);
  Unit1.begin(115200, SERIAL_8N1, 16, 17);
```

```
//-------------------- Declaring Node --------------------//
Node my_node;
my_node = RMaker.initNode("Dhamma Dipa - Control Panel");
//esp_err_t esp_rmaker_scenes_enable();
esp_rmaker_scenes_enable();

//--------------- Adding Devices in Node ------------------//
my_node.addDevice(temperature);
my_node.addDevice(CO2);

Param co2_param("CO2 (ppm)", "custom.param.value",
value((int)DEFAULT_CO2), PROP_FLAG_READ | PROP_FLAG_TIME_SERIES);
CO2.addParam(co2_param);
CO2.assignPrimaryParam(CO2.getParamByName("CO2 (ppm)"));

// Configure Damper switch parameter
my_switch1.addCb(write_callback);  my_node.addDevice(my_switch1);
my_switch2.addCb(write_callback);  my_node.addDevice(my_switch2);
my_switch3.addCb(write_callback);  my_node.addDevice(my_switch3);
delay(50);

RMaker.enableOTA(OTA_USING_PARAMS);
RMaker.enableTZService();
RMaker.enableSchedule();

Serial.printf("\nStarting ESP-RainMaker\n");
RMaker.start();

WiFi.onEvent(sysProvEvent);

#if CONFIG_IDF_TARGET_ESP32
  WiFiProv.beginProvision(WIFI_PROV_SCHEME_BLE,
WIFI_PROV_SCHEME_HANDLER_FREE_BTDM, WIFI_PROV_SECURITY_1, pop,
service_name);
#else
  WiFiProv.beginProvision(WIFI_PROV_SCHEME_SOFTAP,
WIFI_PROV_SCHEME_HANDLER_NONE, WIFI_PROV_SECURITY_1, pop, service_name);
#endif

delay(1000);
Wire.begin();
if (mySensor.begin() == false){
     Serial.println(F("Sensor not detected. Please check wiring.
Freezing..."));
     while (1)
     ; }
cloud = true;
```

```
}
void loop()
{
  //Send_Sensor();

  if(wifi_connected && cloud == true && timer30 >= 60) {   // if sensor
reading ready
    if(mySensor.readMeasurement()) {
    Serial.println("Sending Sensor's Data");
    Send_Sensor();
    timer30 = 0;}
  }

  // Read GPIO0 (external button to gpio_reset device
  if (digitalRead(gpio_reset) == LOW) {
    Serial.printf("reset Button Pressed!\n");
    delay(100);
    int startTime = millis();
    while (digitalRead(gpio_reset) == LOW) delay(50);
    int endTime = millis();
    if ((endTime - startTime) > 2500) {
      Serial.printf("reset to factory.\n");
      RMakerFactoryReset(2);
    }}

// Sending serial data to Board2:

String msg = String(p1) + "!p1!" + String(p2) + "!p2!" + String(p3) +
"!p3!";

  if(Unit1.available())
    Unit1.write(msg.c_str(), msg.length());
    //Serial.print("damper1 = "); Serial.println(damper1);
  //Serial.print("damper2 = "); Serial.println(damper2);
  //Serial.print("damper3 = "); Serial.println(damper3);
  timer30 += 1;
  delay(1000);
}

void Send_Sensor()
{
  float t = mySensor.getTemperature();
  float tt = round(t*10)/10.0;
  int h = int(mySensor.getCO2())+35;
  temperature.updateAndReportParam("Temperature", tt);
  CO2.updateAndReportParam("CO2 (ppm)", h);

}
```

ESP32_Board_2.ino :

```
#include <esp_now.h>
#include <WiFi.h>
#include <Arduino.h>
#include <HardwareSerial.h>

typedef struct message {
    int pos1;
    int pos2;
    int pos3;
};
struct message myMessage;
uint8_t mac_peer1[] = {0x94, 0xB9, 0x7E, 0x10, 0x5E, 0x34};
uint8_t mac_peer2[] = {0xA4, 0xE5, 0x7C, 0xB3, 0x19, 0x2A};
uint8_t mac_peer3[] = {0xA4, 0xE5, 0x7C, 0xB3, 0x05, 0x3F};
esp_now_peer_info_t peer1;
esp_now_peer_info_t peer2;
esp_now_peer_info_t peer3;

HardwareSerial Unit2(2); //Serial Receiver

int p1 = 91; int pp1;
int p2 = 91; int pp2;
int p3 = 91; int pp3;

void setup() {
  Serial.begin(115200);
  Serial.println("Restarted!");
  WiFi.mode(WIFI_STA);
}
  memcpy(peer1.peer_addr, mac_peer1, 6);
  peer1.channel = 1; peer1.encrypt = 0;
  esp_now_add_peer(&peer1);

  memcpy(peer2.peer_addr, mac_peer2, 6);
  peer2.channel = 1; peer2.encrypt = 0;
  esp_now_add_peer(&peer2);

  memcpy(peer3.peer_addr, mac_peer3, 6);
  peer3.channel = 1; peer3.encrypt = 0;
  esp_now_add_peer(&peer3);

  delay(2000);
  Unit2.begin(115200, SERIAL_8N1, 16, 17);
  Serial.println("Serial Ready!");

  }
```

```cpp
void loop() {

  if(Unit2.available()) {
    //  Serial.println(Unit2.read());
      p1 =
Unit2.readStringUntil('!p1!').toInt();Unit2.readStringUntil('!p1!');
      p2 =
Unit2.readStringUntil('!p2!').toInt();Unit2.readStringUntil('!p2!');
      p3 =
Unit2.readStringUntil('!p3!').toInt();Unit2.readStringUntil('!p3!'); }

 pp1 = int(p1);
 pp2 = int(p2);
 pp3 = int(p3);

if(int(p1) == 1) pp1 = 0;
if(int(p2) == 1) pp2 = 0;
if(int(p3) == 1) pp3 = 0;

 Serial.print("pos1 = "); Serial.println(pp1);
 Serial.print("pos2 = "); Serial.println(pp2);
 Serial.print("pos3 = "); Serial.println(pp3);
 delay(100);

 if(p1==0&&p2==0&&p3==0){
   Serial.println("Restarting..");
   ESP.restart();}
 else if(p1==91&&p2==91&&p3==91) { Serial.println("P = 91");}
 else
 sendESPNOWData();
}

void sendESPNOWData() {

  Serial.println("Sending ESPNOW Data..");
  myMessage.pos1 = pp3;  //if inverse, then (91-p1)+cal1; //90-p1?
  myMessage.pos2 = pp2;
  myMessage.pos3 = pp1;
  Serial.println("Data sent");
  esp_now_send(NULL, (uint8_t *)&myMessage, sizeof(myMessage));
}
```

ESP8266_Nodes.ino :

```cpp
#include <Arduino.h>
#include <ESP8266WiFi.h>
#include <espnow.h>

typedef struct message {
    int pos1, pos2, pos3;
} message;

message myMessage;

unsigned long currentMillis = millis();
bool ready = false;
int p1 = 0, p2 = 0, p3 = 0, p = 90;
int relay1 = 4, relay2 = 5; // Damper and TEC relay pins
int led = 13;


void onDataReceiver(uint8_t * mac, uint8_t *incomingData, uint8_t len) {
    Serial.println("Message received.");

  memcpy(&myMessage, incomingData, sizeof(myMessage));
    Serial.print("pos1:");   Serial.println(myMessage.pos1); p1 =
myMessage.pos1;
    Serial.print("pos2:");   Serial.println(myMessage.pos2); p2 =
myMessage.pos2;
    Serial.print("pos3:");   Serial.println(myMessage.pos3); p3 =
myMessage.pos3;
}
void setup() {
  Serial.begin(115200);
  WiFi.disconnect();
  ESP.eraseConfig();

  pinMode(led, OUTPUT);
  pinMode(relay1, OUTPUT);
  pinMode(relay2, OUTPUT);

  WiFi.mode(WIFI_STA);
 // WiFi.setPhyMode(WIFI_PHY_MODE_11N); // Set the WiFi mode to 802.11n
  WiFi.channel(1);  //{3} channel 1, {2} channel  , {1} channel 6
  Serial.print("Mac Address: "); Serial.print(WiFi.macAddress());
  Serial.println("\nESP-Now Receiver");

  // Initializing the ESP-NOW
```

```
  if (esp_now_init() != 0) {
    Serial.println("Problem during ESP-NOW init");
    return;   }
  esp_now_register_recv_cb(onDataReceiver);
digitalWrite(relay1, HIGH);
digitalWrite(relay2, HIGH);
digitalWrite(led, HIGH);
  ready = true;
}
void loop() {
    if(p3 < p) {p=p-1; digitalWrite(led, HIGH);}
    else if(p3 > p) {p=p+1; digitalWrite(led, HIGH);}
    else digitalWrite(led, LOW);
    if(p>90) p = 90;
    if(p<0) p = 0;

    if(p3==0) { digitalWrite(relay1, HIGH); digitalWrite(relay2, LOW);}
    if(p3==90) { digitalWrite(relay2, HIGH); digitalWrite(relay1, LOW);}
    if(p3==45) { digitalWrite(relay1, HIGH); digitalWrite(relay2, HIGH);}

    delay(1666);
}
```

Appendix D: Supplementary Experimental Data

Appendix D-1: Heating potential through TEMs

The focus of this thesis was to examine the cooling potential of the proposed TEC-based heat pipe assisted cooling for wind towers. As indicated in Chapter 5, section 5.4.2, switching the polarity of the current through the TEMs reverses the direction of the heat flux. This was tested on a single-pipe experiment (using the same setup of Experiment 2) as a proof of concept for the proposed system as a versatile solution for all seasons. Table D-1 shows the change in pipe surface temperatures (ΔT) when cooled and heated from an ambient temperature of 22°C against different voltage input.

Table D-1 – Cooling and Heating ΔT using TEC heat pipe conduction

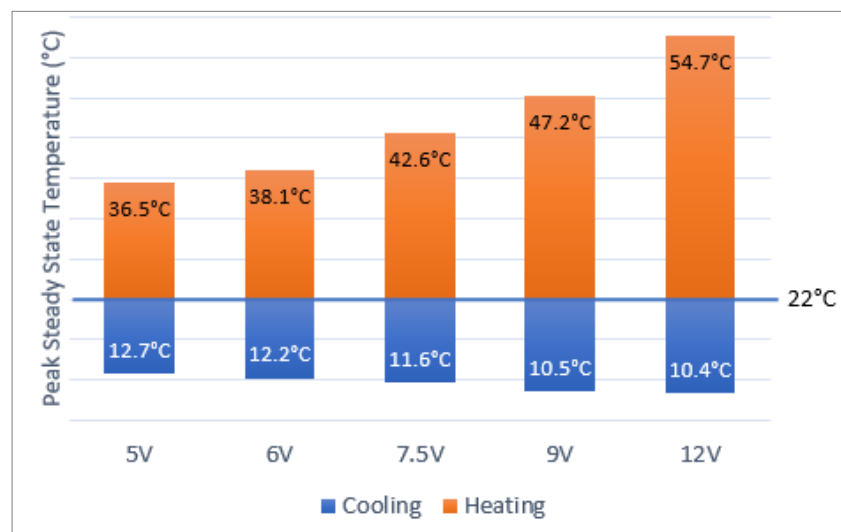| VOLTAGE (V)	5V	6V	7.5V	9V	12V
COOLING (°C)	9.3	9.8	10.4	11.5	11.6
HEATING (°C)	14.5	16.1	22.6	25.2	32.7

Figure D-1 – Single pipe conductive cooling and heating potential using TECs

Figure D-1 shows the bar chart illustrating the peak steady state temperatures achieved for each set of voltage relative. The conductive heating capacity against each input power matched as with cooling, however, the heating tests show a much higher heating capability as compared to cooling capacity thanks to the internal heat (Joule heating) aiding the heat accumulation on the hot side.

Appendix D-2: Experiment 5 – Specifications of Instruments

Table D-2 presents the details of measured variables in experiment 5 and the specifications of the instruments used for these measurements.

Table D-2 – Details of measured variables and instruments used.

Variable	Instrument used for measurement	Calibration	Uncertainty of measurement
Air flow rate	Furness Controls LFE FCO96 Display FCO332	In-situ cross calibration with nozzle box using Furness FCO560 Calibrator Furness Controls (UKAS)	< ±3%
Air temperature readings	PT100 1/10th DIN probes	In-situ 5 point temperature calibration with Isotech MilliK with 935-14-112 PRT Isotech (UKAS)	< ±0.1°C
Air relative humidity readings	Vaisala HMP110	In-situ 8-point calibration with Michell S8000 Mirror Michell (Traceable NIST)	< ±2% RH
Duct pressure	Furness Controls FCO332	In-situ 20 point pressure calibration with Furness FCO560 Calibrator Furness Controls (UKAS)	< ±1% or ±2 Pa
Atmospheric pressure	Druck DPI 260	Furness Controls (UKAS)	< ±0.09% (±90 Pa)
Absorbed electrical power	Yokogawa WT310E	Caltest (UKAS)	< ±1%

Table D-3, Table D-4 and Table D-5 show the data logged from the air temperature readings of fresh air, supply, extract air and exhaust air along with the measured flowrates and power consumption at 25°C, 30°C and 35°C respectively. Q_{elec} refers to the total power consumption of the TEC and heat dissipation fan system.

Table D-3 – Experiment 5 measured data for air flow from 50L/s to 300 L/s at 25℃

Ambient Temp / Air Flow	Temperatures				Volumetric Flow Rate		Mass Flow Rate		Power Consumption
T_{AMB} / VFR	T_{FA}	T_{SUP}	T_{EXT}	T_{EXH}	FA	EXH	FA	EXH	Q_{elec}
(°C/ L/s)	(°C)				(L/s)		(g/s)		(W)
25/50	25.05	24.11	20.03	20.84	53.30	51.60	62.90	61.80	393
25/75	24.95	24.07	20.00	20.60	75.00	73.40	88.60	88.00	393
25/100	24.94	24.44	19.94	20.65	99.00	98.30	117.00	117.80	390
25/200	24.85	24.62	19.96	21.11	198.30	200.90	235.30	241.40	394
25/300	24.99	24.77	20.06	21.10	301.10	297.20	356.60	356.60	399

Table D-4 – Experiment 5 measured data for air flow from 50L/s to 300 L/s at 30℃

Ambient Temp / Air Flow	Temperatures				Volumetric Flow Rate		Mass Flow Rate		Power Consumption
T_{AMB} / VFR	T_{FA}	T_{SUP}	T_{EXT}	T_{EXH}	FA	EXH	FA	EXH	Q_{elec}
(°C/ L/s)	(°C)				(L/s)		(g/s)		(W)
30/50	29.99	27.69	19.96	21.52	49.60	48.50	57.60	57.90	393
30/75	30.13	28.28	20.02	21.40	75.90	73.60	88.10	88.00	393
30/100	30.16	29.13	20.19	21.93	101.60	97.80	118.00	116.80	389
30/200	29.89	29.41	19.86	22.17	201.20	196.10	234.00	234.00	388
30/300	29.95	29.52	20.02	22.05	304.50	288.40	354.10	344.40	397

Table D-5 – Experiment 5 measured data for air flow from 50L/s to 300 L/s at 35°C

Ambient Temp / Air Flow	Temperatures				Volumetric Flow Rate		Mass Flow Rate		Power Consumption
T_{AMB} / VFR	T_{FA}	T_{SUP}	T_{EXT}	T_{EXH}	FA	EXH	FA	EXH	Q_{elec}
(°C/ L/s)	(°C)				(L/s)		(g/s)		(W)
35/50	34.91	31.30	19.98	22.34	50.70	48.20	58.00	57.50	380
35/75	35.04	32.10	19.95	21.96	76.00	71.90	86.80	85.70	393
35/100	35.06	33.42	20.19	22.82	101.30	97.10	115.60	115.30	388
35/200	35.02	34.19	20.09	23.30	200.00	192.00	227.90	227.30	391
35/300	34.95	34.08	19.99	22.60	292.80	295.50	333.00	350.00	397